ANNUAL REPORT

Center for Experimental Nuclear Physics and Astrophysics
University of Washington
April, 2013

Sponsored in part by the United States Department of Energy
under Grant #DE-FG02-97ER41020.

Cover design by Greg Harper and Matt Turner. The background image on the front cover is a photo of a painted steel sheet with the CENPA logo cut into it by the new laser cutter (see Sec. 9.5) attached to the laser cutter honeycomb table (photo by Matt Turner). The top photo depicts grad student Yelena Bagdasarova assembling the e-field electrode system for the detector for the ^{6}He experiment (see Sec. 3.8) in experimental cave 1 (photo by Greg Harper). In the bottom photo, postdoc Frederik Wauters and grad student Rachel Ryan are shown assembling the test time projection chamber for the MuSun experiment (see Sec. 4.4) in the muon lab at CENPA (photo by Michael Murray). The back cover of the report is a photo of the exposed honeycomb table of the laser cutter.

INTRODUCTION

The Center for Experimental Nuclear Physics and Astrophysics, CENPA, was established in 1998 at the University of Washington as the institutional home for a broad program of research in nuclear physics and related fields. Research activities are conducted locally and at remote sites. CENPA has been a major participant in the Sudbury Neutrino Observatory (SNO) and is presently contributing substantially to the KATRIN tritium-beta-decay experiment, the MAJORANA ^{76}Ge double-beta-decay experiment, and to Project 8, a new concept for determining the mass of the neutrino. SNO has evolved into SNO+, a scintillator experiment that will be sensitive to low-energy solar neutrinos and that can be loaded with double-beta decay isotopes such as ^{130}Te. The Muon physics group is developing the MuSun experiment to measure muon capture in deuterium at the Paul Scherrer Institute in Switzerland and a new program to measure the anomalous magnetic moment of the muon at Fermilab to even higher precision than it is presently known from the group's previous work at Brookhaven. The fundamental symmetries program also includes "in-house" research using the local tandem Van de Graaff accelerator with a new experiment to measure the electron-neutrino correlation and Fierz interference in ^{6}He decay, and neutron physics at other locations. We conduct user-mode research on relativistic heavy ions at the Relativistic Heavy Ion Collider at Brookhaven.

Following an international search, we are very pleased to welcome Jason Detwiler to the Department of Physics and CENPA as Assistant Professor. Jason took his PhD with Giorgio Gratta at Stanford, was a Seaborg Fellow at Lawrence Berkeley National Lab after a postdoc with us, and has now returned to Seattle. He leads our effort on MAJORANA.

Postdoctoral Fellow Hok Seum Wan Chan Tseung ("Wan") took a position as Research Scientist at the Mayo Clinic in June, 2012. Peter Winter left in July to become Staff Scientist at Argonne National Laboratory. Andreas Knecht and Brendan Kiburg both departed in August. Andreas took a prestigious CERN Fellowship, and after less than a year was recruited into a permanent position at the Paul Scherrer Institute. Brendan won a highly selective Lederman Fellowship at Fermilab. Pete Alonzi joined us from the University of Virginia in June and is working with the Muon group.

We were very sorry to lose Research Scientist/Engineer Nora Boyd, but cheer her on as she pursues a PhD at Pittsburgh. The new face in our technical staff is Eric Smith, who signed on in October, 2012, and has already pitched in on many projects to great effect.

It was a good year for PhDs. Sara Knaack and Jason Crnkovic, both of whom came to CENPA with the Muon group, graduated with degrees from the University of Illinois in June and December, respectively. Alexis Schubert graduated in December and is now a postdoc with Giorgio Gratta at Stanford. Brandon Wall graduated in March just before we went to press.

We note with sadness the unexpected death of Stuart Freedman in November, 2012. Stuart was a long-standing member of our Advisory Committee, a distinguished physicist, and a close friend to many of us at CENPA. He is greatly missed.

The DOE Office of Nuclear Physics, which provides operating support through programs in Low Energy Nuclear Physics and Heavy Ion Physics, renewed our grant DE-FG02-

97ER41020 for FY12-14 with some additional support for the new program in muon physics. The continued support of CENPA by the Office of Nuclear Physics, especially in the current difficult fiscal climate, is greatly appreciated. In the following paragraphs we record some of the highlights of our past year in research.

- Since being shipped to Germany and installed, the KATRIN detector system has undergone significant upgrades. A custom, high-efficiency heat pipe for improved detector and electronics cooling, 148 preamplifier channels featuring a lower-noise FET, vacuum systems featuring a more robust post-acceleration electrode and high-vacuum chamber, a more uniform illumination system for the photoelectron source, shields against radioactivity emanating from the glass insulators of the detector feedthrough, and high-speed data acquisition to monitor possible magnet quenches have been installed and operational on the detector system at the Karlsruhe Institute of Technology (KIT).

- Commissioning of the upgraded KATRIN detector at KIT is complete. The performance satisfies both the future commissioning needs as well as the physics goals of the experiment. The performance will be reported in a paper being prepared for submission to Nuclear Instruments and Methods.

- In March, 2013, the detector and DAQ systems passed an Operational Readiness Review, the first of the KATRIN systems to undergo such a review. The detector is now ready for use in commissioning the KATRIN spectrometer, beamline, and source hardware.

- CENPA Engineer Tom Burritt designed and built in-beam valves that were installed on the main spectrometer in November, 2012. These valves fit entirely inside superconducting magnets and enable the detector and the prespectrometer to be attached to the main spectrometer while it is under vacuum. The valves will see their first use in May, 2013.

- UW has provided a suite of near-time data analysis tools for the detector data. These data visualization tools are an essential component in efficiently commissioning the remaining KATRIN hardware.

- The HALO supernova detector in SNOLAB, a 79-tonne Pb target instrumented with the low-background neutron proportional counters from SNO, was completed and began regular operations in May, 2012.

- The final MuCap determination of the weak-pseudoscalar coupling of the proton was published in Phys. Rev. Lett. (Editor's choice), with the result $g_P = 8.06 \pm 0.55$; it is in excellent agreement with the precise prediction from chiral perturbation theory.

- The $g-2$ Experiment received CD-0 approval, DOE's statement of mission need under their protocol for the management of large projects. The UW efforts span Beam, Ring, Field, and Detector.

- We commissioned a new area at PSI for the permanent home of the MuSun experiment and completed a test run there in preparation for physics running in 2013 and 2014.

- Optimization of parameters in our ^{6}He source brought it to delivering approximately 10^{10} atoms per second in a stable manner. Presently this is the most intense source of ^{6}He atoms in the world and allows for pursuing precise searches for Tensor currents in the decay of ^{6}He using laser traps.

- Using the ^{6}He source we have made an accurate determination of the ^{6}He lifetime solving previous discrepancies and providing, in combination with ab-initio nuclear-structure calculations, for a determination of the axial coupling constant, g_A. This showed agreement with g_A from neutron beta decay indicating that the quenching of g_A in the nuclear medium in the case of ^{6}He is comparable to or smaller than the uncertainties in the nuclear structure calculations[1,2].

- From STAR data at 62 and 200 GeV we have determined that more-peripheral Au-Au collisions (the 'lower half' of the Au-Au total cross section) are essentially transparent to low-momentum partons and hadrons (i.e., a simple N-N linear superposition, with no secondary scattering). In contrast, the nonjet azimuth quadrupole structure conventionally identified with elliptic flow increases to 60% of its maximum amplitude within the same centrality interval. In more-central collisions (the 'upper half' of the total cross section) parton fragmentation to jets is strongly modified but the quadrupole continues to follow the same systematic trend with centrality. The sharp contrast between quadrupole and dijet systematics casts doubt on claims for formation of a strongly-coupled quark-gluon plasma or "perfect liquid."

As always, we encourage outside applications for the use of our facilities. As a convenient reference for potential users, the table on the following page lists the capabilities of our accelerators. For further information, please contact Greg Harper, Associate Director, CENPA, Box 354290, University of Washington, Seattle, WA 98195; (206) 543 4080, or gharper@u.washington.edu. Further information is also available on our web page: http://www.npl.washington.edu.

We close this introduction with a reminder that the articles in this report describe work in progress and are not to be regarded as publications or to be quoted without permission of the authors. In each article the names of the investigators are listed alphabetically, with the primary author underlined in the case of multiple authors, to whom inquiries should be addressed.

Hamish Robertson, Director — Victoria Clarkson, Assistant Editor
Greg Harper, Associate Director and Editor — Gary Holman, Technical Editor

[1] A. Knecht *et al.*, Phys. Rev. Lett. **108**, 122502 (2012).
[2] A. Knecht *et al.*, Phys. Rev. C **86**, 035506 (2012).

TANDEM VAN DE GRAAFF ACCELERATOR

Our tandem accelerator facility is centered around a High Voltage Engineering Corporation Model FN purchased in 1966 with NSF funds, with operation funded primarily by the U.S. Department of Energy. See W. G. Weitkamp and F. H. Schmidt, "The University of Washington Three Stage Van de Graaff Accelerator," *Nucl. Instrum. Methods* **122**, 65 (1974). The tandem was adapted in 1996 to an (optional) terminal ion source and a non-inclined tube #3, which enables the accelerator to produce high intensity beams of hydrogen and helium isotopes at energies from 100 keV to 7.5 MeV.

Some Available Energy Analyzed Beams

Ion	Max. Current (particle μA)	Max. Energy (MeV)	Ion Source
^{1}H or ^{2}H	50	18	DEIS or 860
^{3}He or ^{4}He	2	27	Double Charge-Exchange Source
^{3}He or ^{4}He	30	7.5	Tandem Terminal Source
^{6}Li or ^{7}Li	1	36	860
^{11}B	5	54	860
^{12}C or ^{13}C	10	63	860
^{*14}N	1	63	DEIS or 860
^{16}O or ^{18}O	10	72	DEIS or 860
F	10	72	DEIS or 860
* Ca	0.5	99	860
Ni	0.2	99	860
I	0.001	108	860

*Negative ion is the hydride, dihydride, or trihydride.

Several additional ion species are available including the following: Mg, Al, Si, P, S, Cl, Fe, Cu, Ge, Se, Br and Ag. Less common isotopes are generated from enriched material. We recently have been producing the positive ion beams of the noble gases He, Ne, Ar, and Kr at ion source energies from 10 keV to 100 keV for implantation, in particular the rare isotopes ^{21}Ne and ^{36}Ar. We have also produced a separated beam of 15-MeV ^{8}B at 6 particles/second.

Contents

1 Neutrino Research

KATRIN

1.1 Overview of the KATRIN experiment

J. F. Amsbaugh, J. Barrett*, A. Beglarian†, T. Bergmann†, L. I. Bodine, T. H. Burritt, N. M. Boyd‡, T. J. Corona§, P. J. Doe, S. Enomoto, J. A. Formaggio*, F. M. Fränkle§, D. L. Furse*, F. Harms†, G. C. Harper, M. Knauer†, A. Kopmann†, E. L. Martin, N. S. Oblath*, D. S. Parno, D. A. Peterson, L. Petzold†, D. Phillips§, A. W. P. Poon¶, P. Renschler†, R. G. H. Robertson, M. Steidl†, J. Schwarz†, D. Tcherniakhovski†, B. A. VanDevender‖, T. D. Van Wechel, B. L. Wall**, K. J. Wierman§, J. F. Wilkerson§, and S. Wüstling†

The goal of the KArlsruhe TRItium Neutrino experiment is to probe the mass of the neutrino to a sensitivity of 200 meV by making a precision measurement of the shape of the electron spectrum resulting from tritium beta decay. Distortion at the high-energy end of the spectrum provides information regarding the mass of the neutrino in a direct, model-independent way.

Tritium is an ideal isotope for this type of investigation. The low Q value facilitates the study of the endpoint of the spectrum, and the half life of 12.3 years makes it compatible with a typical experiment's duration. The KATRIN experimental technique represents the culmination of 64 years of tritium beta decay studies. Electrons from a 10^{11}- Bq, windowless, gaseous tritium source (WGTS) are directed by a chain of superconducting magnets towards a pair of retarding-potential spectrometers. This transport system consists of a Differential Pumping System, utilizing turbomolecular pumps to return tritium escaping the WGTS back to the source, and a Cryogenic Pumping System that traps any remaining tritium on a surface of argon frost, thereby preventing the tritium from entering and contaminating the spectrometers. These two systems reduce the tritium partial pressure by 14 orders of magnitude before reaching the spectrometers. The first spectrometer, the low-resolution pre-spectrometer, has a retarding potential of approximately -18.3 kV, which reduces the electron flux by a factor of 10^7 and leaves only the interesting high energy electrons in the last 300 eV of the spectrum. The second, the main spectrometer, provides a design resolution of 0.93 eV. By varying the precise retarding potential of the spectrometer, only electrons of a well-defined energy pass from the main spectrometer to be counted by the PIN diode detector. Thus the end of the electron spectrum can be mapped out by a series of integrating measurements.

The KATRIN collaboration, formed in 2001, consists of approximately 120 scientists from 5 countries. The experiment adjoins the Tritium Laboratory at the Karlsruhe Institute of

*Massachusetts Institute of Technology, Cambridge, MA.
†Karlsruhe Institute of Technology, Karlsruhe, Germany.
‡Departed August, 2012, presently at University of Pittsburgh, Pittsburgh, PA.
§University of North Carolina, Chapel Hill, NC.
¶Lawrence Berkeley National Laboratory, Berkeley, CA.
‖Pacific Northwest National Laboratory, Richland, WA.
**Graduated March, 2013.

Technology (KIT). The initial US responsibility, to provide the detector and data-acquisition system, has expanded to include major contributions to both the simulation and analysis tasks and to the rear system which is used to monitor the tritium source.

Commissioning of the detector system at KIT is complete and the performance is described (see Sec. 1.4). The system will be used as a tool in commissioning the remaining components of the KATRIN experiment. Data-taking with tritium is expected to begin in late 2015 and to reach the design sensitivity by 2020.

1.2 Status of the KATRIN experiment

P. J. Doe

Construction and commissioning of components for the KATRIN experiment is taking place both on site at the Karlsruhe Institute of Technology (KIT) and at manufacturers' facilities. Currently at KIT are the prespectrometer, the main spectrometer, the monitor spectrometer, and the detector system. Pending the outcome of problems with system isolation valves, the detector will be connected to the main spectrometer and approximately one year will be spent using an electron gun to commission first the main spectrometer, then the spectrometer and prespectrometer as a pair. By the time this task is complete, additional transport and source components will appear on site for commissioning and incorporation into the overall KATRIN apparatus.

The main components of the KATRIN experimental setup are shown schematically in Fig. 1.2-1 and their status is given below.

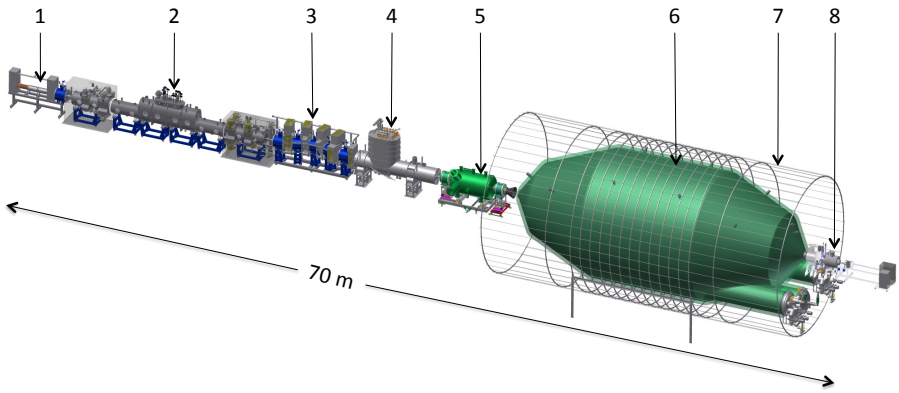

Figure 1.2-1. The layout of the KATRIN experiment. 1) rear system, 2) windowless, gaseous tritium source, 3) differential pumping system, 4) cryogenic pumping system, 5) prespectrometer, 6) main spectrometer, 7) compensation coils for Earth's magnetic field, 8) detector system.

- Rear section (RS)
  The RS of KATRIN establishes the potential of the tritium plasma and, by means of

an electron gun, provides important diagnostics for the entire KATRIN beamline from source to detector.

The design of the RS, which is being led by the University of California at Santa Barbara, has undergone a significant improvement. By installing an additional superconducting solenoid magnet (see Transport section below) between the rear wall of the tritium source and the electron gun, the design is considerably simplified and allows both the rear wall and the electron gun to be isolated from the tritium source, should maintenance be required. Construction of the RS is expected to be complete in April 2014 and commissioning completed by October, 2014, by which time the RS will be required for commissioning the tritium source.

- Windowless, Gaseous Tritium Source (WGTS)
  After successfully demonstrating that it can achieve the necessary temperature stability of the tritium source (ΔT$<$ 10 mK) the central source tube of the WGTS was shipped back to Research Instruments (RI) in October, 2012. The hardware is now being dismantled in preparation for mating to the train of turbomolecular pumps and magnets located at each end of the source, by which means the tritium gas is returned to the source. These magnets have been modified according to the lessons learned in the successful magnet tests carried out at Saclay, incorporating redesigned, replaceable diodes and a safety system allowing the magnets to run in driven mode. Whether to assemble the WGTS at RI or at KIT is under discussion with a decision expected in May, 2013. Assembly of the WGTS is expected to be complete at the end of 2013.

- Transport section
  The first component of the transport system, the differential pumping system (DPS) was delivered to KIT late in 2010. Although it met the tritium reduction design goal the DPS failed the magnet tests due to faulty diode protection for the magnet coils. Modifying the DPS to enable replacement of these diodes was judged to be too uncertain and in December, 2012 the system was removed from the KATRIN experimental hall. A simpler design, using individual magnets of a similar design and manufacture as used in the detector system, has been developed and passed technical review. The order for the five superconducting solenoids has been placed and manufacture begun. In addition, a sixth solenoid has been ordered, enabling significant design improvements to be made to the rear section described above. These magnets will be delivered to KIT in March, 2014. Commissioning of the new DPS will begin in summer of 2014 with completion optimistically scheduled for the end of 2014.

  The cryogenic pumping system (CPS) also suffered problems with its magnet protection diodes. In the case of the CPS it was possible to modify the magnet cryostats to allow access to replace the diodes. This has been successfully done for all seven magnet modules and the first of the replacement diodes has passed cold testing at 200 A. The factory acceptance test of the CPS is expected to take place in February, 2014.

- Spectrometers
  The main spectrometer was baked out over the period 19 December, 2012, to 7 February, 2013, achieving a final pressure of 3.3×10^{-10} mbar and temperature of 300° C. The maximum desired temperature of 350° C was not reached because electrical shorts

appearing between the inner and outer wire planes and a leak in an instrumentation flange resulted in early termination of the baking plan. However, the NEG pumps, which require 350° C to be fully activated, appear to be performing to specification, although as a result of the leak the pump may be close to saturation. A means of regenerating the NEG pumps without baking the entire vessel is being devised.

The shorts between the two wire planes were traced to the 3-mm-diameter CuBe rods used to connect the wire planes. At temperatures above 200° C the modulus of rigidity is reduced by more than a factor of 10, resulting in the wires sagging under their own weight and shorting to other rods. Ways of correcting this situation and replacing the flange seal are under investigation.

The effects of the shorted wire planes have been simulated. The shielding from electrons produced by cosmic ray interactions is reduced by a factor of 10 while the Faraday shielding is unaffected. The electric field uniformity shows variations at the position of the structural members that support the wire planes. By increasing the field of the Earth's compensation coils from 0.3 mT to 0.45 mT the flux tube can be compressed into a region of uniform electric field. Capacitive and resistive measurements showed that none of the 23,440 wires was broken and that none of the wires was shorted to the body of the spectrometer. The plan is to continue with the main spectrometer commissioning in spite of these and other problems.

The spectrometer represents a large capacitor. In order to apply a retarding potential to the hull of the spectrometer extensive safety features must be implemented before the system's final inspection. In the meantime, commissioning can proceed at a low potential. Measuring the transmission function and other properties of the main spectrometer requires the use of a sophisticated electron gun positioned at the upstream end of the spectrometer. Before deploying this electron gun it is proposed to use a simple, UW-supplied flange that, by means of collimating an ^{241}Am source, provides Compton electrons at five well-defined positions.

The UW-supplied in-beam valves allow the main spectrometer to be closed at either end to allowing removal of either the prespectrometer or the detector without bringing the main spectrometer up to atmosphere, thereby avoiding additional bake out cycles. These valves were installed in December, 2012. The valve at the detector end of the spectrometer has developed a problem and no longer seals. X-ray photos reveal the o-ring has a loop outside the groove because the wrong size was installed. However, a fairly quick strategy has been found to minimize the delay to first light," which was originally scheduled for 25 April, 2013.

The prespectrometer, a workhorse for understanding spectrometer performance since 2006, is now in its final location next to the main spectrometer. It will be attached to the main spectrometer in 2013.

The monitor spectrometer, the former, refurbished Mainz spectrometer, is installed and commissioned at KIT. The monitor spectrometer shares the same retarding potential as the main spectrometer. By observing the 17.8-keV line from ^{83m}Kr it is expected to monitor the stability of the high voltage to a sensitivity of 3 ppm. Currently it is being used to study implanted sources and background reduction techniques.

- Detector
  Numerous improvements have been implemented in the detector system and are described below. Commissioning of the system at KIT is now complete and a successful Operational Readiness Review was held on 14 March, 2013. The detector system can now be used for commissioning other KATRIN components, the first of which will be the main spectrometer. Training classes and refresher courses have been held for new users of the system. Some improvements remain to be carried out, but are not expected to impact KATRIN commissioning. The short circuit of two pixels on the detector wafer has been traced to a manufacturing problem which will be addressed by the supplier. A vacuum leak in the γ-source actuator has necessitated the purchase of a replacement unit. Finally, a rate dependence of the detector energy performance will be addressed by reprogramming the filter logic of the FPGA units of the DAQ. In March, 2013, the pinch magnet underwent two quenches. The cause is under investigation but it is suspected that there is a problem with the magnet power supply.

1.3 Detector dead-layer analysis

B. L. Wall

The KATRIN detector response is influenced by the thickness of the focal-plane detector dead layer. We developed an in-situ method to measure the detector dead layer because the standard methods are not practical due to the design constraints of the KATRIN detector system.

The KATRIN method to determine a dead-layer thickness is to use the entire shape of the electron spectrum generated by the detector system's mono-energetic electron source and compare it with simulated spectra generated by the KATRIN Electron Scattering in Silicon (KESS) package[1,2]. The simulated spectra for an assumed dead-layer value are fit to the electron-source energy spectra calculated using a χ^2 minimization technique. Spectra were generated for dead layers of thicknesses from 100 Å to 5000 Å in 100-Å increments. Electron-source data were taken at 1-keV intervals from 12.6 keV to 19.6 keV.

Rather than assuming a completely dead layer, a fraction of the energy deposited in this layer was added to the energy deposited into the active region of the detector. This alteration to the standard view of PIN-diode dead layers assumes that the electron-hole pairs generated in the dead layer do not immediately recombine, but have some probability of diffusing from the dead layer and being collected on the diode contacts.

Inclusion of the diffusion factor improved the fit results for each spectrum most dramatically for the low-energy electron data. For example, the 12.6-keV $\chi^2/n.d.f.$ improved for pixel 33 from 2.16 to 1.25. The χ^2 minimum ($\chi^2/n.d.f. = 1.15$) for all working focal-plane-detector channels occurs for a diffusion factor of $45.9 \pm .1\%$.

[1] B. Wall, *Karlsruhe Tritium Experiment: Detector System Commissioning and In-Situ PIN-Diode Array Dead-Layer Measurement.* PhD thesis, University of Washington, 2013.

[2] P. Renschler, *KESS - A new Monte Carlo simulation code for low-energy electron interactions in silicon detectors.* PhD thesis, Karlsruhe Institute of Technology, 2011.

Fig. 1.3-1 displays the results for a 46% factor with a mean dead layer. A simultaneous fit can be performed to understand the geometric variation in the focal plane detector's dead layer from pixel to pixel. A pixel's rate dependence (s_i) and radial (r_i) and (θ_i) azimuthal positions are combined with a nominal thickness D_0 to describe the pixel's thickness D_i:

$$D_i \quad = \quad D_0 + Ar_i^2 + Es_i + B\cos(\theta_i) + C\sin(\theta_i). \tag{1}$$

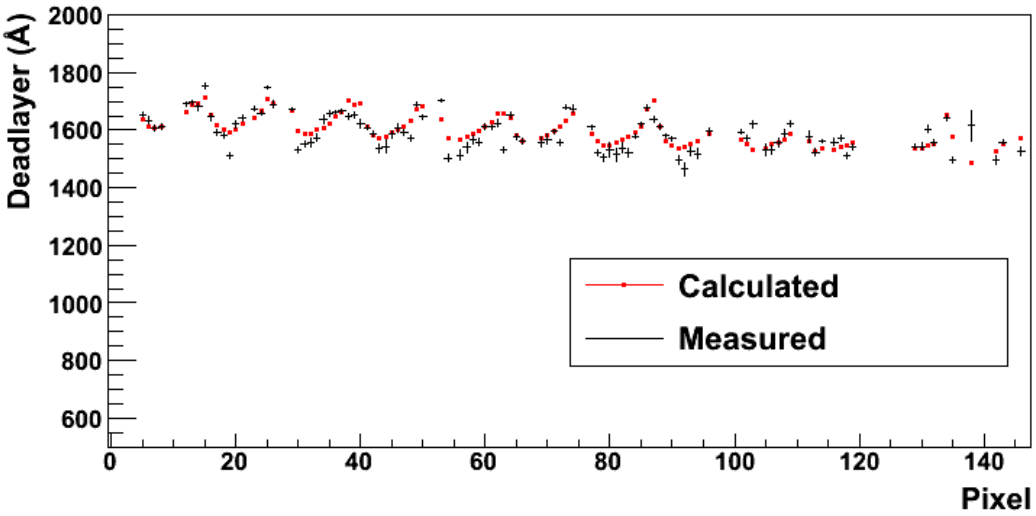

Figure 1.3-1. Measured dead-layer thickness (black) and calculated dead-layer thickness (red) from the fit of Eq. (1) plotted against pixel number.

The rate-dependent factor accounts for the rate dependence of a pixel's resolution caused by a lack of a baseline correction in the trapezoidal filter used by the KATRIN data-acquisition crate[1].

χ^2	n.d.f.	D_0 (Å)	E (Hz/Å)	A (Å/cm^2)	B (Å)	C (Å)
3913	102	1615 ± 1	0 ± 0	0 ± 0	0 ± 0	0 ± 0
2281	101	1554 ± 2	0.060 ± 0.001	0 ± 0	0 ± 0	0 ± 0
1535	99	1659 ± 2	0 ± 0	$-5.9 \pm .2$	43.8 ± 1.7	-28.9 ± 1.3
1423	100	1611 ± 3	0.052 ± 0.002	-5.6 ± 0.2	0 ± 0	0 ± 0
1193	98	1609 ± 3	0.052 ± 0.003	-5.6 ± 0.2	-4.3 ± 3.1	-18.3 ± 1.4

Table 1.3-1. Linear least-square fit parameters from Eq. (1) to the focal plane detector dead-layer pixel data. In each row a fit parameter is added to the minimization.

The multi-parameter fit finds a clear radial dependence of the dead layer as shown by the near-zero correlation factors listed in Table 1.3-2. The correlation between the rate and the azimuthal components is not surprising as the rate has a strong azimuthal dependence. It indicates that rate dependence of the dead layer may not be fully accounted for by the

[1]S. Enomoto, *Internal report: Rate dependence of peak position* (2012).

linear term. Correcting for the rate dependence yields an average dead-layer thickness for the focal-plane detector of 1554 ± 5 Å.

	D_0	A	B	C	E
D_0	1.00	-0.56	0.61	-0.28	-0.81
A	-0.56	1.00	0.03	-0.02	0.08
B	0.61	0.03	1.00	-0.42	-0.84
C	-0.28	-0.02	-0.42	1.00	0.41
E	-0.81	0.08	-0.84	0.41	1.00

Table 1.3-2. Correlation matrix for the linear least-square fit parameters from Eq. (1) to the focal plane detector pixels' dead-layer values.

1.4 Detector commissioning at KIT

J. F. Amsbaugh, A. Beglarian*, L. I. Bodine, T. H. Burritt, N. M. Boyd†, P. J. Doe, S. Enomoto, F. M. Fränkle‡, F. Harms*, E. L. Martin, D. S. Parno, R. G. H. Robertson, M. Steidl*, J. Schwartz*, B. L. Wall§ K. J. Wierman‡, J. F. Wilkerson‡, and S. Wüstling*

The FPD system was commissioned at the Karlsruhe Institute of Technology prior to the upcoming SDS commissioning. The detector system underwent a subsequent operational readiness review and was deemed to be ready for use in SDS commissioning. Some problems were encountered during commissioning and some upgrades are still planned.

- A leak in the HVac system developed due to a crack in the weld between the main part of the HVac chamber and the cyropump standpipe. A new HVac chamber was constructed with a redesigned standpipe and installed in early December, 2012. There is also a known leak on the γ-source actuator bellows resulting in poor vacuum in the XHVac system. The γ-source actuator was removed and the bellows is being replaced by the manufacturer.

- There are two non-working pixels on the 148-pixel focal-plane detector. Due to a flaw in the mask used in their manufacture the two bad pixels are shorted together.

- Pulcinella, the electron-source current meter, stopped working on 21 February, 2013. The problem was traced to a faulty meter board, which was replaced. The new meter board still requires calibration, but is functional for data-taking. The LED and solar power array were also found to be marginal and a new power system is being developed.

- On 1 March, 2013, the pinch magnet quenched while the detector magnet was being ramped down from 3.96 T. The pinch magnet quenched again on 21 March, while both

*Karlsruhe Institute of Technology, Karlsruhe, Germany.
†Departed August, 2012, currently at University of Pittsburgh, Pittsburgh PA.
‡University of North Carolina, Chapel Hill, NC.
§Graduated March, 2013.

magnets were being ramped up. Cyromagnetics, Inc., the manufacturer, suggested the problem may be with the pinch magnet power supply. The power supplies were swapped for testing and the pinch magnet was ramped to 6 T successfully using the detector magnet power supply.

- During commissioning the preamp temperature was found to be unstable in the initial configuration. Over a period of weeks the temperature at the preamps gradually drifted upwards until the heat-pipe condenser set-point temperature was reduced to bring the preamp temperature down again. The temperature is currently controlled only at the heat-pipe condenser. The cooling system has an excess of cooling power available, and a system is already installed with heaters and sensors floating at PAE voltage that has previously been used to control the detector flange temperature. A plan is in place to control the heat-pipe condenser temperature and the preamp temperature separately.

	specified	achieved	comments
magnet stability	<0.1%/month	<0.014%/month	
figure of demerit	1.2	1.139	
post acceleration	10 kV	11 kV	
energy resolution	3 keV	0.6 keV	
XHVac pressure	$<5\text{x}10^{-9}$ mbar	$\sim 5\text{x}10^{-9}$ mbar	known leak
HVac pressure	$1\text{x}10^{-6}$ mbar	$2\text{x}10^{-6}$ mbar	
working channels	>90%	98.6%	short on wafer
detection efficiency	>90%	>93%	requires calibration
detector background	<100 mHz/keV	1.2 mHz/keV	
veto detection efficiency	>90%	97%	
veto dead time	<1%	0.7%	
timing resolution	100 ns FWHM	63 ns FWHM	

Table 1.4-1. Summary of commissioning measurements

1.5 Operator training

T. Bergmann*, S. Enomoto, F. M. Fränkle†, M. Haag*, F. Harms*, M. Mark*, D. S. Parno, J. Schwarz*, K. J. Wierman†, and S. Wüstling*

With the commissioning of the main spectrometer, the FPD system will no longer be run in standalone mode by system experts; instead, it will be operated by shift personnel, most of whom specialize in different parts of the experiment. In order to train these new operators in the use of the system, we ran a weeklong training workshop from 22 to 26 October, 2012, the week after the KATRIN collaboration meeting. Members of the Detector Working Group gave lectures that oriented trainees to the FPD system and acquainted them with nearby hazards; explained how to take data with ORCA software and write scripts to automate

*Karlsruhe Institute of Technology, Karlsruhe, Germany.
†University of North Carolina, Chapel Hill, NC.

measurements; covered common tasks, such as restoring power to the readout electronics or taking a calibration run; summarized useful troubleshooting techniques; and introduced analysis software for the system. In small groups, trainees toured a readout-electronics test setup, practiced data-taking tasks in the experimental hall, and solved several minor system malfunctions induced by the workshop organizers. Our twenty trainees, several of whom are pictured in Fig. 1.5-1, reported satisfaction with the results of the workshop.

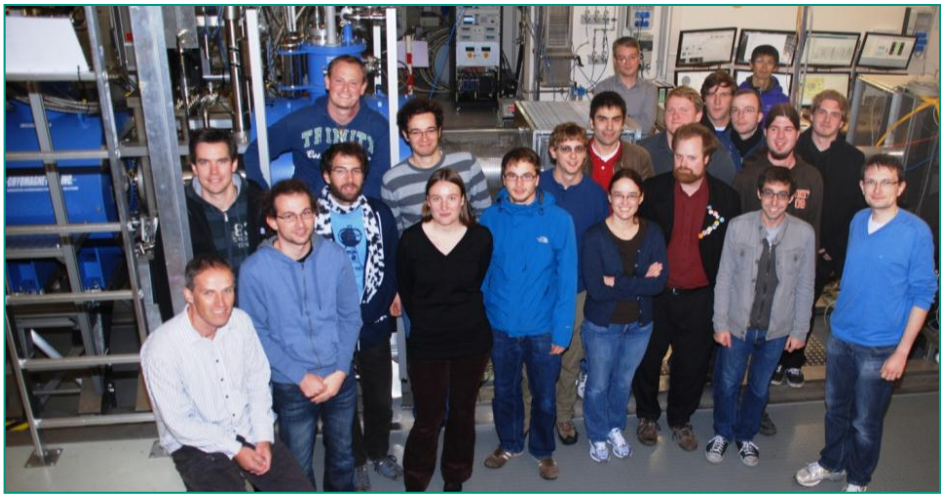

Figure 1.5-1. FPD-system trainees and lecturers in October 2012.

On 18 March, 2013, we provided a one-day course to refresh trainees' memories closer to the anticipated start of commissioning.

In preparation for these training workshops, we have accumulated a complete collection of step-by-step written procedures for operators, and have identified several areas in which the control software can be made more user-friendly. Subsequent training workshops will incorporate material from other subsystems, *e.g.* the electron gun, as they come online.

1.6 System upgrades

J. F. Amsbaugh, A. Beglarian[†], N. M. Boyd[‡], P. J. Doe, F. Harms[†], E. L. Martin, D. S. Parno, R. G. H. Robertson, and J. Schwarz[†]

System upgrades implemented during the detector commissioning at KIT include a more robust post-acceleration electrode, lower-noise preamplifiers, radiation shields on the detector feedthrough pins, and a heat pipe that provides more efficient cooling. The impact of these improvements on detector performance is described earlier (see Sec. 1.4). Ongoing is the implementation of improved firmware signal shaping to reduce degradation of the energy resolution at high event rates (see Sec. 1.7).

[†]Karlsruhe Institute of Technology, Karlsruhe, Germany.
[‡]Departed August, 2012, currently at University of Pittsburgh, Pittsburgh, PA.

- Heat pipe
  During commissioning of the detector system at UW, the cooling of the detector wafer and electronics was found to be marginal, in part because of the thermal resistance of a long copper rod connecting to the pulse-tube cooler. To replace the copper rod, a high-efficiency heat pipe that uses nitrogen as the working fluid was designed, constructed and commissioned at UW and subsequently (July, 2012) installed on the system at KIT. Fig. 1.6-1 shows the heat pipe installed on the detector system.

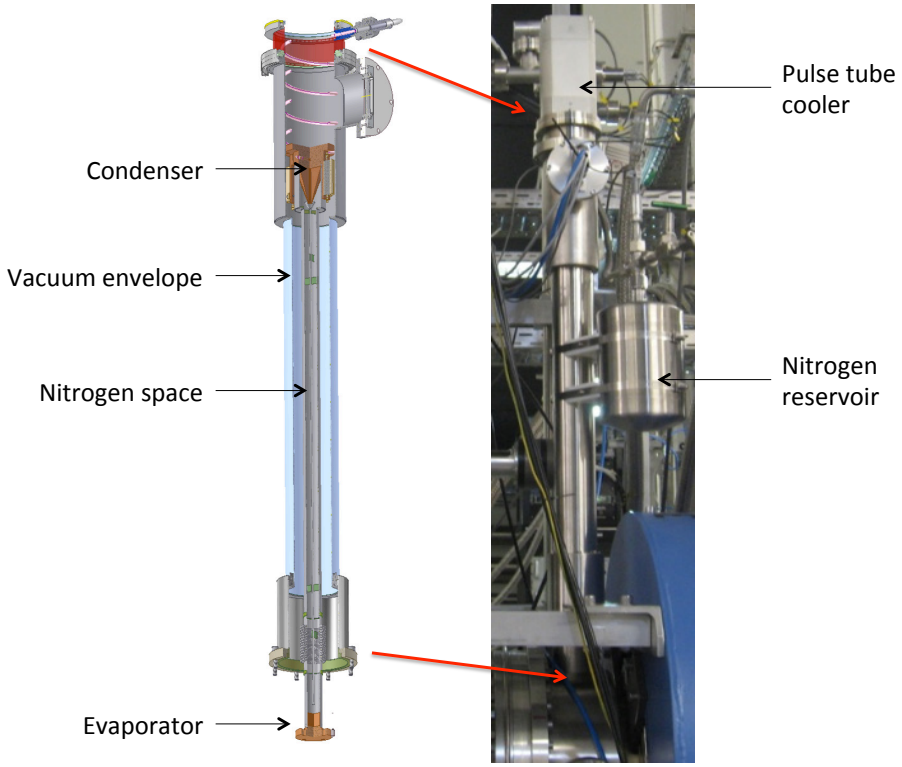

Figure 1.6-1. A schematic of the heat pipe showing the principal components and a photograph of the heat pipe and pulse-tube cooler installed on the detector system.

The working principle and design of the heat pipe are described in the 2012 Annual report[1]. The heat load of the detector system is approximately 25–35 W and the heat pipe was designed to provide a heat flux of 60 W. The response of the detector system to cooling via the heat pipe is shown in Fig. 1.6-2.

A critical parameter is the temperature of the condenser; if it is set too low, nitrogen ice will form around the condenser, reducing its efficiency. It can be seen that approximately 2 days are required for the temperature of the system to stabilize when the setpoint of the condenser temperature control is 76.7 K. This results in an adequate temperature of 0° C for the preamplifiers and −20° C for the preamp carousel, which is more representative of the temperature of the detector wafer. Additional cooling is available from the system but the temperature of the preamplifiers should not go

[1] CENPA Annual Report, University of Washington (2012) p. 10.

below $-40°$ C. The system is robust and stable and further experience is being gained regarding fine control.

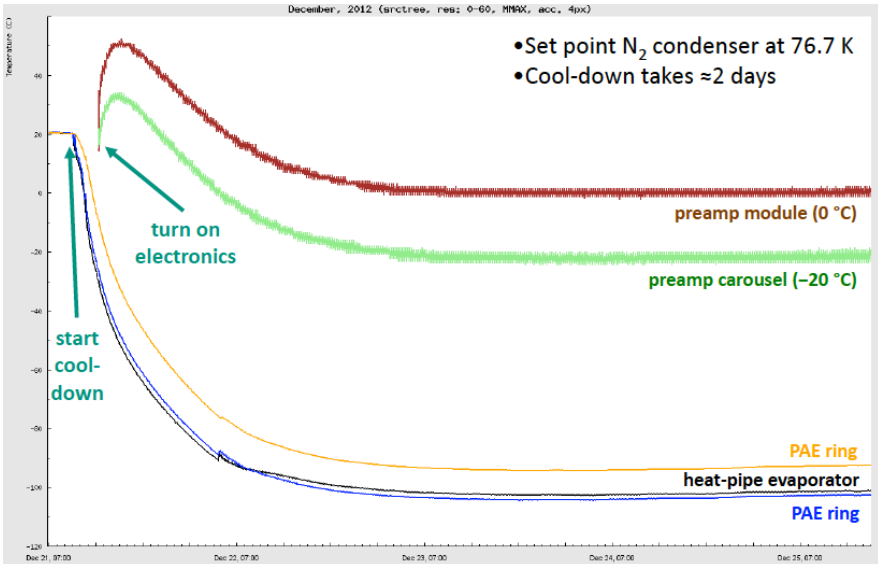

Figure 1.6-2. The performance of the heat pipe and the response of the detector and electronics during the first test of the cooling system.

- Vacuum system
  A more robust post-acceleration electrode was designed to replace the earlier electrode which distorted when subjected to atmospheric pressure. Two electrodes of the new design were made by Communication and Power Industries and shipped to KIT in March, 2012. Tests of the electrodes revealed that one leaked at a rate of 10^{-8} mbar-L/sec through a brazed copper joint. Since both sides of the electrode are under vacuum, a leak of this magnitude is acceptable. This electrode will be used as a spare. Once installed into the detector system in May, 2012, the leak-free electrode was tested at high voltage. It was found that above 11 kV the electrode would undergo increasingly frequent electrical breakdown. Although an acceleration potential of 11 kV will satisfy the commissioning requirements of KATRIN, a plan has been formulated to investigate the cause of the breakdown, hopefully allowing the electrode to reach the design potential of 25 kV.

  In July, 2012, a leak developed in the high-vacuum chamber at a weld where the cryopump attaches to the chamber. A new chamber was designed that resulted in less stress at the weld and also repositioned the vent valves to allow easier access. The new chamber was received and installed at KIT in November, 2012.

  In December, 2012, it was discovered that a leak had developed in the bellows of the γ-source actuator. A replacement actuator was ordered and, in March, 2013, the leaking actuator was returned to the manufacturer for repair.

- Magnet quench monitoring
  When the magnets are operated in driven mode the current in the coil is only recorded

every 10 seconds. A higher sampling rate may help in understanding the cause of quenches. Armen Beglarian, the KIT slow-controls engineer, has implemented a system that samples the currents in the pinch and detector coils at a rate of 100 kHz per magnet. This information is written into a 40-second-long circular buffer. When a quench in either magnet is detected, data are recorded in the buffer for a further 20 seconds before being read out, providing a detailed record for both magnets, before and after a quench event.

- Electron-source illumination
  The photoelectron source is necessary for a wide range of calibration tasks. Ideally the photoelectron disk should be uniformly illuminated to achieve a similar event rate in all pixels. The oblique angle of illumination makes this difficult to achieve and the performance of the original, complicated, illumination device was not acceptable.

  A simple, compact illumination device, consisting of six 255-nm UV LEDs and one red LED, has been designed and constructed at UW. This device is being commissioned and initial tests have achieved a level of illumination that varied by less than a factor of 10 across the photoelectron disk. The variable-intensity UV LEDs may be operated in either pulsed or DC mode. When operated in conjunction with the red LED the illumination device is used to measure the linearity of the electronics. The device fits over the quartz illumination window and hermetically seals the window should it fail, preventing damage to the detector system.

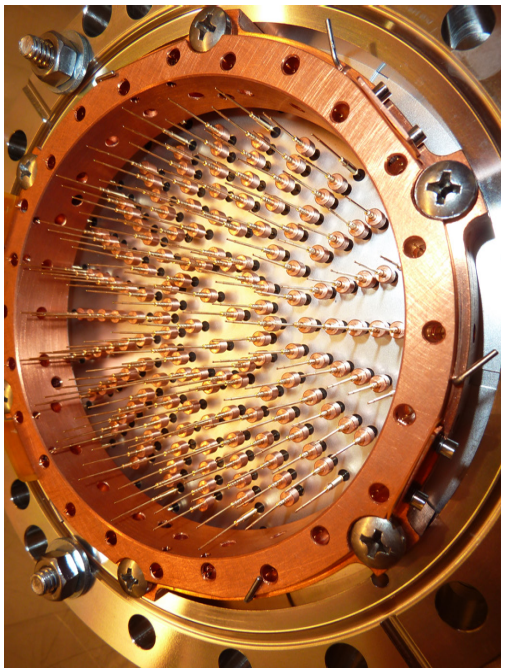

Figure 1.6-3. Copper "donuts" installed on the feedthrough pins of the detector flange.

- Shielding "donuts"
  The glass insulators in the detector signal feedthrough contain high levels of ^{40}K. βs

from the decay of ^{40}K are blocked by copper "donuts" from hitting the detector wafer. These donuts, mounted on the feedthrough pins, can be seen in Fig. 1.6-3. A more detailed description of the shielding donuts can be found in the 2012 Annual Report[1].

A detector-signal feedthough flange equipped with the shielding donuts was installed in the detector system in June, 2012. Analysis of background data is underway in order to quantify the effect of the shielding donuts.

1.7 Detector response simulation

S. Enomoto and D. S. Parno

In the KATRIN FPD DAQ system, energy is reconstructed by a pair of trapezoidal filters implemented in FPGA logic. During commissioning at KIT, we observed a distortion in the reconstructed energy spectrum of photoelectrons incident on the FPD at rates in the tens of kHz, due to the effect of pile-up on these filters. Peak pile-up, in which the interval between electrons is not long enough for separate triggers, suppresses the measured event rate; the energy recorded for such a multiple-occupancy event is sensitive to the exact timing difference. Tail pile-up, in which the pulse from one trigger bleeds into the next, reduces the recorded energy for the second event.

During the KATRIN neutrino-mass measurement, the rate of tritium βs is expected to be less than 1 Hz, so this effect will be negligible. However, the transmission function of the main spectrometer will be measured using an electron gun with rates of up to 100 kHz on a single pixel. Rate-induced errors in the counting of transmitted electrons during this calibration introduce a potentially significant source of systematic error. At such high rates, trace data cannot be recorded, so offline correction is not possible; instead, the problem must be solved through changes either to the FPGA logic or to the analog readout electronics.

To evaluate possible solutions, Sanshiro Enomoto has developed a simulation of the entire detector-signal readout chain. The Detector-Readout Integrated Performance Simulation (DRIPS) begins with signals in an FPD pixel and follows them through the preamplifier, the alternating-current coupling, the anti-aliasing filter, the analog-to-digital converter, and the trapezoidal filter chain in the FPGA logic. The anti-aliasing filter, a fifth-order Bessel filter in the analog electronics, is approximated in this simulation. DRIPS includes voltage (series) noise, current (parallel) noise, and flicker ($1/f$) noise, generated according to a method developed for Planck[2]. The contribution of each component is determined by a fit of the total simulated noise spectrum to the measured noise spectrum. Internal detector processes are not included.

Fig. 1.7-1 compares the simulated energy spectra to measured spectra at three data rates. DRIPS reproduces the spectrum in each case. Based on these results, we have excluded solutions based on changes to the analog electronics. A modification to the FPGA filter logic

[1] CENPA Annual Report, University of Washington (2012) p. 9.
[2] S. Plaszczynski, Fluctuation and Noise Letters **7**, R1 (2007).

is under development. DRIPS is being integrated with the rest of the KATRIN simulation framework.

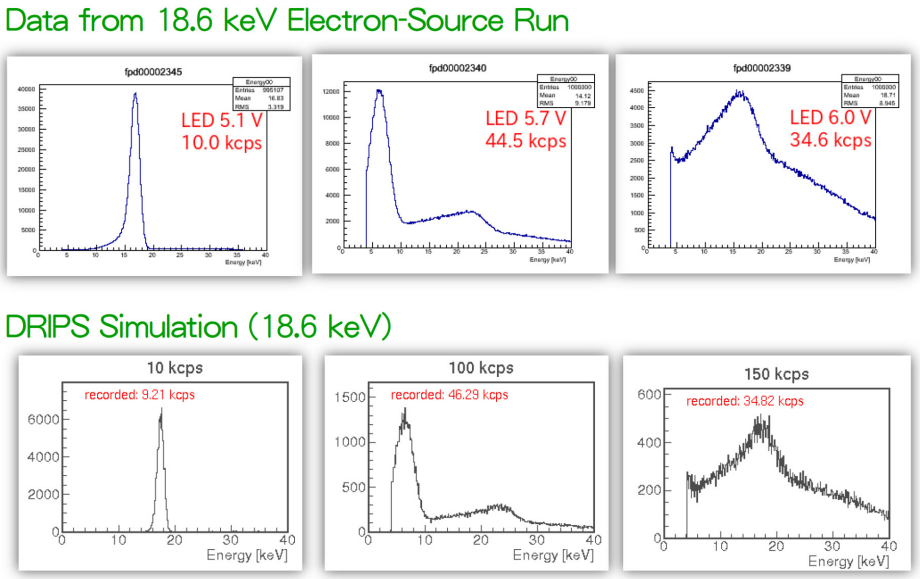

Figure 1.7-1. A comparison of measured (top) and simulated (bottom) energy spectra for 18.6-keV photoelectrons. Left to right, the recorded incident rates are $\sim$ 10 kHz (10 kHz), $\sim$ 45 kHz (100 kHz), and $\sim$ 35 kHz (150 kHz). Like other internal detector effects, the detector dead layer is not included in DRIPS.

1.8 Analysis tools

S. Enomoto and D. S. Parno

We have continued rebuilding our analysis toolkit, moving from a collection of ad hoc tools with poor interoperability to an integrated framework for real-time, near-time, and off-line analysis tasks. The new, sequence-based scheme for the detector analysis framework[1] has evolved into Building Elements for Analysis Sequence (BEANS). While not yet complete, this framework already includes about 100 reusable analysis-logic elements and is in active use. BEANS analysis sequences may be constructed as hand-written C++ code, or with a graphical user interface that allows individual logic elements (*e.g.* the rejection of malfunctioning channels, the readout of energy events, the application of a pre-existing energy calibration, and the creation of a rate histogram) to be dragged and dropped in the appropriate order. Users may also mix these construction styles and may add additional analysis of the BEANS results to the same program.

In order to integrate slow-controls data with the general KATRIN analysis platform, we have assigned unique 15-digit identifiers to all major components, setpoints, and readbacks of the FPD system, in accordance with the KATRIN numbering system. These identifiers allow BEANS to access slow-controls data via the KaLi interface developed for KATRIN.

[1] CENPA Annual Report, University of Washington (2012) p. 14.

Using KaLi, BEANS can also automatically download full runs directly from the KATRIN servers and store calibration results for future analyses.

BEANS has been integrated with our data-acquisition software (ORCA BEANS) and with the KAFFEE automation tool[1] (KAFFEE BEANS). Users can thus develop a BEANS sequence in offline analysis, and then apply the same sequence manually during data taking, or automatically to runs that have completed.

BEANS is distributed via a git repository as part of the KATRIN analysis package. While additional work on documentation and verification is necessary, several examples and case studies are available with the distribution.

1.9 Tritium Recoil-Ion Mass Spectrometer

L. I. Bodine, T. H. Burritt, D. S. Parno, D. A. Peterson, R. G. H. Robertson, T. D. Van Wechel, and D. I. Will

The Tritium Recoil-Ion Mass Spectrometer (TRIMS) experiment is a time-of-flight spectrometer designed to measure the likelihood of dissociation in molecular tritium beta decay. The branching ratio to the $^3HeT^+$ molecule is a litmus test of the calculated final-state distribution used in KATRIN analysis. The numerical calculations of Saenz *et al.*[2] are in stark disagreement with the measured branching ratios of Snell *et al.*[3] and Wexler[4]. The discrepancy must be resolved to provide confidence in the molecular models used in KATRIN.

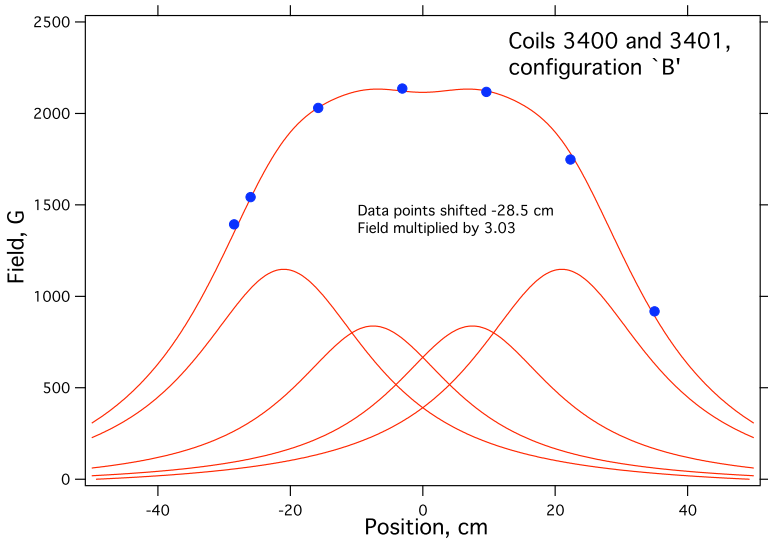

Figure 1.9-1. Magnetic field design and field scan at one-third of the design current.

[1] CENPA Annual Report, University of Washington (2011) p. 12.
[2] Alejandro Saenz, Svante Jonsell and Piotr Froelich, Phys. Rev. Lett. **84**, 242 (2000).
[3] Arthur H. Snell, Frances Pleasanton and H. E. Leming, J. Inorg. Nucl. Chem. **5**, 112 (1957).
[4] S. Wexler, J. Inorg. Nucl. Chem. **10**, 8 (1959).

The extreme-high-vacuum system was designed in conjunction with the required high-temperature-bake-out system. Custom vacuum components have been fabricated and the vacuum system is being assembled in the cleanroom in the Physics/Astronomy Building.

The magnet system was assembled using coils recovered from old Varian NMR magnets. The double Helmholtz arrangement provides a 2-kG field that is uniform to better than 1% over 25 cm. A test of the field configuration can be seen in Fig. 1.9-1 along with the designed field values. The 60-kV high-voltage system design inside the magnet has been modified to use a resistive ring structure.

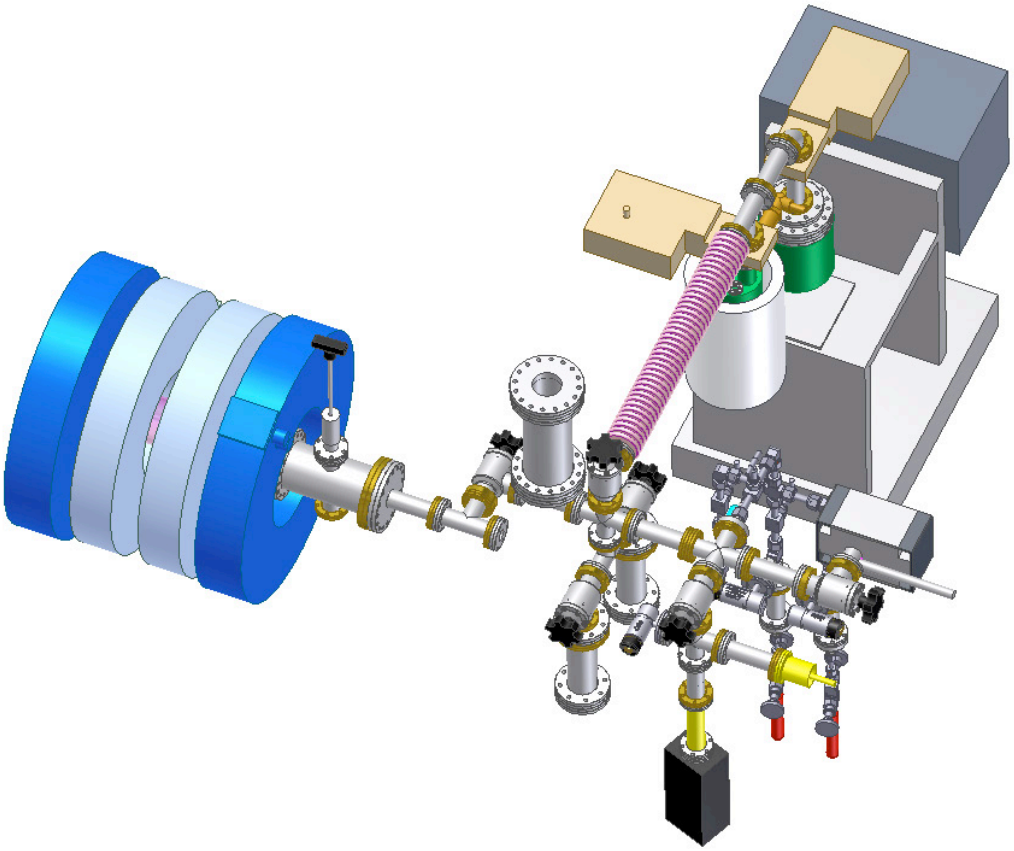

Figure 1.9-2. Inventor model of the TRIMS apparatus.

The data-acquisition system comprises a combination of custom and commercial electronics. Custom preamplifiers and fiber-optic senders have been fabricated and are being characterized. A CAEN digitizer has been purchased and is being characterized with CAEN digital-pulse-processing software.

An Autodesk Inventor computer model of the full experiment was generated to aid in the design process. Fig. 1.9-2 shows a snapshot of the vacuum and magnet model.

Majorana

1.10 Overview of the Majorana Demonstrator

N. M. Boyd*, T. H. Burritt, J. A. Detwiler, P. J. Doe, J. Gruszko, G. C. Harper, A. Knecht†, J. Leon, M. L. Miller‡, D. A. Peterson, R. G. H. Robertson, A. G. Schubert§, and T. D. Van Wechel

The Majorana Demonstrator is a ∼40 kg array of HPGe detectors enriched in ^{76}Ge that is under construction at the Sanford Underground Research Facility in Lead, SD. The primary technical goal of the Demonstrator is the achievement of a radioactive background below 4 counts/tonne/year within a 4-keV region of interest surrounding the 2039-keV Q value for ^{76}Ge neutrinoless double beta ($0\nu\beta\beta$) decay. Such a low background level would justify deeper investment in a much larger tonne-scale experiment with sufficient sensitivity to definitively search for $0\nu\beta\beta$ decay for neutrino masses characteristic of the inverted hierarchy. In the process, the Demonstrator will simultaneously perform a sensitive test of a claimed observation of $0\nu\beta\beta$ decay[1], and will also perform searches for low-mass WIMP dark matter, solar axions, and other physics signals.

The project is at a very exciting stage as the first prototype module is under construction and will be operational within the coming months. The Majorana group at the University of Washington is contributing to the effort on several levels:

- Our group leads the simulation and analysis effort within the collaboration and contributes significantly to efforts in software development, data analysis techniques, background modeling, geometrical models for Monte Carlo simulations, data handling and storage issues, database implementation, and feedback to design teams on the background impact of proposed modifications.
- Part of the UW Majorana group is engaged in the CoGeNT (Coherent Germanium Neutrino Technology) collaboration which is operating a low-threshold germanium detector underground searching for light-mass WIMP dark matter signals. One important benefit of this symbiosis is our development of a novel preamplifier featuring ultra-low noise. This will allow for a lower threshold leading to an improved low-energy analysis and the possibility to veto harmful decays for the $0\nu\beta\beta$ decay measurement as well.
- We have designed, tested, and prototyped ultra-low-background signal and high-voltage cable connectors for use in the Majorana Demonstrator. A number of connectors have been constructed and are currently being installed in the Demonstrator prototype cryostat. We are refining the designs of these connectors and preparing for production for the enriched-Ge Demonstrator cryostats.

*Departed August, 2012, presently at University of Pittsburgh, Pittsburgh, PA.
†Departed July, 2012, presently at Paul Scherrer Institut, Villigen PSI, Switzerland.
‡Presently at Cloudant Inc., Seattle, WA.
§Graduated December, 2012, presently at Stanford University, Stanford, CA.

[1] H. V. Klapdor-Kleingrothaus *et al.*, Phys. Lett. B **586**, 198 (2004).

- Our group is responsible for microdischarge testing of the Picocoax® high-voltage cables intended for deployment in the MAJORANA DEMONSTRATOR. We have designed a test stand that is capable of production testing of the cables under vacuum up to the DEMONSTRATOR specification of 5 kV. Construction of the test stand is currently underway at CENPA.

- We have fabricated low-background parylene gaskets that are being used to seal the DEMONSTRATOR cryostats. We are also using the parylene as a coating for copper-on-copper nuts and bolts in order to prevent galling. We are training collaborators on our coating system and are preparing to ship it to the experimental site for production coating for the enriched-Ge DEMONSTRATOR cryostats.

- Using the expertise of our technical staff the MAJORANA single-string test cryostats were designed and built at CENPA. A total of 7 cryostats were constructed and delivered to the University of North Carolina and the experimental site.

1.11 Simulation and analysis activities for the MAJORANA DEMONSTRATOR

J. A. Detwiler, J. Gruszko, A. Knecht*, J. Leon, M. L. Miller†, and A. G. Schubert‡

The UW MAJORANA group leads the simulation and analysis effort within the MAJORANA collaboration. Much of the low-level software for data I/O, event building, data processing, and simulation was written by CENPA personnel. Members of our group have played a central role in the building and validation of the background model for the MAJORANA DEMONSTRATOR, which provides the radiopurity criteria upon which the experimental design is evaluated. We also participate in the development and implementation of data analysis techniques, geometrical models for Monte Carlo simulations, and data handling, storage, and database technologies.

Our efforts over the past year have focused on background model validation, supporting construction activities, and preparation for data taking with the prototype cryostat. A significant milestone was Alexis Schubert's successful thesis defense, which centered on a highly-detailed background model of a low-background R&D detector, MALBEK, being operated by MAJORANA collaborators at the Kimballton Underground Research Facility in Kimballton, VA. Schubert used collaboration software to simulate backgrounds in MALBEK, and developed tools to couple those simulations with component geometry and radiopurity data to construct a background model against which the detector data could be compared and analyzed. When anomalously high background was observed in the data, the model was able to quickly and definitively isolate a single detector component as the source of contamination, allowing for its efficient replacement with minimal loss of detector live time and with no wasted effort. The model was then used to analyze the detector's background spectrum, providing a good match between simulation and data over several orders of magnitude of

*Departed July, 2012, presently at Paul Scherrer Institut, Villigen PSI, Switzerland.
†Presently at Cloudant Inc., Seattle, WA.
‡Graduated December, 2012, presently at Stanford University, Stanford, CA.

event energy, as shown in Fig. 1.11-1. This effort validated the use of these tools for describing broad energy spectra in low-background high-purity germanium (HPGe) detector systems.

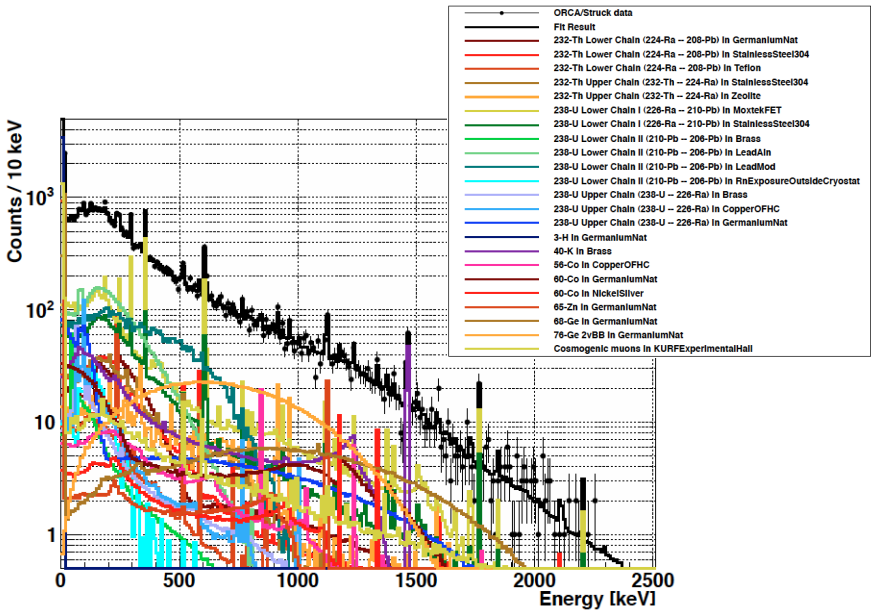

Figure 1.11-1. Comparison of MALBEK data with simulated background spectrum. Excellent agreement was obtained over a broad range of detector energies.

With the start of enriched HPGe detector manufacturing at ORTEC in Oak Ridge, TN, in autumn of 2012, our group has also been significantly involved in data processing and analysis activities supporting DEMONSTRATOR construction. HPGe detector-acceptance test data taken at the manufacturing facility has provided the first exercise of the full data production chain, from data acquisition, to data transfer, to event energy and pulse shape processing, to spectral analysis. We worked with collaborators at Lawrence Berkeley National Laboratory and Oak Ridge National Laboratory to implement, execute, and refine the software tools and were able to provide a timely response on detector acceptance criteria. The tools were modified and augmented to accommodate acceptance tests taken when the detectors arrive at the experimental site. We are in the process of completing the suite of tools required to support detector characterization data taken after the detectors have been re-mounted in their MAJORANA-style detector mounts and loaded into a detector string test cryostat. We are also working closely with the DAQ and electronics groups to tune the hardware to maximize the performance of our signal-processing routines.

Our attention is now turning toward completing preparations for the first data to come from the DEMONSTRATOR prototype cryostat. Major activities include software quality assurance tests, database implementation of run-information recording and automatic data workflow management, refinement of event building routines, optimization of energy estimation and pulse-shape-parameter extraction algorithms, and data monitoring and cleaning routines.

1.12 Low-background cable connectors for MAJORANA

T. H. Burritt, J. A. Detwiler, J. Gruszko, A. Knecht*, J. Leon, D. A. Peterson, and R. G. H. Robertson

The UW MAJORANA group has constructed multiple sets of coaxial high-voltage and signal connectors for the MAJORANA DEMONSTRATOR prototype cryostat. Detector signals are carried from the low-mass front-end (LMFE) preamplifiers through a 24" Picocoax® cable to the signal connector, then through another 61" Picocoax® cable to the vacuum feedthroughs that lead to the post-amplifier. Each set of signal connectors consists of eight paddles contained in a Cu 'garage' enclosure, for a total of 24 signal connections. Each garage will be mounted on top of the cold plate in the cryostat above the detector string. High-voltage cabling follows a similar path, with the baseline design incorporating a 5-channel high-voltage connector block taking the place of the signal garage. Each high-voltage block is required to withstand voltages of up to 5 kV and provide an independent ground path for each channel in order to avoid ground loops.

The signal paddles are fabricated from 0.7-mm-thick fused silica wafers at the Microfabraction Facility (MFF) located in Fluke Hall on the UW campus. The metallic pattern consists of 0.25 μm of Au deposited on a Cr adhesion layer. Strain-relief-hole drilling and dicing of the wafers into paddles is performed at Accu-Tech Laser Processing, Inc. in California. The garages were fabricated via wire electrical discharge machining (EDM) in the instrument shop at the UW Department of Physics. Assembly is performed in the clean room at the Physics/Astronomy Building. The Picocoax® cables are stripped and threaded into the strain relief holes on the paddle. The paddle is placed into a fixture and the coaxial shield and center conductor are attached to the Au with Ag epoxy. The paddles are assembled into a garage using a fine nylon mesh as a contact spring. The connections are tested at room temperature and at liquid nitrogen (LN) temperature prior to shipping using a custom-built cool-down box that allows testing without direct immersion in LN, which would subject the garage to sudden thermal shock, and without the need for vacuum cryogenic systems. Fig. 1.12-1 shows a fully assembled garage ready for packaging and shipment to Lawrence Berkeley National Laboratory (LBNL), where MAJORANA collaborators integrate them with the detector electronic readout.

The paddles must be cleaned prior to assembly. Cases of poor adhesion to the gold traces have led us to investigate several cleaning methods, including boiling in water, ultrasonic cleaning, wiping with alcohol and acetone, and piranha etching. We are also investigating an alternative sapphire substrate to reduce chipping and paddle damage during installation, and methods for simplifying the garage assembly process in the glovebox at the Sanford Underground Research Facility (SURF). The garages are successfully being used in the MAJORANA DEMONSTRATOR prototype and testing cryostats both underground at the experimental site in SURF as well as at test stands operating at LBNL.

The baseline high-voltage connectors incorporate a crimp-and-plug design, in which crimped ends of the coaxial core and ground conductors are pressed together inside of channels in the

*Departed July, 2012, presently at Paul Scherrer Institut, Villigen PSI, Switzerland.

connector block using plastic plugs. The crimps are fabricated from copper rod stock, and are fastened easily and reliably using a custom crimping tool fashioned out of a drill chuck. A custom plug-insertion tool and strain-relief strap were also fabricated to facilitate assembly, manipulation, and installation. HV connector blocks for the DEMONSTRATOR prototype cryostat were fabricated out of Teflon and are being tested at LBNL, as well as at the experimental site in detector-string test stands. We are currently prototyping HV blocks fabricated from highly-radiopure PTFE stock that has been certified for use in the DEMONSTRATOR enriched detector cryostats. We are also investigating improvements in the strain-relief design and minimization of component mass.

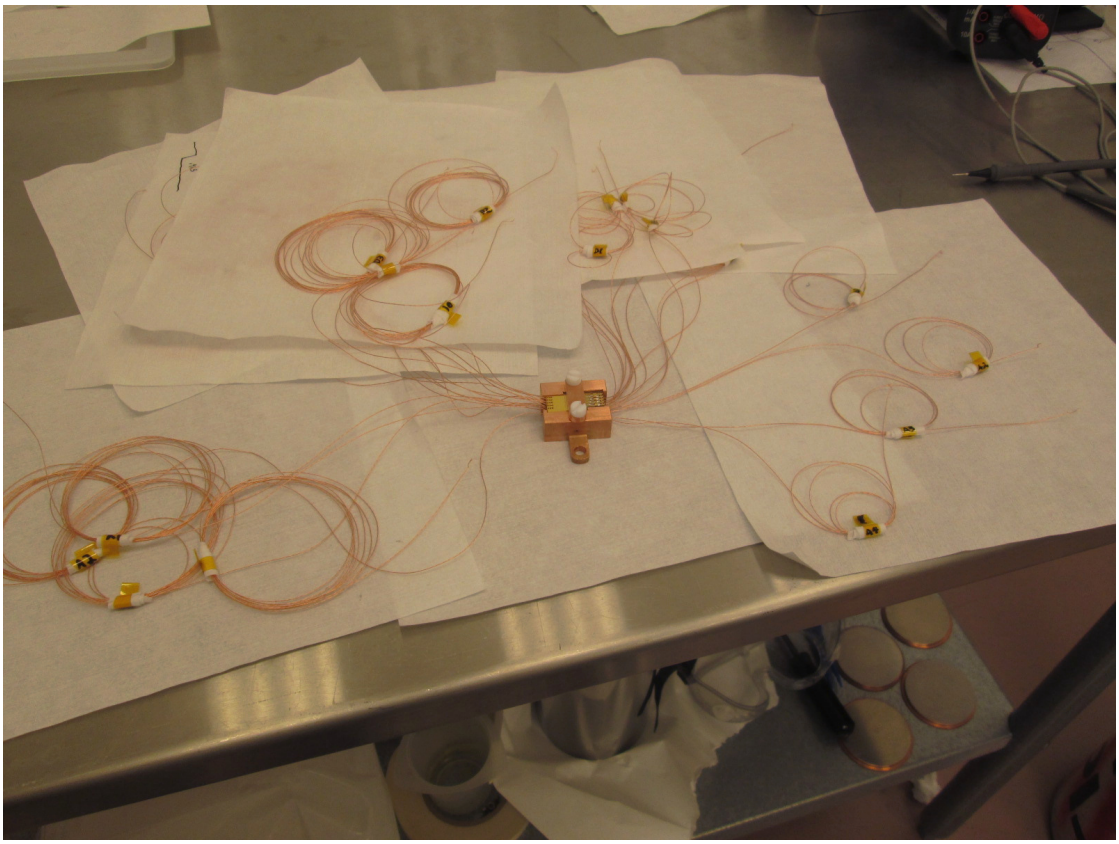

Figure 1.12-1. A fully assembled garage ready for packaging and shipment.

We are also working with MAJORANA collaborators to investigate an alternative HV connection scheme in which connections can be made directly at the detector units rather than at the top of the cold plate. This scheme involves the use of a flat electroformed-copper 'fork' that is pressed against a detector's high-voltage ring using a PTFE nut on one of the detector-unit support rods. If successful, this connection method would eliminate the need for the HV connector blocks for at least the outermost strings in the array, reducing the amount of inactive mass and outgassing plastic inside the cryostat and possibly simplifying HV cable routing. Fifteen such high-voltage forks were fabricated at the UW Department of Physics instrument shop using wire EDM. The HV forks are currently being tested on detector test stands at LBNL and at CENPA.

1.13 Picocoax® high voltage cable testing

T. H. Burritt, J. A. Detwiler, P. J. Doe, J. Gruszko, A. Knecht†, J. Leon, D. A. Peterson, R. G. H. Robertson, and T. D. Van Wechel

We are in the process of performing microdischarge tests of the custom Picocoax® high-voltage cables being implemented in the MAJORANA DEMONSTRATOR. To achieve sufficient sensitivity to neutrinoless double-beta decay, our cables must contribute a minimal amount of natural radioactivity. Our Picocoax® cables, which are made specifically for the MAJORANA collaboration, are fabricated from selected materials using ultra-clean processes. These custom cables must be capable of supplying HPGe detector operating voltages as high as 5 kV without exhibiting discharge that can damage the front-end electronics or mimic detector signals. The latter is particularly worrisome at lower energies, where electronic noise can obscure the pulse shape. Hence microdischarge-free cables are also required for the MAJORANA DEMONSTRATOR's low-energy program to search for other new physics, such as light-mass WIMP dark matter and solar axions.

The Picocoax® cables are first tested at Lawrence Berkeley National Lab (LBNL), and then shipped to UW for higher-sensitivity testing. Our initial system comprised an RF-shielded enclosure in which the central conductor of each cable was connected to a high voltage stack, with the opposite end dressed with a corona ball, and the shield grounded. Preamplification electronics developed for the SNO Neutral Current Detector Array are used in conjunction with an oscilloscope to monitor the baseline for excursions, which are recorded to disk for further investigation. The robustness of the setup was validated with commercially available RG-59 cables, for which only transient signals are observed, indicating a very low level of remnant RF pickup. We then examined sections of the short (21") and long (64") cables that will be used in the prototype module of the DEMONSTRATOR. We found that the cables worked well at voltages up to 4 kV but that increasing the voltage to 5 kV would often result in breakdown. This contradicted evidence from LBNL test stands under vacuum that demonstrated that the cables could withstand the higher voltage.

Concluding that tests of the features of the cable were too sensitive to be performed in air, we have modified our setup to accommodate testing of the cables under vacuum. We have designed and assembled the vacuum test chamber, and are preparing mounting fixtures that will allow rapid production testing of the MAJORANA HV cables. The test stand reproduces as closely as possible the full HV cable path using the same vacuum feedthroughs and HV connector blocks that will be used in the MAJORANA DEMONSTRATOR.

†Departed July, 2012, presently at Paul Scherrer Institut, Villigen PSI, Switzerland.

1.14 Low-background parylene coating and gasket production

N. M. Boyd*, M. D. Busch†, J. A. Detwiler, and M. P. Green†

The UW MAJORANA Group has helped lead the investigation of parylene technologies for use in low-background experiments. Parylene is a polymer with excellent dielectric properties and low natural radioactivity. Our past efforts included a promising implementation of ultra-low mass, low-background ribbon cable to carry detector signals[1]. While ultimately the design was not able to achieve the impedance requirements of the front end being deployed in the MAJORANA DEMONSTRATOR, the cables remain a viable option for future detector systems.

Two other uses of parylene are being implemented in the DEMONSTRATOR. One of these is the use of parylene films as low-background gaskets for the large MAJORANA cryostats. The low-background requirements of the DEMONSTRATOR preclude the use of traditional cryostat sealing solutions such as indium. Parylene offers an alternative that uses a minimal amount of material that is already low in radioactivity. Films are produced in a clean room by parylene-coating large metal sheets polished to a mirror finish. The films are removed from the sheets and cut to size. The gaskets were demonstrated to seal on small prototype cryostats several years ago at the University of North Carolina at Chapel Hill. Just recently they were also demonstrated to hold vacuum on the full-sized prototype cryostat for the MAJORANA DEMONSTRATOR.

Parylene is also being used as a coating for ultra-pure electroformed copper (EFCu) parts. EFCu, which can be grown with exceedingly high radiopurity, is the primary structural component for the innermost region of the MAJORANA DEMONSTRATOR apparatus. All internal metallic structures, including all nuts and bolts, are fabricated from this material. If left bare, these nuts and bolts run a significant risk of galling, which would result in poor fastening strength, and would make it difficult to non-destructively disassemble the apparatus. To prevent galling, all copper-on-copper interfaces are made with either the nuts or the bolts coated in parylene. Since parylene can be applied in thin coatings of the order of 0.001" or thinner, the coatings successfully eliminate the risk of galling with no impact on background or mechanical design.

Parylene film and copper-part coatings have been produced using the parylene coater in the UW clean room. These coatings are being successfully deployed in the MAJORANA DEMONSTRATOR prototype cryostat. For production of the films and part coatings required for the enriched detector cryostats, it will be advantageous to be able to produce the coatings closer to the experimental site. In particular, it is desirable to reduce the amount of time that the EFCu components spend above ground, where they are exposed to cosmic rays that can activate long-lived radioisotopes such as ^{60}Co that pose a background risk for the DEMONSTRATOR. To achieve this, we are preparing to relocate our coating apparatus to a surface facility at the Sanford Underground Research Facility (SURF) in South Dakota and we are training collaborators to assist in the parylene-coating production runs.

*Departed August, 2012, presently at University of Pittsburgh, Pittsburgh, PA.
†University of North Carolina, Chapel Hill, NC.

[1] CENPA Annual Report, University of Washington (2012) p. 19.

1.15 Preamplifier with forward-biased reset for CoGeNT and MAJORANA

A. Knecht*, J. Leon, D. A. Peterson, R. G. H. Robertson, and T. D. Van Wechel

Development continues on a charge-sensitive preamplifier which is continuously reset by the forward-biased gate-to-source junction of the input JFET. The DC stabilization of a conventional charge sensitive amplifier is provided by a high-value feedback resistor in parallel with the feedback capacitor. This resistor provides a DC path for the net input bias and detector currents at the amplifier input, so that the feedback capacitor does not eventually charge to the output saturation voltage. We report on methods used to reduce capacitor dissipation noise and on the characterization of the latest prototypes.

It is possible to operate a JFET with zero volts on the gate or even a small forward bias. A JFET has an operating point where the current of the forward-biased gate cancels the reverse leakage current. The detector leakage of a positively biased detector can also be canceled. A feedback resistor is not required when the JFET operates with the gate open eliminating its noise contribution. Charge feedback can still be applied to the gate through a feedback capacitor. Some other means is needed to stabilize the DC operating point.

We are using a tetrode JFET that has superior noise performance and provides a means of DC stabilization without a DC connection to the control gate. A tetrode JFET has two gates: a control gate that has low input capacitance for improved noise performance, and a second gate, the substrate gate, that can be used to set the drain-source current I_{DS}. There are two feedback loops. A low-pass feedback loop is connected to the substrate gate to stabilize the DC operating point so that the average net charge at the input is zero. The second feedback loop, a feedback capacitor between the preamplifer output and the control gate, provides charge feedback in the preamplifier passband.

Previous results indicated that it may be advantageous to explore the dissipation noise contribution of capacitors with different dielectrics and adhesion layers[1]. To that end, tests were performed with a prototype fitted with a Moxtek MX20 JFET using different capacitors connected to its input. We chose three 1-pF silica-dielectric capacitors of different substrate adhesion layers and a 3-pF vacuum-dielectric capacitor. We can infer the contribution of the different noise sources from a plot of the observed equivalent noise charge[2] as a function of filter peaking time, *i.e.* the noise curve. In the noise curve, dissipation noise shows up as a flat component independent of peaking time. To acquire the noise curve we record the noise power spectral density at the output of the post-amplification stage with a Tektronix DPO4104 scope and LabView software specifically designed for this purpose. From Fig. 1.15-1 we can see that the vacuum-dielectric capacitor, despite having the largest capacitance, displays the lowest dissipation-noise contribution.

*Departed July, 2012, presently at Paul Scherrer Institut, Villigen PSI, Switzerland.

[1] CENPA Annual Report, University of Washington (2012) p. 18.

[2] The equivalent noise charge may also be expressed in terms of an energy needed to generate that charge with a Si detector. This is usually given as a peak full width at half maximum (Si FWHM)

Whereas previous designs of the preamplifier made use of a silica-dielectric feedback capacitor, over the past year we have focused on developing a prototype with a vacuum-dielectric feedback capacitor with the promise of achieving improved noise performance based on its diminished dissipation noise. In the latest prototypes the gain loop is split between the preamplifier and the post-amplifier box, which means that there are fewer components near the detector. Making this change improves compatibility of our preamplifier with common detector cryostats.

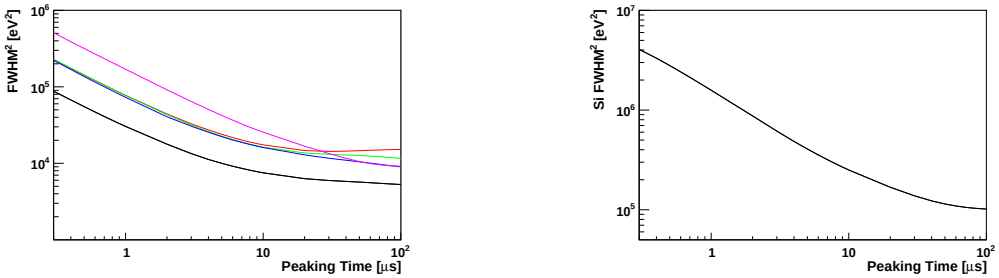

Figure 1.15-1. Left: Si FWHM as a function of peaking time for late-2012 prototype with MX20 JFET at -60° C. Black: open input. Purple: vacuum capacitor, 3 pF. Red: fused silica with NiCr substrate, 1pF. Green: fused silica with Cr substrate, 1 pF. Blue: fused silica with Titanium substrate, 1 pF. Right: Si FWHM as a function of peaking time for early-2013 prototype with MX30 JFET and Hamamatsu Si diode connected at -60° C.

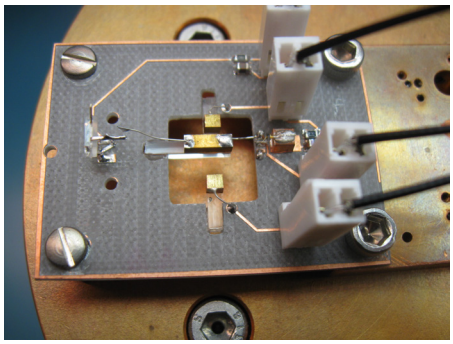

Figure 1.15-2. Early-2013 preamplifier prototype featuring the block vacuum-dielectric feedback capacitor.

Our first efforts to create a vacuum-dielectric feedback capacitor used carefully spaced copper blocks suspended in a hole in the preamplifier board (see Fig. 1.15-2). We measured its capacitance to be 0.17 pF, which is within our design specs. Thus far we have tested this prototype with an MX40 JFET, for which we measured a FWHM in Si of 90 eV. This result falls short of the best noise performance we have achieved with the silica-dielectric design and an MX30 JFET (38 eV FWHM in Si). In order to make a direct comparison, we are currently testing the latest prototype with an MX30 JFET. Fig. 1.15-1 shows the noise curve for this prototype with an MX30 JFET and a Hamamatsu S3096-02 Si diode connected to its input, with a minimum of 319 eV FWHM in Si. Further tests with this JFET and without the diode are planned to confirm the improvements of the new design. Finally, we are also in the process of developing an improved version of the vacuum-dielectric capacitor that may be used as a simple circuit-board component.

1.16 MAJORANA single-string-test cryostat

M. D. Busch*, M. P. Green*, and G. C. Harper

Seven string-test cryostats have been designed and built to test, characterize, and store assembled Ge detector strings until ready to install in the MAJORANA DEMONSTRATOR cryostats[1]. Parts for all seven units (Fig. 1.16-1) were fabricated at UW and shipped to UNC for assembly and testing. The string-test cryostat is based on a standard commercial detector dipstick cryostat, but is large enough to accommodate a full single string, and uses all-metal seals to

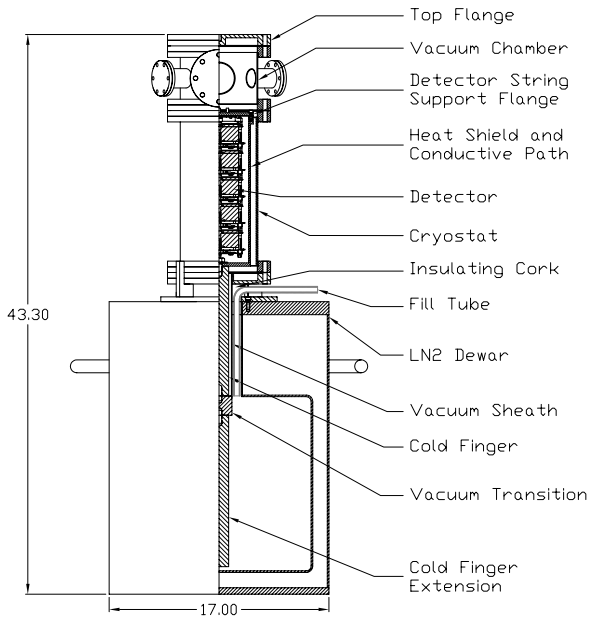

Figure 1.16-1. Cross sectional diagram of the MAJORANA single string test cryostat.

prevent diffusion of radon into the vacuum space. A high-conduction thermal path is provided via a 4-cm-diameter copper cold-finger structure and a thick-walled copper heat shield. All of the parts machined at UW for the test cryostat are currently at the Sanford Underground Research Facility (SURF) in Lead, South Dakota and are being assembled. The Ge crystals are expected to cool to a temperature below 90 K in the test cryostats. The top plate of the heat shield cooled to 81 K during unloaded thermal tests, 9 K below the design specification.

*University of North Carolina, Chapel Hill, NC.

[1]Final Design Report, The MAJORANA DEMONSTRATOR, The MAJORANA Collaboration, February, 2012.

SNO+

1.17 Overview of the SNO+ experiment and CENPA's contribution

I. Guinn, J. Kaspar, L. Kippenbrock, T. J. Major, N. R. Tolich, and H. S. Wan Chan Tseung*

SNO+ is a large-volume underground liquid scintillator neutrino experiment presently under development at the SNOLAB facility in Sudbury, Ontario, Canada. It is a multi-purpose detector whose reach extends to the following areas of neutrino physics: neutrinoless double beta decay, geo-neutrinos, reactor neutrinos, and low-energy solar neutrinos. In addition, a large liquid scintillator detector serves as an excellent supernova neutrino monitor. The SNO+ collaboration recently decided to switch from ^{150}Nd to ^{130}Te as their double beta decay isotope. We plan to load the scintillator with 0.3% Te, which would provide approximately 180 kg of ^{130}Te in a 3.5-m radius spherical fiducial volume. After one year of data this should give us a 90% C.L. sensitivity of approximately 4×10^{25} years (neutrino mass sensitivity of 70 to 100 meV). There is an R&D effort underway to increase the amount of Te loaded into the scintillator which could allow complete coverage of the inverted hierarchy.

SNO+ will use a lot of the infrastructure left behind by the completed Sudbury Neutrino Observatory (SNO) experiment including the acrylic vessel (AV), photomultiplier tubes, and most of the electronics. The main engineering work involved anchoring the AV to the floor which has been completed. The detector will be filled with water in the next few months and that will be replaced with liquid scintillator starting at the beginning of next year. Data-taking is scheduled to start in mid-2014.

In SNO+ the data rate is expected to be two orders of magnitude higher than in SNO and therefore updates to the SNO electronics and data acquisition (DAQ) system are needed. CENPA is responsible for updating the DAQ into a faster, ORCA-based system compatible with the electronics upgrades that are being planned by the University of Pennsylvania. These include new XL3 cards for controlling the 19 data crates. Software for operating the XL3s through ORCA has been written and tested at the typical rates expected from SNO+. The full DAQ system was commissioned this year. The status of the DAQ work is described in more detail (see Sec. 1.18). CENPA is also responsible for the SNO+ slow-control system, which monitors and records a large number of detector-related variables at a rate of ∼1 Hz. This system was installed and commissioned this year. The status of the slow control visualization software is described in more detail (see Sec. 1.19).

To achieve the goals of the experiment it is imperative to understand the optical properties of the scintillator. At CENPA we developed an experiment to study scattering. This work is described in more detail (see Sec. 1.20).

*Departed July, 2012, presently at Mayo Clinic, Rochester, MN.

1.18 SNO+ data acquisition software

M. A. Howe*, J. Kaspar, N. R. Tolich, H. S. Wan Chan Tseung†, and J. F. Wilkerson*

The SNO+ DAQ software is based on ORCA, a general-purpose, highly modular, object-oriented, acquisition and control system. The DAQ system pulls data from the VME trigger crate. Nineteen data crates, operating in an independent asynchronous way, push data into the DAQ system. On the ORCA side, XL3s, the data crate FPGA controllers, are served by circular buffers running in parallel in independent threads. A data manager pulls data from the buffers and serializes them into the data stream. The SNO+ design data rate is 450 Mbit/s.

The final ORCA DAQ commissioning took place during the first air-fill run in March, 2012. Most crates were ramped to HV for two weeks for the first time after four years of electronics upgrades and DAQ development. A couple of TBs of data were recorded and new operators were trained. The data were analyzed and used to optimize both electronics and software. The new XL3 controllers and DAQ were proven stable and reliable.

The second live test, in October 2012, demonstrated the full data chain works reliably. Electronics were initialized from a dedicated Couch DB implemented by the University of Pennsylvania's electronics group. ORCA provides a user interface, additional adjustments, and safety logic on top of these settings to optimize performance under HV. A new readout code for the trigger card increased the maximum trigger rate from 40 kHz to 150 kHz and further minimized dead-time. Live-time accuracy was improved by a new type of data packet added at run boundaries. In general, the readout loop is never stopped and does not contribute to dead time. An OrcaRoot translator converts all monitoring information into a JSON stream for our online monitoring tools. TELLIE, the new LED calibration system, was commissioned during this run, too. A new laser calibration system underwent its first tests in spring, 2013.

All the low-level DAQ functionality is tested and commissioned. A couple of further requests are expected from the calibration group to integrate a new manipulator of the calibration sources. Some high-level helper functions are in development to guide less experienced operators through the most common detector operations *e.g.* ramping HV. All the run configurations are stored in Couch DB so that any run can be repeated anytime in the future. The work on the DB user interface is in progress, as well as its integration with the slow-control and monitoring tools. The run templates, covering various run types, were added into the DB. These are the joint configuration files for DAQ to perform a run and analysis tools to simulate and evaluate the data.

This year DAQ went from the development phase into its maintenance period. Minor software improvements are probable as the experiment will be moving through new phases including a partial water fill, a water fill, and various scintillator fills. The UW group will also contribute to operator training.

*University of North Carolina, Chapel Hill, NC.
†Departed July, 2012, presently at Mayo Clinic, Rochester, MN.

1.19 SNO+ slow control and monitoring tools

L. A. Kippenbrock, T. J. Major, and N. R. Tolich

SNO+ features a "slow-control" system which monitors and controls the state of various parts of the detector. Specifically, the slow-control monitors rack voltages, crate currents, the status of magnetic compensation coils installed around the detector, voltage and temperature signals from the XL3 cards that control the electronics crates, and the status of the emergency stop and mine power. Additionally, the slow-control system can send a reset command to each XL3 and can turn on or off the compensation coils remotely.

In the last year, the input/output servers (IOSs) have been installed in their final location, and cables have been run from the IOSs to the electronics racks. The circuits controlling the XL3 resets and compensation coils have been installed and demonstrated to work.

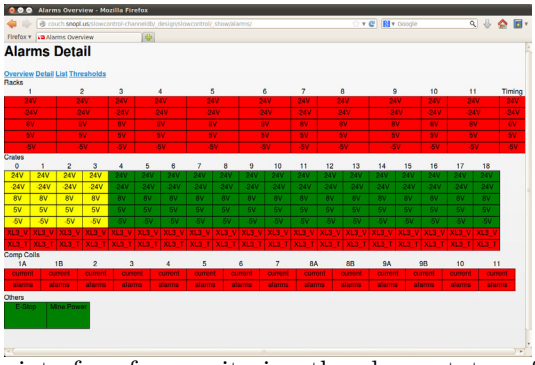

Figure 1.19-1. The web interface for monitoring the alarm status of SNO+ slow-control channels.

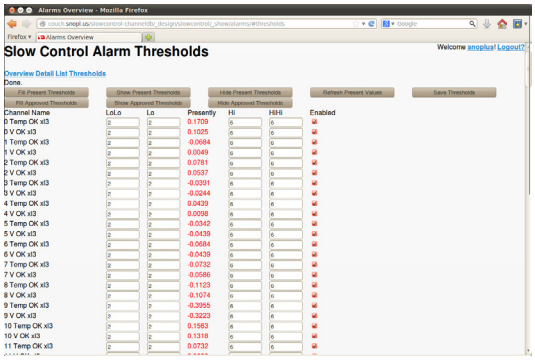

Figure 1.19-2. The web interface for adjusting SNO+ slow-control channel alarm thresholds.

Additionally, software has been written which collects data from each channel at 5-second intervals and saves alarms when appropriate. This software also has the ability to take action (*e.g.* sending an email) each time the alarm status changes. A web interface (Fig. 1.19-1) has been written to make it easy to quickly see which system statuses are acceptable, which are disabled, and which are throwing alarms. Another web interface (Fig. 1.19-2) allows an operator to quickly adjust thresholds at which a channel signals an alarm.

1.20 Measurement of light scattering in liquid scintillators considered for SNO+

T. J. Major and N. R. Tolich

The SNO+ experiment will utilize approximately one kiloton of liquid scintillator inside an acrylic sphere surrounded by light water. Several different scintillator solutions are being considered using various amounts of double-beta isotope and fluorescing agents. These solutions undoubtedly vary in their scattering response as a function of wavelength and scattering angle and possibly polarization as well. It is important to understand the light scattering properties of whichever solution is ultimately used in SNO+ and to consider this information in the choice of scintillator solution.

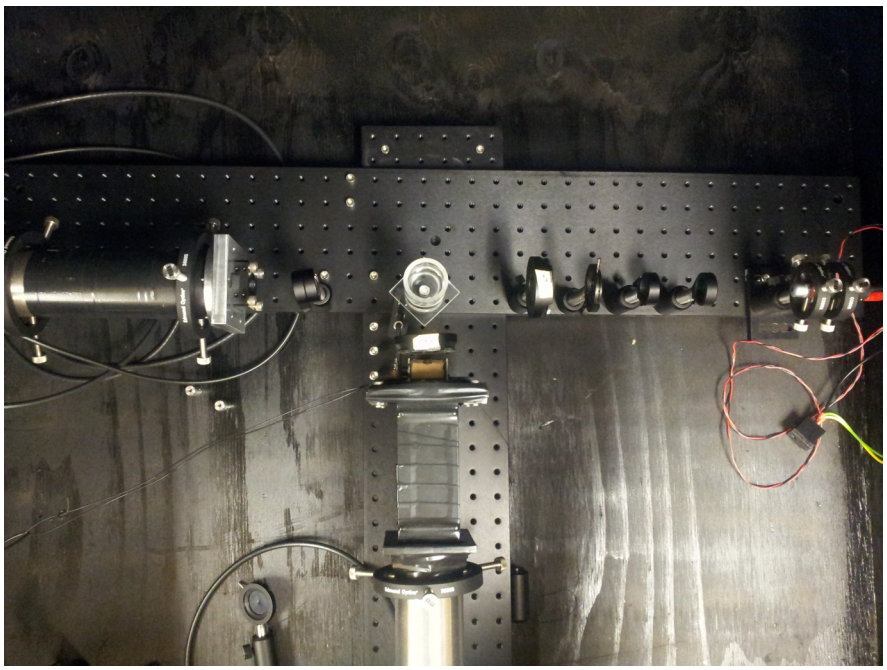

Figure 1.20-1. The current scattering measurement apparatus featuring an interchangeable laser, a turntable, and two PMTs.

An apparatus (see Fig. 1.20-1) has been constructed to measure the scattering light by liquids as a function of wavelength, scattering angle, and polarization. This information allows one to determine the amount of Rayleigh scattering versus scattering due to absorption/reemission. The apparatus consists of five interchangeable lasers, a photomultiplier tube (PMT) with a baffle to collect scattered light, and a turntable to adjust scattering angle. A second PMT is used to normalize the scattering intensity to the intensity of the incident light and allow an absolute measurement to be made.

HALO

1.21 The HALO supernova detector

C. A. Duba*, T. H. Burritt, F. Duncan[†‡], J. Farine[‡], A. Habig[§], A. Hime[¶], M. A. Howe[††], C. Kraus[‡], D. A. Peterson, R. G. H. Robertson, K. Scholberg[‖], M. Schumaker[‡], J. Secrest[**], T. D. Van Wechel, C. J. Virtue[‡], R. Wendell[‖], J. F. Wilkerson[††], S. Yen[‡‡], and K. Zuber[§§]

The Helium And Lead Observatory, HALO, has begun its mission as a dedicated supernova neutrino detector at SNOLAB. Designed to minimize downtime, HALO is at all times prepared to intercept neutrinos emitted by a supernova almost anywhere in our galaxy. The neutrino target material in HALO is 79 tonnes of lead, originally part of the Deep River Cosmic Ray Station. Charged- and neutral-current ν-Pb interactions produce neutron-unstable states and the subsequent emission of neutrons. A set of 128 ^{3}He proportional counters from CENPA, originally brought to Sudbury for the final phase of the SNO experiment, are arrayed throughout the target medium to detect the burst of neutrons that would signal the arrival of supernova neutrinos (Fig. 1.21-1).

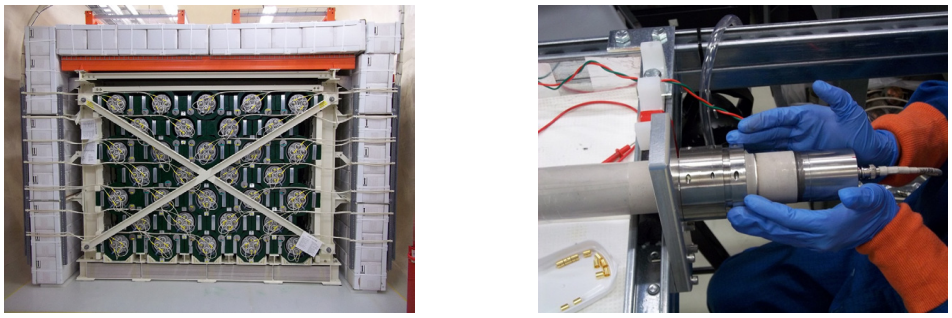

Figure 1.21-1. (left) The Helium And Lead Observatory (HALO), a dedicated supernova detector, fully instrumented and active at SNOLAB. (right) The process of installing end caps.

Contributions from CENPA were essential to reaching this operational milestone. The ^{3}He detectors are equipped with end caps produced with our CNC lathe. Metals in the underground laboratory experience accelerated corrosion so the end caps are sealed to prevent air exchange and the anode contacts are gold-plated to ensure these detectors will have a long operating life (Fig. 1.21-1). The preamplifiers, ADCs, high-voltage system, and most

*Digipen Institute of Technology, Redmond, WA.
†SNOLAB, Sudbury, ON, Canada.
‡Laurentian University, Sudbury, ON, Canada.
§University of Minnesota Duluth, Duluth, MN.
¶Los Alamos National Laboratory, Los Alamos, NM.
††University of North Carolina, Chapel Hill, NC.
‖Duke University, Durham, NC.
**Armstrong Atlantic State University, Savannah, GA.
‡‡TRIUMF, Vancouver, BC, Canada.
§§TU Dresden, Dresden, Germany.

of the cable stock for HALO have been adapted from CENPA's contributions to the SNO experiment.

The beginning of operation is far from the end of activities developing and improving HALO. A system that may need to operate for decades with minimal downtime requires an electronics system with few potential single points of failure. This principle guides the ongoing efforts to improve the detector power and data-acquisition systems. The system has been split between the left and right sides of the detector to ensure partial function in the event of the failure of any one component. Parallel VME crates, each with their own single-board computers, communication boards, and ADCs have been installed, and each side of HALO uses separate high-voltage supplies with independent control systems. An internal network between these components is being configured with backup connections implemented using a spanning tree architecture. Control and acquisition is performed with ORCA software, which has been modified for HALO to include a "fail-over" system. A secondary data-acquisition computer has recently been set up underground. It will monitor the primary system and will take over acquisition in the event of hardware, software, or power failure. A large UPS system has been installed which allows HALO to operate through multiple-hour laboratory power outages. This UPS is expandable which will allow the battery life to be extended in the future.

HALO is monitored remotely by collaboration members. This typically requires less than 15 minutes per day. As work on the electronics hardware for HALO is completed, more time will be invested in the monitoring and alert software. The goal will be to create easier-to-use monitoring tools which will allow the remote shifts to be distributed among more of the collaborators. Also, HALO will be able to produce alerts for more possible problems to ensure fixes can be implemented quickly. These will be the goals over the coming year, in addition to measurements of the background neutron rate, the detector efficiency, and coincident event rates. These measurements are essential to participation in the SuperNova Early-Warning System (SNEWS) which demands a stringent false-alert rate from member experiments. These activities ensure that HALO will be active at the moment of the next galactic supernova and will alert the astrophysical community through SNEWS.

Project 8

1.22 Status of the Project 8 neutrino mass experiment

M. Buuck, J. A. Formaggio*, D. Furse*, M. Jones‡, J. Kofron, B. LaRoque†, E. L. McBride, B. Monreal†, R. G. H. Robertson, L. J Rosenberg, G. Rybka, and B. A. VanDevender‡

Existing experimental constraints on neutrino mass come from oscillation experiments ($m_\beta \geq 0.02$ eV) and the Mainz experiment ($m_\beta < 2$ eV). The KATRIN experiment (see Sec. 1.1) is designed to probe the neutrino mass with a sensitivity of about 0.2 eV with a MAC-E spectrometer similar to that used at Mainz and Troitsk. The Project 8 collaboration

*Massachusetts Institute of Technology, Cambridge, MA.
‡Pacific Northwest National Laboratory, Richland, WA.
†University of California, Santa Barbara CA.

is building a prototype to explore the possibility of performing a neutrino-mass measurement based on a low-temperature radiometry technique which promises sensitivity into the $0.02\ \text{eV} < m_\beta < 0.2\ \text{eV}$ region. The technique hinges upon the passive detection of cyclotron radiation emitted from a trapped electron with energy near the endpoint of the β decay spectrum[1].

Examining this concept in the Project 8 prototype revolves around a detector fabricated from a section of WR42 waveguide immersed in a strong background magnetic field generated by a superconducting solenoid magnet. A carrier-free dilute gas of ^{83m}Kr provides a source of monoenergetic electrons from internal conversion. A fraction of these electrons can become trapped in a weak magnetic bottle induced by a small coil around the waveguide cell volume. The resulting cyclotron radiation is amplified by low-noise-temperature amplifiers provided by the National Radio Astronomy Observatory, converted to a digital signal, and recorded.

Data have been taken using the Project 8 detector system as constructed over the past year. Presently, efforts are underway to establish a limit on the total observable rate of electrons trapped as a result of ^{83m}Kr decay in the detector volume. In addition, adaptation of the CASPER astrophysics hardware DAQ to the Project 8 receiver data stream is underway to enable online triggering and analysis.

[1] B. Monreal and J. Formaggio, Phys. Rev. D **80**, 051301, (2009).

2 Fundamental symmetries and non-accelerator-based weak interactions

Torsion-balance experiments

2.1 Overview of the CENPA torsion-balance experiments

E. G. Adelberger

A surprisingly large number of ideas for solving open problems in fundamental physics, many of which are directed at unifying gravity with the rest of physics, predict new ultra-weak forces mediated by conjectured low-mass particles. String-theory ideas are particularly prolific in this regard, as the conjectured extra dimensions and the large number of low-mass particles all produce new forces. The discovery of such forces would have a revolutionary impact, and sufficiently sensitive upper bounds on the forces severely constrain the theories.

Motivated by these considerations, the CENPA Eöt-Wash group develops advanced torsion-balance techniques for sensitive mechanical measurements and applies them to address problems of current interest. We have produced the most sensitive tests of the equivalence principle[1], tested the Newtonian inverse-square law to the shortest distances[2], and tested certain Lorentz-violating properties of electrons five orders of magnitude below the Planck scale and non-commutative geometry at the 10^{13}-GeV level[3]. We currently operate 7 different torsion-balance instruments. Each one is devoted to a particular topic and is often the thesis project of an individual graduate student. At this moment one of the instruments is used for tests of the equivalence principle, two are used to probe short-range gravity, two are used to search for new electron-spin-dependent forces, and two are dedicated to investigating the subtle factors that limit the sensitivities of delicate mechanical experiments. The gravity group's expertise with mechanical systems and small forces has led to involvement in the gravitational-wave detectors LIGO and LISA. For Advanced LIGO we are developing a beam balance to measure ground tilt. The contributions below outline our progress in this area during the past year.

This work is primarily supported by NSF grant PHY-0969199 and the salaries, etc. of faculty, students and postdocs are covered by the NSF. Costs of some equipment used in both NSF- and DOE-sponsored research are shared between the two funding sources.

[1] S. Schlamminger *et al.*, Phys. Rev. Lett. **100**, 041101 (2008).
[2] D. J. Kapner *et al.*, Phys. Rev. Lett. **98**, 021101 (2007).
[3] B. R. Heckel *et al.*, Phys. Rev. D **78**, 092006 (2008).

2.2 Progress on a rotating torsion-balance test of the equivalence principle

E. G. Adelberger, J. H. Gundlach, B. R. Heckel, H. E. Swanson, and T. A. Wagner

We investigated the sensitivity of the differential gravitational acceleration of beryllium and aluminum to changes in the analysis parameters. Different segmentation of the data prior to fitting to harmonics of the turntable rotation frequency resulted in changes of up to 2σ to the determined differential acceleration of beryllium and aluminum. Overlap of drift with the harmonic terms in fitting the pendulum angle dominated the effect, but the method for excluding data due to transient events also contributed. If the data are random and uncorrelated, the results should be independent of the segment choices. A weighted average using overlapping segments effectively reduced the dependence due to different overlap of drift with the harmonic terms. Identification of transient events prior to segmentation of the data reduced the sensitivity due to differences in identifying and removing transient events after segmentation.

The data were separated into segments 2 turntable rotations long and fit with offset and linear drift terms plus harmonics of the turntable rotation frequency. Our data analysis procedure takes differences between the averages of segments taken using different orientations of the pendulum[1]. Our original analysis used non-overlapping segments. Segments were assigned based on the turntable angle modulo 720°. An improved analysis method uses a weighted average of overlapping segments with the segment start angle incremented by 90°. The weights are determined from the covariance computed based on the inclusion of the same data point in multiple segments.

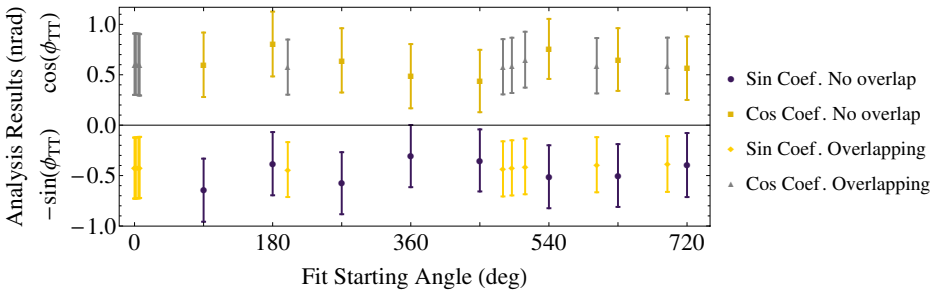

Figure 2.2-1. Results for Be-Al analysis using different segmentation choices. Error bars are 1-sigma statistical. The results are corrected for apparatus tilt, but not other systematic effects.

Fig. 2.2-1 shows the difference in Fourier components for the first harmonic of the turntable rotation frequency between the Be-Al and Al-Be pendulum test body configurations using both the original non-overlapping segments and the averaged overlapping segments. These results are proportional to the differential acceleration for the equivalence principle test but do not include systematic effects other than a correction for tilt.

[1]S. Schlamminger *et al.*, Phys. Rev. Lett. **100**, 041101 (2008).

2.3 NewWash FPGA rotation controller

H. E. Swanson and T. A. Wagner

The NewWash turntable consists of a low-friction air bearing, an eddy-current drive motor, and a 36000-line incremental angle encoder with two read heads, each providing quadrature sine and cosine outputs to interpolate between stripes. Absolute calibration comes from an output marking a single stripe at a known angle in the lab. We have implemented a new rotation controller in a National Instruments NI PCIe-7842R module. The board is based on a Virtex-5 LX 50R FPGA and has 8 independent ADC and DAC channels with 250-kHz sample rates plus many digital I/O ports. Instead of a hardware descriptive language (HDL) commonly used in other platforms, a version of LabView is used to program the FPGA. National Instruments also provides a C API to connect to a host DAQ program running on the same computer. The outermost structure of the controller's program is a while loop which continues as long as the controller is enabled. The simplified flow diagram in Fig. 2.3-1 describes each iteration around the loop.

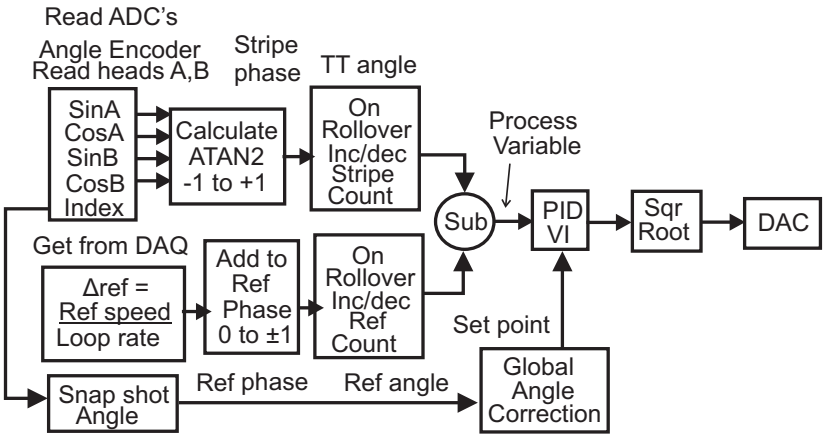

Figure 2.3-1. FPGA-based turntable motor controller.

Currently the loop executes at a 5-kHz update rate. The angle encoder's quadrature sine and cosine amplitudes are first symmetrized using an average of maximum and minimum values from previous stripes. The ATAN2 virtual instrument (VI) computes the stripe phase advance as the stripes are traversed. When this differs from the previous value by more than π, the stripe count is advanced. The desired speed divided by the loop rate gives the reference (Ref) phase advance per loop iteration. As with the stripe phase, the Ref count is advanced when the Ref phase rolls over. Representing the angles with integer and fractional parts circumvents limitations in the fixed-point math supported by the FPGA. The difference between the turntable (TT) and Ref angles produces the process variable given as input to the PID VI. This sub VI is provided in a National Instruments library of functions. Its loop gains are set in the host DAQ. The set point for the PID loop is currently zero but we allow for future modifications to correct for angle encoder imperfections. The square root of the PID output is sent to the DAC as the eddy-current motor torque is proportional to I^2.

2.4 NewWash torsion-balance upgrade

E. G. Adelberger, A. Emerman*, F. Fleischer, H. E. Swanson, and T. A. Wagner

The NewWash DAQ came into operation more than 10 years ago. Recently the DSP plug-in card, an integral part of the system, failed and due to its age and unsupported operating system we decided on a complete rebuild of the system.

All connections between the DAQ system and the torsion balance were re-mapped and recorded in an Excel spreadsheet. The old lab-built interface electronics required kernel support from the Windows 98 driver model which is no longer supported. They were replaced by digital I/O ports on the new data-acquisition hardware boards. We re-designed the temperature sensor multiplexers to use the ADC 'convert' signal from the hardware. Each read of the designated MUX channel now sequences through the temperature sensors adding them to the data stream. An LVDT position sensor was mounted between the torsion fiber top support and the vacuum can. Previously only stepper motor counts were available as a proxy for this distance. New high-resolution tilt sensors were mounted under the rotating balance and their preamplifiers were mounted in close proximity to minimize noise pickup. A web camera was added to view the turntable in real time for monitoring.

The new DAQ computer consists of an Intel core i7 CPU running at 3.4 GHz with 16 GB RAM and National Instruments data-acquisition hardware. The NI PCIe 6323 multi-function board is used for acquiring sensor data and provides the timing reference for data acquisition. The NI PCIe 7842R, a real-time FPGA board, is used to control the turntable. A GPIB interface board provides communication with the function generator and lock-in amplifiers associated with the autocollimator. The operating system is Microsoft Windows 7 Enterprise.

Software development was done in *C#* using Microsoft Visual Studio 2007 and National Instrument's Measurement Studio and DAQmx technologies. The .NET acquisition code is a complete rewrite of the previous acquisition software and uses a multi-threaded event-driven architecture. Raw sensor data is read at a 2-kHz rate. This is filtered through a second-order Butterworth filter with configurable time constants and further averaged for desired event rates less than 10 Hz. Some features include: scope displays of the raw sensor data, configurable graphic plots of sensor event data, FFT plots of sensor data, real-time data exchange with the turntable controller (see Sec. 2.3), and complete stepper motor control. Lock-in amplifier parameters can be set, read out, and included in the run metadata. The HDF5 file format was chosen for its efficiency in storing binary data and sensor metadata and for its wide-spread support as a standardized scalable data format. As a second option, an XML file containing tags for run and sensor metadata as well as space separated columns of sensor data is also available. Currently the legacy data format used by the other balances is not supported but can be obtained using a Python conversion script.

*Reed College, Portland, OR.

2.5 New bounds on ISL deviations from the Fourier-Bessel experiment

E. G. Adelberger and T. S. Cook

We have completed the analysis of our latest inverse-square law (ISL) test of gravity at short distances. With this test we have confirmed with 95% confidence that the Newtonian description of gravity holds for lengths down to 42 μm ($|\alpha| \geq 1$ limit), which improves upon our previous measurement of 56 μm[1].

After completion of our final data set[2], we looked for false signals at our 120-ω and 18-ω science frequencies from magnetic interactions, electrostatic interactions with the shield membrane, temperature modulations, seismic activity, and frictional torques in our drive system. No major systematic effects were found.

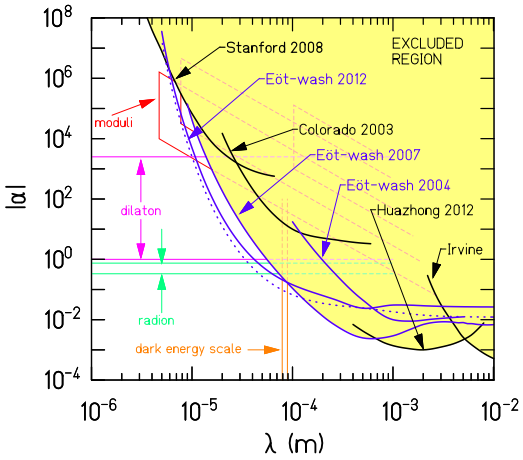

Figure 2.5-1. 95% exclusion of α for given values of λ. The solid line marked "Eöt-wash 2012" represents the worked described here. The dotted line represents the sensitivity our experiment would have had had it not favored the addition of a Yukawa potential.

We parameterized ISL-violating physics with the addition of a Yukawa potential to the standard Newtonian potential

$$V = -\frac{GMm}{r}\left(1 + \alpha\, e^{-r/\lambda}\right) \ , \tag{1}$$

where α is the strength relative to gravity and λ is the length below which the new physics "turns on". We fitted our torque data with various choices of λ while α was an unconstrained fit parameter. Our data favored the addition of a Yukawa potential at λ =75 μm with $\alpha = -0.14 \pm 0.05$, yet still provided new 95% exclusion limits from $\lambda = 6 - 80\mu$m (Fig. 2.5-1). Because the favored Yukawa had only 2.7σ resolution, and was feasibly a statistical anomaly, we do not consider this a positive measurement of new physics.

[1] D. J. Kapner *et al*, Phys. Rev. Lett. **98**, 021101 (2007).
[2] CENPA Annual Report, University of Washington (2012) p. 36.

2.6 Upgrade of the Fourier-Bessel short-range gravity experiment

E. G. Adelberger, T. S. Cook, F. Fleischer, C. D. Hoyle*, J. G. Lee, H. F. Leopardi*, and H. E. Swanson

In order to achieve the maximum possible sensitivity to short-range deviations from the inverse-square law with our Fourier-Bessel or wedge pendulum experiment, we have started to work on a comprehensive upgrade of the existing apparatus. The principle of the experiment and the design of the wedge pendulum have been described in previous annual reports[1,2].

We have identified several issues limiting the experimental sensitivity. The most important ones are the flatness of the pendulum, the attractor and the electrostatic shield, the relative alignment between the attractor and the shield and the excess noise observed for pendulum-shield separations smaller than a few hundred μm. We decided to rebuild part of the experimental setup to address these problems. In the following, the major components of this upgrade are described.

We have investigated options for an in-situ alignment of the electrostatic shield using vacuum-compatible actuators and a flexure. In terms of actuators, geared-down DC motor actuators from Physik Instrumente, GmbH & Co KG, have been chosen as the most promising candidates. The design of the new, in-situ adjustable shield-attractor setup is largely complete. In order to gain enough room for the new additions, we are replacing the lower vacuum chamber with a new one of increased diameter. This also allows us to address a stiffness problem of the existing setup by introducing a much more rigid support structure. The foil stretcher used for the electrostatic shield is replaced with a new design. Further, the pumping system is being upgraded by increasing the diameter of all pump-line components.

In order to improve the flatness of the pendulum and attractor surfaces, which so far show height variations of about $8 - 9$ μm, we researched assembly methods for mounting the patterned tungsten foil to its glass substrate. We also investigated a strategy to fill in the holes in the pattern with a low-viscosity epoxy. While slightly reducing the density contrast, this should allow for much easier modeling of the mass distribution and capacitance. In addition we believe that it might mitigate the excess noise problem at small separations between the pendulum and the shield.

In summary, we have started to upgrade several components of the Fourier-Bessel experiment. This upgrade is expected to optimize the performance of the wedge pendulum and to achieve significant gains in testing the inverse-square law at even shorter distances.

*Humboldt State University, Arcata, CA.

[1] CENPA Annual Report, University of Washington (2011) p. 35.
[2] CENPA Annual Report, University of Washington (2012) p. 36.

2.7 Parallel-plate inverse-square law test

J. H. Gundlach, C. A. Hagedorn, M. D. Turner, and K. Venkateswara

The parallel-plate experiment[1] has finished its second science run. Initial systematic tests are complete; the apparatus waits for any final questions we need to ask.

Analysis of this run is nearly complete. While not initially blind, the analysis proceeds as if the measurement were blind. This is in support of a planned subsequent measurement, which can be completely blind.

A previous partial science run was hampered by a significant systematic effect. The necessarily-varied attractor-foil capacitance tuned an LC resonance within the apparatus which coupled to the pendulum feedback loop. Interruption of the circuit with a large real impedance fixed it; residual signal was invariant under changes of the impedance by 10^6.

The foil interferometer[2] was stable to less than a fringe (330 nm) throughout the 50-day science run. In Fig. 2.7-1, we present a preliminary measurement of the foil's displacement with attractor position, as reconstructed from 1316 differential measurements.

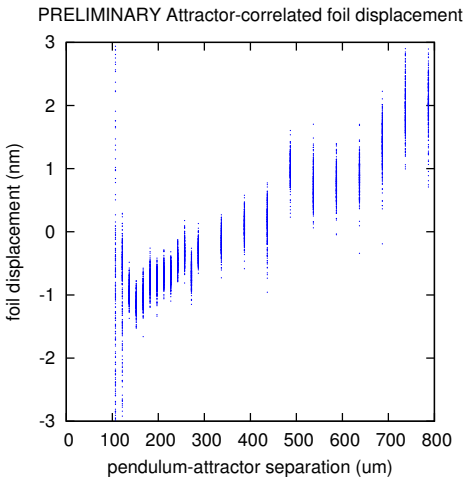

Figure 2.7-1. Bootstrapped reconstruction of the attractor-correlated foil displacement. The scatter of the points should be regarded as a 99% confidence interval.

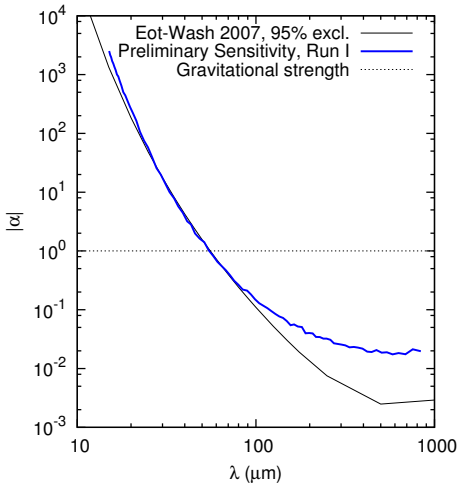

Figure 2.7-2. Statistical sensitivity for Yukawa interaction with strength α relative to gravity and scale λ, as bootstrapped from measured torque-difference uncertainties.

The run's statistical sensitivity is shown in Fig. 2.7-2. Magnetic, thermal, and thermal-gradient systematic tests are complete, and await the final version of the analysis software. The experiment is fundamentally noise-limited; re-enabling control of the pendulum-foil contact voltage will allow sensitive operation at closer pendulum-foil separations. Final results from this science run are expected in spring or early summer, 2013.

[1] CENPA Annual Report, University of Washington (2012) p. 37.
[2] CENPA Annual Report, University of Washington (2011) p. 35.

2.8 Constraints on long-range, macroscopic spin-dependent forces

E. G. Adelberger, B. R. Heckel, and W. A. Terrano

New low-mass bosons can mediate macroscopic forces of many types. Traditional "fifth-force"-type measurements set very stringent limits on forces which couple via scalar or vector bosons (Fig. 2.8-1), but are relatively insensitive to forces carried by pseudo-scalar or pseudo-vector particles, such as forces that couple at tree-level to the macroscopic spin of the test bodies. A comprehensive analysis of all possible spin-coupled interactions finds three which produce new spin-dependent forces between stationary, spin-polarized sources[1]. All three (spin-dot-spin, spin-cross-spin, and dipole-dipole) can be mediated by a spin-1 boson with axial and vector couplings g_A and g_V:

$$V_1 = \frac{g_A^2}{4\pi r}(\hat{\sigma}_1 \cdot \hat{\sigma}_2)e^{-r/\lambda} \tag{1}$$

$$V_2 = -\frac{g_A g_V \hbar}{4\pi m_e c r^2}(\hat{\sigma}_1 \times \hat{\sigma}_2 \cdot \hat{r})\left(1+\frac{r}{\lambda}\right)e^{-r/\lambda} \quad \text{and} \tag{2}$$

$$V_3 = -\frac{(g_A^2+g_V^2)\hbar^2}{16\pi m_e^2 c^2 r^3}\left[(\hat{\sigma}_1 \cdot \hat{\sigma}_2)\left(1+\frac{r}{\lambda}\right) - (\hat{\sigma}_1 \cdot \hat{r})(\hat{\sigma}_2 \cdot \hat{r})\left(3+\frac{3r}{\lambda}+\frac{r^2}{\lambda^2}\right)\right]e^{-r/\lambda}\ ; \tag{3}$$

where $r = r_1 - r_2$ and $\lambda = \hbar/(m_b c)$ is the interaction range of a boson of mass m_b.

To search for these interactions, we used the spin-dipole pendulum[2] and four spin sources made using the same principles[3]. We looked for torques on the pendulum as its spin direction is rotated relative to the sources. The torques should depend on the locations and orientations of the spin sources as described in Eqs. (1) to (3).

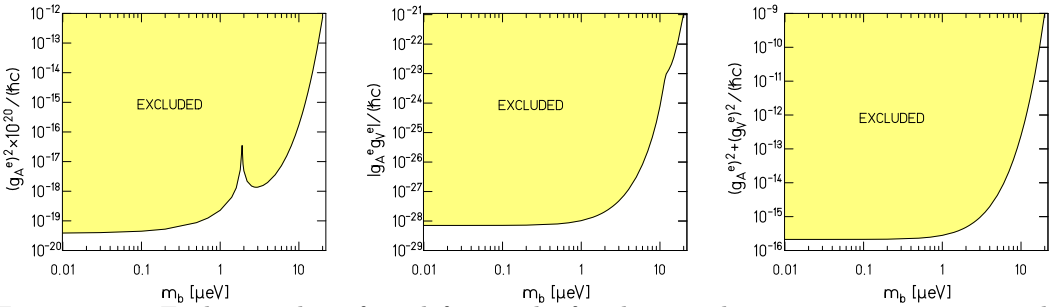

Figure 2.8-1. Exclusion plots, from left to right for the spin-dot-spin, spin-cross-spin and dipole-dipole interactions. The cusp at 20 μeV in spin-dot-spin is due to cancellations between the arms of the source.

Data were taken for several months with the spin sources oriented in several different directions, providing simultaneous sensitivity to all three potentials.

[1] B. A. Dobrescu and I. Mocioiu, J. High Energy Phys. **11**, 005 (2006).
[2] CENPA Annual Report, University of Washington (2004) p. 7.
[3] CENPA Annual Report, University of Washington (2007) p. 30.

2.9 First data and preliminary results from a search for short-range spin-coupled forces

E. G. Adelberger, B. R. Heckel, and W.A. Terrano

We have taken our first data with the torsion pendulum designed to look for spin-coupled forces[1]. Initial data had a very large 1-ω magnetic signal which swamped our 10-ω science signal. Changing the thickness of the MuMetal screen separating the attractor from the pendulum and adding metglas around the attractor hardly affected the 1-ω signal. Adding a second screen reduced the 1-ω signal (Fig. 2.9-1) to a level where we could take usable data to set limits on new spin-dipole interactions (Fig. 2.9-2). We are attaining limits of 2 nrad per day, nearly the thermal limit. No signal is resolved at this point.

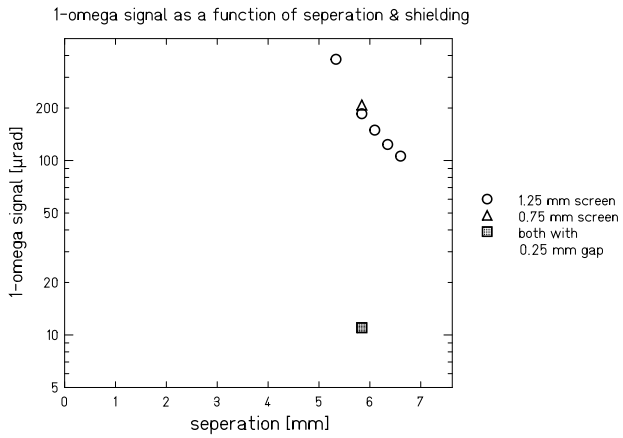

Figure 2.9-1. Magnetic 1-ω signal, showing the effectiveness of different screen shield configurations. We have made a screen with 3 layers of 0.25-mm shields with 0.20-mm gaps.

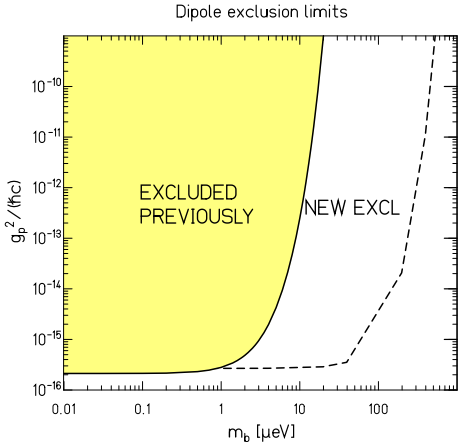

Figure 2.9-2. Preliminary limits on the dipole-dipole interaction from the new pendulum. The solid line is from $\sim$ 5 months of data taking with the old spin pendulum (see Sec. 2.8). The dashed line corresponds to one day of data with the new 10-pole pendulum.

We have made a new set of screening shields with a larger number of thinner layers of MuMetal allowing us to move from a 6-mm source-pendulum separation to a 4-mm separation. Since the interaction goes as $1/r^3$ and the length scale of the pendulum is only 3 mm, this could give us nearly another order of magnitude in sensitivity to new physics. We have also made a gravitational dummy of the attractor to set constraints on gravitational systematics associated with the density difference between $SmCo_5$ and Alnico.

[1] CENPA Annual Report, University of Washington (2007) p. 38.

2.10 Progress toward a hydrogen-rich equivalence-principle pendulum

E. G. Adelberger, B. R. Heckel, and W. A. Terrano

Ordinary luminous matter is believed to be less than one quarter of the total mass of the universe but these estimates rely on the assumption that the only long-range interaction between dark and luminous matter is gravity. This important assumption can be tested in the lab by looking for an equivalence-principle-violating interaction between the dark matter in our galaxy and a composition dipole in our pendulum, as any non-gravitational interaction is expected to violate the equivalence principle. The sensitivity of an equivalence-principle test is proportional to the degree to which the test bodies differ. To date, all equivalence-principle tests have employed test bodies that have varying degrees of neutron excess. One can gain roughly a factor of 10 in sensitivity by using test bodies of polyethylene (PE, which has a 1 in 7 proton excess) and beryllium (which has a 1 in 9 neutron excess)[1].

The prototype PE pendulum was significantly noisier than our previous equivalence-principle test[2]. The noise was significantly worse during the day than at night or on weekends, suggesting that the pendulum is more sensitive to seismic noise. To investigate the source of the noise, we have taken data with a dummy pendulum made without polyethylene and more rigidly assembled, but with the same size and moment of inertia. This tests the suspension system and the new optical path. We also validated the quality of the optical path and improved the mirrors.

The dummy pendulum led us to fix two major sources of noise in the system. A leak was found in a vacuum window near the fiber attachment which we sealed with leak sealant from K. J. Lesker, Co. We also found that the turntable was introducing noise to the system. Flipping the direction of rotation cleared the bearings allowing the dummy pendulum to operate at thermal noise. The PE pendulum is still quite noisy. Activity during recent building modifications made for poor data-taking conditions. We are investigating whether poor alignment of the mounting post could be coupling modes of the pendulum more strongly, perhaps introducing noise from modes which our seismic isolation does not attenuate efficiently.

2.11 Development of a second-generation hydrogen-rich equivalence-principle pendulum

E. G. Adelberger, B. R. Heckel, J. G. Lee, and W. A. Terrano

We are developing a second-generation hydrogen-rich equivalence-principle pendulum using what we have learned from our prototype (see Sec. 2.10). The major improvements involve reducing the mass and gravitational moments of the pendulum and designing test bodies which are removable and more rigidly secured to the frame. A good active/passive mass ratio can be maintained at the same time by eliminating the encasing shield[3].

[1] E. G. Adelberger, J. H. Gundlach, B. R. Heckel, S. Hoedl, and S. Schlamminger, Prog. Part. Nucl. Phys. **62**, 102 (2009).

[2] CENPA Annual Report, University of Washington (2012) p. 34.

[3] CENPA Annual Report, University of Washington (2012) p. 35.

The encasing shield serves two purposes: providing electrostatic shielding of the pendulum and azimuthally symmetrizing the significant outgassing of the hydrocarbon. We have successfully gold-coated both polyethylene and polypropylene by sputtering with a chromium adhesion layer which could alleviate the two concerns.

In the case that gold-coating does not limit the outgassing sufficiently, we are testing other coatings. Parylene-C is a vapor-deposited plastic which is pin hole free at 0.001" thickness. We are also investigating thicker metallic coatings. A base layer of copper is deposited by sputtering to avoid using a nickel-strike. Standard electroplating procedures follow to produce a thick coating. An example of a copper-electroplated polypropylene piece can be seen in Fig. 2.11-1. We are currently performing outgassing measurements on the test pieces with various coatings (see Sec. 2.12).

Figure 2.11-1. Copper-electroplated polypropylene, with about 0.005"-thick copper coating.

We also looked at other hydrogen-rich materials as possible test-bodies: lithium borohydride, $LiBH_4$, and ammonia borane (AB), NH_3BH_3. In isotropically purified forms these would give a 20% larger Z/μ than polypropylene. Lithium borohydride has been ruled out as it reacts violently with water. Ammonia borane was successfully compressed from a powder into a pellet, but concerns remain over the low temperatures at which it emits hydrogen.

2.12 Outgassing measurements of plastic test bodies

B. R. Heckel, J. G. Lee, and W. A. Terrano

We are currently performing outgassing measurements on the plastic test bodies intended for use in a second-generation hydrogen-rich equivalence principle test[1] (see Sec. 2.11). The test pieces include both bare and coated UHMW polyethylene (PE) and polypropylene (PP). We determine the outgassing rates using a pressure rise-time measurement and we can check for consistency based on the pump-down curves.

The testing apparatus uses a turbomolecular pump backed by a scroll pump. A metal-sealed gate valve separates the pump from a 6-way conflat cross serving as the test chamber, where a nude hot ion gauge measures the pressure. A second bellows valve allows venting to nitrogen for consistency between measurements of different samples. Using this venting procedure we observe a consistent empty chamber outgassing rate (see Fig. 2.12-1).

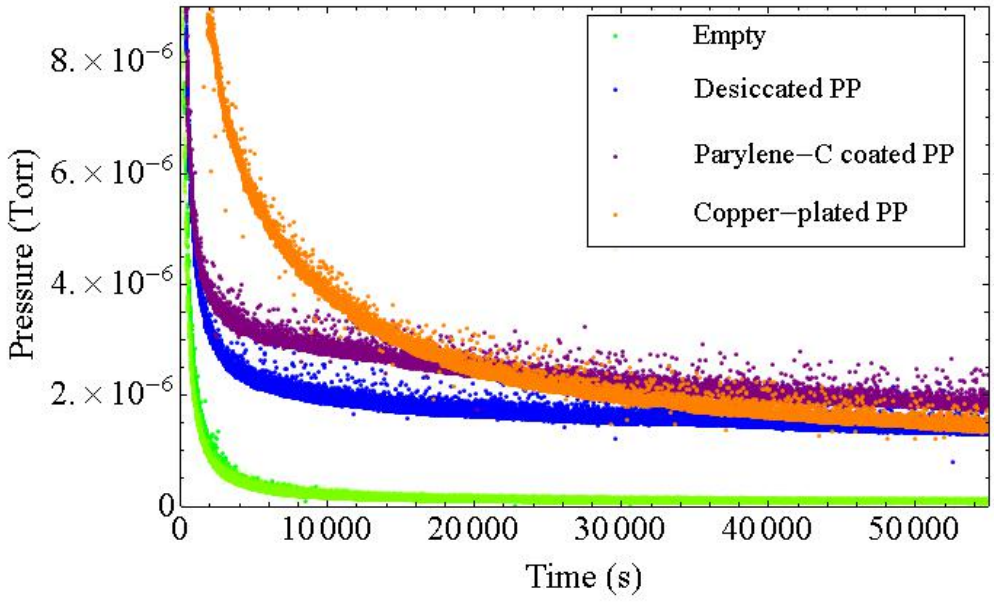

Figure 2.12-1. Pump-down curves. The four curves in green were taken with an empty chamber and all lie nearly on top of each other. The other curves for a desiccated piece of polypropylene, parylene-C coated polypropylene, and copper-electroplated polypropylene (blue, purple, and orange respectively) were spaced between the empty chamber runs.

Initial measurements led to complications from heating of the chamber by the hot ion gauge. However, by adjusting the DAQ program to take discrete measurements, the rate of rise may be interpolated. Using this method, we have established some initial estimates

[1] CENPA Annual Report, University of Washington (2012) p. 35.

of the outgassing rates for a piece of desiccated PP , parylene-C coated PP, and copper-electroplated PP (Table 2.12-1). A cold cathode gauge will be placed on the apparatus to ensure there are no large pressure spikes.

Test Piece	Outgassing Rate (Torr-L-cm^{-2} s^{-1})
Desiccated Polypropylene	4×10^{-9}
Parylene-C coated Polypropylene	7×10^{-8}
Electroplated Polypropylene	4×10^{-8}

Table 2.12-1. Outgassing rates of polypropylene test pieces.

2.13 Status of the cryogenic torsion balance

E. G. Adelberger, F. Fleischer, B. R. Heckel, and H. E. Swanson

The cryogenic torsion balance has been mentioned in earlier annual reports[1,2,3]. Operating a torsion balance at low temperature should make significant reductions in thermal noise possibly thereby increasing the sensitivity of our experiments to very small forces.

As mentioned in the previous annual report[4], thermal radiation from room temperature surfaces led to a reheating of the pendulum and made stable operation at low temperature impossible. We have solved this problem by adding cold infrared (IR) filters thermally anchored to the thermal shields and by adding some baffles and selective blackening of surfaces using a vacuum-compatible coating. We have now demonstrated that it is possible to operate the torsion balance below 10 K.

The achievable Q values were studied by recording the amplitude decay of the torsion oscillation starting from ~ 1 mrad and fitting these data using an exponential decay function. While tungsten fibers at room temperature yield Q values below 4000, values of about 10000 were measured for the same fiber material at low temperature. As copper-beryllium (CuBe) was reported[5] to perform better than tungsten at cryogenic temperatures, we also tested a fiber made from this material. With CuBe, low-temperature Q values of up to 36000 were observed.

Both the lower temperature and the decreased mechanical losses should reduce the thermal noise level, which is given theoretically (in terms of torque) by $\tau^2(\omega) = 4kT/\kappa Q\omega$. Unfortunately, the autocollimator currently in use in this experiment has an intrinsic noise level very close to the room temperature thermal noise of the torsion balance. Therefore it cannot resolve any possible improvement from cooling to cryogenic temperatures. We are currently working on a modified optical setup with multiple bounces off the pendulum mirror

[1] CENPA Annual Report, University of Washington (2009) p. 28.
[2] CENPA Annual Report, University of Washington (2010) p. 40.
[3] CENPA Annual Report, University of Washington (2011) p. 37.
[4] CENPA Annual Report, University of Washington (2012) p. 39.
[5] M.K. Bantel and R.D. Newman, J. of Alloys and Compounds, **310**, 233 (2000).

to increase the twist-angle sensitivity. Beyond this, we are also investigating possible concepts for a new, more sensitive optical angle measurement.

In summary, we have demonstrated operation of the cryogenic torsion balance at its design temperature and we have found substantial improvements in terms of Q value. The next step will be to test if these improvements result in the expected decrease of the thermal noise level.

2.14 Continued development of a dedicated gravity gradiometer system

J. H. Gundlach, C. A. Hagedorn, M. D. Turner, and K. Venkateswara

We have continued the development of a low-cost gravity gradiometer, as introduced in last year's annual report[1]. Significant progress has been made in determining a suitable on-board drive system that allows for precise control of the active masses while minimizing the introduction of systematic effects. We have also developed a wireless power-transmission system that provides sufficient power to the pendulum. Completion of a functional system and deployment in the area of our rotating equivalence-principle test is expected this year.

2.15 Multi-slit autocollimator

T. B. Arp, J. H. Gundlach, C. A. Hagedorn, M. D. Turner, and K. Venkateswara

The gravitational experiments performed at CENPA require precise measurement of the angular deflection of a torsion balance. This is achieved using autocollimating angle sensors, or autocollimators, which are insensitive to the swing motion of a torsion pendulum. We developed a multi-slit autocollimator (MSA) with a large dynamic range that is optimized for low-frequency performance. A MSA differs from a standard autocollimator by using an illuminated array of slits instead of a single light source to act as many autocollimators in parallel. This MSA differentially measures the angle between a target mirror and a reference mirror. The angle is read out by imaging the slits (reflected from the target and reference mirrors) onto a linear CCD. The MSA is intended for use in the LIGO tiltmeter (see Sec. 2.17) but it also advances our autocollimator technology. It was designed to have a 10-mrad dynamic range and sensitivity of 1 nrad/$\sqrt{\text{Hz}}$ at frequencies down to 10^{-2} Hz.

The autocollimator was designed and built last year[2] and has since been optimized to meet the design goals. New data-acquisition software with novel pattern-recognition algorithms was developed to read the angle information from the CCD at high speed (3300 frames/second.) Major improvements in the low-frequency noise came from increasing the thermal stability of the CCD and the light source. In addition, the autocollimator, originally run in air, is sensitive to air currents and air-pressure changes which inject low-frequency noise. In order to test the MSA without this effect, a vacuum chamber was obtained and the autocollimator

[1] CENPA Annual Report, University of Washington (2012) p. 39.
[2] CENPA Annual Report, University of Washington (2012) p. 43.

was operated inside at pressures of ∼10 Torr. Fig. 2.15-1 shows the current noise performance of the MSA compared to a standard autocollimator used in gravity experiments.

The MSA has met its engineering goals with ∼1 nrad/$\sqrt{\text{Hz}}$ resolution at frequencies down to 10^{-2} Hz with a linear response over a measured dynamic range of 10 mrad. Noise tests have been performed using at a static angle target. The testing of the autocollimator on a real torsion balance, the tilt sensor for which it was optimized, is underway.

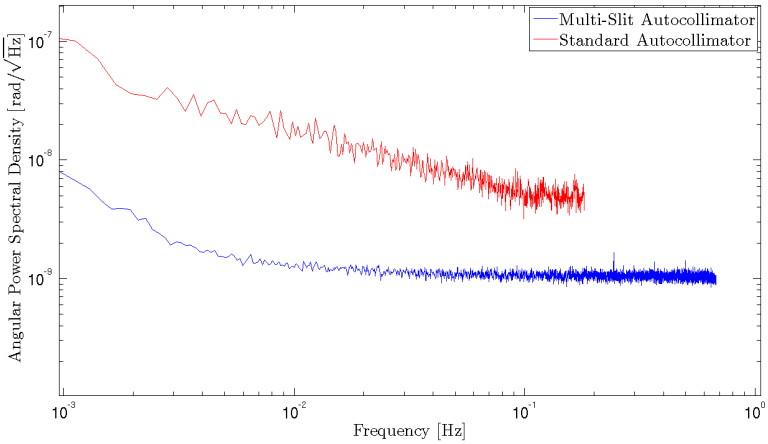

Figure 2.15-1. Noise spectra of the multi-slit autocollimator and a standard autocollimator.

2.16 Improved interferometric quasi-autocollimator

J. H. Gundlach, C. A. Hagedorn, M. D. Turner, K. Venkateswara, and A. Zhdanova

Precise angular deflection measurement devices (e.g. autocollimators) are a critical part of torsion balance experiments, and we are developing an optical system (described in previous annual reports[1,2]) that uses the principal of weak-value amplification to achieve sensitivities of 10^{-11} rad/$\sqrt{\text{Hz}}$. This instrument is called the interferometric quasi-autocollimator, or iQuAC. A proof-of-concept iQuAC has been successfully built, and a more stable prototype is being developed – a top view of the current iQuAC can be seen in Fig. 2.16-1.

A custom base plate of thick aluminum for the iQuAC was designed and built. The stiff material will reduce the amplitude and raise the frequencies of mechanical vibration. The plate's improved thermal conductivity will reduce thermal gradients and attenuate low frequency motion. The new design reuses optical components from the prototype, but components are mounted without posts/holders to limit vibration susceptibility. The new layout shortens the optical path in the interferometer to add thermal stability and reduce dispersion. Attempts to characterize the new apparatus were limited by minor electronic and alignment errors.

[1] CENPA Annual Report, University of Washington (2010) p. 42.
[2] CENPA Annual Report, University of Washington (2011) p. 38.

The new iQuAC may require seismic isolation, as did the prototype. Atmospheric twinkle may be important at such high sensitivity; we will experiment with vacuum operation.

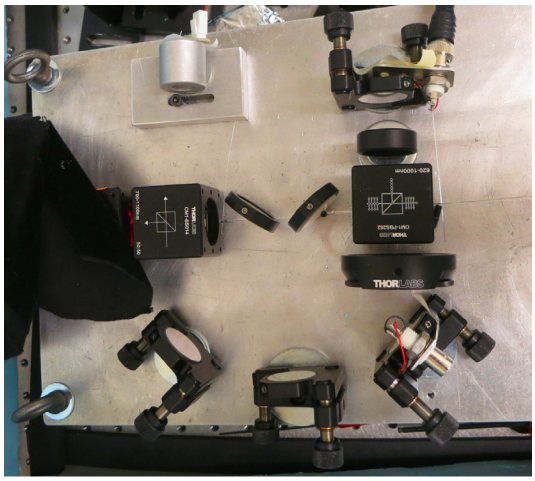

Figure 2.16-1. A top view of the iQuAC. Note the close spacing of the optics, minimizing laser dispersion.

2.17 Progress on development of a precision tiltmeter for advanced LIGO

T. B. Arp, J. H. Gundlach, C. A. Hagedorn, M. D. Turner, and K. Venkateswara

Advanced LIGO (aLIGO) is a next-generation gravitational-wave detector system expected to make first detections when turned on in 2015. Key among the improvements in the new detector is a better seismic isolation system to cancel the effect of ground motion on the mirrors. This is done through an active control system which measures the ground motion through seismometers and applies a corrective force on the optics platform. However, at low frequencies (10 mHz to 0.5 Hz) seismometers are strongly affected by ground rotation/tilt which can interfere with the ability to correct the motion. Thus, aLIGO needs a ground rotation sensor or tiltmeter to accurately distinguish between horizontal motion and tilt. The requirements for the sensitivity of the tiltmeter are more than an order of magnitude more stringent than commercial tiltmeter sensitivities.

As reported last year[1], we are developing a tiltmeter consisting of a very-low-frequency flexure beam balance. We measure its angle using an autocollimator mounted to the floor/platform. Above its resonance frequency the balance remains inertial, thus the autocollimator measures ground tilt. Horizontal ground motion is rejected by locating the center of mass at the pivot point of the flexure. The prototype beam consists of a 0.75-m aluminum tube with 1.8-kg brass weights attached at each end. It is suspended by two copper beryllium flexures $\sim$40 μm thick.

[1]CENPA Annual Report, University of Washington (2012) p. 41.

Over the last year we made several improvements to our design and achieved better rotation sensitivity. To improve the sensitivity of our autocollimator we put in place a simple scheme of multiple bounces of the laser beam. With four bounces from the target mirror we achieved a noise level of $\sim$1 nrad/$\sqrt{Hz}$ over the required frequency range.

Using a wire EDM we made new flexures out of beryllium copper and silicon bronze. The silicon bronze flexures were about 40-μm-thick and had the smallest angular stiffness yet. The beam was then suspended from these flexures and the center of mass adjusted to within 10 μm of the pivot. This balance had the best noise performance to date. Fig. 2.17-1 shows the amplitude spectral-density plot of 5000 seconds of data taken under quiet conditions at night. The expected tilt signal was small so this could be interpreted as the limiting instrument noise. At frequencies above $\sim$50 mHz we are limited by the autocollimator noise and at lower frequencies we are probably limited by down-conversion of high-frequency seismic motion.

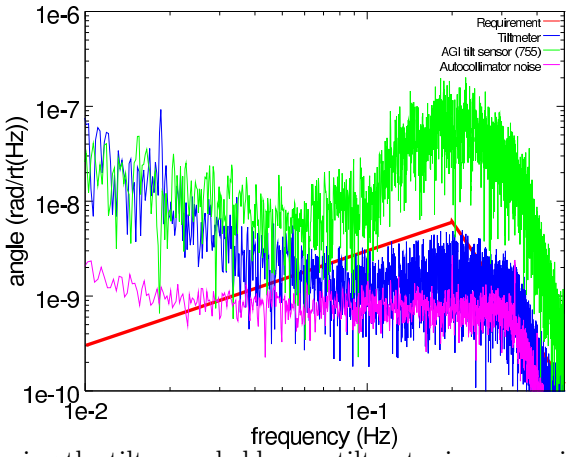

Figure 2.17-1. Plot showing the tilt recorded by our tiltmeter in comparison to a commercial AGI tilt sensor. Also shown are the autocollimator noise and aLIGO requirements.

To investigate the low-frequency noise further, we made flexures out of monocrystalline silicon wafers and suspended the bar from them. The flexures were made using an hydroxide etching technique. The thicknesses were reduced to 60–100 μm. The beam was then carefully suspended from the flexures. We were successfully able to suspend the nearly 4-kg balance from two 80-μm-thick silicon flexures. The center of mass was adjusted close to the pivot to produce a balance with a period of nearly 90 seconds.

Unfortunately the balance proved much noisier than our earlier balances. Once again, the reason was probably the down-conversion of high-frequency seismic noise to low-frequency tilt through higher-order modes of the flexure. The problem was worse with the silicon flexures due to the long thin shape of the flexure as opposed to the semi-circular metal flexures. We plan to mitigate this seismic down-conversion noise by using an additional stage of horizontal vibration isolation.

With the low-frequency noise mitigated we ought to be limited by the autocollimator noise alone. By using the new multi-slit autocollimator being developed by the group we expect to attain the sensitivity required by aLIGO.

Non-accelerator-based weak interactions

2.18 Calibrations for the UCNA experiment and foil thickness measurements at CENPA

A. García, R. Hong, T. G. MacDonald*, and D. Tarazona for the UCNA collaboration

The energy response and linearity of each PMT are important for the β-energy reconstruction in the UCNA experiment[1]. They are calibrated with conversion electron sources: ^{139}Ce, ^{113}Sn, and ^{207}Bi. The radioactive material in each source is sealed between aluminized Mylar foils through which the β particles lose energy. Therefore, it is important to measure the thicknesses over the active part of these calibration source foils.

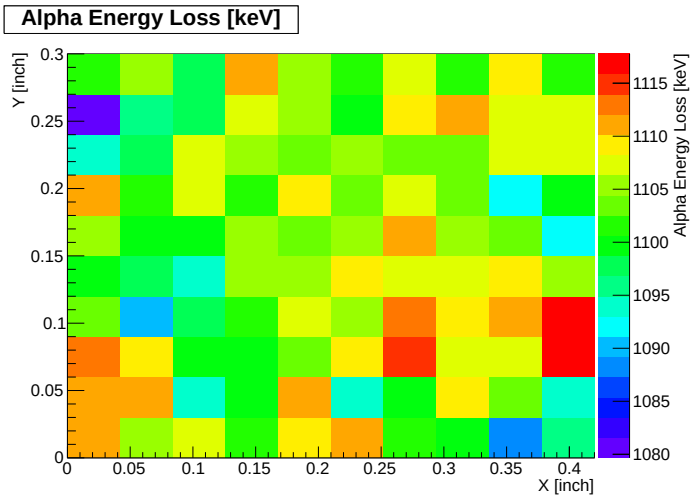

Figure 2.18-1. Color map of α-energy loss on ^{207}Bi source foil.

The thicknesses of the foils were determined via the energy loss of 5485.6-keV α particles from a collimated 1-μCi ^{241}Am source. The device to scan the foil thicknesses was developed at CENPA[2] in 2011. In order to stabilize the detector response a Peltier cooling unit was employed in 2012 to cool down the silicon detector and the temperature of the detector was monitored by an RTD sensor. During the measurement the temperature was varied around 3° C, while the leakage current through the silicon detector was about 15 nA. For each foil we scanned 10×10 points around the center, with x-stepsize 0.042" and y-stepsize 0.030". The α beam spot size on the foil was about 0.040 inches. At each point, we took data for 10 minutes, during which about 500 counts were collected. During each run, points within one column (same x coordinate) can be scanned automatically, while the transition from one column to another must be done by hand. We ran detector response calibrations for 50 minutes before every other column scan, with the foil away from the α beam.

*Departed February, 2013, presently at Astronics, Kirkland, WA.

[1] M. P. Mendenhall *et al.*, (UCNA Collaboration), Phys. Rev. C **87**, 032501 (2013).
[2] CENPA Annual Report, University of Washington (2012) p. 46.

We scanned all three source foils. A typical α-energy-loss map is shown in Fig. 2.18-1. We also scanned a piece of aluminized Mylar foil with a nominal thickness of 6 μm for comparison. The average α-energy loss, relative uniformity and converted effective thicknesses are shown in Table 2.18-1. The α-energy-loss-to-thickness conversion is done by Monte Carlo simulation. The measured and nominal thicknesses agree well with each other for the 6-μm comparison foil. For the three source foils, the thicknesses are about 9.4 μm, larger than the nominal 6-μm thickness specified by the manufacturer. This might be due to the adhesives that seal the source package.

Foil name	Average E_α loss [keV]	Uniformity [%]	Effective thickness [μm]
^{139}Ce	1125	1.3	9.47±0.12
^{113}Sn	1120	2.6	9.42±0.24
^{207}Bi	1100	1.4	9.27±0.13
6-μm Mylar	690	0.4	5.94±0.02

Table 2.18-1. Average α-energy loss, uniformity and effective thicknesses.

The detailed thicknesses of the calibration foils are included in the Monte Carlo simulations of scintillator energy deposition and the systematic uncertainty from the energy reconstruction amounts to 0.31% of A[1], the β-asymmetry correlation coefficient in neutron β-decay.

2.19 Search for an electric dipole moment of ^{199}Hg

Y. Chen, E. N. Fortson, B. Graner, B. Heckel, and E. Lindahl

Atomic EDM experiments offer perhaps the most sensitive probe of CP violation in theories of physics beyond the Standard Model, and our measurements of the ^{199}Hg EDM over the years have achieved the most precise EDM limit on any system. Searches in diamagnetic atoms, such as ^{199}Hg provide bounds on nuclear EDMs that would most likely originate from CP-violating interactions within and between nucleons. Our current upper limit for the EDM of ^{199}Hg is $|d(^{199}\mathrm{Hg})| < 3.1 \times 10^{-29} e\,\mathrm{cm}$, a seven-fold improvement in the upper limit over our previous work[1]. This project is supported primarily by the NSF (PI. Fortson, co-I Heckel).

The current version of the ^{199}Hg EDM apparatus uses ultraviolet (UV) laser light to polarize and measure the spin precession frequency of ^{199}Hg atoms in 4 vapor cells, 2 of which (the inner pair) have oppositely directed electric fields. All cells lie in a uniform magnetic field. The frequency difference between the inner pair of cells is sensitive to an EDM while the outer cells are used to monitor the magnetic field and its linear gradient. The experiment is now sensitive to spin precession frequency shifts on the 10^{-10} Hz scale. A blind frequency offset is added to the inner-cell frequency difference to mask the EDM signal until the analysis of an entire data set is complete. A comprehensive description and review of our ^{199}Hg EDM experiment was published recently[2].

[1] W. C. Griffith *et al.*, Phys. Rev. Lett. **102**, 101601 (2009).
[2] M. D. Swallows *et al.*, Phys. Rev. A **87**, 012102 (2013).

In the past year we have re-assembled our EDM apparatus and have begun to take test data. Our achievements include:

a) The construction of new ^{199}Hg vapor cells with lifetimes in excess of 400 s. The cells were bonded without glue to prevent the disappearance of ^{199}Hg over time.

b) The acquisition and commissioning of a commercial UV laser system accompanied by an improved method to equally split the laser beam between the 4 vapor cells.

c) Implementation of a new "in the dark" frequency-precession detection method. The precessing ^{199}Hg spins are probed at the beginning and end of a 240-s probe interval, allowing the ^{199}Hg atoms to interact with the applied electric field in the absence of UV laser light. This method reduces systematic errors and improves our ability to measure small frequency differences between adjacent vapor cells.

d) Assembly of a cell enclosure vessel with a SnO-coated center electrode plane to remove any metallic materials in the vicinity of the vapor cells. New high-voltage feedthroughs reduce leakage currents to the vessel.

Our current experimental sensitivity from test data we have taken is 2 times better than in our 2009 experiment. We are working on another factor of 2 improvement through better control of the pointing stability of our laser beams. We expect to begin taking EDM data during the summer of 2013.

3 Accelerator-based physics

Nuclear structure and nuclear astrophysics

3.1 Overview of the nuclear-structure experiments at CENPA

A. García

During the past year we completed two experiments on nuclear-structure issues related to weak interactions and nuclear astrophysics.

Using the ^{6}He source we have made an accurate determination of the ^{6}He lifetime. This showed agreement with the axial coupling constant, g_A, from neutron beta decay indicating that modification in the nuclear medium in the case of ^{6}He is at most similar to the uncertainties in the nuclear-structure calculations[1,2].

We completed analysis and published work on nuclear-structure issues related to double-beta decays. In particular we have determined the electron-capture branch from ^{116}In which allows us to benchmark nuclear models used in this region of the nuclear chart[3].

Our involvement in nuclear astrophysics is at a reduced level but we used our source to produce implanted targets of ^{36}Ar that will be used for an experiment later in 2013.

3.2 ^{6}He Lifetime and g_A in nuclei

A. García, R. Hong, A. Knecht*, P. Müller†, H. E. Swanson, I. S. Towner‡, W. Williams†,¶, C. Wrede‖, and D. W. Zumwalt

The β decays of ^{3}H and ^{6}He can play an important role in testing nuclear wave-function calculations and fixing low-energy constants in effective field theory approaches. Before our measurement there were large discrepancies between measurements of the ^{6}He half-life.

Using our atomic ^{6}He source we have made an accurate determination of the ^{6}He lifetime resolving previous discrepancies and providing, in combination with ab-initio nuclear-structure calculations, a determination of the axial coupling constant, g_A. This showed agreement with g_A from neutron beta decay indicating that modification in the nuclear medium

*Departed July, 2012, presently at Paul Scherrer Institut, Villigen PSI, Switzerland.
†Argonne National Laboratory, Argonne, IL.
‡Cyclotron Institute, Texas A&M University, College Station, TX.
¶Presently at Old Dominion University, Norfolk, VA.
‖Presently at the National Superconducting Cyclotron Laboratory, Michigan State University, East Lansing, MI.

[1] A. Knecht *et al.*, Phys. Rev. Lett. **108**, 122502 (2012).
[2] A. Knecht *et al.*, Phys. Rev. C **86**, 035506 (2012).
[3] C. Wrede *et al.*, Phys. Rev. C **87**, 031303(R) (2013).

in the case of ^{6}He is at most similar to the uncertainties in the nuclear-structure calculations[1,2].

3.3 Preparations for an ^{36}Ar(^{3}He, α)^{35}Ar experiment and the role of ^{34}Ar(p, γ)^{35}Ar in novae

S. Bishop*, A. García, R. Ortez, and C. Wrede†

During classical nova explosions the accretion of hydrogen-rich material onto a white dwarf star prompts nucleosynthesis by thermonuclear radiative proton capture coupled with the further emission of energy by nuclear beta decay. In order to model such explosions it is necessary to measure the responsible nuclear reaction rates. In particular an experiment planned to take place at Maier-Leibnitz-Laboratorium (MLL), Germany, aims to measure the resonance energies of the ^{34}Cl$(p,\gamma)^{35}$Ar reaction, which is important for calculating the endpoint of nucleosynthesis in the hottest classical nova events. To induce this reaction, a beam of ^{3}He^{2+} will be incident on a ^{36}Ar target, and the emitted ^{4}He will then be momentum analyzed by a quadrupole-dipole-dipole-dipole(Q3D) magnetic spectrograph. The momentum measurements will be used to determine the excitation energies of ^{35}Ar which are the same resonance states created in the ^{34}Cl$(p,\gamma)^{35}$Ar reaction.

Particular attention is needed when creating ^{36}Ar targets because it is a noble gas and would normally require the use of a container to retain it. This introduces a number of difficulties with performing precision measurements with the most notable being interactions with the container windows. CENPA has the necessary equipment for producing solid targets by ion implantation with high isotopic purity and well-known uniformity and composition profile. In particular the ^{36}Ar target that will be used at the MLL was created at CENPA by using natural-abundance argon gas in the direct extraction ion source (DEIS), ionizing the argon, accelerating it, and bending it with a 90° analyzing magnet which enabled the selection of the desired isotope. The beam of ^{36}Ar was then focused onto a 30-μg/cm^2 carbon foil into which about 2 μg/cm^2 of ^{36}Ar was implanted. In order to improve the uniformity of implantation, magnetic steerers were used to raster the beam over an collimator with a diameter of about 0.8 cm. To minimize the accumulation of contaminants on the foil, a liquid nitrogen cold trap was inserted just before the collimator. During about 40 hours of implantation we made two ^{36}Ar targets to be used for the experiment.

*GSI, Darmstadt, Germany.
†Michigan State University, East Lansing, MI.

[1] A. Knecht *et al.*, Phys. Rev. Lett. **108**, 122502 (2012).
[2] A. Knecht *et al.*, Phys. Rev. C **86**, 035506 (2012).

3.4 Electron capture on ^{116}In and nuclear structure related to 2β decay

A. Algora*, J. Äystö†, V. V. Elomaa†, T. Eronen†, A. García, J. Hakala†, V. S. Kolhinen†, I. D. Moore†, H. Penttilä†, M. Reponen†, J. Rissanen†, A. Saastamoinen†, S. K. Sjue‡, H. E. Swanson, and C. Wrede§

Using Penning-trap-assisted decay spectroscopy at the University of Jyväskylä we have measured the electron-capture decay branch of ^{116}In to be $[2.46 \pm 0.44(\text{stat.}) \pm 0.39(\text{syst.})] \times 10^{-4}$. We found that the corresponding Gamow-Teller transition strength is compatible with the most recent value extracted from the (p, n) charge-exchange reaction, providing a resolution to longstanding discrepancies. This transition can now be used as a reliable benchmark for nuclear-structure calculations of the matrix element for the neutrinoless double-β decay of ^{116}Cd and other nuclides.

Last year we finished the data analysis and published a brief summary of this work[1].

Accelerator-based weak interactions

3.5 Overview of the ^{6}He experiments at CENPA

Z. T. Alexander, Y. S. Bagdasarova, T. M. Cope, X. Fléchard¶, A. García, R. Hong, Y. Kim, A. Knecht‖, E. Liénard¶, P. Müller**, O. Naviliat-Cuncic††, D. W. Storm, H. E. Swanson, F. Wauters, and D. W. Zumwalt

In the Standard Model of particle physics the electroweak currents are mediated by vector and axial-vector currents. We are using the beta decay of ^{6}He to search for *tensor* currents, a manifestation of new physics predicted by some theories that go beyond the Standard Model. As opposed to the currents of the Standard Model, tensor currents flip the chiralities of the particles and consequently affect the correlations and the shape of the beta spectrum. Presently we are focused on determining the electron-antineutrino correlation coefficient by trapping ^{6}He in a laser Magneto-Optical Trap (MOT) at the level of 0.1% (about 1 order of magnitude improvement over previous measurements). We will achieve this by measuring the momenta of the emitted electrons and of the Li ions. The electrons will be detected with a combination of a multi-wire proportional chamber and a scintillator, while the Li ions will be detected by electrically guiding them onto a position-sensitive micro-channel plate (MCP)

*Instituto de Física Corpuscular, University of Valencia, Valencia, Spain.
†University of Jyväskylä.
‡Los Alamos National Lab, Los Alamos, NM.
§Michigan State University, East Lansing, MI.
¶LPC-Caen, ENSICAEN, Université de Caen, Caen, France.
‖Departed July, 2012, presently at Paul Scherrer Institut, Villigen PSI, Switzerland.
**Argonne National Laboratory, Argonne, IL.
††National Superconducting Cyclotron Laboratory, Michigan State University, East Lansing, MI.

[1] C. Wrede *et al.*, Phys. Rev. C **87**, 031303(R) (2013).

detector. In order to gather enough statistics for a determination at the level of 0.1%, the trap must be continuously populated with approximately 1000 atoms of ^{6}He ($t_{1/2} \approx 0.8$ s) for a period of about one week.

Because the laser system cannot work from the electronic ground state of ^{6}He, the atoms are excited to a metastable state at about 20 eV. This is achieved by radio-frequency (RF) excitation in the presence of another noble gas (Kr at about 1 mTorr, for example). This process is inefficient: only about one in 10^5 of the atoms that are subjected to it come out in the metastable state. As a consequence the experiment needs an intense source of ^{6}He. The tandem accelerator at CENPA is well suited for this purpose and we have reached a production rate of approximately 10^{10} atoms per second[1]. Presently this is the most intense source of ^{6}He atoms in the world. This allows us to make these precise measurements in a timely manner.

During the last year we made much progress in the detector setup systems and in the He trapping systems for the electron-neutrino correlation experiment. The following articles describe progress in each area. Our goal is to collect the first data during the summer of 2013.

3.6 Beta detector for the ^{6}He experiment

Z. T. Alexander, Y. S. Bagdasarova, T. M. Cope, X. Fléchard*, A. García, R. Hong, Y. Kim, A. Knecht†, E. Liénard*, P. Müller‡, O. Naviliat-Cuncic§, D. W. Storm, H. E. Swanson, F. Wauters, and D. W. Zumwalt

We constructed a β particle detector for the ^{6}He experiment. It measures the total energy and the hit position of the β particle from the ^{6}He decay. We use it to start the measurement of the time of flight (TOF) of the recoil ^{6}Li ion, and the energy spectrum of the β particle. The position sensitivity is used to identify backscattering and other sources of systematic uncertainties.

The β detector chamber sits on top of the magneto optical trap (MOT) chamber where the ^{6}He atoms are trapped. A cross-sectional view of the β-detector chamber is shown in Fig. 3.6-1. At the very bottom of the chamber, there is a 1.5-inch-diameter, 127-μm-thick beryllium window fusion-bonded to the stainless-steel window holder. It is strong enough to separate the ultra-high vacuum in the MOT chamber from the 1-atm proportional gas in the detector chamber without severe deformation, while allowing the β particles to penetrate without too much energy loss and straggling. The window holder is designed to be sealed to the middle section of the chamber with indium wire sealing. The multi-wire proportional chamber (MWPC) sits right above the beryllium window. It has two cathodes at the top

*LPC-Caen, ENSICAEN, Université de Caen, Caen, France.
†Departed July, 2012, presently at Paul Scherrer Institut, Villigen PSI, Switzerland.
‡Argonne National Laboratory, Argonne, IL.
§National Superconducting Cyclotron Laboratory, Michigan State University, East Lansing, MI.

[1] A. Knecht *et al.*, Nucl. Instrum. Methods Phys. Res., Sect. A **660**, 43 (2011).

and the bottom, with 24 wires grouped by 4 on each board. The wire directions of the two cathodes are perpendicular to each other. One anode is between the two cathodes, with 18 inter-connected wires. The chamber is filled with an atmosphere of 10% CO_2 in Ar for gas multiplication. The anode is biased to ∼2500 V during operation and gives the energy deposition in the MWPC while the induced charges on the cathodes are read through each wire group and the position of the avalanche can be reconstructed via the "charge center of gravity" algorithm. Above the MWPC, a 1.5-inch-thick BC408 plastic scintillator can fully stop all the β particles from the ^{6}He decay. The scintillation light is transported through a Lucite light pipe and sensed by a Hamamatsu R1250 photomultiplier tube (PMT). The PMT signal corresponds to the total kinetic energy of the incoming β particle. The top section of the detector chamber is sealed to the light pipe with an o-ring and there are four ports for gas handling and electronic feedthroughs.

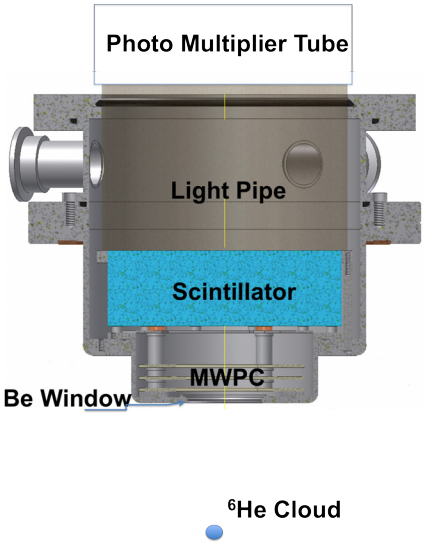

Figure 3.6-1. Cross-sectional view of the β detector chamber.

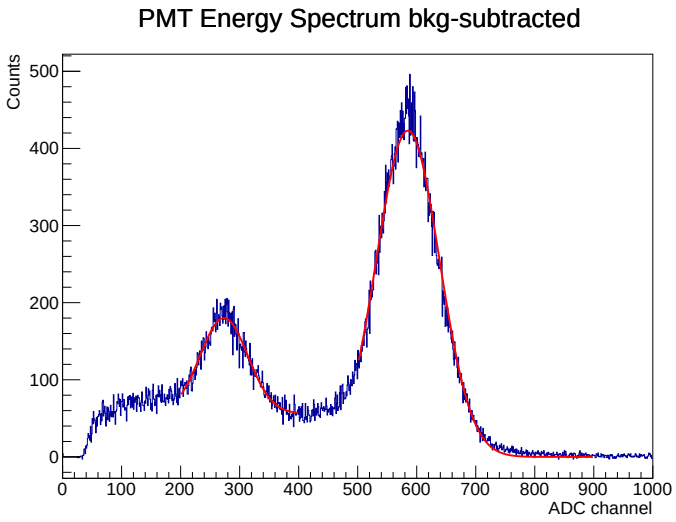

Figure 3.6-2. PMT spectrum of the ^{207}Bi source with coincidence trigger fitted with 2 Gaussian functions.

The β detector was tested using a ^{90}Sr β source. By triggering on the coincidence of the MWPC anode and the PMT signals, the background in the PMT is suppressed. Comparing the background-subtracted PMT-single trigger rate with the coincidence trigger rate, we found the efficiency of the MWPC to be about 94%. The energy calibration is done using the conversion electrons from the ^{207}Bi source. Since the MWPC is not sensitive to γ rays, two Gaussian peaks corresponding to the two energies of conversion electrons are observed in the PMT spectrum (see Fig. 3.6-2) when triggered in coincidence with the MWPC and the width of the 1.0637 MeV peak indicates a ∼9% energy resolution for 1-MeV electrons.

This β detector is now mounted on a test chamber in order to test the coincidence measurements of both β particles and recoil ions from untrapped ^{6}He decays. The preamplifiers for the MWPC cathodes and the position reconstruction algorithm are still under development.

3.7 Laser setup for the ^{6}He experiment

Z. T. Alexander, Y. S. Bagdasarova, T. M. Cope*, X. Fléchard†, A. García, R. Hong, Y. Kim, A. Knecht‡, E. Liénard†, P. Müller§, O. Naviliat-Cuncic¶, D. W. Storm, H. E. Swanson, F. Wauters, and D. W. Zumwalt

Since last year we have increased the ^{6}He trap efficiency to a trap size of ∼500 atoms and capture rate of ∼1000 atoms/s. To trap helium atoms we need to excite the ground-state atoms into the 2^3S_1 metastable state which is achieved via radio-frequency (RF) discharge. To increase the metastable flux of the ^{6}He atoms, we implemented a recirculation system so that helium atoms can pass through the RF discharge several times before decaying. After recirculation we see a factor of ∼5 increase in the total number of decays inside the magneto-optical trap (MOT) chamber using a Si PIN diode detector, which is in line with conductance calculations made before the improvement. However, we only see an increase in the total trap size, as measured via atomic fluorescence, by a factor of 3 because the discharge conditions change after recirculation which slightly reduces the metastable fraction per pass.

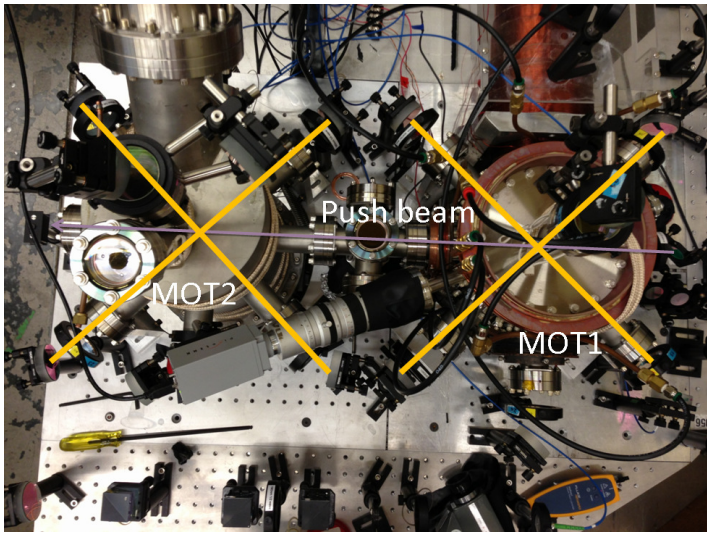

Figure 3.7-1. On the right is the primary MOT capture chamber. A push beam enters from a side window and transfers momentum to the trapped atoms in the direction of the second MOT.

Using the Si PIN diode detector, we observed a high rate of background ^{6}He decays from untrapped atoms. This exceeded the decays expected from atoms in the trap by a factor of 100. To reduce the background a second MOT chamber has been installed next to the primary MOT chamber and is connected by a 6-way cross for differential pumping (Fig. 3.7-1). We implemented an atomic transfer scheme whereby an additional laser beam pulses with a ∼2-ms length to push the atoms out of the first trap and into the second trap

*Departed March, 2013.
†LPC-Caen, ENSICAEN, Université de Caen, Caen, France.
‡Presently at Paul Scherrer Institut, Villigen PSI, Switzerland.
§Argonne National Laboratory, Argonne, IL.
¶National Superconducting Cyclotron Laboratory, Michigan State University, East Lansing, MI.

within ∼15 ms. The 6-way cross also forms a transverse cooling stage to optically collimate the atoms which have begun to spread transversely after leaving the first trap. Using these techniques we report a transfer efficiency of over 60% from tests with ^{4}He. A small aperture tube with diameter 5 mm will be installed to increase differential pumping between each chamber to minimize the background atoms while allowing nearly all of the trapped atoms into the final detection chamber.

3.8 Electric-Field systems and ion-detection setup for the ^{6}He experiment

Z. T. Alexander, Y. S. Bagdasarova, T. M. Cope*, T. O'Conner†, X. Fléchard‡, A. García, R. Hong, Y. Kim, A. Knecht§, E. Liénard‡, P. Müller†, O. Naviliat-Cuncic¶, D. W. Storm, H. E. Swanson, F. Wauters, and D. W. Zumwalt

The electric field used to collect the ^{6}Li recoil ions on the ion detector below the magneto optical trap (MOT) is generated by an array of seven, equally-spaced electrodes held at variable potentials (Fig. 3.8-1). The potential on each electrode is determined by simulation to yield the most uniform field in the region of ion flight. The applied voltages range from −3 kV on the bottom electrode to 25 kV on the top electrode, producing a mean field of 170 V/mm, with an rms variation of 1.38 V/mm, and a collection efficiency of about 85% for the coincident ions. The high voltage is supplied by a stacked configuration of remotely controlled Spellman MP Series high-voltage supplies, each with a continuously variable output of 0-5 kV and a stability of $< 0.007\%$/hr.

Figure 3.8-1. Electrode array and ion detector inside the MOT chamber. The uniform electric field pulls the ions toward the detector in parabolic trajectories (green). Designed by T. O'Conner.

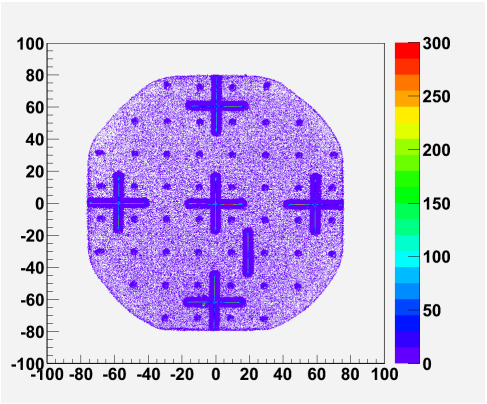

Figure 3.8-2. Image of the mask on the MCP without background correction as read out by the delay line anodes. The axes show the difference in readout time between the ends of each anode in ns. The color scale is the number of events.

*Departed March, 2013.
†Argonne National Laboratory, Argonne, IL.
‡LPC-Caen, ENSICAEN, Université de Caen, Caen, France.
§Departed July, 2012, presently at Paul Scherrer Institut, Villigen PSI, Switzerland.
¶National Superconducting Cyclotron Laboratory, Michigan State University, East Lansing, MI.

The ion detector consists of two micro-channel plates (MCPs) and two delay-line anodes wound along the x and y directions directly below the MCPs. A 2.5-kV difference is applied across the MCPs so that when an ion strikes a channel an electron avalanche is produced which is collected by the anodes on the other side. The charge signal propagates to the opposite ends of each anode and is read out by the FASTER DAQ system[1]. We extract the position of the ion at the MCPs from the time difference of the signal at both ends of the anode. Fig. 3.8-2 shows a position calibration image of an α source at the center of the MOT emitting through a mask placed in front of the MCPs.

The electrode array assembly is complete and ready for high-voltage testing. The ion detector is ready to take ^{6}He data.

3.9 The ^{6}He experiment and limits on tensor-type weak currents from nuclear and neutron β decays

Z. T. Alexander, Y. S. Bagdasarova, T. M. Cope*, X. Fléchard†, A. García, R. Hong, Y. Kim, A. Knecht‡, E. Liénard†, P. Müller§, O. Naviliat-Cuncic¶, D. W. Storm, H. E. Swanson, F. Wauters, and D. W. Zumwalt

The fast, pure Gamow-Teller β decay of ^{6}He is a particularly attractive transition to search for a tensor contribution to the V-A charged-current weak interaction. The isotope is available in large quantities from a reaction produced at the CENPA Van de Graaff accelerator facility. The ∼1-s lifetime allows manipulation by ion or atom traps and nuclear-structure-dependent corrections can be calculated within an *ab initio* framework.

The β-ν correlation is sensitive to tensor couplings in the following way:

$$a_{\beta\nu,^6He} \simeq \Big(-\frac{1}{3} + \frac{1}{3}\frac{C_T^2 + C_T'^2}{C_A^2}\Big)\Big(1 - \langle\frac{m_e}{E}\rangle\frac{C_T + C_T'}{C_A}\Big), \quad (1)$$

with $C_i^{(\prime)}$ the coupling constants in the Jackson, Treiman and Wyld formalism[2], and $\langle E\rangle$ the total energy of the β particle. This energy-dependent factor motivates the development of an energy sensitive β detector with a low-energy threshold ((see Sec. 3.6)). In contrast to the β-ν correlation, a direct measurement of the Fierz interference term b_{Fierz} is sensitive only to a tensor interaction coupling to left-handed neutrinos, $b_{Fierz} \sim (C_T + C_T')/C_A$.

*Departed March, 2013.
†LPC-Caen, ENSICAEN, Université de Caen, Caen, France.
‡Departed July, 2012, presently at Paul Scherrer Institut, Villigen PSI, Switzerland.
§Argonne National Laboratory, Argonne, IL.
¶Department of Physics and Astronomy and National Superconducting Cyclotron Laboratory, Michigan State University, East Lansing, MI.

[1] http://faster.in2p3.fr/

[2] J. D. Jackson, S. B. Treiman, and H. W. Wyld, Jr, Phys. Rev. **106**, 517 (1957).

Recent data in nuclear[1] and neutron[2] decays, including a 5σ shift in the 2012 Particle Data Group recommended value for the neutron lifetime[3], motivated a new evaluation of the limits on tensor currents from neutron and nuclear β decays. In addition, the quark-level effective-field-theory framework of Battacharya *et al.*[4] and recent lattice-QCD calculations of the nuclear form factors allow for a direct comparison of the obtained limits to those from other low-energy probes and the LHC.

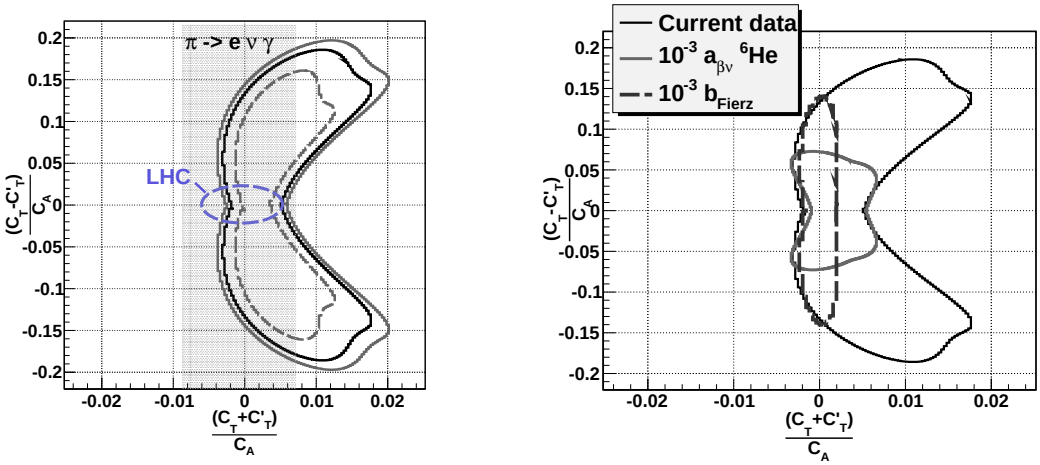

Figure 3.9-1. *Left:*Current limits on tensor currents from neutron and nuclear β decay data (68 %, 90 %, and 95 % C.L.) compared to those from radiative pion decay and the LHC (90 % C.L.) . The LHC limits are obtained from *p-p* cross-section data assuming that the particle(s) that mediate exotic interactions lie above the production threshold. *Right:* Projected 90% confidence limits for a 10^{-3} measurement of $a_{\beta\nu,^6He}$ or the Fierz interfierence term.

A χ^2 minimization of the most precise neutron and nuclear β-decay data available was performed by adopting a model with 5 free parameters: C_A/C_V, the axial-to-vector coupling strength, and C_T, $C_T^{'}$, C_S and $C_S^{'}$, the coupling constants for exotic scalar and tensor currents, allowing both left- and right-handed chiralities. The χ^2 surface was used to construct confidence-level contours as shown in Fig. 3.9-1(left). There is full agreement with the V-A model, and the limits obtained are dominated by the ^{6}He measurements of Johnson *et al.*[5], the relative polarization measurements of Carnoy *et al.*[6], and the neutron lifetime and β-asymmetry parameter. For left-handed couplings, β-decay data yield better bounds than those from radiative pion decay[7] and current LHC data[8]. Fig. 3.9-1(right) shows the projected limits for a 0.1% β-ν correlation measurement from the ongoing ^{6}He experiment at CENPA, and a 0.1% envisaged measurement of b_{Fierz}. Both measurements will have a sizable impact on the overall bounds.

[1] F. Wauters *et al.*, Phys. Rev. C **82**, 055502 (2010).
[2] M. P. Mendenhall *et al.*, Phys. Rev. C **87**, 032501(R) (2013).
[3] J. Beringer *et al.*, (Particle Data Group), Phys. Rev. D**86**, 010001 (2012).
[4] T. Bhattacharya *et al.*, Phys. Rev. D **85**, 054512 (2012).
[5] C. H. Johnson, F. Pleasonton, and T. A. Carlson, Phys. Rev. **132**, 1149 (1963).
[6] A. S. Carnoy *et al.*, Phys. Rev. Lett. **65**, 3249 (1990).
[7] M. Bychkov *et al.*, Phys. Rev. Lett. **103**, 051802 (2009).
[8] V. Cirigliano *et al.*, arXiv:1210.4553 [hep-ph] (2012).

3.10 Tests of radioactivity production for the ^{6}He experiment

T. M. Cope*, A. García, and Y. Kim

The target used for production of ^{6}He consists of molten lithium (Li) separated from the beamline vacuum by a 50-μm-thick stainless-steel (SS) foil. The deuterium beam traverses this window and produces activity that may restrict access to the target neighborhood as we make longer irradiations. In particular, one of the isotopes produced is ^{56}Co, with a 77-day half-life. Thus, we decided to consider alternatives for this window. The element to be used has to be compatible with Li. Beryllium (Be) and Titanium (Ti) are possible window materials (similar chemical properties to Fe and not extremely expensive).

Be poses health risks, is more expensive, and there are other issues that need to be examined. It is not clear how we would provide a vacuum-tight window. Be is usually fusion bonded to SS but the temperature at which this bond is rated is close to the temperature of our Li target and we expect more neutrons to be produced by the beam with a Be window compared to a SS or Ti window. Thus, we have postponed consideration of Be as a window.

We simultaneously irradiated foils of SS and Ti with an 18-MeV deuterium beam, the same ion beam and energy that we use for production of ^{6}He. The principal active isotope produced in the Ti bombardment is ^{48}Ti, with a 16-day half-life. The activities read with a hand-held monitor 20 days after irradiation were similar. In principle a Ti window provides an improvement but there are other activities produced in both irradiations. Careful comparisons are still ongoing.

3.11 ^{7}Li target monitoring system for the ^{6}He experiment

Z. T. Alexander and A. Knecht†

We have created a program using LabViews graphical programming interface to allow monitoring the target during ^{6}He production. The target monitoring system measures the temperatures of the target and the cup that is used to conduct heat away and keep the target within a reasonable temperature range. Another reason to use both temperature measurements is to insure that the cup has not thermally decoupled from the target leading to the possibility of equipment damage. For this reason the monitoring system is interlocked with the deuterium beam and is set to stop the beam current if the target temperature exceeds 350° C. The versatility of the LabView programming language allows us to monitor many interesting quantities such as collimator currents and the ^{6}He production count. In the future, if other properties of the target need to be monitored, it will be simple to implement because the code can be easily modified to include new quantities of interest. The monitoring program also records and stores all of the data from a given run into a data file organized by the date of the run. The data file can then be directly read by a second program that graphs and tabulates the data from the specific run. This allows easy viewing of older runs as well as a way to quickly access data from a specific run.

*Departed March, 2013.

†Departed July, 2012, presently at Paul Scherrer Institut, Villigen PSI, Switzerland.

4 Precision muon physics

4.1 Overview of the muon physics program

L. P. Alonzi, J. F. Amsbaugh, J. D. Crnkovic*, A. García, N. S. Froemming, G. C. Harper, D. W. Hertzog, P. Kammel, J. Kaspar, B. Kiburg†, S. A. Knaack‡, M. H. Murray, D. J. Prindle, R. A. Ryan, M. W. Smith, H. E. Swanson, F. Wauters, P. Winter§, and T. Zhao

The Precision Muon Group is involved in a series of fundamental experiments that determine Standard-Model parameters, low-energy effective-field-theory constants, or provide sensitive tests for new physics. With strong CENPA support, the group has grown considerably. The highlights from a very productive year are described in the series of articles that follow. Briefly, we note:

- The final paper[1] from the MuLan measurement of the positive muon lifetime was published in January, 2013. This project is now complete. We measured a lifetime of $\tau_\mu = 2\,196\,980.3 \pm 2.2$ ps (1.0 ppm), and determined the fundamental Fermi Constant, $G_F = 1.166\,378\,7(6) \times 10^{-5}$ GeV^{-2} (0.5 ppm).

- The final result from our MuCap determination of g_P, the weak-pseudoscalar coupling of the proton, was published in January, 2013[2]. The novel hydrogen time projection chamber (TPC) technique employed is relatively immune to the poorly known molecular physics complications that plagued previous efforts. The result, $g_P = 8.06 \pm 0.55$, is in excellent agreement with the 8.26 ± 0.23 prediction from chiral perturbation theory. Our publication was recognized as an Editor's Suggestion and was described in an American Physical Society synopsis summary[3] and in several press releases. The lead UW analyzers, Kiburg and Winter, have obtained excellent new research positions at Fermilab (Lederman Fellow) and Argonne (Assistant Physicist), respectively. Graduate student Knaack, completed her Ph.D. on a three-fold improved determination of the molecular formation rate $\lambda_{pp\mu}$, which is a process that must be understood well for a clear interpretation of the final result of our MuCap experiment.

- The MuSun experiment will determine the muon capture rate in deuterium to 1.5%. A well-measured $\mu^- + d \to \nu_\mu + n + n$ process can be used to fix the unknown low-energy constant arising in the effective-field-theory description of the two-nucleon weak interaction in related systems, such as *pp* fusion and the neutrino breakup reactions in the heavy-water SNO experiment. In 2012, we commissioned a new beamline area at

*Graduated December, 2012
†Presently at Fermi National Accelerator Laboratory, Batavia, IL.
‡Graduated June, 2012, presently at Wisconsin Institute for Discovery, Madison, WI.
§Presently at Argonne National Laboratory, Argonne, IL.

[1] V. Tishchenko *et al.*, (MuLan Collaboration), Phys. Rev. D. **87** 052003 (2013).
[2] V. A. Andreev *et al.*, (MuCap Collaboration), Phys. Rev. Lett. **110**, 12504 (2013).
[3] physics.aps.org/synopsis-for/10.1103/PhysRevLett.110.012504.

the Paul Scherrer Institute (PSI) that will be devoted to nuclear physics. The MuSun experiment was then installed in its new and permanent home and a commissioning run was carried out. One critical installation was the introduction of prototype amplifiers within the cryogenic volume of the TPC which improved the energy resolution by a factor of 2. Graduate student Ryan and postdoc Wauters are now leading the effort to install a full complement of CENPA-produced cryo-amplifiers in time for our high-statistics physics runs in 2013 and 2014. Data obtained in our first physics run in 2011–using an initial simpler incarnation of the experiment and beamline designed for the MuLan/MuCap campaign–are being analyzed by graduate student Murray. Prindle is providing expert detailed simulation assistance.

- One of the strongest hints of new physics is the persistent difference between the measurement and Standard-Model prediction for the muon anomalous magnetic moment, a_μ. Both are known to ~ 0.5-ppm precision. The current discrepancy $a_\mu(Expt - Thy)$ exceeds 3 standard deviations and is suggestive, but not yet definitive, of new physics. We co-led (Hertzog) the proposal to mount a next-generation muon $g-2$ experiment with a factor-of-4 improved overall precision goal. Fermilab E989 is approved, has CD-0 status, and the Project is moving forward rapidly. The Brookhaven superconducting storage ring is largely dismantled and will be moved in 2013 to a new custom building being prepared at Fermilab. The UW group is involved in the simulation of muon injection into the storage ring (Froemming), the refurbishment of hundreds of fixed NMR probes used to monitor the precision magnetic field (García, Swanson), and the design and construction of the 24 calorimeter stations that will be used to measure the anomalous precession frequency (Hertzog, Kammel, Zhao, Alonzi, Harper, Smith). During the past year, a test magnet system was prepared for the NMR work and extensive detector and electronics development work was completed. UW is the lead institute on a consortium MRI proposal submitted to NSF in February, 2013. If funded, it will support the equipment funds for six domestic universities that will build the detector, electronics, and data-acquisition systems for the precession frequency measurement.

- The hadronic vacuum polarization contribution to a_μ has the largest "theoretical" uncertainty in the SM evaluation. It can be determined using exclusive e^+e^- cross section data and a dispersion relation; thus, the uncertainty is actually experimental. Crnkovic completed his Ph.D. this year based on data from the Belle experiment (where we are limited members). We measured the reaction $e^+e^- \to \pi^+\pi^-\pi^0\gamma_{ISR}$, where γ_{ISR} is a hard, initial-state radiated photon that down-shifts the collision energy to permit the 3π cross section to be determined from threshold to above the J/ψ resonance. It is the first such effort using Belle data and required the development of many analysis tools and procedures. Postdoc Kaspar concentrated on the delicate radiative corrections and Monte Carlo tests of certain systematics. The 2013 plan is to expand the effort to similar channels and submit the work for publication.

- The new Muon Campus at Fermilab will host the $g-2$ experiment and an ultra-sensitive test of charged-lepton flavor violation using the muon-to-electron conversion process. The Mu2e experiment will look for a monoenergetic electron in the reaction $\mu^- \to e^-$ (no neutrinos) in the field of a nucleus, such as aluminum. The smoking-gun

signature of the $\sim$ 105-MeV electron will be tested to a branching-ratio sensitivity below 10^{-16}. The process is in competition with ordinary muonic nuclear capture, which can emit protons and neutrons that constitute background in the experiment. We are co-leading (Kammel) the AlCap experiment at PSI that will measure the proton spectrum following atomic μ^-Al formation. This effort will run in 2013–2014.

MuCap

4.2 The final result of the MuCap experiment

D. W. Hertzog, P. Kammel, B. Kiburg*, S. A. Knaack†, and P. Winter‡

Muon capture on the proton,

$$\mu^- + p \to n + \nu_\mu, \tag{1}$$

is a basic charged-current weak process. At the low momentum transfer involved, the Standard Model electroweak interaction reduces to an effective Fermi interaction between the lepton current L_μ and the hadronic current J_μ. While L_μ retains its simple $\gamma_\mu(1-\gamma_5)$ structure, the hadronic current $J^\mu = V^\mu - A^\mu$ between nucleon states is modified by quantum chromodynamics (QCD), as expressed by the introduction of four nucleon form factors. The vector, magnetic, and axial form factors are well determined by Standard Model symmetries and data. Remaining is the pseudoscalar form factor g_P which is by far the least known of these nucleon form factors. The goal of the MuCap experiment was to determine g_P with precision by measuring the rate Λ_S for the process described in Eq. (1). The pseudoscalar term in the axial current has played a significant role in nuclear/particle physics, in particular its deeper understanding as a consequence of chiral symmetry and its breaking. By now chiral effective field theory allows a robust and rather precise prediction which has been verified up to two-loop order. Its experimental verification is considered a basic test of QCD symmetries.

Muon capture on hydrogen is the most direct method to determine g_P and experimental efforts span a period of 50 years. Experiments before MuCap only achieved limited precision and even showed some internal inconsistencies because of severe experimental challenges. The controversial experimental situation is discussed in review[1]. The MuCap experiment applied a novel technique based on a 10-bar, ultra-pure hydrogen time projection chamber (TPC), which was essential to reduce the molecular formation that complicated the interpretation of previous experiments. MuCap has measured Λ_S to a precision of 1% and unambiguously determined the pseudoscalar form factor of the proton with 7% uncertainty[2].

The main analysis of the MuCap experiment extracts the lifetime of negative muons stopped in the hydrogen gas in order to infer the singlet muon capture rate Λ_S. The lifetime

*Presently at Fermi National Accelerator Laboratory, Batavia, IL.
†Graduated June, 2012, presently at Wisconsin Institute for Discovery, Madison, WI.
‡Presently at Argonne National Laboratory, Argonne, IL.

[1] P. Kammel, K. Kubodera, Annu. Rev. Nucl. Part. Sci. **60**, 327 (2010).
[2] V. A. Andreev *et al.*, (MuCap Collaboration), Phys. Rev. Lett. **110**, 12504 (2013).

is extracted from the difference of the arrival time of the muon in the hydrogen target and the subsequent time of the decay electron, both of which are detected in dedicated scintillators (μSC and eSC in Fig. 4.2-1, respectively). The time projection chamber is an active hydrogen target and allows reconstruction of the muon track in order to select those that stopped in the central region of the TPC, far from materials that would alter the lifetime. Fig. 4.2-1 shows a typical good muon together with its track reconstructed from the signals in the TPC. Tracking detectors for the incoming muon (μPC) and the outgoing electron (ePC) provide additional handles to select clean events.

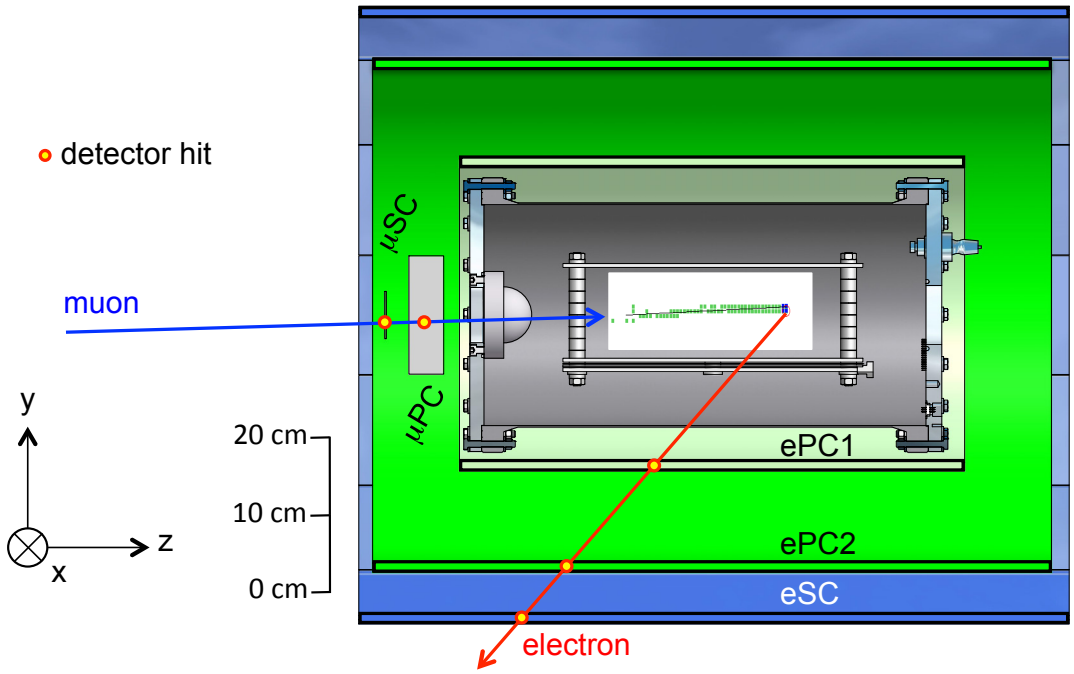

Figure 4.2-1. A side view of the MuCap experiment with the main detector systems.

The full analysis comprised a detailed study of the dependence of the extracted lifetime on the variation of the selection criteria for the reconstructed muons and decay electrons[1]. An outstanding issue was the distortion of the disappearance rate due to capture from molecular states. Since the capture rate from these molecular states differs from that of muonic hydrogen atoms, a small but significant correction is required. We have completed an analysis of the formation rate of muonic hydrogen molecules[2] which strongly reduced the uncertainty of this correction. The final singlet capture rate has been determined to be $\Lambda_S = 714.9 \pm 5.4_{\text{stat.}} \pm 5.1_{\text{syst.}}\,\text{s}^{-1}$, leading to a pseudoscalar form factor of $g_P = 8.06 \pm 0.55$, in good agreement with the prediction from chiral perturbation theory ($g_P = 8.26 \pm 0.23$). MuCap thus unambiguously verifies a fundamental prediction of low-energy QCD.

[1] B. E. Kiburg, *A Measurement of the Rate of Muon Capture in an Ultra-Pure Protium Gas Time Projection Chamber*, PhD thesis, University of Illinois at Urbana-Champaign, 2011.

[2] S. A. Knaack, *A Determination of the Formation Rate of Muonic Hydrogen Molecules in the MuCap Experiment*, PhD thesis, University of Illinois at Urbana-Champaign, 2012.

MuSun

4.3 Muon capture on deuterium, the MuSun experiment

D. W. Hertzog, P. Kammel, M. H. Murray, D. J. Prindle, R. A. Ryan, and F. Wauters

The goal of the MuSun experiment[1] is a measurement of the rate Λ_d for the semileptonic weak process $\mu^- + d \to \nu_\mu + n + n$ to a precision of better than 1.5%. Λ_d denotes the capture rate from the doublet hyperfine state of the muonic deuterium atom in its $1s$ ground state.

Muon capture on deuterium is the simplest weak-interaction process on a nucleus that can both be calculated and measured to a high degree of precision (see the discussion in a recent review of this field[2]). Effective field theories (EFTs) have been developed to calculate electro-weak observables in few-body systems following Weinberg's pioneering work. Very recently fully self-consistent calculations in a rigorous QCD-based EFT scheme have been published (Table 4.3-1). These calculations can establish quantitative relations between muon capture and electro-weak astrophysical processes of fundamental importance which have never been measured directly. These include *pp* fusion, which is the primary energy source in the sun and main sequence stars, and the νd reaction, which provided convincing evidence for solar neutrino oscillations at the Sudbury Neutrino Observatory.

Λ_d (s^{-1})	year	Method	Reference
386	2002	EFT*	Ando *et al.*, Phys. Lett. B**533**, 25-36
416±6	2010	SNPA, EFT*	Ricci *et al.*, Nucl. Phys. A**837**, 110
392.0±2.3	2011	EFT*	Marcucci *et al.*, Phys. Rev. C**83**:014002
399±3	2012	EFT	Marcucci *et al.*, Phys.Rev.Lett. **108**, 052502
383.8-392.4	2012	EFT	Adam *et al.*, Phys. Lett. B**709**, 93-100
470±29	1986	Electron	Bardin *et al.*, Nucl. Phys A**453**, 591-604
409±40	1989	Neutron	Cargnelli[3]

Table 4.3-1. Recent theoretical and experimental results on muon capture rate Λ_d from the doublet state of the μd atom. EFT* denotes a hybrid EFT calculation. "Electron" denotes that the capture rate was measured with the lifetime technique, in contrast to deriving this rate from the capture neutrons.

While μd capture could serve as the benchmark for the axial-current interaction in the two-nucleon system, the present experimental situation is inadequate to provide much guidance. The best existing experiments (see Table 4.3-1) are not precise enough and the most precise result differs from modern theory by almost three standard deviations. If true, such a discrepancy would have major ramifications for the above-mentioned astrophysics processes. The prospect of a precise MuSun result has stimulated recent fully self-consistent EFT calculations.

[1] http://muon.npl.washington.edu/exp/MuSun.

[2] P. Kammel, K. Kubodera, Annu. Rev. Nucl. Part. Sci. **60**, 327 (2010).

[3] Proceedings of the XXIII Yamada Conf. on Nuclear Weak Processes and Nuclear Structure, Osaka, Japan, 1989.

The MuSun experiment, shown in Fig. 4.3-1, measures Λ_d with the so-called lifetime technique: $\lambda_{\mu d} = \lambda_{\mu^+} + \Lambda_d$. Most parts of the detector are inherited from MuCap including the muon entrance detectors (two thin scintillator slabs and a wire chamber) and the electron detector (two cylindrical wire chambers surrounded by a hodoscope consisting of a double layer of scintillator paddles). However, the conditions of the active target must lead to an unambiguous extraction of Λ_d, independent of muonic atomic physics complications occurring after the muon stops in deuterium (Fig. 4.3-2). The transition between the upper μd quartet to the lower μd hyperfine state, λ_{qd}, is slow and, once a $dd\mu$ molecule is formed, muon-catalyzed dd fusion occurs on a time scale of nanoseconds, recycling the muon. Our studies demonstrated that atomic-physics uncertainties are reduced to a negligible level at optimized target conditions of T = 30 K and 6% liquid-hydrogen density (Fig. 4.3-2). To achieve these conditions a new high-density cryogenic ionization chamber (CryoTPC) filled with ultra-pure deuterium was developed as an active target to monitor the muon stopping location and muon-catalyzed fusion reactions.

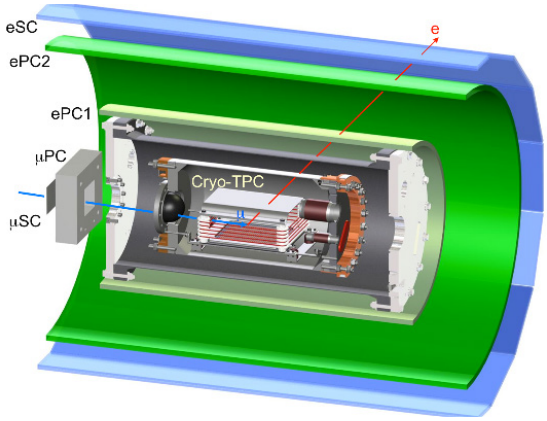

Figure 4.3-1. Drawing of the MuSun muon and electron detectors.

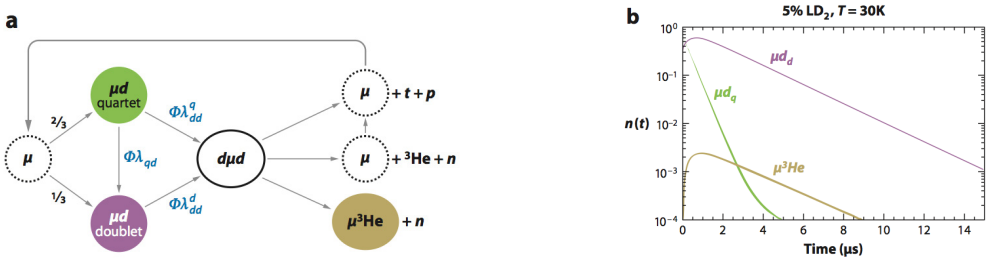

Figure 4.3-2. *Left:* The complex molecular dynamics of of negative muons in D_2. *Right:* At the optimized target condition, the majority of the muons populate the μd doublet state after 2 μs.

The summer, 2011, production data is being analyzed towards a first physics result. Last fall, the MuSun experiment moved to the new πE1 beam area which now serves as the dedicated location for its detectors. The new beamline was fully commissioned in preparation for a second physics run this fall. In addition, several hardware upgrades are being prepared including new cryogenic preamplifiers for the TPC readout.

4.4 Hardware developments at UW towards the 2013 production run

F. Gray*, D. W. Hertzog, P. Kammel, D. A. Peterson, D. J. Prindle, M. H. Murray, R. A. Ryan, F. Wauters

The goal of the MuSun experiment is to observe muon capture in D_2 using an active time-projection-chamber (TPC) target. However, muons can also stop in any of the materials within the TPC, which will distort the extracted lifetime depending on the Z of the stopping material. In order to control this distortion all surfaces within the TPC will be coated with a high-Z material. These materials have a much larger capture rate than deuterium such that the lifetime fit of the data can be adjusted to start after these captures have occurred.

The TPC pad plane is one such surface that must be coated in a high-Z material. The pad plane previously consisted of gold-plated macor due in part to the ease with which this design can be machined. Unfortunately this design suffered from poor peeling strength. A new pad plane, which consists of a 35-40-μm silver coating on a thin metal primer layer, allows for the machining of the pads after metalization without peeling at the edges.

The TPC consists of a cathode at -80 kV placed 72 mm above the anode pad plane so that ionized electrons drift towards the pad plane. To improve timing resolution and minimize the dependence of the charge seen at the anode on the original separation between the ionized charge and the pad plane, a Frisch grid is placed between the cathode and the anode. An optimal voltage of -3.5 kV is needed to obtain full transparency of the grid. In previous runs the optimal grid voltage could not be achieved due to sparking from the grid to other points within the TPC. One reason for this sparking is a flaw in the construction of the grid. A new design uses tensioned wires soldered to the surface of a tungsten plate. This design should allow the optimum voltage to be reached in the 2013 production run.

The electronics chain following each pad consists of a charge-sensitive preamplifier followed by an amplifier from which the data is then digitized. In the 2011 run an energy resolution of 29 keV was obtained and was not well understood. After numerous tests, including beam tests during the 2012 run, a few major upgrades in the electronics were decided upon. The preamplifiers were previously mounted outside of the vacuum chamber and connected to the TPC via long kapton cables. To reduce the amount of noise picked up by the connecting cables all 48 preamplifier channels will be moved inside the chamber and mounted several centimeters from the cold flange to the TPC. In addition, a new cooling system for all 48 preamplifiers will be integrated for the 2013 run to reduce thermal noise. During the 2012 run prototype preamplifiers were installed and a pulser resolution of 17 keV was achieved compared to the previous resolution of 29 keV, as shown in Fig. 4.4-1.

One challenge to relocating the preamplifiers within the chamber is fitting the new electronics into the confined space. David Peterson of the CENPA electronics team and Fred Gray of Regis University have worked on creating smaller, more compact layouts of the previous circuitry to fit the preamplifier in the allotted space. In addition, engineers from Petersburg

*Regis University, Denver, CO.

Nuclear Physics Institute (PNPI) designed a new preamplifier circuit to reduce the noise contributions further and work within the new space constraints. The circuit is currently being tested and compared to the boards with the design from the 2012 run. A design decision will be made based on these comparative tests and 48 new preamplifiers, along with the cooling system, will be installed and tested at PSI in summer, 2013.

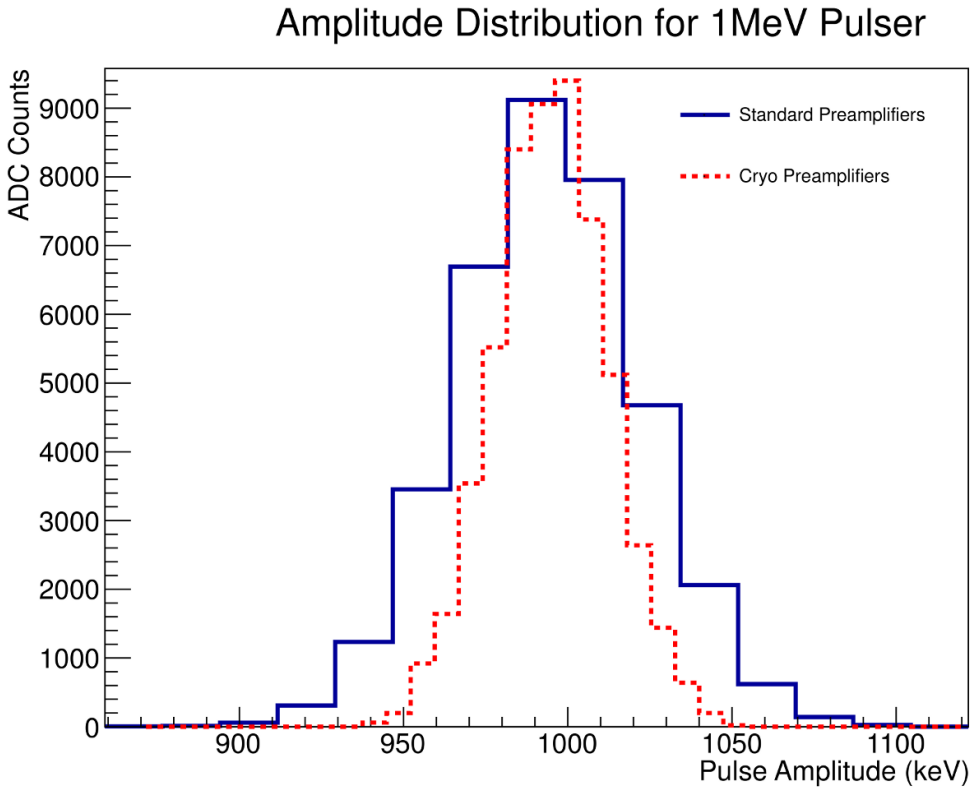

Figure 4.4-1. Pulse-amplitude distribution of a test charge injected in a standard and a cryo preamplifier connected to the fully operational TPC. The electronics resolution is 29 keV and 17 keV, respectively.

Another measurement challenge arises from muon capture on impurities within the deuterium gas, consisting mostly of nitrogen and oxygen. When a muon transfers from deuterium to one of the impurities, a muonic X-ray is emitted, which can be detected by an X-ray detector. An array of 5 NaI detectors will be built and integrated into the system for in-situ impurity monitoring during the 2013 production run.

4.5 The 2012 run, moving into the new πE1 area

D. W. Hertzog, P. Kammel, M. H. Murray, D. J. Prindle, R. A. Ryan, and F. Wauters

The πE3 beam at the Paul Scherrer Institute, previously used by the MuSun and MuCap experiments, is no longer available for particle physics. In the same experimental hall, a new low-energy muon beamline was constructed as an extension of the already existing πE1 area.

The goal of the 2012 run was twofold: install and commission the experiment in the new area with the new muon beam and dedicate two weeks of beam time to systematic studies and testing new hardware.

The MuSun experiment is mounted on three platforms: the electron detector, the time-projection-chamber (TPC) platform, and the gas purification system (Fig. 4.5-1). The new area was designed so that the whole system can be rolled back freeing up space without needing to remove the experiment from the experimental area (as was the case in πE3). Because the extended πE1 area now serves as a permanent home for the apparatus, great care was taken to properly connect and optimize all detector/readout systems. During 2013 several improvements are planned such as a liquid nitrogen lines and a tent with temperature and humidity control.

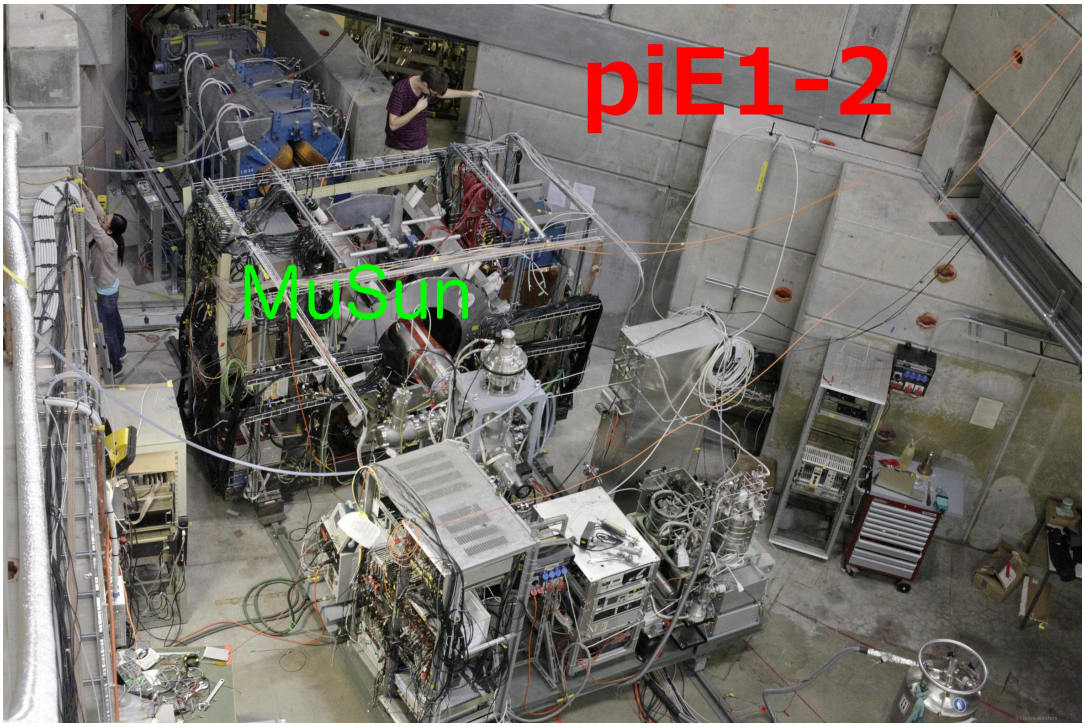

Figure 4.5-1. The MuSun experiment installed in the extended πE1 area.

After some initial beam tests in 2011 showed promising muon yields, the μ^+ and μ^- intensities and the muon-electron separation were optimized reaching 62 kHz of μ^- intensity at the nominal momentum. In addition, a muon-beam extinction efficiency of more than a factor of 100 was achieved, and the observed momentum width $dp/p < 3\%$ was superior to that of πE3. As a last step, a good muon stopping rate in the TPC was achieved. In conclusion, the MuSun apparatus connected to the new beamline is in good shape for a second production run this Fall.

A major highlight of the 2012 commissioning and test run was the installation of two 2-channel preamplifier prototypes inside the vacuum, close to the TPC. In addition, two X-ray detector prototypes were successfully tested (see Sec. 4.4).

4.6 Analysis of R2011 data

D. W. Hertzog, P. Kammel, M. H. Murray, D. J. Prindle, R. A. Ryan, and F. Wauters

In summer, 2011, a data set of 5×10^9 negative muon decays was collected in the $\pi E3$ muon beamline of the Paul Scherrer Institute. The first measurement of Λ_d is expected from this albeit not at the final target precision of 1.5%. The analysis of R2011 data has realized working software toolsets, high-level physics studies, and an established MuSun simulation framework.

The data have been systematically divided into datasets based on consistent sets of experimental parameters, allowing for controlled systematic studies. The Stage 1 analysis code has become more robust, allowing for a full analysis pass of the R2011 data set in June 2012. This processing was performed on the Texas Advanced Computing Center (TACC) computing cluster Lonestar. The Stage 2 analysis code uses the output of the Stage 1 analysis to perform specific studies and implement algorithms that require tuning and experimentation, such as the time-projection-chamber (TPC) muon tracking. This analysis and post processing is performed largely on the CENPA Rocks computing cluster although using the full statistics requires the much larger hard disk space ($\sim$50 TB) of the TACC Lonestar cluster. A software package, LtFit, has been developed to facilitate the fitting of decay-time distributions in a standardized fashion. LtFit additionally implements levels of data blinding on top of the hardware (clock) blinding of the R2011 dataset, including a relative blinding between the μ^- and μ^+ datasets.

Tracking of muons stopping in the TPC is one difficult facet of MuSun data analysis. The active TPC target allows the reconstruction of the 3D muon stop position ensuring that every accepted event has a muon stopped in deuterium. However, the algorithm defining a muon stop must accept muons independent of their decay time to avoid distorting the measured lifetime. Any coupling to the decay electron or the time of a muon-catalyzed fusion reaction can induce a different acceptance for early or late decays. To demonstrate time-independence of the muon stop definition, the cuts are varied and the extracted muon lifetime is examined. In the neighborhood of the cut parameters and thresholds the lifetime must be stable indicating a lack of time dependence.

Studies of the muon lifetime as a function of parameters such as stop position in the TPC, energy deposited by the stopping muon, and azimuthal angle of the electron track have been performed. For negative muons a muon stop algorithm that is robust in all of these dimensions has not been achieved. This is the focus of the analysis. For positive muons reasonable consistency and stability of the measured lifetime has been shown for variations of these parameters. Because positive muons do not induce muon-catalyzed fusion and do not undergo nuclear capture in wall materials, they provide a clean indication that muon-catalyzed fusion products or a leaky muon stop definition are to blame for the erroneous lifetime dependence on stop definition parameters in the μ^- data.

4.7 Status of the Monte Carlo simulation

D. W. Hertzog, P. Kammel, M. H. Murray, D. J. Prindle, R. A. Ryan, and F. Wauters

The MuSun measurement of the μ^- capture rate on deuterium is complicated by $dd\mu$ molecular formation and subsequent muon-catalyzed dd fusion. The rates for the various atomic physics processes are well known but there is a question of how they will affect the measurement. One approach to quantify this is through Monte Carlo simulation.

The MuSun Monte Carlo chain has a number of parts starting with a Geant4 based simulation of the detector and atomic physics, continuing with an electronic response simulation and concluding with utility classes to compare analyzed events with Monte Carlo input.

The Geant4 simulation includes a reasonably detailed simulation of all the detector components the incoming muon can see as well as most of the detector elements the Michel electron is likely to interact with. The initial muon distribution is based on a beam-transport model from the target to the final focus at the MuSun entrance detectors. The atomic physics capture of the μ^- on deuterium as well as the subsequent (rare) molecular formation and fusion is simulated in detail, although it is still being fine-tuned. The detailed Geant response to particles, the so-called physics list, is also being fine-tuned to provide the optimum simulation realism for a reasonable amount of computing time. The Geant4 simulation, usually the slowest step in the simuation, is fast enough that we can reasonably produce several 10^9-sized event samples and calculate the μ^- capture rate under a few scenarios.

The electronic response package, mcresponse, reads the output of the Geant4 simulation and produces a file in the same format as the data acquisition. The emphasis so far has been to make the simulation of the time projection chamber (TPC) realistic. The drift ionization is divided into small time bins and then the electronic shaping, informed by a SPICE calculation, is applied. Finally, a non-linear baseline restoration is performed. The addition of electronic noise is currently being studied. One option is to add signals from forced-trigger events. We would like to understand the source of the electronic noise and add the appropriate theoretical noise. The TPC, the electron wire chambers, the gondola scintillator detectors, and the entrance counters are all simulated.

After the event reconstruction the Monte Carlo information is made available through a few helper classes. Currently this information is taken from the sensitive detector information stored by the Geant4 simulation. We do not yet have the full decay/interaction chain although we plan to save this in Geant and make it available through utility classes in the reconstruction stage.

To date the Monte Carlo has been used to understand why we only see about 60% of the muons that impinge on the entrance counters and how the Michel electron can affect the measured rates. We have started to study how $\mu dd \to p + t + \mu$ can affect the muon capture rate and will be validating this calculation in the near future.

g-2

4.8 Overview of the $g-2$ experiment

L. P. Alonzi, J. D. Crnkovic, A. García, N. S. Froemming, D. W. Hertzog, P. Kammel, J. Kaspar, B. Kiburg*, M. W. Smith, H. E. Swanson, P. Winter†, and T. Zhao

The anomalous magnetic moment of the muon, $a_\mu = (g-2)/2$, can be calculated and measured to sub-ppm precision. The comparison between theory and experiment represents one of the most sensitive challenges to the completeness of the Standard Model (SM). The E821 measurement at Brookhaven National Lab (BNL)[1] and the SM theory have uncertainties of 0.54 ppm and 0.42 ppm, respectively. The difference between experiment and theory (Exp-SM) is $(287 \pm 80) \times 10^{-11}$, or a 3.6σ significance[2,3,1] (see Fig. 4.8-1a), a tantalizing hint for "new physics". The previous measurement is highly cited (see Fig. 4.8-1b), and the discrepancy generates considerable new physics speculation, from supersymmetry (SUSY) to Dark Photons and beyond. To this end we co-lead the development of a next-generation $g-2$ experiment (E989) which has been approved at Fermilab with a precision goal of 0.14 ppm.

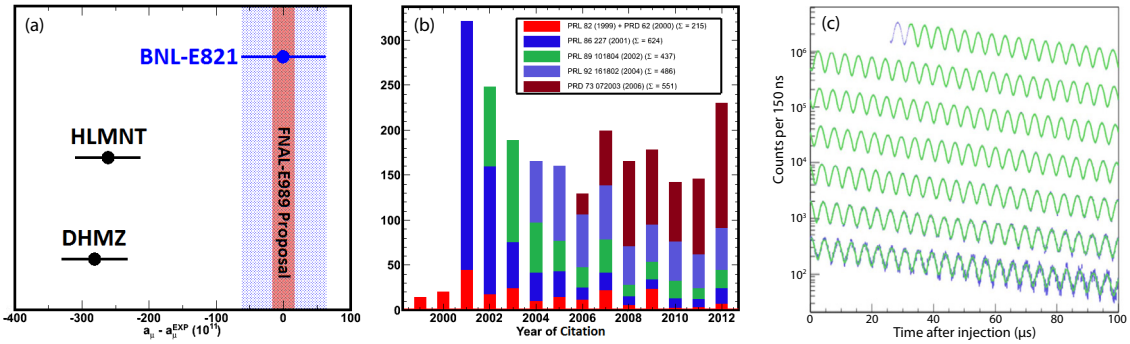

Figure 4.8-1. a) Comparison of two recent SM evaluations (HLMNT[2], DHMZ[3]) and the earlier BNL $g-2$ experiment[1]. The narrow band represents the goal of Fermilab E989. b) Citations to the BNL $g-2$ experiment by year. c) Data (blue points) and fit (green line) of the anomalous precession frequency, ω_a, from one of the BNL running years. E989 will acquire 20 times the entire BNL data set.

The Standard Model uncertainty is dominated by quantum loops involving hadrons, specifically the hadronic vacuum polarization (HVP) and the hadronic light-by-light (HLbL) scattering. The relative uncertainties are 0.35 ppm and 0.22 ppm, respectively. The HVP contribution is obtained from $e^+e^- \to hadrons$ cross sections. The optical theorem, cross-sections, and appropriate dispersion relation are used to accurately determine a_μ(HVP). Low-energy cross sections are obtained from experiment and drive the uncertainty on the HVP contribution. A reduction to ~ 0.25 ppm on the time scale of a new $g-2$ experiment

*Presently at Fermi National Accelerator Laboratory, Batavia, IL.
†Presently at Argonne National Laboratory, Argonne, IL.

[1]Muon g-2 Collaboration: G.W. Bennett *et al.*, Phys. Rev. D **73** 072003, (2006).
[2]Hagiwara *et al.*, J. Phys. **G38**, 085003 (2011).
[3]Davier *et al.*, Eur. Phys. J. **C71**, 1515 (2011).

is expected based on upcoming experiments. Our group is contributing to these measurements as described below (see Sec. 4.14). Crnkovic completed his thesis in December, 2012, using Belle data to determine the exclusive cross section $e^+e^- \to \pi^+\pi^-\pi^0$ using the initial-state-radiation technique. Kaspar has worked on the important radiative corrections (see Sec. 4.15) and a paper is planned for 2013 as well as measurements of several other related exclusive channels. The HLbL scattering contribution must be determined from low-energy QCD models or from Lattice QCD. Our INT Workshop[1] on the HLbL scattering contribution stimulated considerable work and the theory community continues to make progress especially in ambitious efforts to use lattice QCD to determined both HVP and HLbL terms.

The muon anomaly is proportional to the ratio ω_a/ω_p, where ω_a is the anomalous precession frequency of the muon spin in a magnetic field (see Fig. 4.8-1c) and ω_p is a measure of that average magnetic field carried out using proton nuclear magnetic resonance (NMR). Both frequencies must be determined to 0.1 ppm, including systematic uncertainties. The statistics required exceed those obtained at Brookhaven by a factor of 20 and the new experimental plan can realize this in 1.5 years of data taking. Our UW group is involved in both the ω_a and ω_p measurements.

The E989 experiment received CD-0 status in 2012. The BNL Storage Ring is being relocated to Fermilab with an expected shipment date for the delicate superconducting coils set for June, 2013 (contract awarded). A new building is being prepared with special environmental controls (stability of floor and precise temperature control) to house the ring and experiment. The Fermi National Accelerator Laboratory (FNAL) accelerator complex is being retooled in parts to provide a custom pure muon beam to the experiment. An upgraded suite of detectors and associated electronics will be required as well as improvements in the magnetic-field mapping system. The experimental plans have evolved rapidly and we continue to play a major role in much of this work. The $g-2$ project work is organized in teams. At UW our large and diverse local group is working on the Beam, Ring, Field, and Detector teams. We describe some of this work in the articles that follow: injection (see Sec. 4.11); NMR probes (see Sec. 4.13), detector studies (see Sec. 4.10), and detector development (see Sec. 4.9).

One of the major efforts we made this year was the organization of a National Science Foundation Major Research Initiative (MRI) instrumentation development proposal with UW as the lead institute representing six domestic universities and one international partner. The proposal, if funded, will support the ω_a measurement equipment: detectors, electronics, and data acquisition. Our UW group is responsible for the electromagnetic calorimeters, together with their associated readout devices and mechanics. CENPA engineers designed the prototypes used for the mechanical housings and a series of custom preamp/amplifier summing boards that are needed to operate the silicon photo-multiplier (SiPM) readout devices. As part of the field team we have refurbished a large-area dipole magnet at CENPA and shimmed it to provide a uniform field. The magnet will be used to test the NMR probes from the BNL experiment.

[1] http://www.int.washington.edu/PROGRAMS/11-47w/

4.9 Detector laboratory developments and simulation studies

L. P. Alonzi, G. C. Harper, D. W Hertzog, B. Kiburg*, M. W. Smith, P. Winter†, and T. Zhao

The past year has been very exciting in the Muon group detector lab. We started by analyzing the test beam data collected at Fermilab in April, 2012. Then with the arrival of Pete Alonzi we built a complementary simulation effort. We also hosted graduate students Robin Bjorkquist from Cornell and Kasunori Yai from Osaka. In December we received a new model Hamamatsu Multi Pixel Photon Counter (MPPC, aka SiPM). This device is similar to ones we tested previously but is now set up in a surface-mount configuration (Fig. 4.9-1). The CENPA electronics shop produced a new readout board for this detector. We also obtained a new digitizer capable of recording 4 channels at 5 GS/s with 12-bit depth.

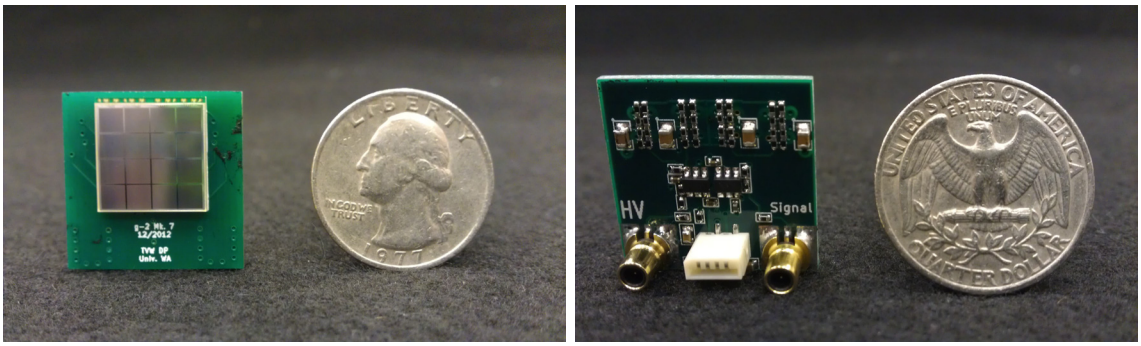

Figure 4.9-1. Front and rear images of the new surface-mount MPPC from Hamamatsu. The device is mounted on the board fabricated by CENPA.

The main focus of the detector lab this year was studying the proposed calorimeter design for the new $g-2$ experiment. In particular we strove to characterize its performance with regards to the systematic uncertainty arising from *pileup*. For $g-2$ pileup means multiple particles entering the calorimeter at the same time. In the previous experiment, E821, pileup was one of the driving systematic uncertainties. Our approach to reduce the uncertainty from pileup is twofold. The first step is to improve the time resolution of the detector. The second is to segment the calorimeter.

To study the time resolution of the device we set up a laser to emit two pulses of light spaced 5 ns apart. These pulses had the characteristic amount of light we would expect in the $g-2$ experiment. Fig. 4.9-2 shows the detector response. This plot shows data collected with the new waveform digitizer running at a sampling rate near the design specifications for the experiment.

There is no trouble identifying the two pulses in this detector. The benchmark we need to reach is separation of pulses at 5 ns. The data we collected in January shows we will be able to meet and surpass this goal with the new MPPC technology. The next step is to build

*Presently at Fermi National Accelerator Laboratory, Batavia, IL.
†Presently at Argonne National Laboratory, Argonne, IL.

a software analysis suite to identify these pulses. Graduate student Matthias Smith is hard at work on this pulse-fitting software.

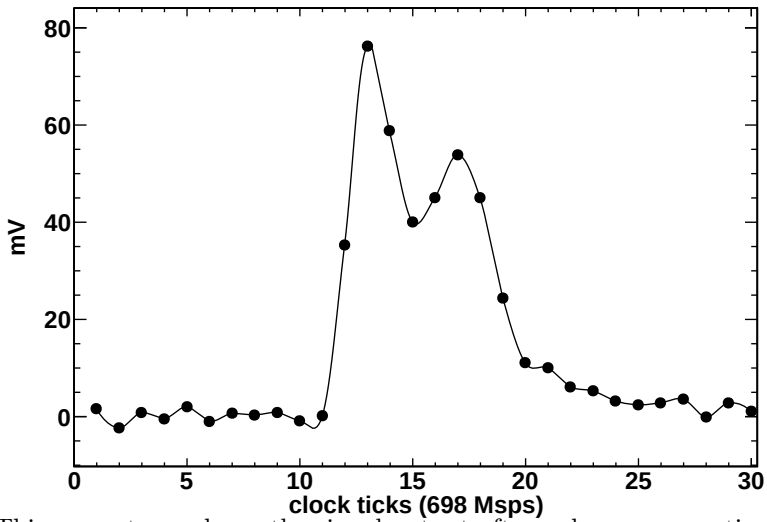

Figure 4.9-2. This scope trace shows the signal output after pole-zero correction. The two pulses (1275 pe, and 800 pe) are clearly separated.

Great progress was made on understanding the effect of segmenting the calorimeter. A key question that had remained unanswered was, "How much does segmentation reduce pileup?" Efforts on this front began with the test beam at Fermilab. We took data with an array of PbF_2 crystals as described in last year's annual report[1]. Since then the data have been analyzed and used as an input to simulation. The comparison of simulation data and test-beam data is shown in Fig. 4.9-3. The left plot represents the energy containment and sharing between neighboring crystals. For the test beam we moved the electron beam across the face of the calorimeter starting in the middle of one crystal and sweeping to the middle of its neighbor. At each step we recorded the energy deposited in the primary crystal. That energy deposition is shown on the vertical axis and the beam position is shown on the horizontal axis (the red line represents the test beam data). A clear transition in energy deposition is shown as the beam moves from one crystal to the next. A simulation with identical conditions was conducted and those data are shown as the histogram in the background. There is excellent agreement between the measurement data and the simulation. Therefore we can proceed to addressing the question of pileup reduction through segmentation.

Next we simulated the detector response for multiple particles hitting the calorimeter at the same time. We used a realistic calorimeter flux and for each event shot two particles at the calorimeter. Plotted on the horizontal axis of Fig. 4.9-3 (right) is the distance between the impact locations on the face of the calorimeter of the two hits (the inset picture of the calorimeter shows this coordinate). Plotted in black is the cumulative distribution function for pileup events. For example, 100% of pileup events have $R > 0$ cm and 66% of pileup events have $R > 6$ cm. By determining the pileup identification efficiency of the calorimeter and comparing with the black curve we can determine the amount of pileup suppression.

[1] CENPA Annual Report, University of Washington (2012) p. 69.

We conducted the simulation for two different calorimeter segmentations. The red curve represents the 5 x 7 segmentation, which means 3-cm square-faced crystals. The blue curve is for 6 x 9 segmentation (2.5 cm crystals). These lines represent the efficiency of the clustering algorithms to successfully identify both hits. For small R the efficiency is low, meaning that the pulses were mostly indistinguishable. As R increases the efficiency transitions to near 100%. In fact the transition occurs faster for the smaller segmentation. As a result our design has shifted to the 6 x 9 segmentation. Finally, looking at the transition point of the blue curve to near-perfect efficiency and comparing with the black curve, we can say that the 6 x 9 segmentation allows us to eliminate 66% of the pileup.

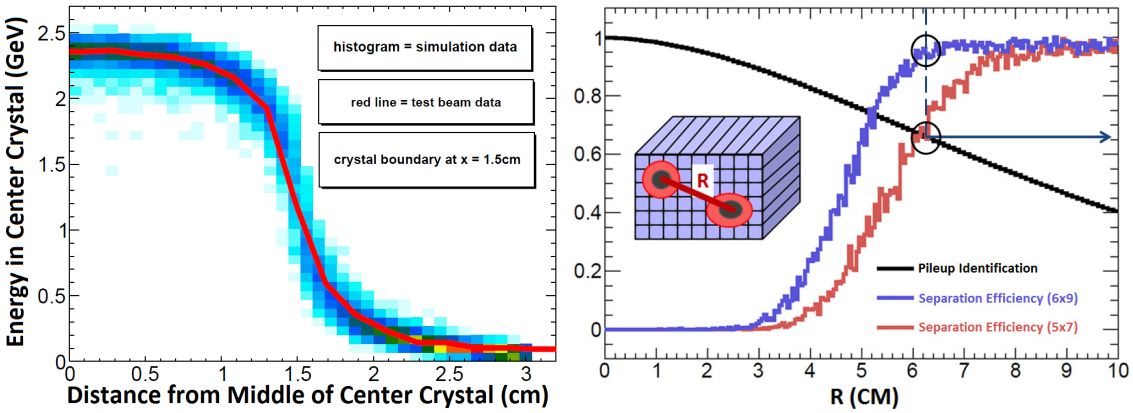

Figure 4.9-3. Left: A comparison of test-beam data and simulation data. This plot shows the shower leakage into neighboring crystals as a function of the beam incidence position. Right: Pileup separation efficiency curves for two different crystal segmentations, 6x9 and 5x7, which correspond to 2.5-cm and 3-cm crystals respectively (blue and red). The variable R is the distance between the two incident electrons and is shown graphically in the inset. The black curve represents the amount of pileup rejected for a certain R value.

The plans for the upcoming year include building a prototype of the calorimeter in a 5 x 5 crystal configuration with 2.5 x 2.5 x 14 cm crystals each coupled to a surface mount MPPC. This prototype will be evaluated at a test-beam run most likely at SLAC.

4.10 Lead fluoride crystal (PbF_2) transmission diagnostic tests

L. P. Alonzi, J. D. Crnkovic, A. García, N. S. Froemming, D. W Hertzog, P. Kammel, J. Kaspar, B. Kiburg*, M. W. Smith, H. E. Swanson, P. Winter†, and T. Zhao

The upcoming $g-2$ experiment will have 24 detector stations with 6 x 9 segmentation leading to an installation of 1296 total PbF_2 crystals with additional spare crystals on the side. It is important to have an efficient way to assess the quality of the crystals as they become a part of the experimental apparatus. The Ocean Optics tabletop optics kit is a convenient avenue for performing such measurements. The package includes a USB2000+ digital interface, a PX-2 ultraviolet source, and SpectraSuite analysis software. Furthermore, the optical kit facilitates easy measurement of the effects from other elements in the crystal interface.

*Presently at Fermi National Accelerator Laboratory, Batavia, IL.
†Presently at Argonne National Laboratory, Argonne, IL.

What is the integral characteristic of the PbF_2 crystal for our experiment? The crystals are responsible for producing photons which are measured in our calorimeter and the light yield from the crystals is purely Cherenkov which peaks in the ultraviolet regime. In light of this fact, the most important characteristic of the crystals is low-wavelength transmission. The transmission spectrum for PbF_2 "turns on" at a wavelength of 250 nm. The xenon source bundled with the Ocean Optics kit is excellent for the situation; it has an emission spectrum ranging from 230 nm to 800 nm. The proposed solution is to make a relative transmission test of the crystal at several transverse positions. Several different transmittance tests attest to the uniformity of the crystal and the relative transmission is then compared to PbF_2 from the literature. Fig. 4.10-1 shows the results of one such crystal-quality evaluation. The transmittance of each crystal locale is shown to be consistent with small variance.

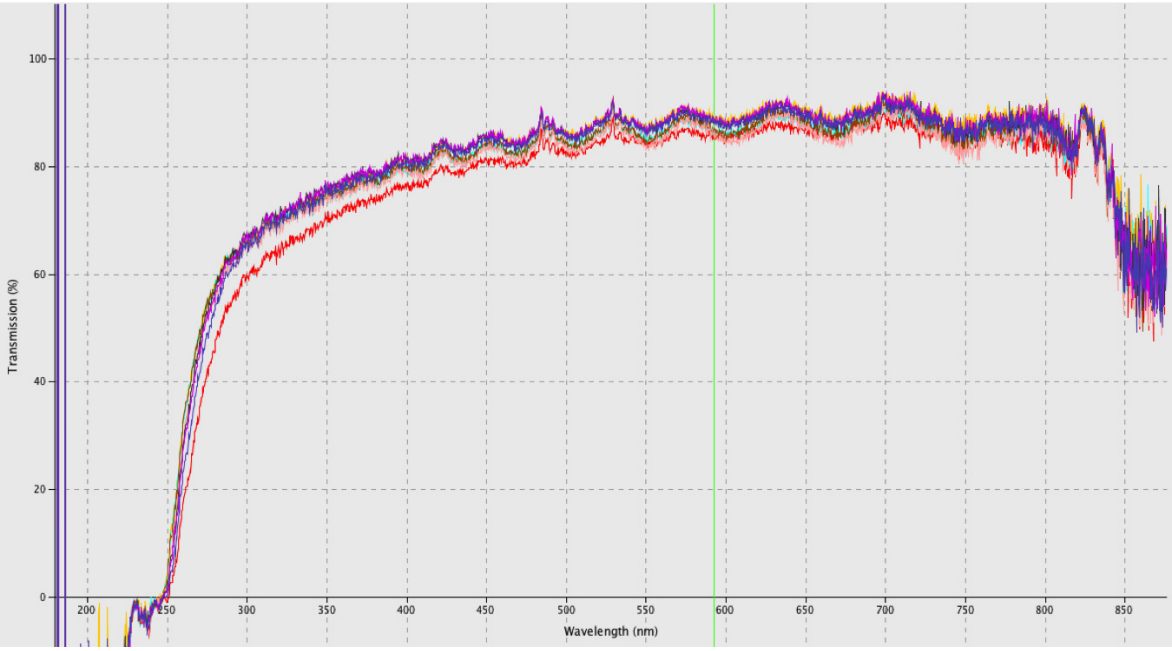

Figure 4.10-1. The results of a diagnostic test performed on one of the PbF_2 crystals in our lab. The transmission spectrum is consistent for each different path through the crystal and, more importantly, the ultraviolet transmission matches expectations.

4.11 Optimizing injection efficiency

N. S. Froemming, D. W. Hertzog, and P. Kammel

Precise determination of a_μ involves coupling a polarized muon beam to a very pure dipole magnetic field; as a result, the muon trajectories are nearly perfectly circular. On the other hand, upstream accelerator components dictate that the muons are brought to the entrance of the storage ring as a *linear* beam. Stringent material, geometrical, and field-uniformity

constraints make injecting muons into the storage ring one of the most challenging tasks of the entire experiment[1].

Over the past year, the University of Washington (UW) has played a key role in assessing muon loss in the injection path via detailed tracking simulations (Fig. 4.11-1A). We have also contributed to the verification of existing simulation tools, while developing important new simulation tools for the E989 experiment. Fig. 4.11-1B shows an example of one such simulation tool, conceived and written at UW, that allows users to easily specify the incident muon beam's phase-space parameters and inject the beam at a set of appropriate locations (cf. Fig. 4.11-1A).

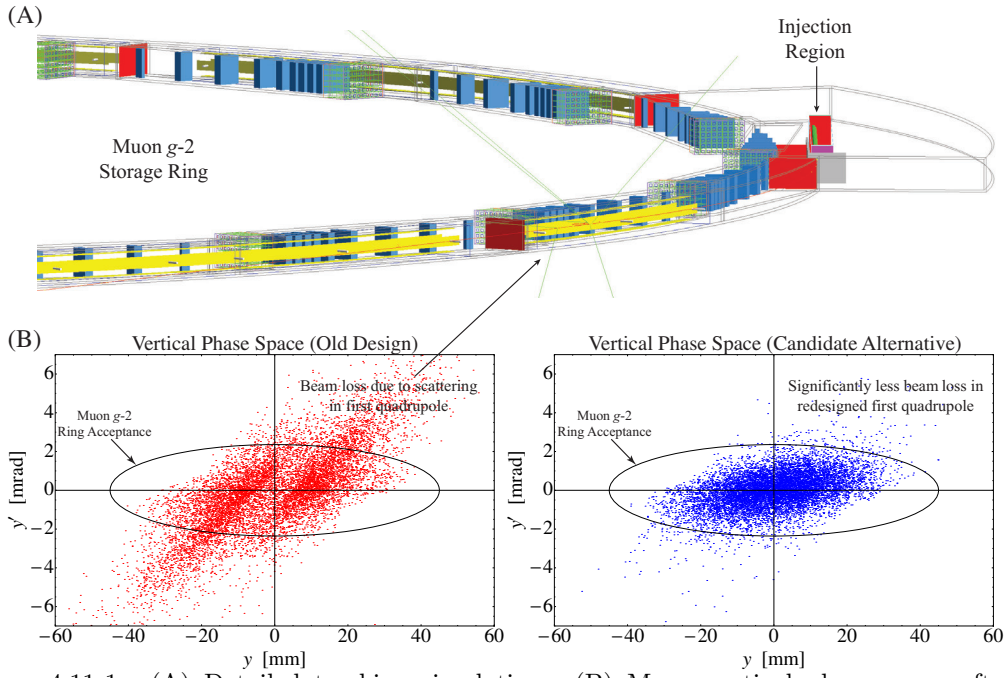

Figure 4.11-1. (A) Detailed tracking simulation. (B) Muon vertical phase space after scattering in the first quadrupole (yellow): existing (left) and candidate alternative (right) designs.

The simulation tool has been used extensively to investigate beam loss during injection, and to assess muon-injection transmission and storage efficiency. Our studies led to the discovery that many more muons were being lost due to scattering and energy loss in the first electric quadrupole plates and standoff support system than had been previously believed (Fig. 4.11-1A, yellow). As a result of these simulations, the first electric quadrupole and support system are now being redesigned.[2] Thus, our simulation efforts are leading to actual design changes that will improve the injection efficiency in the new muon $g-2$ experiment at Fermilab.

[1] It is estimated that, in the Brookhaven experiment, only 2-3% of the muons injected were actually stored.

[2] Brookhaven National Laboratory is leading the quadrupole redesign effort. We proposed a new quadrupole support that has become their "default design".

4.12 Overview and progress of the field team

L. P. Alonzi, J. D. Crnkovic, A. García, N. S. Froemming, D. W. Hertzog, P. Kammel, J. Kaspar, B. Kiburg*, M. W. Smith, H. E. Swanson, P. Winter†, and T. Zhao

Measuring the muon anomalous magnetic moment a_μ to greater precision also requires a precise determination of the magnetic field in the muon-storage region. In the most recent measurement (E821) the average field seen by all muons was known with an error of 0.17 ppm. Reducing the error on a_μ requires knowledge of the field to at least this precision and our target is to improve this to 0.085 ppm. The path forward includes better shimming of the field in the reassembled muon storage ring, improving the field-measurement system and providing a more accurate calibration. The field-measurement system is comprised of over 400 probes based on the nuclear magnetic resonance (NMR) of protons in water. The system has two parts: a trolley system that runs on rails inside the storage vacuum measures field multipoles as a function of azimuth around the ring and a system of fixed probes mounted at each pole face measures the dipole field in the gap. The trolley requires about two hours for a measurement when muons are excluded from the ring. The fixed-probe system makes continuous measurements that are used to interpolate between less frequent trolley runs.

The University of Washington team is responsible for the system of fixed probes. As a first step we are working on resurrecting the existing E821 system. This includes providing a working set of probes either by refurbishing existing ones or constructing new ones, and restoring or upgrading the associated electronics and data acquisition system. Verifying the operation of the probes requires a 1.45-Tesla field with sufficient uniformity and we have re-purposed one of the dipole magnets of the momentum filter to provide this field (see Sec. 4.13). We have also built electronics for measuring the proton free induction decay (FID) in the probes that is independent of the E821 system. A new PC and interface to the existing VME electronics has been purchased to upgrade the non-functioning data acquisition system. At Fermilab extensive Opera modeling of the storage-ring magnet has reproduced the E821 configuration. This gives confidence in its ability to inform shimming decisions.

We are presently working on shimming our magnet to improve its homogeneity to make it more appropriate to test different aspects of the NMR probes and identifying broken parts of the existing E821 system. Once this is done we will start a process of fixing the old NMR probes and building new ones as necessary.

---

*Presently at Fermi National Accelerator Laboratory, Batavia, IL.

†Presently at Argonne National Laboratory, Argonne, IL.

4.13 Preparations for restoring the NMR field-measurement system

L. P. Alonzi, J. D. Crnkovic, A. García, N. S. Froemming, G. C. Harper, D. W. Hertzog, P. Kammel, J. Kaspar, B. Kiburg*, T. G. MacDonald, R. Ortez, M. W. Smith, H. E. Swanson, D. Tarazona, P. Winter†, and T. Zhao

The magnetic-field measuring system for the $g-2$ muon storage ring uses over 400 nuclear-magnetic-resonance (NMR) probes. These all need to be checked and will likely need refurbishing to make the system operational. The probes have an operating range of 1.45 ± 0.025 T and require a minimum field uniformity of 250 ppm. The last dipole of the momentum-filter spectrometer in cave 1 is rated at 1.7 T and has parallel pole faces. It has a gap of 2.75 inches which makes it suitable for testing the probes as well as determining the effects of magnetic fields on the detector electronics and the susceptibility effects of electronics materials on the field.

To prepare the magnet the vacuum chambers and downstream quadrupole magnet were removed to allow access to the pole gap. The resulting test magnet station is shown on the left in Fig. 4.13-1. The spectrometer's power supply and control electronics were no longer considered sufficiently reliable to meet the stability requirements and were not used. Two 200-amp Bruker power supplies were moved from the linac area in the accelerator tunnel and placed next to the magnet. These were powered from existing circuit breakers in the accelerator tunnel. The current required for 1.45 T operation was about 325 Amps. The two supplies are connected in parallel with diode isolation as shown on the right in Fig. 4.13-1. Cooling water for the magnet and power supplies was obtained from the lab's condenser water system.

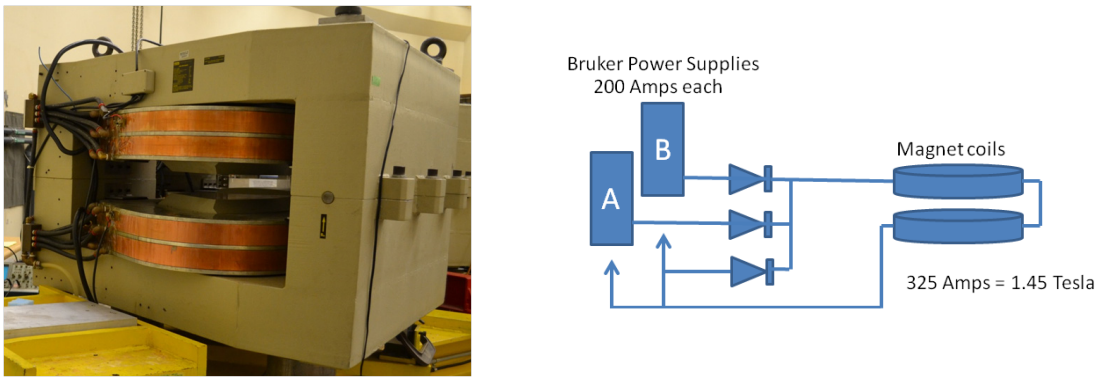

Figure 4.13-1. Left: The momentum-filter dipole configured to test $g-2$ NMR probes. Right: Power-supply connections showing diode isolation.

As part of the momentum filter, this dipole served to refocus trajectories of particles with different momenta and has pole faces with trapezoidal shapes. The measured field gradient going from wide to narrow pole edges is about 1000 ppm. Simulations done with Comsol are in agreement with a field gradient of this magnitude but show that if shims are added on the narrow pole edges the gradient can be reduced by more than an order of magnitude.

*Presently at Fermi National Accelerator Laboratory, Batavia, IL.
†Presently at Argonne National Laboratory, Argonne, IL.

4.14 Cross-section measurements via initial-state radiation at Belle

J. D. Crnkovic, D. W. Hertzog, and J. Kaspar

The most recent measurement of the muon anomalous magnetic moment (a_μ) suggests the possibility of new physics beyond the Standard Model. The largest source of uncertainty in the Standard Model (SM) prediction comes from the leading-order hadronic vacuum polarization (HVP) component. The HVP uncertainty is primarily due to the inability to calculate contributions below 3 GeV in perturbative QCD. The low-energy contributions are instead derived from experimentally measured exclusive cross sections of electron-positron annihilation to hadrons[1,2]. The low-energy HVP component in the SM calculation of the running of the fine-structure constant, $\alpha(s)$, that is also derived from the same exclusive cross sections used to calculate a_μ. There is recent interest in having a more precise value of $\alpha(s)$ at the Z boson mass ($\alpha(M_Z^2)$)[1,2] as it will allow for a better understanding of physics at the electroweak scale.

The direct method of obtaining these cross sections is to vary the center-of-mass energy of the initial electron-positron system. Fixed-energy colliders, such as B-factories, can alternatively use an initial-state radiation (ISR) photon to lower the effective invariant mass of the hadron system. Fig. 4.14-1 shows the leading-order ISR Feynman diagram. The $\sigma(e^+e^- \to \pi^+\pi^-\pi^0)$, $\sigma(e^+e^- \to \pi^+\pi^-\eta)$, $\sigma(e^+e^- \to K^+K^-\pi^0)$, and $\sigma(e^+e^- \to K^+K^-\eta)$ channels are four such HVP contributions to the calculation of a_μ. The $\pi^+\pi^-\pi^0$ channel provides the second largest contribution to a_μ[1,2], and both the $\pi^+\pi^-\pi^0$ and $\pi^+\pi^-\eta$ channels are relevant to the precision goals of the new Fermilab Muon $g-2$ experiment[3]. Measuring cross sections for the $K^+K^-\pi^0$ and $K^+K^-\eta$ processes is a natural continuation of measuring the corresponding pion cross sections due to the events sharing the same topology. The aim of our current research is to precisely measure all four cross sections using the ISR method on Belle data obtained at the KEK-B factory in Tsukuba, Japan.

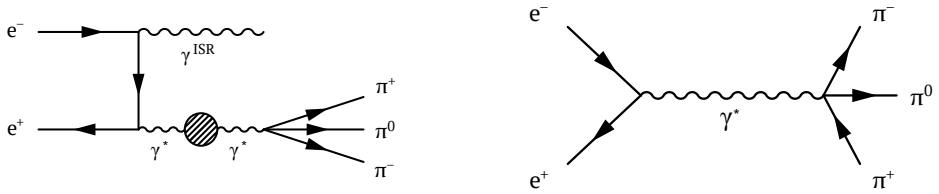

Figure 4.14-1. The leading-order Feynman diagram for the $e^+e^- \to \pi^+\pi^-\pi^0$ process, as measured by the initial-state radiation method, is given on the left. The tree-level diagram of the same process is given on the right, and is used in a dispersion relation to derive hadronic vacuum polarization.

We ported the Belle analysis framework to the CENPA computing cluster. This allows local processing of Belle data as well as the production and processing of the Belle Monte Carlo. The measurement of a $\pi^+\pi^-\pi^0$ *visible* cross section forms the basis of the recently

[1] M. Davier *et al.*, Eur. Phys. J. C **71**, 1515 (2011) [Erratum-ibid. C **72**, 1874 (2012)] [arXiv:1010.4180 [hep-ph]].

[2] K. Hagiwara *et al.*, J. Phys. G **38**, 085003 (2011).

[3] `http://muon-g-2.fnal.gov/`

completed thesis for Jason Crnkovic[1], and this result is presented at the 12th International Workshop on Tau Lepton Physics[2]. Fig. 4.14-2 shows the visible cross section reported at the 12th International Workshop on Tau Lepton Physics.

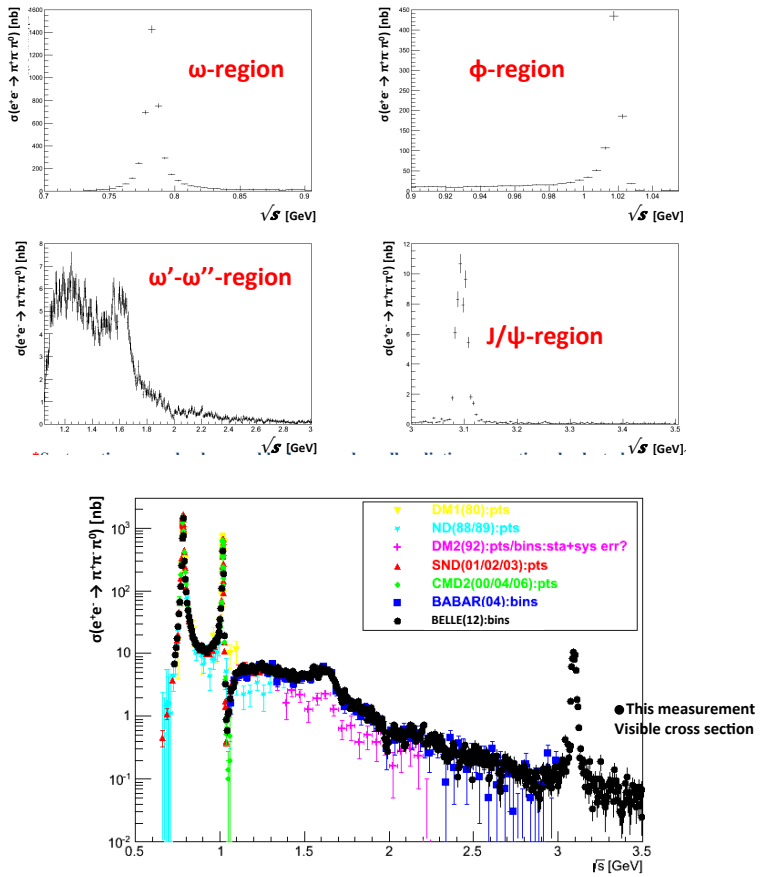

Figure 4.14-2. A measured $e^+e^- \to \pi^+\pi^-\pi^0$ visible cross section using Belle data[2]: (top) linear plotting broken into final-state mass regions and (bottom) logarithmic plotting over the full final-state mass range along with previous $e^+e^- \to \pi^+\pi^-\pi^0$ cross-section measurements.

A visible cross section for the $\pi^+\pi^-\pi^0$ process and a preliminary visible cross section for the $\pi^+\pi^-\eta$ process have been calculated. Studies of the systematic uncertainties are in progress and the visible cross sections will be turned into dressed cross sections with suitable radiative corrections calculated from the Belle Monte Carlo. Finally, the measurement procedure developed for the $\pi^+\pi^-\pi^0$ and $\pi^+\pi^-\eta$ processes (with suitable modifications) will be applied to the $K^+K^-\pi^0$ and $K^+K^-\eta$ processes. The goal of this analysis is to gain a better local understanding of initial-state radiation physics and its effect on cross section measurements and hadron vacuum polarization.

[1] *Measurement of the* $e^+e^- \to \pi^+\pi^-\pi^0$ *Cross Section by the Radiative Return Method Using BELLE Data*, Jason C. Crnkovic, PhD thesis, (December, 2012).

[2] Measurement of the e+e- -> pi+pi-pi0 Cross Section at Belle using Radiative Return, Jason Crnkovic, The 12th International Workshop on Tau Lepton Physics (TAU2012), Nagoya, Japan, September 17 – 21, 2012.

4.15 Contribution to the magnetic dipole moment of the muon from Belle data

J. D. Crnkovic, D. W. Hertzog, and J. Kaspar

The hadronic vacuum polarization (HVP) and hadronic light-by-light scattering are leading contributions to the Standard Model uncertainty of the muon magnetic anomaly (see Sec. 4.8). The optical theorem (Fig. 4.15-1) provides a way to calculate HVP from experimentally measured $e^+e^- \to$ hadrons cross-sections. The HVP value also provides a direct comparison of the cross-sections obtained by different experiments, and validates our results in energy regions mastered by scanning experiments.

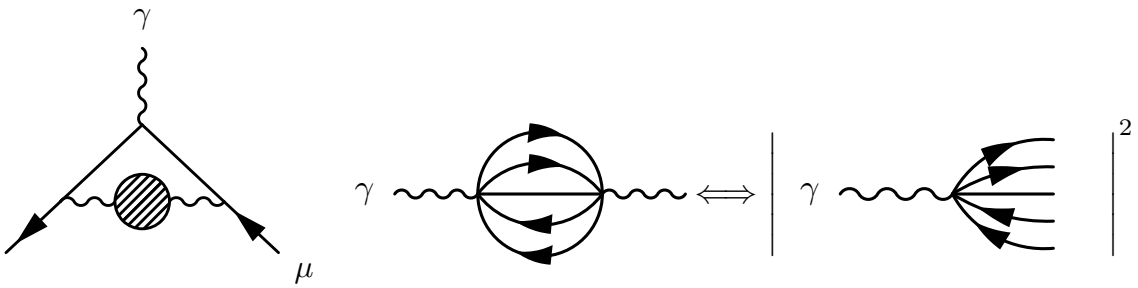

Figure 4.15-1. The leading hadronic contribution to the muon anomalous magnetic moment is shown on the left. On the right side the optical theorem relates the photon propagator to photon decay, and opens an experimental way to calculate the hadronic contribution.

The measured cross-sections (see Sec. 4.14) already include corrections for detector efficiency and acceptance. Radiative return serves as the energy-scanning tool. The photon propagator includes higher order quantum loop effects. The primary decay vertex suffers with final state radiation. The recipe to convert a measured cross-section into its HVP contribution is shown in Fig. 4.15-2:

1. The measured cross-section is corrected for final state radiation. The considered effects include real photons and vertex corrections. Our goal is to correct for the real photons which are not registered by the Belle detector and to remove the vertex corrections. The joint probability of these two kinds of effects is analytically calculated from QED. The PHOTOS MC generator estimates the probability of the real photons only. A combination of the analytical calculation and PHOTOS simulation disentangles these two groups. PHOTOS is also used to place the event into the correct energy bin because the missed real photons could have caused the event to be erroneously assigned to a lower energy bin.

2. The vacuum polarization is removed. From the previous step the momentum transfered to hadrons is correct so the contributions from the higher-order QED loop diagrams can be subtracted. An up-to-date numerical evaluation[1], coming in a convenient ROOT package, is used to adjust the cross-section by $\sim 3\,\%$. The correction is truly detector-independent, and can be improved anytime in the future if desired.

[1] `http://cmd.inp.nsk.su/~ignatov/vpl/`

3. The initial state radiation (ISR) is factored out. The cross section is a product of the leading-order s-channel hadronic decay and the probability of the ISR photons to carry out the appropriate energy. The angular distribution of the leading ISR photon has been included in the detector acceptance. A modified PHOKHARA event generator (with the hadronic part turned off) estimates the energy-density functions of both the ISR photons in the next-to-leading order approximation. Extra care is given to this correction because the second ISR photon is not registered by the Belle detector.

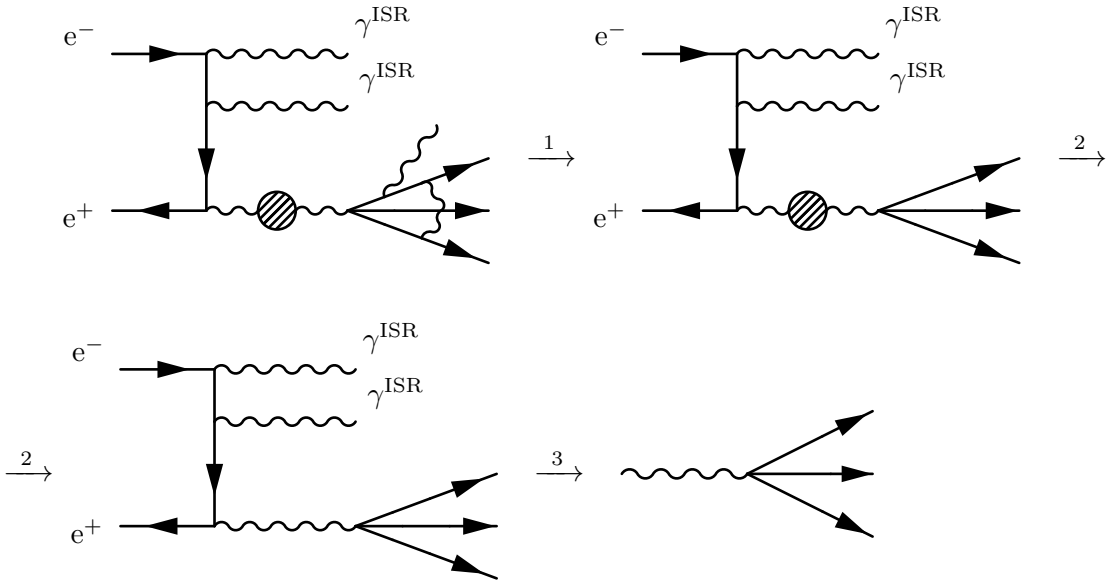

Figure 4.15-2. The path from the cross-section as measured by the Belle detector to the cross-section entering the dispersion relation to calculate the hadronic contribution to the muon anomalous magnetic moment. First, the final state radiation is corrected for. In step two the vacuum polarization is adjusted. Finally, the initial state radiation is removed.

Finally, having determined the s-channel leading-order cross-section, it is fed into the dispersion integral and the HVP contribution is derived. The implementation of the previous three steps is well advanced and verified on the $e^+e^- \to \pi^+\pi^-\pi^0$ cross-section. This year we will finish the implementation and apply it on $\pi^+\pi^-\eta$, $2\pi^+2\pi^-$, $\mathrm{K^+K^-\pi^0}$, $\mathrm{K^+K^-}\eta$ processes. The dispersion relation divides the provided cross section by the $\mathrm{e^+e^-} \to \mu^+\mu^-$ cross-section. Therefore the bin-by-bin ratios as measured by the detector can be used to mitigate some systematic effects, and are being considered as a cross-check in energy regions with favorable $\mu^+\mu^-$ rates. Our main goal is to prepare the Belle cross-section data in the clarity and quality sufficient for the future experts who will combine data across various experiments when $g-2$ results become available. A paper summarizing the results is in preparation.

AlCap

4.16 Charged-particle emission after muon capture: the AlCap experiment

D. W. Hertzog, P. Kammel, M. H. Murray, T. H. Nam*, F. Wauters, and K. Yai*

The observation of neutrino flavor oscillation means that lepton number is not fully conserved. However, the predicted charged-lepton flavor violation (CLFV) by a minimal extension of the Standard Model including massive neutrinos, is extremely small (branching ratio of $\mathcal{O}(10^{-50})$). Thus, any experimental observation of CLFV is an unambiguous signal of new physics. Various extensions to the Standard Model predict CLFV rates that are within reach of next-generation experiments, probing new physics phenomena both at the grand unified theory (GUT) and the TeV scale[1].

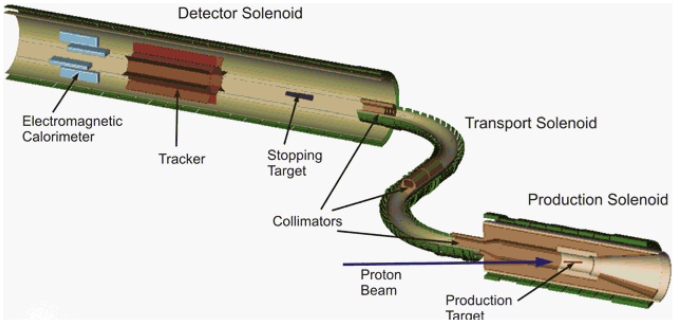

Figure 4.16-1. Schematic layout of the planned Mu2e experiment at FNAL.

The most stringent limits on CLFV in muon decays come from the MEG[2] and SINDRIUM II[3] experiments, with an upper limit on the $\mu \to e\gamma$ branching ratio of 2.4×10^{-12} and on the $\mu^- Au \to e^- Au$ branching ratio of 7.0×10^{-13}, respectively. Two new experiments searching for CLFV in the $\mu N \to eN$ process are under construction, Mu2e at FNAL (Fig. 4.16-1) and COMET at J-PARC, both aiming at a sensitivity better than 10^{-16} are currently. Both experiments utilize a multi-kW proton beam to produce a high-intensity negative muon beam. These negative muons form muonic atoms in the stopping target, after which they decay in orbit ($\mu^- \to e^- \nu_\mu \overline{\nu}_e$) or undergo muon capture on a nucleus of the target material ($\mu^- + N(A,Z) \to \nu_\mu + N(A, Z-1)$). The event signature for the CLFV process, $\mu^- + N(A,Z) \to e^- + N(A,Z)$, is a mono-energetic electron with an energy of about 105 MeV, far above the end-point energy of the Michel spectrum (52.8 MeV).

Candidate electrons are subsequently detected by a cylindrical tracker and an electromagnetic calorimeter. A major background for these detectors arises from muon capture on

*University of Osaka, Osaka, Japan.

[1] Y. Kuno and Y. Okada, Rev. Mod. Phys. **73** 151-202 (2001).
[2] J. Adam *et al.*, Phys. Rev. Lett. **107**, 171801 (2011).
[3] W. Bertl *et al.*, Eur. Phys. J. C **47**, 337 (2006).

the target material, $\mu^- + N(A,Z) \rightarrow \nu_\mu + N(A,Z-1)$. This process is often accompanied by the emission of charged particles, neutrons, and photons. In particular, protons with a momentum in the range of the candidate electrons dominate the background for the tracking detector.

There is no experimental data in the relevant energy range on charged-particle emissions following muon capture on Al and Ti, two candidate target materials. The AlCap experiment is a joint effort by the COMET and Mu2e collaborations, led by the University of Washington and Osaka University, to measure the energy spectrum and yield of charged particles emitted after muon capture on those materials. The target precision for the proton rate and spectrum is 5%. These data will serve as an important input for the design of the Mu2e and COMET tracking detectors.

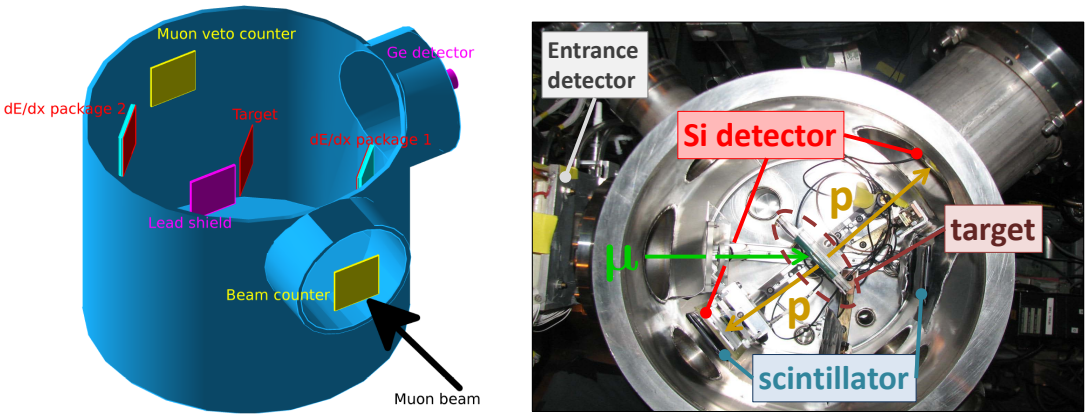

Figure 4.16-2. *Left:* Sketch of the AlCap experiment. The positions of the detector and absorbers are currently being optimized by Geant4 Monte-Carlo simulations. *Right:* Current status of the AlCap detector chamber.

Fig. 4.16-2 shows the proposed layout of the AlCap detector chamber. The incoming muons are detected by two detectors, a plastic scintillator and a wire chamber. The thin Al or Ti target (25 - 100 μm) is tilted facing the Si detectors to optimize the stopping fraction of the muons and minimize straggling of the emitted charged particles. The main detector is a pair of 5 x 5-cm, 1500-μm-thick Si detectors positioned on opposite sides of the target foil. Several plastic scintillator detectors will be strategically positioned behind the Si detectors to veto Michel electron hits. A 65-μm-thick Si detector can be added to provide particle identification. To determine the absolute stopping fraction a high-purity germanium detector will observe the element-specific muonic X-rays of the stopping target. In addition, the Al or Ti foils can be replaced by an active Si target to further determine the response of the apparatus.

The first data-taking will occur at the end of 2013. Four weeks of beam time have been allocated at the πE1 beamline at the Paul Scherrer Institute, benefiting from the well tuned muon beam from the preceding MuSun experiment. The UW muon group is hosting the development of the experiment, providing lab space and hardware support for the visiting students, T. H. Nam and K. Yai, from Osaka University.

5 Axion searches

ADMX (Axion Dark Matter eXperiment)[1]

5.1 Status of the ADMX experiment

C. Boutan, M. Hotz, D. Lyapustin, L. J Rosenberg, G. Rybka, A. Wagner, and D. I. Will

The Axion Dark Matter eXperiment (ADMX) is a large-scale RF-cavity search for galactic dark-matter axions. This experiment has been in operation since the mid-1990s, and was moved to CENPA in 2010. ADMX is currently undergoing warm commissioning and will soon have sufficient sensitivity to either detect or rule out the QCD-axion hypothesis at high confidence. We plan to begin data-taking this summer and we will have either discovered the axion or excluded a large fraction of the allowed axion mass range by 2015.

The axion was postulated three decades ago to explain why QCD conserves the discrete symmetries P (parity) and CP (charge conjugation times parity). QCD's predictions depend upon a parameter θ. When θ differs from zero, QCD violates P and CP. Since the strong interactions appear to be P- and CP-symmetric in the laboratory, θ must be very small. The upper limit on the neutron electric-dipole moment requires $|\theta| < 10^{-10}$. However, in the Standard Model, P- and CP-violation by the weak interactions feeds into the strong interactions so that the expected value of θ is of order unity. The inability of the Standard Model to account for P- and CP-conservation by the strong interactions is called the "strong CP problem". Peccei and Quinn proposed a solution to this problem in which the Standard Model is modified so that θ becomes a dynamical field and relaxes to zero. The theory's underlying broken continuous symmetry results in the existence of a new particle called the axion. The axion is the quantum of oscillation of the θ field and has zero spin, zero electric charge, and negative intrinsic parity. So, like the neutral pion, the axion can decay into two photons.

Despite, however, the prodigious predicted local density of dark-matter axions (in the neighborhood of 10^{14}/cc), the expected electromagnetic signal would be extraordinarily weak, around 10^{-23} W in the ADMX apparatus. Our present ADMX Collaboration (with original core institutions UW, Lawrence Livermore National Lab (LLNL), Florida, National Radio Astronomy Observatory (NRAO), and Berkeley) constructed and operated a large-scale dark-matter axion experiment that, for the first time, reached sensitivity to plausible dark-matter axions. This experiment consists of a large microwave cavity immersed in a static magnetic field. Nearby galactic-halo axions scatter from the static field and convert into microwave photons within the cavity.

The ADMX detection apparatus is essentially an extraordinarily low-noise radio receiver with an RF cavity forming a tuned tank circuit. A short electric-field probe couples power

[1]ADMX is supported by the DOE Office of High-Energy Physics and makes use of CENPA resources by recharge to the cost center.

from the cavity into a cryogenic amplifier which is cooled to near the cavity temperature, around 2 K.

Figure 5.1-1. Progress of the ADMX experiment site at CENPA. *Left*: July, 2011, showing the initial magnet installation. *Middle*: November, 2011, showing the beginnings of flooring and clean room. *Right*: February, 2013, showing the clean room with experimental insert, helium-liquefaction system, and data-acquisition racks.

The last operation of the ADMX experiment, fitted with superconducting quantum interference device (SQUID) amplifiers, completed a scan of the 1.9–3.5-μeV axion mass range and published the results for conservative estimates of dark matter density. With further analysis we have since published a search for axions under different models of how dark matter may be distributed in our galaxy[1].

Figure 5.1-2. Assembly of the new ADMX experimental insert

The motivation for lowering the system noise temperature is clear: (i) for a given axion-photon coupling the scan rate grows inversely as the square of the system temperature and (ii) for a given scan rate the power sensitivity increases as the system temperature drops. In ADMX the system noise temperature is essentially the noise temperature of the amplifier plus the cavity physical temperature. We developed SQUID amplifiers in the 100–1000-MHz range specifically for ADMX and this development allowed more than an order-of-magnitude reduction in system noise temperature.

[1] J. Hoskins *et al.*, Phys. Rev. D **84**, 121302(R) (2011).

ADMX is currently being retrofit for lower-temperature operation. We intend to use a pumped ^{3}He system to reach a temperature of 300 mK then install a dilution refrigerator capable of reaching 100 mK. The cryogenics of these temperatures are considerably more technically challenging than those of the last operating point and require a complete redesign of the experimental insert. Construction of this new insert began in winter, 2011, and we are presently undergoing warm commissioning. A helium-liquefaction system has been installed in the east end of the CENPA accelerator tunnel and we are beginning to plumb the system. We anticipate being able to cool the experiment in late spring and beginning a round of data taking this summer.

6 Relativistic Heavy Ions

6.1 UW URHI program overview

T. A. Trainor

The UW ultra-relativistic-heavy-ion (URHI or Event Structure) program, in cooperation with the URHI group at UT-Austin) has established a detailed description of nuclear collisions from the Relativistic-Heavy-Ion Collider (RHIC) that contradicts claims for creation in Au-Au collisions of a strongly-coupled flowing quark-gluon medium with novel properties, including opacity to jets and small viscosity— a "perfect liquid". We have published a long paper on angular correlations in Au-Au collisions[1] that describes discovery of a *sharp transition* in minimum-bias jet (minijet) characteristics appearing at the midpoint of Au-Au centrality measured by the fractional cross section σ/σ_0 for both 62- and 200-GeV collisions. At either energy minijet correlations in more-peripheral collisions follow N-N binary collision scaling expected for in-vacuum jets with *no secondary scattering* of partons or hadrons, consistent with *transparency*—linear superposition of N-N collisions—and inconsistent with formation of a dense, thermalized partonic medium opaque to jets. In more-central collisions minijets undergo quantitative changes, but some aspects are still consistent with perturbative quantum chromodynamics (pQCD).

Substantial evidence indicates that the systematics of the nonjet azimuth quadrupole related to quantity v_2 are incompatible with a hydro interpretation as "elliptic flow." Comparison of quadrupole centrality dependence with minijet trends reveals that the quadrupole amplitude rises to 60% of its maximum value within the centrality interval where Au-Au collisions are transparent, where there is no significant secondary scattering of partons or hadrons (see Sec. 6.2)[2]. Other evidence against a hydro interpretation includes p_t dependence of v_2 and properties of an inferred *quadrupole spectrum*. An alternative production mechanism for the azimuth quadrupole may involve pQCD color-dipole interactions.

Survival of almost all minimum-bias jets as resolved correlation structure in central Au-Au collisions presents major problems for quark-gluon plasma (QGP) interpretations. The response has been multiple reinterpretations of the same-side 2D "jet-cone" peak structure as a flow manifestation. Strategies include (a) projection of 2D jet structure onto 1D azimuth and interpretation of 1D Fourier series fits as representing flows and (b) conjectured "glasma flux tubes" coupled to radial flow producing elongated same-side peak structure that emulates jet correlations. We responded with papers demonstrating the relation between flow claims and jet structure and inconsistencies between flow interpretations and the *complete* systematics of jet-related spectrum and correlation structure[3,4]. Predicted characteristics of glasma flux tubes are incompatible with measured jet-related correlations[5]. Those issues and others are explored in a recent invited review of the RHIC experimental program[6].

[1] G. Agakishiev *et al.* (STAR Collaboration) [UW-UTA principal authors], Phys. Rev. C **86**, 064902 (2012).
[2] T. A. Trainor, D. T. Kettler, D. J. Prindle and R. L. Ray, arXiv:1302.0300, submitted to Phys. Rev. C.
[3] T. A. Trainor, J. Phys. G **40** 055104 (2013).
[4] T. A. Trainor, D. J. Prindle, and R. L. Ray, Phys. Rev. C **86**, 064905 (2012).
[5] T. A. Trainor, J. Phys. G **39**, 095102 (2012).
[6] T. A. Trainor, arXiv:1303.4774, RHIC review invited by the Editors, Advances in High Energy Physics.

Given the growing uncertainty of RHIC heavy-ion data interpretations, provocative new p-p results from the LHC and reinterpretation of p-p collision phenomenology at RHIC energies take on new importance. Additional issues relate to (a) p-p *underlying-event* (UE) studies (e.g., Fermilab CDF) and (b) the relevance of p-p centrality to hadron and dijet production. What determines p-p collision dynamics and the hadronic final state (hadron yields, correlations, dijet production)? What is relevant to A-A collisions? We recently published a study of conventional UE analysis and theoretical conjectures about p-p centrality in the context of minimum-bias jet spectrum and correlation structure[1]. The p-p centrality issue remained unresolved. Sec. 6.3 is a followup: dijet production is $\propto n_s^2$ where hadron soft component n_s represents low-x gluons. The eikonal approximation central to the semiclassical A-A Glauber model does not apply to p-p collisions. p-p centrality is not a relevant concept for a collision process that must be described as a single quantum transition.

The controlling parameter for p-p collisions appears to be the number of event-wise *participant partons* (gluons) from the proton wave function estimated by multiplicity soft component n_s. How deep in momentum fraction x is a proton penetrated in a given p-p collision? Participant partons in p-p collisions are analogous to participant nucleons in A-A. Sec. 6.4 tests the p-p "Glauber" model with angular correlations vs n_s: how do correlation components scale with the number of participant gluons? Sec. 6.5 explores the η-dependence of hadron yields and spectra and buttresses the fluctuating low-x gluon role for three correlation components. Sec. 6.6 and Sec. 6.7 explore conventional UE analysis and assumptions. We observe that (a) transverse (to dijet axis) multiplicity $N_\perp$ includes a substantial contribution from triggered dijets misinterpreted as due to multiple parton interactions (MPI) and (b) minijet angular correlations contribute strongly to the UE transverse azimuth region (TR) contrary to assumptions. We conclude that all p-p collisions are described by three components: (i) pQCD dijets (hard), (ii) projectile-nucleon fragments (soft) and (iii) a substantial nonjet (NJ) quadrupole component in higher-multiplicity p-p collisions. MPI may play a role, but only in higher-multiplicity events where the pQCD dijet probability approaches unity.

Minijets in p-p collisions have been misrepresented by Monte Carlos (e.g., PYTHIA) and therefore erroneously discounted in A-A collisions. To clarify such issues we have measured p-p trigger-associated (TA) correlations. Sec. 6.8 and Sec. 6.9 present 1D trigger-particle spectra and a two-component model (TCM) derived from single-particle p_t spectra that describes the 1D trigger-particle spectra accurately. Sec. 6.10 and Sec. 6.11 present 2D trigger-associated correlations and a 2D TCM that can describe certain aspects of the data histograms accurately. What cannot be described by a TCM based on 1D projections is the TA hard component isolated by subtracting the TCM soft component. Sec. 6.12 presents TA hard components that can be compared quantitatively with measured jet fragmentation functions and pQCD parton spectra. The low-p_t kinematic limits of jets manifesting as clusters of charged hadrons are clearly demonstrated. The great majority of jet fragments appears in the low-p_t region where hydro is assumed to dominate A-A collisions. Sec. 6.13 presents variations of the TA hard component with azimuth relative to the trigger particle, again demonstrating the triggered-dijet contribution to the TR inconsistent with UE assumptions but also revealing possible k_t softening of recoil-partner jets compared to trigger jets. These

[1] T. A. Trainor, Phys. Rev. D **87**, 054005 (2013).

new TA data and models provide an extensive description of minijet phenomenology in p-p collisions that may be used to better understand QCD phenomena in A-A collisions.

6.2 Challenging claims for "elliptic flow" from RHIC heavy ion collisions

D. T. Kettler, D. J. Prindle, R. L. Ray*, and T. A. Trainor

The nonjet (NJ) azimuth quadrupole measured by *per-pair* quantity $2v_2^2\{2D\} = \langle\cos[2(\phi_1 - \phi_2)]\rangle$ derived from model fits to 2D angular correlations is conventionally interpreted to represent "elliptic flow," a hydrodynamic response to initial-state A-A overlap asymmetry by a conjectured dense and locally-equilibrated medium (quark-gluon plasma or QGP). However, when compared to minimum-bias jet systematics, quadrupole data appear to be inconsistent with a hydro interpretation. Fig. 6.2-1 (first) shows $v_2\{2D\}$ data in a conventional plotting format vs participant number N_{part} that obscures the lower 50% of the total cross section ($N_{part} < 50$). In contrast, plots of the *per-particle* measure $A_Q = \rho_0 v_2^2$ vs relative impact parameter b/b_0 are well described by a Gaussian over a broad range of energies. The energy trend of the Gaussian amplitude is shown in the second panel: linear on $\log(\sqrt{s_{NN}})$ above 13 GeV.

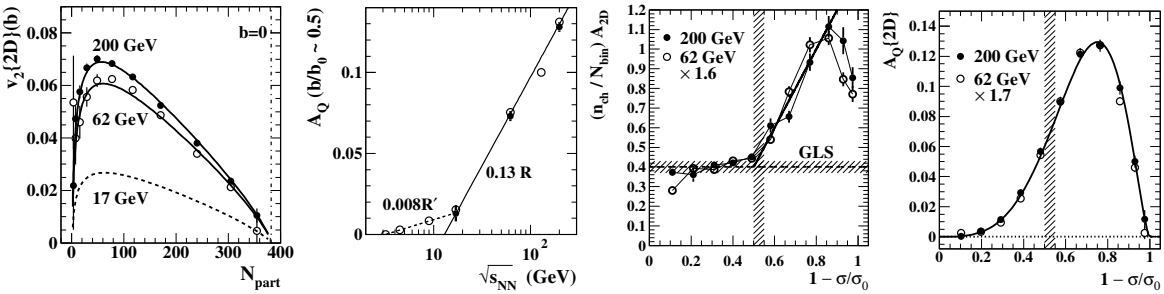

Figure 6.2-1. First: Nonjet quadrupole measure $v_2\{2D\}(b)$ inferred from 2D model fits. Second: Energy dependence of quadrupole amplitude A_Q. Third: Minijet SS 2D peak amplitude from 200 GeV Au-Au collisions showing binary-collision scaling (GLS, A-A transparency) up to a *sharp transition* at 50% of total cross section. Fourth: Nonjet azimuth quadrupole increases to 60% of its maximum value within the Au-Au transparency region.

Fig. 6.2-1 (third) shows the amplitude of the SS 2D minijet peak scaled by the number of binary N-N collisions N_{bin} vs fractional cross section σ/σ_0. Over half that interval jet systematics indicate that Au-Au collisions are *transparent*—linear superpositions of N-N collisions (Glauber linear superposition or GLS). The fourth panel shows that the NJ quadrupole increases to 60% of its maximum value within the same centrality interval where *no secondary scattering* of partons or hadrons (no equilibration) is observed. The possibility to generate the NJ quadrupole by pressure gradients in a dense flowing medium is then unlikely. The transverse momentum p_t dependence of the NJ quadrupole further contradicts hydro interpretations. The corresponding quadrupole source boost distribution is inconsistent with Hubble expansion of a flowing bulk medium suggests instead fragmentation of a radially-expanding thin eccentric cylinder. The $\log(\sqrt{s_{NN}})$ energy dependence in the second panel is consistent with that for jet production illustrated in the third panel by the factor 1.6

*University of Texas, Austin, TX.

applied to 62-GeV data to compare with 200-GeV data (vs factor 1.7 for quadrupole data in the fourth panel). Note that the same energy-dependence factor applies to jets from all Au-Au centralities (third panel), albeit jets are strongly modified in more-central collisions (deviations from the GLS trend). Such detailed comparisons suggest that above 13 GeV NJ quadrupole and dijet production represent two facets of QCD manifested within high-energy nuclear collisions: long-wavelength and short-wavelength radiation from interactions of QCD colored objects.

6.3 A p-p "Glauber model" – centrality b vs soft gluon x

T. A. Trainor

The charged-particle multiplicity n_{ch} from p-p collisions fluctuates over a large interval depending strongly on collision energy. Dijet production is closely correlated with n_{ch}. Recently it was found that a nonjet quadrupole is measurable for p-p collisions and also varies strongly with n_{ch}. The question arises what role centrality or impact parameter b may play in p-p collisions and how it is correlated with those observables. Fig. 6.3-1 (first) shows p-p event number distributions on n_{ch} for four collision energies. The distribution modes (maxima) show little energy dependence, but the large-n_{ch} tails are strongly energy dependent. The second panel shows p-p p_t spectrum hard-component multiplicity n_h (interpreted to represent dijet production) vs soft-component multiplicity n_s. The trend is $n_h \propto n_s^2 \approx n_{ch}^2$ to the uncertainty limits of the data. That trend can be compared with the systematics of Au-Au collisions where (for transparent Au-Au collisions) $n_h \propto N_{bin} \propto N_{part}^{4/3} \approx n_{ch}^{4/3}$. Exponent 4/3 reflects the *eikonal approximation* wherein each participant nucleon interacts only along a straight-line trajectory. The p-p trend implies instead that each participant (parton $\rightarrow$ gluon) can interact with *any* participant in the partner nucleon: the eikonal approximation is not valid.

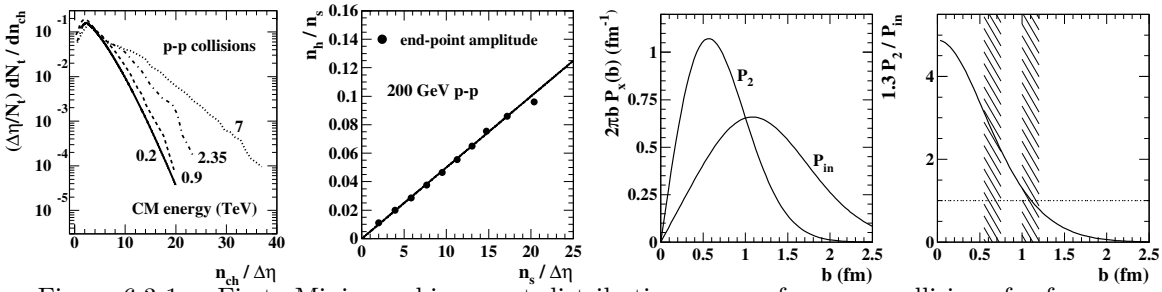

Figure 6.3-1. First: Minimum-bias event distribution on n_{ch} from p-p collisions for four collision energies. Second: Hard-component multiplicity n_h vs soft-component multiplicity n_s. Third: Model of dijet production vs impact parameter. Fourth: Ratio of P_2 to P_{in}.

Fig. 6.3-1 (third) represents a theoretical model of p-p collisions in which the probability of dijet production P_2 depends on impact parameter b due to the transverse distribution of low-x gluons inferred from deep-inelastic scattering (DIS) data. P_{in} is the probability for inelastic p-p collisions. The fourth panel shows the ratio P_2/P_{in}, the rate of dijet production per inelastic p-p collision. The hatched bands indicate impact parameter ranges supposedly corresponding to imposed trigger conditions. The essential result is that the rate of dijet

production within that model can vary only by a factor less than 5, whereas the observed dijet rate corresponding to $n_h \propto n_s^2$ varies over a factor of 100 for an accessible range of n_{ch}. The measured dijet rates and the n_s^2 trend appear to contradict any significant role for impact parameter in p-p collisions. An alternative model is based on the number of *participant gluons* determined by the initial conditions and degree of penetration of the nucleon wave function on momentum fraction x. Deeper penetration in some events produces a larger participant number and greater dijet production. The fluctuating extent of x penetration is reflected in the first panel, the *mean* depth increasing logarithmically with collision energy. If N_{part} is the number of participant gluons then $N_{bin} = N_{part}^2$ is the number of binary encounters that may produce a dijet according to a pQCD cross section depending on dijet energy Q.

6.4 p-p angular correlation systematics vs low-x gluons

D. J. Prindle and T. A. Trainor

2D correlations on angular differences $(\eta_\Delta, \phi_\Delta)$ have been measured for seven n_{ch} classes of 200-GeV p-p collisions. The 2D data histograms are fitted with a model function including four main elements: (a) same-side (SS) 2D Gaussian, (b) away-side (AS) 1D dipole, (c) nonjet quadrupole, (d) 1D Gaussian on η_Δ. Their amplitudes, represented respectively by A_{2D}, A_D, A_Q and A_{soft}, are defined as *per-particle* referring to final-state hadrons. In this case we want correlations expressed per *soft-component* hadron (low-x gluon) and so rescale the amplitudes by factors (n_{ch}/n_s). For p-p collisions hadron multiplicity soft component n_s is adopted as a proxy for the number of participant low-x gluons N_{part}. p-p centrality (impact parameter b) is not relevant, since each participant may interact with any participant in the partner nucleon (no eikonal approximation). The number of gluon participants fluctuates over a large interval determined by event-wise initial conditions. The mean value is determined by the collision energy. We seek the trends of four phenomena with the number of low-x gluon participants.

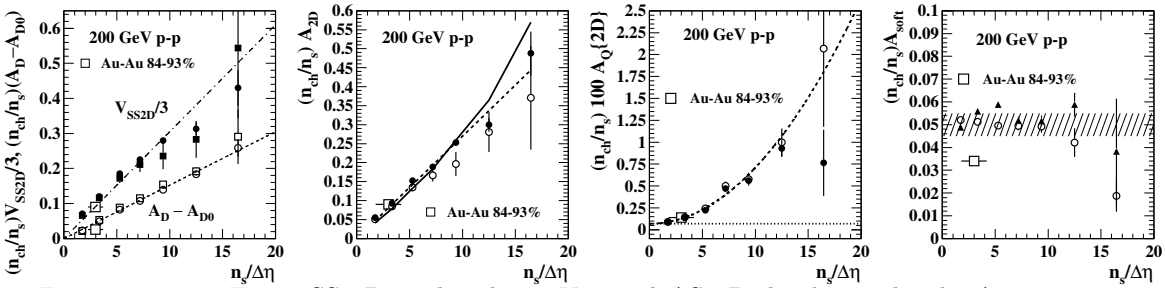

Figure 6.4-1. First: SS 2D peak volume V_{SS} and AS 1D dipole amplitude A_D vs n_s. Second: SS 2D peak amplitude A_{2D} vs n_s. Third: Nonjet quadrupole amplitude A_Q vs n_s. Fourth: Soft-component amplitude A_{soft} vs n_s.

Fig. 6.4-1 (first) shows SS 2D peak volume V_{SS2D} (all hadron pairs associated with dijets) and AS dipole amplitude A_D vs n_s. The dash-dotted line is a *prediction* based on a pQCD dijet total cross section 2.5 mb. A_{D0} estimates a small nonjet dipole contribution from global momentum conservation. Both measures scale $\propto n_s^2$ to the uncertainty limits of the data, consistent with dijet production and no eikonal approximation. The second panel checks

the effect of SS 2D peak widths on the volume calculation. Fig. 6.4-1 (third) shows the rescaled nonjet quadrupole A_Q data revealing a quadratic trend corresponding to quadrupole $\propto n_s^3$. The value of A_Q for non-single-diffractive (NSD) p-p collisions ($n_s/\Delta\eta \approx 2.5$) is consistent with a pQCD prediction for v_2 based on a color-dipole model and with peripheral Au-Au measurements. The fourth panel shows that the soft component is $\propto n_s$ consistent with projectile nucleon dissociation as the source: each noninteracting participant gluon fragments to a charge-neutral pair of low-p_t hadrons with nearly equal rapidities. The data trends taken together are consistent with a model in which a number of low-x gluons "freed" from the parent nucleon may then fragment individually (soft) or scatter from participants in the partner nucleon to produce dijets (hard). In addition, a quadrupole component varying as $N_{part}^3 \to N_{part}N_{bin}$ emerges as a significant correlation component for larger n_{ch}. Whereas the quadrupole component from Au-Au collisions varies as $N_{part}(b)N_{bin}(b)\epsilon_{opt}^2(b)$, that in p-p collisions varies as $N_{part}N_{bin}$ (effectively averaged over b). The similarities are notable.

6.5 n_{ch} dependence of angular correlations and η distributions for particles produced in 200-GeV p-p collisions

D. Prindle and T. A. Trainor

We have analyzed 200-GeV proton-proton collisions recorded by the STAR detector at RHIC. About 12×10^6 minimum-bias-triggered events were recorded during a period when detectors were placed very close to the beamline to measure forward protons from double Pomeron exchange. During this data-taking period the low-luminosity beam was tuned to be especially clean and there is no indication of pileup, a serious problem for most minimum-bias analyses, making this a particularly good data sample for us to analyze.

A previous study[1] found that spectra from proton-proton collisions can be described by soft and hard components whose amplitudes depend on event multiplicity. We have defined 7 multiplicity bins ranging from $2 \leq n_{tracks} < 4$ to $25 \leq n_{tracks} < 50$. For each multiplicity bin we form two-particle correlations on $(\eta_\Delta, \phi_\Delta)$ which are well described by a model with a same-side 2D Gaussian and away-side dipole, a quadrupole, a 1D Gaussian on η_Δ, and a narrow 2D exponential at $(0, 0)$. An example is shown in Fig. 6.5-1 where the first panel is the model, the second panel the data and the third panel the residuals. The fourth panel shows the same-side 2D Gaussian and away-side dipole, associated with hard scattering, whose amplitudes depend strongly on event multiplicity.

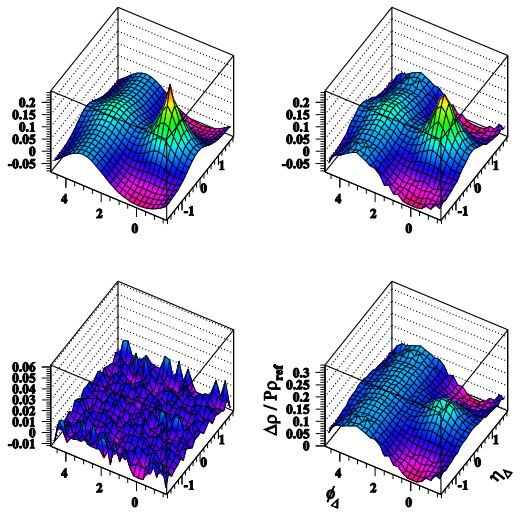

Figure 6.5-1. Multiplicity bin $15 < n_{tracks} < 20$ First panel is model, second data, third residual and fourth is 2D Gaussian plus away-side dipole

[1] J. Adams *et al.*, Phys. Rev. D **74**, 032006 (2006).

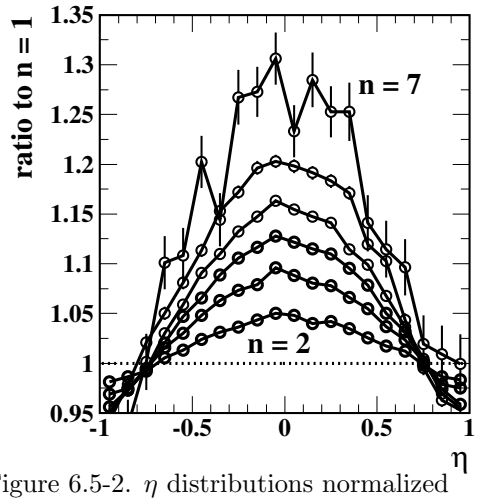

Figure 6.5-2. η distributions normalized to multiplicity bin n=1.

In this analysis we include tracks within the full barrel of the STAR time-projection chamber (TPC), $|\eta| < 1$. The η distribution is distorted by detector, especially electronic, artifacts but since these are independent of multiplicity for even the highest multiplicity proton-proton collisions recorded by STAR we can normalize by the lowest multiplicity bin and observe the change in shape as we increase event multiplicity. In Fig. 6.5-2 we see that with increasing multiplicity particles are more peaked at mid-rapidity, as one would expect if the multiplicity increase is due to low-x gluons.

6.6 Transverse multiplicity $N_\perp(p_t)$ systematics for 200-GeV p-p collisions

T. A. Trainor

The *underlying event* (UE) in those p-p collisions that include a triggered dijet is that part of the final state complementary to the dijet. Accurately separating dijet and UE presents technical challenges. The UE is probed in the *transverse region* (TR) on azimuth relative to trigger direction ϕ_{trig} ($|\phi - \phi_{trig} - \pi/2| < \pi/6$). The TR *by assumption* contains no contribution from the triggered dijet. The particle yield integrated within the TR and some η acceptance $\Delta\eta$ is transverse multiplicity $N_\perp$. UE diagnostics include the $dN_\perp(p_t)/dp_t$ spectrum and the $N_\perp(p_{t,trig})$ angular density responding to some trigger condition $p_{t,trig}$ (individual particles or jet). Measured systematics are interpreted to indicate that an additional contribution to the UE may come from multiple parton interactions (MPI, minimum-bias dijets not correlated with the triggered dijet).

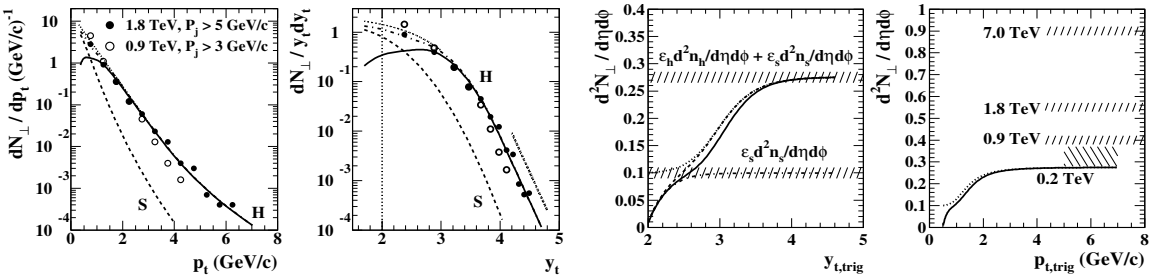

Figure 6.6-1. First: Transverse region (TR) multiplicity $N_\perp(p_t)$ spectrum on p_t. Second: $N_\perp$ spectrum on transverse rapidity y_t. Third: $N_\perp$ angular density vs trigger $y_{t,trig}$ for 200-GeV p-p collisions. Fourth: Comparison of $N_\perp$ vs trigger trends for four collision energies.

Fig. 6.6-1 (first) shows $N_\perp(p_t)$ spectra for 1.8-TeV (dots) and 0.9-TeV (open circles) p-p collisions. The 1.8-TeV data are extrapolated to $p_t = 0$ (dotted curve) to infer a total yield

2.5 times greater than that expected from the soft component ("beam-beam remnants"). The second panel shows the same data vs transverse rapidity y_t described by the two-component model (TCM, dash-dotted curve), the sum of soft (dashed) and hard (solid) components. The soft component is consistent with expected nucleon dissociation at 1.8 TeV. The hard component is consistent with minimum-bias (mini)jets in hard events (at least one jet). The increased yield is not a factor 2.5, only 30% of the total, and is consistent with the expected base of the triggered dijet extending across the TR, not excluded from the TR as assumed.

Fig. 6.6-1 (third) shows $N_\perp(y_{t,trig})$ vs increasing trigger condition, a simulation based on the measured TCM for 200-GeV p-p collisions. The lower hatched band shows the soft-component contribution. The increase above $y_t = 2.5$ ($p_t \approx 0.8$ GeV/c) is attributed to increasing MPI in *more-central* p-p collisions. However, the simulation reveals that the increase is actually due to increased dijet rate within events that are otherwise consistent with minimum-bias p-p (centrality not relevant). There is no significant MPI contribution to such events. The fourth panel compares the trend for 200 GeV with those measured at higher energies. A similar dependence on trigger condition is observed. The increase with collision energy may be due to increased dijet rates at higher energies resulting from expected deeper penetration in nucleon momentum fraction x and therefore more low-x gluon participants.

6.7 Jet angular correlations and the p-p underlying event

T. A. Trainor

The *underlying event* (UE) in p-p collisions is defined as those hadrons complementary to a triggered high-energy dijet. The composition of the UE is of considerable interest in the context of searches for physics beyond the Standard Model at the LHC. UE studies in combination with Monte Carlo representations of p-p collisions (e.g., PYTHIA) suggest that multiple parton interactions (MPI) make a substantial contribution to the UE. However, two issues emerge: (a) the triggered dijet is defined by algorithms (e.g., "jet cone") that assume 2D jets localized on angles (η, ϕ) (cone radius $R < 1$) and (b) p-p Monte Carlos assume a QCD parton-spectrum lower limit that conflicts with minimum-bias jet (minijet) measurements.

Fig. 6.7-1 (first) shows a parametrization of p_t-integral (minimum-bias or MB) 2D angular correlations from 200-GeV p-p collisions including a same-side (SS) 2D peak and away-side (AS) 1D peak on azimuth. Both peaks are broad on azimuth and overlap. The second panel shows a projection of the first panel onto azimuth illustrating the strong peak overlap. The hatched bands indicate the so-called *transverse region* (TR), *by assumption* excluding the triggered dijet, that is said to reflect the UE. But it is apparent that MB jets must make a substantial contribution to the TR. It can also be shown that all triggered dijets of any energy must include the same MB angular structure as a base. Thus, the *transverse multiplicity* $N_\perp$ integrated within the TR must include a substantial contribution from the triggered dijet.

Fig. 6.7-1 (third) shows MB 2D jet angular correlations for 200-GeV p-p collisions without correction for finite η acceptance (thus including only detected pairs) and corresponding

to "hard" p-p events (containing at least one jet). The fourth panel (lower curves) is a projection of the third panel onto 1D azimuth. The line labeled "soft" is the soft-component (projectile dissociation or "beam-beam remnant") contribution uniform on azimuth. The upper solid line approximates the measured $N_\perp$ for 1.8-TeV p-p collisions with soft (0.05) and hard (0.09) contributions. The inferred hard component of 1.8 TeV $N_\perp$ is consistent with MB jet correlations measured at 200 Gev. We conclude that the TR includes a substantial contribution from any triggered dijet, contrary to UE assumptions. The triggered-dijet contribution is misassigned to MPI production predicted by Monte Carlos that include a pQCD parton spectrum extending *too low in energy*, leading to MB dijet total cross sections *too large by a factor 10 or more.*

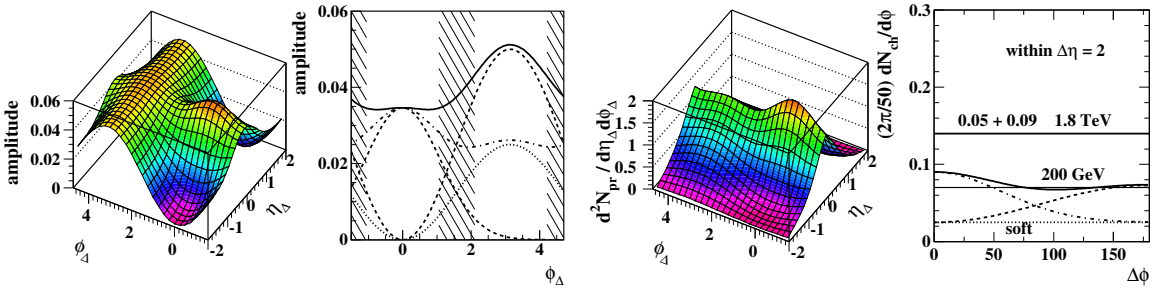

Figure 6.7-1. First: 2D model of jet-related p_t-integral angular correlations from non-single-diffractive 200-GeV p-p collisions. Second: Projection of 2D correlations onto 1D azimuth showing SS and AS contributions. Third: 2D angular correlations from hard events with no correction for finite η acceptance. Fourth: Projection of the third panel onto 1D azimuth compared with results inferred from 1.8-TeV p-p collisions (upper solid line).

6.8 n_{ch} dependence of trigger spectra from 200-GeV p-p collisions

D. Prindle and T. A. Trainor

A common way to study jet-related properties of particle production is to use correlations with respect to a trigger, either a high-p_t particle or a jet[1]. Both these choices introduce biases that are difficult to quantify. In the case of the high-p_t trigger the p_t cut affects a combination of jet energy and jet fragmentation. For the jet-triggered case the jet finder excludes or includes particles into the jet in a way that complicates the interpretation of the associated particles.

We have analyzed 12×10^6 minimum-bias-triggered proton-proton collisions recorded by STAR at RHIC. The beam was very clean so there was very little if any pileup and the trigger was efficient even at very low multiplicity. For our trigger-associated analysis we define the trigger as the highest-p_t particle in the event, allowing us to look at all trigger-associated combinations. In this article we examine the trigger spectra. Within the context of the two-component spectra model we have a precise statistical understanding of which triggers were due to the soft component and which were due to the hard component. This allows us to extract information about particles correlated with jet fragments as well as giving us

[1]T. Affolder *et al.*, Phys. Rev. D **65**, 092002 (2002).

a handle on the underlying event (those particles not associated with a jet) while imposing minimal biases on jet properties.

In Fig. 6.8-1 we show the trigger spectra and two-component prediction for several multiplicity bins. There are three components to the trigger spectra: the soft component from events without hard scattering, the soft component from events with hard scattering, and the hard component. Here we show the sum of the components as the solid line. Note that as the multiplicity increases the minimum trigger y_t also increases. This is partly due to having a higher fraction of events with a hard component but mostly due to the fact that as one samples more particles the highest y_t will increase on average. The two-component-spectra model gives an excellent description of the trigger spectra.

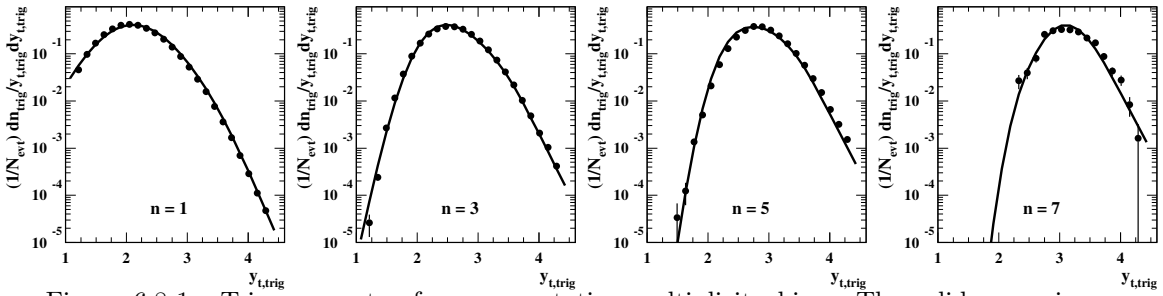

Figure 6.8-1. Trigger spectra for representative multiplicity bins. The solid curve is a prediction based on the two-component-spectra model.

6.9 Modeling 1D trigger spectra from 200-GeV p-p collisions

D. J. Prindle and T. A. Trainor

In the context of jet reconstruction a *trigger particle* is defined as the single hadron in each p-p collision event with the greatest p_t or y_t, denoted by trigger transverse rapidity $y_{t,trig}$ or y_{tt}, and is assumed to be a proxy for a parent parton. Given the previously-determined two-component model (TCM) for single particle (SP) spectra an expression can be derived for the trigger-particle spectrum corresponding to events in some multiplicity class n_{ch}. The expression is based on compound probabilities: a trigger particle is sampled from either a soft (no jets) or hard (at least one jet) event. From a given event the trigger is sampled from either the soft (either event type) or hard (hard events only) spectrum component. Soft and hard spectrum components denoted by $S_0(y_t)$ and $H_0(y_t)$ were derived from previous SP spectrum analysis. The unit-normal trigger spectrum is then described by

$$\begin{aligned}\frac{1}{N_{evt}(n_{ch})}\frac{dn_{trig}}{y_{tt}dy_{tt}} &= P_s(n_{ch})G_s(y_{tt},n_{ch})F_s(y_{tt}) + P_h(n_{ch})G_h(y_{tt},n_{ch})F_h(y_{tt},n_{ch}) \quad (1)\\ &= T_{ss}(y_{tt},n_{ch}) + T_{hs}(y_{tt},n_{ch}) + T_{hh}(y_{tt},n_{ch}).\end{aligned}$$

Soft and hard event probabilities are defined by $P_s(n_{ch}) = \exp[-n_j(n_{ch})]$ and $P_h = 1 - P_s$, where n_j is the pQCD predicted number of jets in angular acceptance $\Delta\eta$ given di-jet total cross section 2.5 mb. Spectrum models F_x are defined for soft and hard events with $F_s(y_{tt}) = S_0(y_{tt})$ and $F_h(y_{tt},n_{ch}) = p'_s(n_{ch})S_0(y_{tt}) + p'_h(n_{ch})H_0(y_{tt})$, and with p'_s the

probability of sampling from the soft component of a hard event. Factors $G_x(y_{tt}, n_{ch}) = G_{x0}(n_{ch}) \exp[-\kappa n_{x\Sigma}(y_{tt}, n_{ch})]$ are *void probabilities*, where $n_{x\Sigma}(y_{tt}, n_{ch})$ is the integrated multiplicity above y_{tt} within $\Delta\eta$ and κ is an $O(1)$ constant that accounts for non-Poisson correlations (*e.g.*, due to jets). By definition a sampled trigger particle at y_{tt} has no accompanying higher-y_t particles. Factors $G_{x0}(n_{ch})$ are defined by the requirement that products $G_x F_x$ must be unit normal, consistent with the unit-normal condition on the total trigger spectrum.

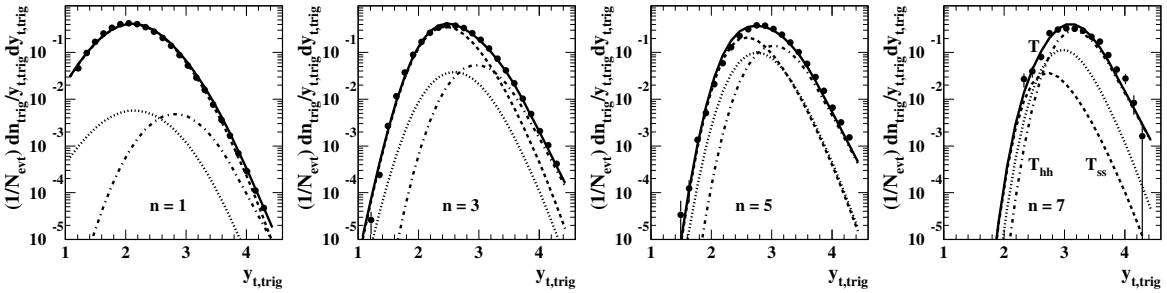

Figure 6.9-1. Unit-normal trigger-particle $y_{t,trig}$ spectra (points) for four multiplicity classes (1,3,5,7) from 200-GeV p-p collisions with two-component model functions (curves).

Fig. 6.9-1 shows measured trigger spectra (points) for four multiplicity classes (1,3,5,7) with $n_{ch}/\Delta\eta$ varying from 1.7 to 16. The solid curves are Eq. (1). The broken curves show the three terms in the equation for soft events (dashed) and soft (dotted) and hard (dash-dotted) components of hard events. For large event multiplicities almost all triggers come from hard components of hard events, that is, from minimum-bias jets or minijets. Parameter κ can modify the falloff at small $y_{t,trig}$. The value ranges from 1 at left to 1.3 at right. No other parameter was altered to accommodate the data. The solid curve is thus a TCM prediction.

6.10 n_{ch} dependence of trigger-associated distributions from 200-GeV p-p collisions

D. Prindle and T. A. Trainor

We have done an analysis of 12×10^6 proton-proton collisions taken during very clean beam time with an efficient minimum-bias trigger. In our trigger-associated study we have defined the trigger to be the highest y_t particle in the event. All other particles are called associated particles. We examine characteristics of the associated particles in this article.

It is common to divide the associated particles into three azimuthal regions: toward ($|\Delta\phi| \leq \pi/3$), transverse ($\pi/3 < |\Delta\phi| \leq 2\pi/3$) and away ($2\pi/3 < |\Delta\phi| \leq \pi$). The toward region is expected to be dominated by fragments from the jet which contributed the trigger particle. The away region is expected to be dominated by the back-to-back jet. We divide the away region in two to look for possible k_t effects. It is usually assumed that the transverse region is sensitive to particle production that is unrelated to the jets, the so-called underlying event.

In Fig. 6.10-1 we show the 2D trigger versus associated y_t spectra for the away region for low and high-multiplicity bins. The first and third panels are the raw spectra. For each

trigger particle (on the horizontal axis) all associated particles from the event are plotted on the vertical axis. A projection onto the vertical axis thus gives the associated spectrum, which is the overall spectrum excluding the one trigger particle per event. A projection onto the horizontal axis gives the trigger spectrum weighted by the event multiplicity. A first step toward isolating the hard component is to remove the influence of the trigger spectra. We divide the raw spectra by the trigger spectra to get panels two and four. By construction, in these histograms the integral over associated particles for a given trigger y_t is the event multiplicity. This is responsible for the increase in intensity for small trigger y_t noticeable in panel two. In the context of jets the trigger axis is related to the hard-scattered parton and the associated axis is related to the fragmentation of the hard-scattered parton. These histograms are still dominated by the soft component.

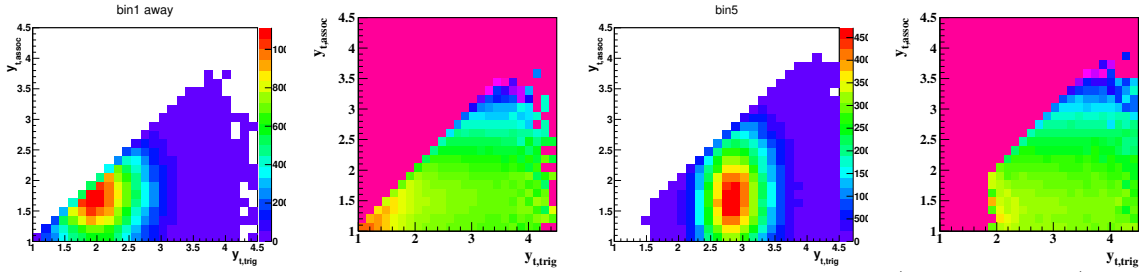

Figure 6.10-1. 2D trigger-associated spectra for a low multiplicity bin (left two panels) and a high multiplicity bin (right two panels). The first and third panels are the raw 2D trigger-associated histograms with the trigger y_t on the horizontal axis and the associated particle on the vertical axis. The second and fourth panels have the trigger spectra divided out.

6.11 Modeling 2D trigger-associated correlations from p-p collisions

D. J. Prindle and T. A. Trainor

Trigger-associated (TA) correlations can be employed to study minimum-bias jet structure in nuclear collisions. For each event with multiplicity n_{ch} the *trigger* particle (largest momentum) defines the trigger rapidity y_{tt}. The remaining $n_{ch} - 1$ *associated* particles form a spectrum on $y_{t,assoc}$ or y_{ta}. The integral over an ensemble of events within an n_{ch} class produces a 2D TA histogram. The two-component model (TCM) can be used to generate a TA model function. We extend the TCM to *conditional* associated spectrum components $F_x(y_{ta} : y_{tt})$ defined as TCM components $S_0(y_t)$ or $H_0(y_t)$ extending up to trigger condition y_{tt} but set to zero above that point. Combining the conditional associated spectra with corresponding soft and hard event types and trigger spectra we can define a 2D model for unit normal $F(y_{ta}, y_{tt}, n_{ch})$

$$\begin{aligned} F(y_{ta}, y_{tt}, n_{ch}) &= P_s(n_{ch})G_s(y_{tt}, n_{ch})F_s(y_{tt})F_s(y_{ta} : y_{tt}) \\ &+ P_h(n_{ch})G_h(y_{tt}, n_{ch})F_h(y_{tt}, n_{ch})F_h(y_{ta}, n_{ch} : y_{tt}) \\ &= T_s(y_{tt}, n_{ch})F_s(y_{ta} : y_{tt}) + T_h(y_{tt}, n_{ch})F_h(y_{ta}, n_{ch} : y_{tt}), \end{aligned} \quad (1)$$

where $F_s(y_{ta} : y_{tt}) = S_0''(y_{ta} : y_{tt})$ for soft and $F_h(y_{ta}, n_{ch} : y_{tt}) = p_s'(n_{ch})S_0'(y_{ta} : y_{tt}) + p_h'(n_{ch})H_0'(y_{ta} : y_{tt})$ for hard event types. The associated-particle number for a given n_{ch} class

is fixed at $n_{ch} - 1$. The total associated-particle number must then be $N_{evt}(n_{ch})(n_{ch} - 1)$. A sum over all events (triggers) must return the parent $F_x(y_t)$ to be consistent. Independent sampling from parent distribution $F_x(y_t)$ (for fixed sample number n_{ch}) must then satisfy

$$F_x(y_t) \quad = \quad \int dy_{tt} y_{tt} G(y_{tt}) F_x(y_{tt}) F_x(y_t : y_{tt}), \tag{2}$$

and each conditional probability $F_x(y_t : y_{tt})$ (associated particles) must be unit normal on y_t.

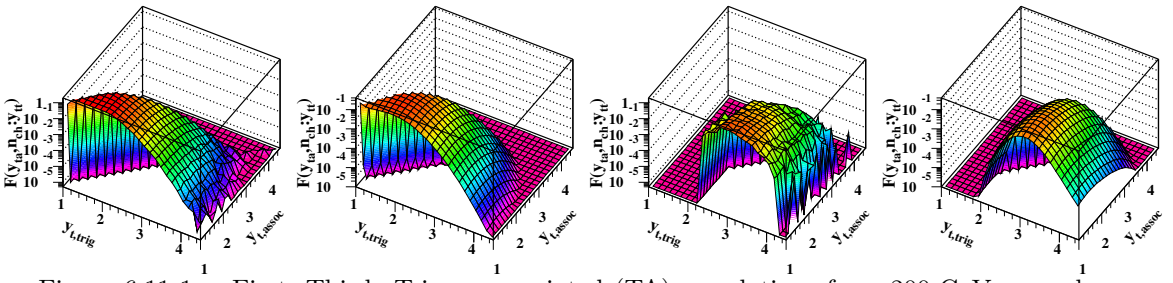

Figure 6.11-1. First, Third: Trigger-associated (TA) correlations from 200-GeV p-p collisions for multiplicity classes (1,7). Second, Fourth: Two-component models for the same data.

Fig. 6.11-1 shows TA data (panels 1,3) and 2D TCM model (panels 2,4) for multiplicity classes (1,7). The model provides an accurate description of the soft components from soft and hard events. The 2D TA hard component can then be isolated by subtraction of the soft-component model as for single-particle (SP) spectra. In general, the 2D-data hard component should deviate from the TCM model derived from 1D SP spectra. Such deviations provide further details of minimum-bias jet structure and are the principal object of TA analysis. The ratio F/T (TA histogram divided by trigger spectrum) can be compared directly with measured jet-fragmentation-function (FF) ensembles from e-e collisions (LEP and HERA).

6.12 Hard components from 2D trigger-associated correlations vs pQCD

D. J. Prindle and T. A. Trainor

Trigger-associated (TA) correlations from 200-GeV p-p collisions can be described by a two-component model (TCM). The 2D TCM is derived from a 1D TCM for single-particle p_t spectra. If the TCM soft-component model function is subtracted from TA histograms the result is a hard component representing hadrons from parton fragmentation to jets. By hypothesis the *trigger* hadron in each event is (with some probability) the proxy for a parent scattered parton. The remaining hard-component *associated* hadrons represent jet fragments.

Fig. 6.12-1 (first) shows the TA hard component for high-multiplicity 200-GeV p-p collisions wherein the probability that a trigger hadron represents a parent parton is large. The mode at trigger rapidity $y_{tt} \approx 3.1$ corresponds to $p_t \approx 2$ GeV/c. The second panel shows an ensemble of jet fragmentation functions (FFs) on y from LEP and HERA e-e collisions multiplied by a minimum-bias pQCD parton spectrum on y_{max} with a mode near 3 GeV

($y_{max} \approx 3.8$)[1]. The correspondence of the two data systems is notable. At lower parton energies the mean trigger momentum is 2/3 – 3/4 of the parent parton momentum, indicating the quantitative relation between the p-p TA hard component and pQCD jet systematics.

Fig. 6.12-1 (third) shows measured 2D TA correlations from p-p collisions with the TCM soft component subtracted, divided by the corresponding measured 1D trigger-particle spectrum. The fourth panel shows the ensemble of measured FFs for jets extending from parton energy 2 GeV ($y_{max} \approx 3.1$, CLEO data) to 100 GeV ($y_{max} \approx 8$, LEP II data) from the same cited reference. Again the correspondence is notable. Such comparisons between minimum-bias TA correlations from p-p collisions and measured jet phenomenology described by pQCD confirm the presence of minijets extending down to 2-3-GeV partons in high-energy nuclear collisions. The TA data reveal the kinematic limits of jet structure manifested as hadrons: trigger particles extend down to 0.8 GeV/c and associated particles (jet fragments) extend down to 0.35 GeV/c. Minijet structure appears to be *unmodified* in Au-Au collisions (A-A transparency) over the more-peripheral half of the total cross section and quantitatively modified but still consistent with pQCD in some aspects for more-central collisions.

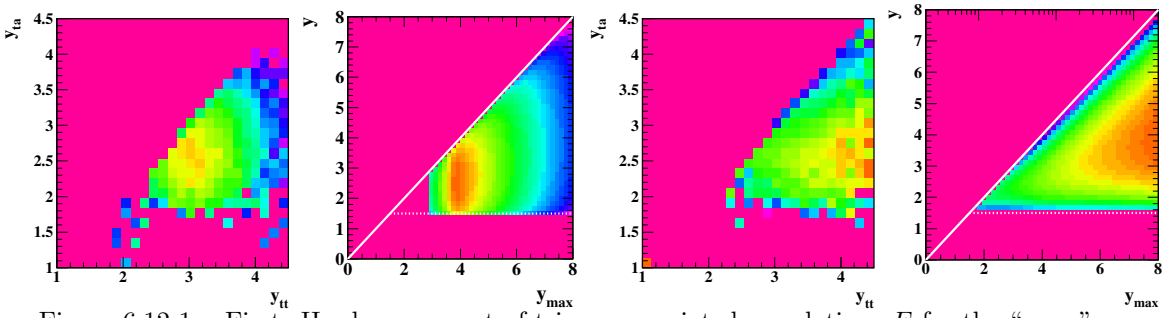

Figure 6.12-1. First: Hard component of trigger-associated correlations F for the "away" azimuth region. Second: FFs folded with pQCD parton spectrum. Third: F = TA correlations divided by T (1D trigger spectrum) from 200-GeV p-p collisions. Fourth: Conditional fragmentation functions (FFs) on y vs parton rapidity y_{max} from LEP-HERA e-e data.

6.13 The p-p underlying event and trigger-associated jet correlations

D. J. Prindle and T. A. Trainor

In a separate report we show that the hard component of p-p trigger-associated (TA) correlations can be isolated by subtracting a soft component of the TA two-component model (TCM). The hard component consists of fragments from minimum-bias scattered partons with trigger hadrons as their proxies. The trigger momenta are 2/3–3/4 of the parton momenta within the range covered by these data. We now consider the azimuthal dependence of associated-particle spectra relative to trigger-particle direction in the context of underlying-event (UE) studies.

Fig. 6.13-1 (first) shows several azimuth regions defined relative to the trigger-particle direction. Conventional UE analysis assumes that a high energy triggered dijet is confined to

[1] T. A. Trainor, Phys. Rev. C **80**, 044901 (2009).

the *toward* (T) and *away* (A) azimuth regions. The remaining *transverse region* (TR) should then provide access to the UE *complementary* to the triggered dijet. However, p_t-integral or minimum-bias jet (minijet) angular correlations reveal that a substantial fraction of the dijet must contribute to the TR, contradicting UE assumptions. We find that measured hard components of TA correlations provide further evidence to buttress that conclusion.

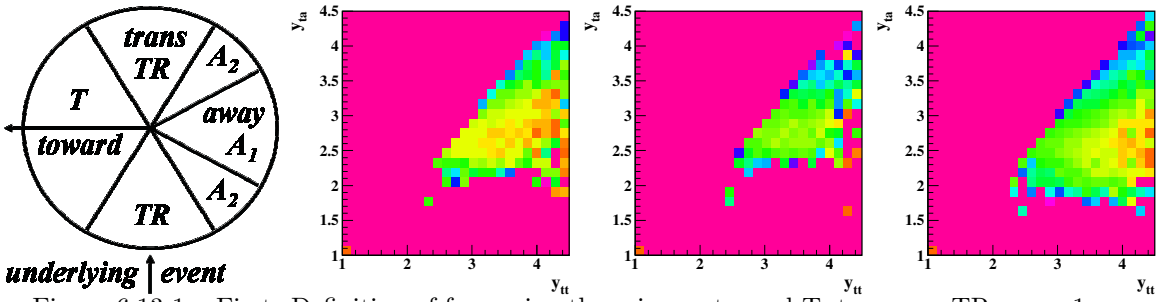

Figure 6.13-1. First: Definition of four azimuth regions – toward T, tranverse TR, away 1 A1, away 2 A2. Second: T hard component. Third: TR hard component. Fourth: A = A1 + A2 (away) hard component.

Fig. 6.13-1 (second, third, fourth) show hard components for the T, TR, and A azimuth regions respectively. Comparison of hard components for T and TR regions reveals that a substantial fragment contribution to the TR region correlated with the triggered dijet is present, contradicting the conventional UE analysis assumption of no such contribution. The p_t composition of the first two TA distributions is harder than that of the third. The T and TR regions are bounded at 0.8 GeV/c ($y_t \approx 2.3$) whereas A extends down to 0.35 GeV/c ($y_t \approx 1.8$). The yield in A is significantly larger than that in the T region, similar to spectrum evolution with centrality in Au-Au collisions where jet (fragmentation) modifications conserve total parton energy within jets but transport some of the energy from a few fragments at larger p_t to many more fragments at smaller p_t. However, in the p-p case the difference in momentum content of triggered and recoil jets may be due to the effect of an initial-state parton k_t that boosts one parton but retards the other, leading to an energy asymmetry in the lab frame. Subregions A_1 and A_2 are intended to explore the effects of k_t bias in more detail. The summed $\vec{k}_t$ should add vectorially to parton momentum *transfer* $\vec{Q}$. Added in the perpendicular direction it would favor dijet energy symmetry and acoplanar region A_2, whereas in the parallel direction it would favor energy asymmetry and coplanar region A_1.

7 Other research

7.1 Status of nonlocal quantum communication test

J. G. Cramer, B. Parris*, and D. B. Pengra

The question we have been investigating in this experiment is whether the intrinsic nonlocality of standard quantum mechanics is the private domain of Nature, as is generally assumed by the physics community, or whether in special circumstances the nonlocal connection between subsystems can be used to send signals from one observer to another. The basic scheme, as described in the references, is to use the which-way information implicit in momentum-entangled photon pairs to create a signal as the presence or absence of an interference pattern at the receiving end, depending on whether or not which-way information was extracted at the sending end of the experiment.

With the aid of generous private contributions and some use of CENPA resources, we have continued work on this test of nonlocal quantum communication, which has been reported in the past six years[1,2,3,4,5,6]. The Mark I configuration of the experiment, as described in the first two references, employed a high-power argon-ion laser operating at about 1 W in the ultraviolet at 351 nm, which pumped nonlinear crystals (BBO or $LiIO_3$) to produce pairs of momentum-entangled 702-nm photons, on which measurements were subsequently performed, mainly by attempting to detect an interference pattern with a cooled quantum-sensitive camera and later with avalanche photodiodes operated in the linear mode. It was concluded that the detectors used were too insensitive and that signal-to-noise limitations from fluorescence photons competing with the downconverted photons in the crystals prevented the planned measurements with the initial Mark I configuration.

The work was moved to the Optics Laboratory on the 2nd floor of the Physics-Astronomy Building, which offered the advantage that the experimental area could be darkened without interference with other experiments. A new Mark II experimental configuration, described in the 2011 CENPA Annual Report[5], used a periodically-poled potassium titanyl phosphate (ppKTP) crystal with a 10-μm poling length and dimensions 1 mm$\times$2 mm$\times$30 mm made by Raicol, Inc. The ppKTP crystal was maintained at 50° C in a precision crystal oven and optically pumped with a 405-nm Sacher Littow-type grating-stabilized diode laser. A system of avalanche photodiodes (APDs) operated in the Geiger mode was used to detect the single 810-nm photons. Problems with detector noise (spontaneous avalanches $\sim$ 10,000 counts/second) were encountered. We tried re-purposing an X-ray detector cryostat to cool an array of APDs with light fibers attached to temperatures as low as 77 K with liquid nitrogen, but we found

*Presently at the University of Oregon, Eugene, OR.

[1]CENPA Annual Report, University of Washington (2007) p. 52.
[2]CENPA Annual Report, University of Washington (2008) p. 42.
[3]CENPA Annual Report, University of Washington (2009) p. 41.
[4]CENPA Annual Report, University of Washington (2010) p. 93.
[5]CENPA Annual Report, University of Washington (2011) p. 94.
[6]CENPA Annual Report, University of Washington (2012) p. 89.

that the avalanche threshold voltage and detector noise level diminished together with temperature, so that the spontaneous avalanche counting rate remained relatively constant with temperature. We also investigated whether the noise problem could be reduced or eliminated by pulsing the pump laser. At best, pulsing gained perhaps a factor of 10 improvement in signal-to-noise, but this was insufficient to deal with the noise problem.

In early 2012 the Sacher grating-stabilized diode laser failed, partly as a result of operation in the pulsed mode. Repair by Sacher proved to be prohibitively expensive. It was replaced by a high-power Opnext HL40023MG blue-violet laser diode nominally rated for 400 mW at wavelength 405 nm. The Opnext laser unit was extensively tested using the Optics Laboratory's high-precision grating spectrograph. It was determined that the Opnext unit could produce in excess of 700 mW with good line shape at central wavelengths ranging from 402 nm to 408 nm, depending on the operating temperature of the diode. We found that operating the Opnext unit at around 60° C produced a good laser line at 405 nm as needed for the experiment. The implication of this work was that a superior source of entangled 810-nm photon pairs could be produced by pumping the ppKTP crystal with a temperature-stabilized Opnext HL40023MG laser diode. We did not, however, proceed to develop the needed temperature control at that time. Unfortunately, despite further work in 2012, no way was found to reduce the noise in the APDs to an acceptable level.

The Mark II version of the experiment has now been concluded without results. The two preliminary versions of the experiment have highlighted important problems, pointing to an improved Mark III experimental design now in development. We have learned the following lessons: (1) Avalanche photodiodes, even when cooled to as low as 77 K with liquid nitrogen, are simply too noisy to meet the single-photon detection requirements of the experiment and cannot be used for the needed non-coincident single photon counting; (2) the choice of a grating-stabilized laser in the Mark II design resulted in pump power levels that were too low for efficient production of entangled photon pairs and ultimately led to declining output and laser failure (the choice of a "bare" temperature stabilized single-mode laser diode would have been better); (3) the Mach-Zehnder interferometers used in the preliminary experiments are very difficult to align and maintain, and they accept too many optical modes, so that the interference patterns produced, instead of being an "on" bright spot or an "off" dark spot, is a "bulls-eye" interference patterns with a bright or dark center (single mode interferometer operation would have been better); and (4) at a pump wavelength of 405 nm and entangled photon pairs at 810 nm, the use of fiber optics and commercially available fiber-based devices is limited in the present experimental design because the operating wavelength is too far from the communications-industry-standard wavelengths of 1064, 1310 (O-Band), and 1550 nm (C-Band). Longer wavelength pump lasers and modified poling of the ppKTP crystal are needed.

With these lessons in mind, we are working on a Mark III version of the experiment that would use (1) cryogenic noise-free superconducting-transition detectors[1] to efficiently detect the photons of interest, (2) an entangled photon-pair source using a 1-W, 532-nm green diode pump laser to produce photon pairs at 1064 nm from a ppKTP nonlinear crystal with

[1]Daiji Fukuda *et al.*, Opt. Express **19** 870 (2011).

350-μm poling length, and (3) a fiber-based set of switched Mach-Zehnder interferometer units optimized for 1064 nm to replace the system of lenses, prisms, and mirrors used in the previous versions. We have been encouraged to prepare a pre-proposal aimed at seeking funding from a government agency to support construction and operation of the new Mark III version of the experiment.

7.2 Energy deposition and micro dosimetry in water for fast ions in radiation therapy

H. Bichsel

Studies of the interactions of fast heavy ions with water made in relation to cancer therapy have been published[1,2] in past annual reports. A detailed report was written and published[3] in the last year.

A description of the subject was presented at the CENPA Monday meeting on 9 January, 2012.

A study of similar methods for relativistic particles was also published[4] recently.

Both of these studies may be of interest in connection with the installation of two proton cyclotrons for radiation therapy in Seattle.

[1] CENPA Annual Report, University of Washington (2010) p. 98.

[2] CENPA Annual Report, University of Washington (2011) p. 91.

[3] "Stochastics of Energy Loss and Biological Effects of Heavy Ions in Radiation Therapy," Hans Bichsel, chapter 1 in *Theory of Heavy Ion Collision Physics in Hadron Therapy*, Advances in Quantum Chemistry, D. Belkic, ed., vol. 65, J. R. Sabin and E. Braendas, series eds., Elsevier (2013) and AP, ISBN: 978-0-12-396455-7, ISSN:0065-3276.

[4] "The interaction of radiation with matter," Hans Bichsel, chapter 2 in Landolt-Boernstein, vol. 21 *Elementary Particles, Nuclei and Atoms*, subvol. B, "Detectors for Particles and Radiation," C. W. Fabian and H. Schopper, eds., Springer (2011), ISBN: 978-3-642-03605-7, ISSN:1615-1844.

8 Education

8.1 Use of CENPA facilities in education and course work at UW

G. C. Harper

CENPA has always maintained a prominent role in broadscope, practical, hands-on training for both undergraduate and graduate students at the University of Washington. One of the most significant and unique advantages that our students enjoy is direct participation in the ongoing local research at CENPA and the engineering contributions to our off-site collaborations.

We have been increasing our presence in undergraduate and graduate education and since spring 2011 we have provided an accelerator-based laboratory course in nuclear physics. This began as an undergraduate special-topics course in physics, course number 499, and has evolved into Physics 576, Selected Topics in Experimental Physics (see Sec. 8.2). Another undergraduate classroom application of CENPA facilities included the use of one of our radioactive sources in a radiochemistry course this year and last (see Sec. 8.3) for activating materials to be used in laboratory experiments.

We continue to provide extensive hands-on training for both undergraduate and graduate students. Our electronics shop is available for use by the students (see Sec. 9.4) where they can learn electronic design and assembly. In the student shop (see Sec. 9.6) all users are trained in machine-tool operation and safety. Finally, CENPA has a long history of teaching students accelerator and ion-source operation (see Sec. 8.4).

8.2 Accelerator-based lab class in nuclear physics

A. García, G. C. Harper, E. B. Smith, and D. I. Will

We have developed a graduate-level lecture and laboratory class for the purpose of teaching aspects of nuclear theory and techniques for nuclear physics experiments, including student operation of the tandem accelerator system to achieve beam on an experimental target[1].

The class met twice a week during the winter 2013 quarter, once for a 1-1/2 hour lecture and again in groups for a 1-1/2 hour lab session. The list of subjects we covered were:

1. Atomic nucleus. Basics of nuclear physics, nuclear energy, orders of magnitude.
2. Attenuation of photon radiation. Solid-state detectors (Ge and Si).
3. Ranges of ions and electrons. The weak interaction. Radioactivity and radiation damage and health risks (α, β, γ, and neutron activity).
4. Deciphering a mystery γ spectrum. Gauging the level of radioactivity and assessing health risks.

[1] Phys 576, Nuclear Physics: Sources, Detectors, and Safety, http://faculty.washington.edu/agarcia3/phys576.

5. Tandem-accelerator function and ion optics. Tuning beam in CENPA accelerator.
6. Rutherford back-scattering. Deciphering a mystery spectrum and the contents of a mystery foil.
7. Fission and fusion. The functioning of reactors.
8. Nuclear astrophysics: nucleosynthesis in stars.
9. Sources of positrons for positron emission tomography.

Ninteen students attended the Winter of 2012 sessions. Students engaged enthusiastically in discussions during lectures and in laboratory sessions.

8.3 Radiochemistry and nuclear-chemistry education program in the UW Department of Chemistry

K. A. Krohn*, D. I. Will, and W. H. Zoller†

The tracer principle using radionuclides is critically important in disciplines ranging from basic chemical and biochemical mechanisms to human medicine, from atmospheric chemistry to geochemistry, and from materials science to cosmology. Several years ago the Howard Hughes Foundation funded nuclear-detection instrumentation for Chemistry 410, a lecture/laboratory course in Radiochemistry and Nuclear Chemistry taught each winter quarter and limited by equipment workstations to 16 students. In order to maintain a fresh course the curriculum is updated each year to reflect the application interests of students. The basic science of radiation detection and the safe handling of isotopes are covered in the first four sessions. The students are then taken to various working laboratories to gain hands-on experience in using radionuclides to answer important science questions.

One trip is to the Washington State Department of Health Laboratory for a practical experiment in counting long-lived α and β emitters. The exercise is done in the context of a realistic terrorism scenario where the students are presented with an unknown sample wipe test and asked to gauge the magnitude of the threat. A second trip is to the Applied Physics Laboratory to use X-ray fluorescence to analyze an unknown substance.

Protein labeling by radio-iodination is a common method for attaching an exogenous label to important biological molecules. This exercise provides practical experience in handling open sources of radionuclides and teaches the role surveys play in detecting radioactive contamination following the laboratory exercise. Chelation labeling is another approach for attaching a detectable signal to an interesting molecule. We do an experiment using ^{99m}Tc, which is commonly used for medical imaging.

While many radionuclides are commercially available, an even larger number need to be made on demand. The nuclear reactions for this purpose use neutrons or charged particles to induce nuclear reactions. The students gain experience with both methods. We use the

*Professor of Radiology & Radiation Oncology, Adjunct Professor of Chemistry, University of Washington, Seattle, WA.

†Emeritus Professor, Department of Chemistry, University of Washington, Seattle, WA.

UW Medical Center cyclotron to make $^{13}NH_3$ for imaging the heart muscle using positron emission tomography. The students learn basic aspects of cyclotron engineering and medical imaging instrumentation as well as radiochemical synthesis in a clean room so that the radiopharmaceutical product is safe for human injection. We also make radionuclides using neutrons. Because a reactor is not available at UW, we use the α-Be neutron source from CENPA for this purpose. The neutrons are thermalized by scattering through polyethylene and are used to irradiate different pure elements for neutron-activation analysis and then to identify the composition of an unknown alloy.

8.4 Student training

G. C. Harper, D. R. Hyde, D. A. Peterson, E. B. Smith, and D. I. Will

Students at CENPA receive training in a variety of technical laboratory skills that include accelerator operation, machining, and electronics. During accelerator crew training students are taught to operate the ion sources and the tandem Van de Graaff accelerator. These students practice generating an ion beam, charging the tandem, and tuning the beam through the accelerator. Frequently, these individuals also gain experience with vacuum systems and cryogenics as dictated by the needs of their experiment.

CENPA student shop training was received by more than 14 individuals (including staff, RAs, REU students, and undergraduate hourlies) this year, many of whom completed our training course. These students have learned to safely operate a variety of machines including lathes, milling machines, drill presses, saws, grinders, metal shears and breaker, hand tools, and power tools. Several students were trained to use an oxygen/acetylene cutting torch. Additionally, students have been trained on the student shop NC 2-Axis Trak milling machine in order to make complicated parts for their research projects.

In the electronics shop, instruction in soldering, wiring, and the use of basic electrical and electronic components was given to at least four students.

9 Facilities

9.1 Facilities overview

G. C. Harper

CENPA constantly updates and improves its facilities and provides the best possible resources and research environment for its users as new experiments emerge and as the demands of research change with time. In addition we maintain high-quality shop services that are available to the faculty, staff, and students.

The computational facilities at CENPA remain at the front edge of technology. As always, personal desktop and portable computers are maintained and the technology kept current. The NPL Data Center (NPLDC) which previously contained a single high performance cluster, ATHENA, now provides the infrastructure to multiple clusters and department appliances (see Sec. 9.3).

The FN tandem Van de Graaff accelerator lab constantly evolves. The accelerator lab is a hands-on training facility for students. The students are trained to operate the accelerator and ion sources. A physics laboratory course using the accelerator to perform nuclear-physics experiments has also been developed (see Sec. 8.2). The accelerator can be quickly switched between two different operational modes to provide a wide energy range with high beam intensity (see Sec. 9.2).

The CENPA electronics shop provides modern surface-mount technology and miniature cable-manufacturing equipment on site and in appropriately clean areas. The shop continues to do custom design work for specialty preamps as well as dedicated multichannel data-aquisition (DAQ) systems. The shop also interacts with the on-campus Washington Technology Center, taking advantage of much of the capital-intensive, high-tech equipment there that is more effectively used as a cost-shared facility. The electronics-shop staff also provides training for students and other staff members (see Sec. 9.4).

The CENPA instrument shop and student shop provide a unique climate for a research facility. The student shop is headed by an instrument maker who provides safety training and instruction to students, staff, and faculty. Our main instrument shop is manned by two highly skilled instrument makers with decades of experience working in the university and research environments (see Sec. 9.6). Recently one of our graduate students, Matt Turner, received funding for two proposals submitted to the Student Technology Fee Committee at UW. These proposals were for a laser cutter and a 3D printer (see Sec. 9.5). The laser cutter is currently installed in our high bay area and is operational.

Laboratory space is reallocated as needed, as new large experiments are initiated at or move to CENPA. The entire east end of the accelerator tunnel, continues to be modified to house the ADMX experiment. New lab space has been opened up to provide testing facilities for the development of experiments and detectors for the muon and neutrino programs (see Sec. 9.7).

9.2 Van de Graaff accelerator and ion source operations and development

Z. T. Alexander, N. M. Boyd*, T. M. Cope†, G. C. Harper, T. G. MacDonald‡, D. A. Peterson, E. B. Smith, T. D. Van Wechel, and D. I. Will

The tandem was entered only one time this year. On 22 June, 2012, the tank was opened after observing instability in the terminal voltage at 8.8 MV, indicative of a possible column resistor failure or disconnection. Inspection upon entering the tank revealed that one resistor shorting wire needed reseating and another such wire had fallen off requiring re-connection. These occurred in the tube 2 section of the tandem. Additional leak checking revealed a leak in the "T" (top) high-voltage (HV) feedthrough of the terminal electrostatic-steerer-feedthrough flange. Vacuum sealant (K. J. Lesker Co.) applied to the ceramic-metal seal of the HV feedthrough stopped the leak.

ACTIVITY SCHEDULED	**DAYS SCHEDULED**	**PERCENT of TIME**
Ion implantation, deck ion sources	13	4
Nuclear-physics research, accelerator	25	7
Subtotal, ion implant or nuclear-physics research	38	11
Development, maintenance, or crew training	81	22
Grand total	119	33

Table 9.2-1. Tandem Accelerator Operations 1 April, 2012, to 31 March, 2013.

During the 12 months from 1 April, 2012, to 31 March, 2013, the tandem pellet chains operated 233 hours, the sputter-ion source (SpIS) operated 0 hours, and the direct-extraction-ion source (DEIS) operated 461 hours. Additional statistics of accelerator operations are given in Table 9.2-1.

Ion beams produced using the DEIS this year included 17.0–17.8-MeV ^{2}H for the ^{6}He experiment, 1.0-MeV ^{1}H for the Physics 576 class, 56-MeV ^{16}O for crew training, and ^{36}Ar for an implantation required for research performed by the fundamental-symmetries group.

9.3 Laboratory computer systems

G. T. Holman

CENPA is a mixed shop of Windows 7, XP, Mac OS X and various Linux distributions. Windows 7 is installed on new systems but we are still running Windows XP for data-acquisition systems. In previous years the IT focus was directed toward server consolidation,

*Departed August, 2012, presently at University of Pittsburgh, Pittsburgh, PA.
†Departed March, 2013.
‡Departed February, 2013, presently at Astronics, Kirkland, WA.

network security, process documentation and removal of redundant processes. We continue to utilize Xen virtualization to drive most web pages, Elogs, wiki, calendar, tracking, and document servers. The CENPA website and research group web pages are run on a virtual Debian server and utilize the Drupal web framework. The NPL mail server still provides NPL presence but all email is relayed to UW email hardware as this allows users direct management.

Two Dell 510 20-TB servers (Lisa and Marie) offer user storage, print server capability, and improved backup policy. Linux, Windows and Mac workstations are now backed up to the Lisa 20-TB raid farm from which they are written to LTO tape by the Physics Computer Center on a three-month backup retention plan. Lisa runs the Crash Plan Pro backup application which supports Linux, Mac, Windows, and Solaris operating systems and provides differential and encrypted backups. Whereas workstations rely on Crash Plan Pro for backups, all servers use rsync and rsnapshot. Marie provides 20 TB for research, user, and shared group data.

The NPL Data Center (NPLDC) provides critical infrastructure supporting high-performance scientific-computing applications that cannot be efficiently executed on typical commodity server infrastructures (e.g., the Amazon EC2 Cloud). NPLDC space is shared by Physics, the Institute for Nuclear Theory (INT), CENPA, and the Astronomy departments. In previous years the space housed a single cluster that was treated as one computational resource, also known as Athena. The data requirements in the NPLDC have also rapidly grown. Approximately one third of the rack space is dedicated to non-cluster hardware: NFS scratch storage, SQL, MySQL, and backup servers. These servers constitute over 200 TB of raw disk space. The computational clusters instances continue to use 23.7 TB of SAN storage on a HP/Polyserve NFS Cluster. This is an order-of-magnitude increase in specialized, low-cost storage for both cluster and desktop scientific computing.

Today, to meet the wide and highly specialized array of research requirements, the cluster has been separated into specific instances. The computational hardware infrastructure supports six different instances of the cluster: three cluster instances that leverage Infiniband interconnects (classified as HPC clusters) and three clusters that primarily run single-threaded applications (non-HPC clusters.) The HPC clusters primarily use Torque/Maui via the three clusters' dedicated front ends.

This year we made the initial hardware purchase for the accelerator controller upgrade. The purchase included a Dell T3600 computer, Measurement computing analog and digital boards, and relay racks and solid state relays. This controller upgrade phase will replace the high-energy vaccuum satellite control segment.

Our computing and analysis facility consists of:

- The NPL data center as a shared resource with Physics, the Institute for Nuclear Theory (INT), and the Astronomy department.
- A mix of Linux servers: Debian, Redhat, and Ubuntu distributions.
- One VMS/VAXstation and two VMS Alphas for legacy computing.

- Macintosh systems for the SNO+, KATRIN, MAJORANA, and emiT groups.
- A VAXstation for the linac and vacuum systems control and display system.
- Various Windows XP desktop JAM systems (Java-based software for acquisition and analysis), plus two laptops for transport to other installations.
- A Shorewall Linux-based logical firewall to protect the bulk of CENPA's PCs and servers.
- We provide additional legacy co-location services for the INT and the Physics Nuclear Theory group in the form of one VMS Alphastation 500, which is not directly used by lab personnel.

9.4 Electronic equipment

D. A. Peterson and T. D. Van Wechel

The electronics shop is responsible for the design and construction of new laboratory electronic equipment, as well as the maintenance and repair of existing CENPA electronics. Projects undertaken by the electronics shop in the past year included the following:

1. Continued MAJORANA preamplifier development. Designed and built a new split front-end with the JFET and feedback components located at the detector with the remaining gain stage of the the front-end located remotely outside of the cryostat at the post amplifier.

2. Made signal paddle connectors (Au on quartz) at the UW micro fabrication facility (MFF) for the MAJORANA DEMONSTRATOR.

3. Fabricated test input capacitors with Ti, Cr, NiCr substrates on fused silica at MFF for the MAJORANA preamplifier.

4. Set up system for Picocoax® high voltage cable microdischarge testing for MAJORANA.

5. Built a UV light-emitting diode (LED) source illumination device for KATRIN focal-plane-detector calibration.

6. Built preamplifier boards for the MuSun experiment.

7. Designed and built four versions of Nanopore preamplifier boards with a single channel to 32 channels.

8. Constructed two preamplifier boards with fiber optic output senders for the KATRIN Tritium Recoil Ion Mass Spectrometer.

9. Built a duplexor for the $g-2$ pulsed nuclear magnetic resonance (NMR) system.

10. Designed and built several readout boards for the evaluation of silicon photomultipliers for the $g-2$ experiment.

11. Designed a voltage-controlled oscillator (VCO) ramp generator board for Project 8.

12. Built a shaper board for use with the Star preamplifers used by the ^{6}He experiment.

9.5 New computer-controlled fabrication tools for student use

T. G. MacDonald*, M. D. Turner, and D. I. Will

We have acquired a CNC laser-cutter system and a large-volume 3D printer for student use at CENPA. This equipment was funded by the the UW Student Technology Fee (STF), which is used to fund on-campus technology for student use. The STF has previously funded the purchase of a lathe and CNC mill for the student shop.

We became interested in acquiring a laser cutter due to previous outsourced laser-cut work for the Eöt-Wash group. Laser cutting is inherently contact-free, and so can be used to avoid the introduction of impurities or for cutting delicate materials, among other uses. The laser cutter is a $200,000 Kern HSE100 system, with a 400-W Coherent CO_2 laser, 4-ft by 8-ft bed, metal-cutting option, and a rotary stage.

The laser cutter was delivered in October, 2012. We have installed it in the high-bay area near the student shop. Installation included running two new vent lines, installing a 100-A outlet, and constructing a curtain enclosure. The system became operational in January, 2013. A training protocol has been established and the system has already been used for a number of different projects.

We are awaiting delivery of our 3D printer, expected around press time. Its build volume is roughly a 300-mm cube, and it is able to print objects using thermoplastics such as ABS, PLA, nylon, polycarbonate, and PEEK. We expect it to be used for rapid prototyping, fabrication of non-critical parts, and production of parts using low-background plastics.

9.6 CENPA instrument shops

J. H. Elms, G. C. Harper, D. R. Hyde, and H. Simons

The CENPA main instrument shop completed several large projects this year.

1. Five cryostats for testing single-crystal strings for the MAJORANA experiment. These consisted of several oxygen-free high-conductivity (OFHC) copper parts and required CNC lathe machining (see Sec. 1.16)
2. Large cavity compression ring (15 3/4" dia.), cavity supports, helium mother dewar, various electronic panels, massive cryo-cooler braid (15 braids in one bundle), and various baffles for the main ADMX cryostat (see Sec. 5.1).

*Departed February, 2013, presently at Astronics, Kirkland, WA.

3. Foil stretcher, screen mount, auto-collimator quarter-wave-plate holder, new high-precision bearing holder, quarter-inch-diameter collet-type quartz fiber holder for the gravity experiments (see Sec. 2.1).
4. Large conflat with 16 feedthroughs of various sizes, additional matching parts and hardware, lithium cup and heater block for the ^{6}He experiment (see Sec. 3.5).
5. Complete new high vacuum chamber assembly for the KATRIN heat pipe (see Sec. 1.6).
6. Various light pipes, clamps and adapter rings, macor parts and assemblies for new pad planes, and gas tube assembly without the heat exchanger for MuSun (see Sec. 4.3).

The student shop produced several small projects in addition to providing machine-tool training and safety training for the faculty, staff, and students.

1. A small-scale, crystal-detector and photomultiplier-tube box for testing a variety of detector arrays for the muon group's $g-2$ experiment (see Sec. 4.8).
2. Small parts for the NCDs used in the HALO project (see Sec. 1.21).
3. Cryostat pit installation components for ADMX (see Sec. 5.1).
4. Various parts for torsion-balance experiments (see Sec. 2.1).
5. An aluminum vacuum mounting plate for the UCNA experiment (see Sec. 2.18).
6. A high-voltage power-supply enclosure for ^{6}He (see Sec. 3.8).
7. A stainless-steel feedthrough flange for the MuSun time-projection chamber (TPC) project (see Sec. 4.3).

9.7 Building upgrades

N. M. Boyd* and D. I. Will

Numerous building deferred maintenance items, alterations and upgrades were completed this year. Much of this work was funded by University of Washington (UW) research building maintenance and upgrade funds. Power and cooling water were run for relocated magnets and their power supplies repurposed for NMR testing. Electrical power was run and vent holes were cored and vent ducts were installed for a new laser cutter bought with student technology funding (see Sec. 9.5). UW campus 13.8-kV upgrades at the North Physics Lab (NPL) included the following: dual, switchable feeder trunks to replace a single lead-encased trunk, new 13.8-kV switches and fusing, and a new 13.8-kV-to-480-VAC, 750-kVA step-down transformer, plus replacement of numerous asbestos-bearing items. UW steam-usage-monitoring telemetry was installed. A new 1200-A, 480-VAC electrical panel was installed for the Axion Dark Matter eXperiment (ADMX) (see Sec. 5.1). Several rooms have been carpeted and repainted. A persistently noisy air handler has been properly repaired and quieted. The UW emergency alert annunciator system has been installed in the Van de Graaff Accelerator and the Cyclotron Buildings. Two hundred feet of storm water and sanitary sewer lines have been run under our N-12 parking lot and east service drive so storm

*Departed August, 2012. Presently at University of Pittsburgh, Pittsburgh, PA.

runoff from the CENPA Instrument Shop and one exterior Cyclotron Building drain could be diverted out of the sanitary sewer system. The diversion of storm water from the Shop is complete. Support posts have been installed for portions of the tunnel pit ceiling altered during installation of the ADMX magnet cryostat. Our old chiller and open condenser-loop cooling tower were replaced with a new variable-frequency-drive chiller and a new cooling tower with closed condenser loop and much of the system piping was replaced or upgraded. Conduits and utility boxes were installed for various UW campus communications: fibers, phone, Ethernet, facilities net and wifi.

Several maintenance, alterations and upgrades have begun. A Linde 1410 helium liquefier, its compressor and its chiller were delivered and are being installed. Two concrete foundation pads were poured for a shed for ADMX pumps and for the ADMX chiller. Installation of helium boiloff gas recovery compressors is in progress. Installation of UW campus wifi has begun. This will replace local NPL wifi.

Planning is well underway for a complete reroof of the more than 50% of the North Physics Lab exposed roof system which was not replaced in the past two decades. This replacement will bring roofer safety and building roof insulation up to current codes. Copper flashing (which is rapidly being stolen) will be replaced by stainless steel. Better building security is also in the plan. A feasibility study for excavating and resealing underground portions of the Cyclotron Building is in progress. This feasibility study will at the very least result in a construction plan sufficiently detailed for accurate pricing. This work is being done with University of Washington funds for research building repair and maintenance. Money for the actual work will be requested by UW facilities engineering in the next biennial budget.

10 CENPA Personnel

10.1 Faculty

Eric G. Adelberger[1]	Professor Emeritus
Hans Bichsel[1]	Affiliate Professor
John G. Cramer[1]	Professor Emeritus
Jason Detwiler[2]	Assistant Professor
Peter J. Doe	Research Professor
Sanshiro Enomoto	Research Assistant Professor; CENPA Fellow
Frank Fleischer[1]	Research Assistant Professor
Alejandro García	Professor
Jens H. Gundlach[1]	Professor
Blayne R. Heckel[1]	Professor; Chair
David W. Hertzog	Professor
C. D. Hoyle[1,3]	Affiliate Assistant Professor
Peter Kammel	Research Professor
Michael L. Miller[1,4]	Affiliate Research Assistant Professor
R. G. Hamish Robertson	Professor; Director
Leslie J Rosenberg[1]	Professor
Gray Rybka[1,5]	Research Assistant Professor
Stephan Schlamminger[1,6]	Research Assistant Professor
Kurt A. Snover[1]	Research Professor Emeritus
Derek W. Storm[1]	Research Professor Emeritus
Nikolai R. Tolich	Assistant Professor
Thomas A. Trainor	Research Professor
Robert Vandenbosch[1]	Professor Emeritus
William G. Weitkamp[1]	Research Professor Emeritus
John F. Wilkerson[1,7]	Affiliate Professor
Tianchi Zhao	Research Associate Professor

10.2 CENPA External Advisory Committee

Baha Balantekin	University of Wisconsin
Stuart Freedman[8]	UC Berkeley and Lawrence Berkeley National Laboratory
Wick Haxton	UC Berkeley and Lawrence Berkeley National Laboratory
William Zajc	Columbia University

[1] Not supported by DOE CENPA grant.
[2] Arrived September, 2012.
[3] Affiliated faculty, Humboldt State University, Arcata, CA.
[4] Affiliated faculty, currently at Cloudant, Inc.
[5] Research faculty effective May, 2012.
[6] On leave to N.I.S.T., November, 2010.
[7] Affiliated faculty, University of North Carolina, Chapel Hill, NC.
[8] Deceased, November 10, 2012.

10.3 Postdoctoral Research Associates

L. Peter Alonzi[1]
Jarek Kaspar
Brendan Kiburg[2]
Andreas Knecht[3]
Diana Parno
Hok Wan Chan Tseung[4]
Krishna Venkateswara[5]
Andrew Wagner[5]
Frederik Wauters
Peter Winter[6]

10.4 Predoctoral Research Associates

Yelena Bagdasarova
Laura Bodine
Christian Boutan[5]
Ted Cook[5]
Jason Crnkovic[5,7]
Nathan Froemming
Brent Graner
Julieta Gruszko[5,8]
Charles Hagedorn[5]
Ran Hong
Michael Hotz[5]
David Kettler
Luke Kippenbrock[9]
Sara Knaack[5,10]
Jared Kofron
John G. Lee[1]
Jonathan Leon
Dmitry Lyapustin[5]
Timothy Major
Eric Martin
Michael Murray
Rachel Ryan[1]
Alexis Schubert[11]
Matthias Smith[1]
William Terrano[5]
Matthew Turner[5]
Todd Wagner[5]
Brandon Wall[12]
David Zumwalt[5]

10.5 NSF Research Experience for Undergraduates participants

Jarrett Moon	New Mexico State University
Rachel Osofsky	Carleton College
Scott Yantek	Stanford University

[1] Arrived June, 2012.
[2] Departed July, 2012, currently at Fermi National Accelerator Laboratory.
[3] Departed July, 2012, currently at Paul Scherrer Institut, Villigen PSI, Switzerland.
[4] Departed July, 2012, currently at the Mayo Clinic.
[5] Not supported by DOE CENPA grant.
[6] Departed July, 2012, currently at Argonne National Laboratory.
[7] Graduated December, 2012
[8] Arrived January, 2013.
[9] Arrived December, 2012.
[10] Graduated July, 2012, currently at the Wisconsin Institute for Discovery.
[11] Graduated December, 2012, currently at Stanford University, Stanford, CA.
[12] Graduated March, 2013.

10.6 University of Washington graduates taking research credit

Niklas Mueller	Nikolai Tolich, Advisor

10.7 University of Washington undergraduates taking research credit

Shawn Apodaca	Nikolai Tolich, Advisor
Trevor Arp	Jens Gundlach, Advisor
Jennie Chen	Blayne Heckel, Advisor
Tyler Cope[1]	Alejandro García, Advisor
Patrick Godwin	Nikolai Tolich, Advisor
Holly Hess	Eric Adelberger, Advisor
Richard Hong[2]	Nikolai Tolich, Advisor
Eric Lee-Wong	Blayne Heckel, Advisor
Troy MacDonald[3]	Alejandro García, Advisor
Stephen Plachta	Jens Gundlach, Advisor
Wei Quan	Nikolai Tolich, Advisor
Richard Seng[4]	Nikolai Tolich, Advisor
Devin Short[5]	Alejandro García, Advisor
Thomas Wolowiec	Leslie Rosenberg, Advisor
Alexandra "Sasha" Zhdanova	Charlie Hagedorn, Advisor

10.8 Professional staff

John F. Amsbaugh	Research Engineer	KATRIN vacuum systems
Nora M. Boyd[6]	Research Engineer	ADMX installation, accelerator
Tom H. Burritt	Research Engineer	Design of KATRIN detector system
Gregory C. Harper	Associate Director	Accelerator, ion sources
Gary T. Holman	Systems Manager	Computer systems
Duncan J. Prindle, Ph.D.	Research Scientist	Heavy ion research
Hendrik Simons	Instrument Maker	Shop supervisor
Eric B. Smith[7]	Research Engineer	Accelerator, ion sources
H. Erik Swanson, Ph.D.	Research Physicist	Precision experimental equipment
Timothy D. Van Wechel	Research Engineer	Analog and digital electronics design
Douglas I. Will	Senior Engineer	Cryogenics, ion sources, buildings

[1] Departed March, 2013.
[2] Arrived September, 2012, departed December, 2012.
[3] Graduated and departed February, 2013, currently at Astronics, Kirkland, WA.
[4] Arrived January, 2013, departed March, 2013.
[5] Graduated and departed September, 2012.
[6] Departed August, 2012, currently at the University of Pittsburgh.
[7] Arrived October, 2012.

10.9 Technical staff

James H. Elms	Instrument Maker
Ian Guinn[1]	Research Technologist
David R. Hyde	Instrument Maker
David A. Peterson	Electronics Technician

10.10 Administrative staff

Victoria A. Clarkson	Administrator
Robert S. Shupe	Fiscal Specialist 2

10.11 Part-time staff and student helpers

Zachery Alexander
Trevor Arp
Tyler Cope[2]
Rachel LeFree[3]
William Livingston[4]
Brynn MacCoy[5]
Sean MacDonald[6]
Troy MacDonald[7]
Elizabeth McBride[8]
Nick McMillan[9]
Ronaldo Ortez[10]
Joben Pedersen[6]
Stephen Plachta
Clifford Plesha
Peter Senchyna[9]
Devin Short[5]
Arielle Steger[11]
Aaron Stoll
David Tarazona Gonzalez[12]
Kazimir Wall[13]
Skylar Wheaton[13]

[1] Arrived July, 2012, departed September, 2012.
[2] Departed March, 2013.
[3] Departed July, 2012.
[4] Arrived June 2012, departed August, 2012.
[5] Graduated and departed September, 2012.
[6] Arrived January, 2013.
[7] Graduated and departed February, 2013, currently at Astronics, Kirkland, WA.
[8] Graduated June, 2012.
[9] Arrived July, 2012.
[10] Arrived September, 2012.
[11] Graduated and departed December, 2012.
[12] Arrived August, 2012.
[13] Arrived June, 2012.

11 Publications

Publications and presentations with a date of 2012 or 2013 are included below. Some entries from early 2012 may therefore also appear in the 2012 Annual Report.

11.1 Published papers

1. "Precision Measurement of the ^{6}He Half-Life and the Weak Axial Current in Nuclei," A. Knecht*****, R. Hong, D. W. Zumwalt, B. G. Delbridge, A. García*****, P. Müller, H. E. Swanson, I. S. Towner, S. Utsuno, W. Williams, and C. Wrede, Phys. Rev. Lett. **108**, 122502 (2012).†

2. "Search for a T-odd, P-even triple correlation in neutron decay," T. E. Chupp, R. L. Cooper, K. P. Coulter, S. J. Freedman, B. K. Fujikawa, A. García*****, G. L. Jones, H. P. Mumm, J. S. Nico, A. K. Thompson, C. A. Trull, F. E. Wietfeldt, and J. F. Wilkerson, Phys. Rev. C **86**, 035505 (2012).†

3. "Precision Measurement of the ^{6}He Half-Life and the Weak Axial Current in Nuclei," A. Knecht*****, R. Hong, D. W. Zumwalt, B. G. Delbridge, A. García*****, P. Müller, H. E. Swanson, I. S. Towner, S. Utsuno, W. Williams, and C. Wrede, Phys. Rev. C **86**, 035506 (2012).†

4. "Measurement of the neutron β-asymmetry parameter A_0 with ultracold neutrons," B. Plaster, R. Rios, H. O. Back, T. J. Bowles, L. J. Broussard, R. Carr, S. Clayton, S. Currie, B. W. Filippone, A. García, P. Geltenbort, K. P. Hickerson, J. Hoagland, S. Hoedl, G.E. Hogan, B. Hona, A. T. Holley, T. M. Ito, C.-Y. Liu, J. Liu, M. Makela, R. R. Mammei, J. Martin, D. Melconian, M. P. Mendenhall, C. L. Morris, R. Mortensen, R. W. Pattie, Jr., M. L. Pitt, J. C. Ramsey, R. Russell, A. Saunders, R. Schmid, S. J. Seestrom, S. Sjue, W. E. Sondheim, E. Tatar, B. Tipton, R. B. Vogelaar, B. VornDick, C. Wrede, Y. P. Xu, H. Yan, A. R. Young and J. Yuan, Phys. Rev. C **86**, 055501 (2012).†

5. "Performance of the Los Alamos National Laboratory spallation-driven solid-deuterium ultra-cold neutron source," A. Saunders, M. Makela, Y. Bagdasarova, H. O. Back, J. Boissevain, L. J. Broussard, T. J. Bowles, R. Carr, S. A. Currie, B. Filippone, A. García, P. Geltenbort, K. P. Hickerson, R. E. Hill, J. Hoagland, S. Hoedl, A. T. Holley, G. Hogan, T. M. Ito, Steve Lamoreaux, Chen-Yu Liu, R. R. Mammei, J. Martin, D. Melconian, M. P. Mendenhall, C. L. Morris, R. N. Mortensen, R. W. Pattie, M. Pitt, B. Plaster, J. Ramsey, R. Rios, A. Sallaska, S. J. Seestrom, E. I. Sharapov, S. Sjue, W. E. Sondheim, W. Teasdale, A. R. Young, B. VornDick, R. B. Vogelaar, Z. Wang, Yanping Xu, Rev. Sci. Instrum. **84**, 013304 (2013).†

An ***** denotes the CENPA lead author of a publication.

A † denotes a publication describing work fully or partially supported by the DOE grant.

6. "Electron capture on ^{116}In and implications for nuclear structure related to double-beta decay," C. Wrede*, S. K. L. Sjue, A. García*, H. E. Swanson, I. Ahmad, A. Algora, V.-V. Elomaa, T. Eronen, J. Hakala, A. Jokinen, V. S. Kolhinen, I. D. Moore, H. Penttilä, M. Reponen, J. Rissanen, A. Saastamoinen, J. Äystö, Phys. Rev. C **87**, 031303 (2013).†

7. "Decay studies for neutrino physics: Electron capture decays of ^{100}Tc and ^{116}In," A. García*, S. Sjue, H. E. Swanson, C. Wrede, D. Melconian, A. Algora and I. Ahmad, Hyperfine Interact. (2012). (DOI 10.1007/s10751-012-0619-2.)†

8. "Search for time-reversal symmetry breaking in neutron beta decay," A. García*, T. E. Chupp, R. L. Cooper, K. P. Coulter, S. J. Freedman, B. K. Fujikawa, G. L. Jones, H. P. Mumm, J. S. Nico, A. K. Thompson, C. A. Trull, F. E. Wietfeldt, and J. F. Wilkerson, Proceedings of PAVI11, the 5th International Workshop "From Parity Violation to Hadronic Structure and more..." Il Nuovo Cimento C **35**, 68 (2012).†

9. "Weak Interaction Studies with ^{6}He," A. Knecht*, Z. T. Alexander, Y. Bagdasarova, T. M. Cope, B. G. Delbridge, X. Fléchard, A. García*, R. Hong, E. Liénard, P. Müeller, O. Naviliat-Cuncic, A. S. C. Palmer, R. G. H. Robertson, D. W. Storm, H. E. Swanson, S. Utsuno, F. Wauters, W. Williams, C. Wrede, and D. W. Zumwalt, CIPANP 2012 Proceedings.†

10. "Detailed report of the MuLan measurement of the positive muon lifetime and determination of the Fermi constant,"MuLan Collaboration: V. Tishchenko, S. Battu, R. M. Carey, D. B. Chitwood, J. Crnkovic, P. T. Debevec, S. Dhamija, W. Earle, A. Gafarov, K. Giovanetti, T. P. Gorringe, F. E. Gray, Z. Hartwig, D. W. Hertzog*, B. Johnson, P. Kammel*, B. Kiburg, S. Kizilgul, J. Kunkle, B. Lauss, I. Logashenko, K. R. Lynch, R. McNabb, J. P. Miller, F. Mulhauser, C. J. G. Onderwater, Q. Peng, J. Phillips, S. Rath, B. L. Roberts, D. M. Webber, P. Winter*, and B. Wolfe, Phys. Rev. D **87**, 052003 (2013).

11. "Measurement of Muon Capture on the Proton to 1% Precision and Determination of the Pseudoscalar Coupling g_P," V. A. Andreev, T. I. Banks, R. M. Carey, T. A. Case, S. M. Clayton, K. M. Crowe, J. Deutsch, J. Egger, S. J. Freedman, V. A. Ganzha, T. Gorringe, F. E. Gray, D. W. Hertzog*, M. Hildebrandt, P. Kammel*, B. Kiburg*, S. Knaack*, P. A. Kravtsov, A. G. Krivshich, B. Lauss, K. R. Lynch, E. M. Maev, O. E. Maev, F. Mulhauser, C. Petitjean, G. E. Petrov, R. Prieels, G. N. Schapkin, G. G. Semenchuk, M. A. Soroka, V. Tishchenko, A. A. Vasilyev, A. A. Vorobyov, M. E. Vznuzdaev, and P. Winter*, Phys. Rev. Lett. **110**, 012504 (2013).†

12. "Magnetic Dipole Moment of the Doubly-Closed-Shell Plus One Proton Nucleus Sc-49," T. Ohtsubo, N. J. Stone, J. R. Stone, I. S. Towner, C. R. Bingham, C. Gaulard, U. Koester, S. Muto, J. Nikolov, K. Nishimura, G. S. Simpson, G. Soti, M. Veskovic, W. B. Walters, and F. Wauters, Phys. Rev. Lett. **109**, 032504 (2012).

An * denotes the CENPA lead author of a publication.

A † denotes a publication describing work fully or partially supported by the DOE grant.

13. "γ-ray constraints on the properties of unbound ^{32}Cl levels," C. Wrede*****, A. García, D. Melconian, S. Triambak, and B. A. Brown, Phys. Rev. C **86**, 047305 (2012).†

14. "Measurement of the electron neutrino and total ^{8}B solar neutrino fluxes with the Sudbury Neutrino Observatory phase-III data set," B. Aharmim, S. N. Ahmed, J. F. Amsbaugh, J. M. Anaya, A. E. Anthony, J. Banar, N. Barros, E. W. Beier, A. Bellerive, B. Beltran, M. Bergevin, S. D. Biller, K. Boudjemline, M. G. Boulay, T. J. Bowles, M. C. Browne, T. V. Bullard, T. H. Burritt, B. Cai, Y. D. Chan, D. Chauhan, M. Chen, B. T. Cleveland, G. A. Cox, C. A. Currat, X. Dai, H. Deng, J. A. Detwiler, M. DiMarco, P. J. Doe, G. Doucas, M. R. Dragowski, P.-L. Drouin, C. A. Duba, F. A. Duncan, M. Dunford, E. D. Earle, S. R. Elliott, H. C. Evans, G. T. Ewan, J. Farine, H. Fergani, F. Fleurot, R. J. Ford, J. A. Formaggio, M. M. Fowler, N. Gagnon, J. V. Germani, A. S. Goldschmidt, J. T. M. Goon, K. Graham, E. Guillian, S. Habib, R. L. Hahn, A. L. Hallin, E. D. Hallman, A. A. Hamian, G. C. Harper, P. J. Harvey, R. Hazama, K. M. Heeger, W. J. Heintzelman, J. Heise, R. L. Helmer, R. Henning, A. Hime, C. Howard, M. A. Howe, M. Huang, P. Jagam, B. Jamieson, N. A. Jelley, K. J. Keeter, J. R. Klein, L. L. Kormos, M. Kos, C. Kraus, C. B. Krauss, A. Kruger, T. Kutter, C. C. M. Kyba, R. Lange, J. Law, I. T. Lawson, K. T. Lesko, J. R. Leslie, J. C. Loach, R. MacLellan, S. Majerus, H. B. Mak, J. Maneira, R. Martin, N. McCauley, A. B. McDonald, S. McGee, C. Mifflin, G. G. Miller, M. L. Miller, B. Monreal, J. Monroe, B. Morissette, A. W. Myers, B. G. Nickel, A. J. Noble, H. M. O'Keeffe, N. S. Oblath, R. Ollerhead, G. D. Orebi Gann, S. M. Oser, R. A. Ott, S. J. M. Peeters, A. W. P. Poon, G. Prior, S. D. Reitzner, K. Rielage, B. C. Robertson, R. G. H. Robertson, E. Rollin, M. H. Schwendener, J. A. Secrest, S. R. Seibert, O. Simard, J. J. Simpson, P. Skensved, M. W. E. Smith, T. J. Sonley, T. D. Steiger, L. C. Stonehill, G. Tesic, P. M. Thornewell, N. Tolich*****, T. Tsui, C. D. Tunnel, T. D. Van Wechel, R. Van Berg, B. A. VanDevender, C. J. Virtue, B. L. Wall, D. Waller, H. Wan Chan Tseung, J. Wendland, N. West, J. B. Wilhelmy, J. F. Wilkerson, J. R. Wilson, J. M. Wouters, A. Wright, M. Yeh, F. Zhang, and K. Zuber (SNO Collaboration), Phys. Rev. C **87**, 015502 (2013); arXiv 1107.2901.†

15. "Empirical Survey of Neutrinoless Double Beta Decay Matrix Elements," R. G. H. Robertson*****, Mod. Phys. Lett. A **28**, No. 8, 1350021 (2013); arXiv 1301.1323.†

16. "The forbidden pleasures of experimental physics," A. García*****, Proceedings of IX Latin American Symposium on Nuclear Physics and Applications, AIP Conf. Proc. **1423**, 257 (2012).†

17. "Challenging claims of nonjet 'higher harmonic' components in 2D angular correlations from high-energy heavy-ion collisions," T. A. Trainor*****, D. J. Prindle, and R. L. Ray, Phys. Rev. C **86**, 064905 (2012).†

An ***** denotes the CENPA lead author of a publication.

A † denotes a publication describing work fully or partially supported by the DOE grant.

18. "Anomalous centrality evolution of two-particle angular correlations from Au-Au collisions at $\sqrt{s_{\rm NN}} = 62$ and 200 GeV," L. Adamczyk, J. K. Adkins, G. Agakishiev, M. M. Aggarwal, Z. Ahammed, A. V. Alakhverdyants, I. Alekseev, J. Alford, B. D. Anderson, C. D. Anson, A. Aparin, D. Arkhipkin,E. Aschenauer, G. S. Averichev, J. Balewski, A. Bannerjee, Z. Barnovska, D. R. Beavis, R. Bellwied, M. J. Betancourt, R. R. Betts, A. Bhasin, A. K. Bhati, P. Bhattarai, H. Bichsel, J. Bielcik, J. Bielcikova, L. C. Bland, I. G. Bordyuzhin, W. Borowski, J. Bouchet, E. Braidot, A. V. Brandin, S. G. Brovko, E. Bruna, S. Bueltmann, I. Bunzarov, T. P. Burton, J. Butterworth, X. Z. Cai, H. Caines, M. Calderon, D. Cebra, R. Cendejas, M. C. Cervantes, P. Chaloupka, Z. Chang, S. Chattopadhyay, H. F. Chen, J. H. Chen, J. Y. Chen, L. Chen, J. Cheng, M. Cherney, A. Chikanian, W. Christie, P. Chung, J. Chwastowski, M. J. M. Codrington, R. Corliss, J. G. Cramer, H. J. Crawford, X. Cui, M. S. Das, J. Daugherity, A. Davila Leyva, L. C. De Silva, R. R. Debbe, T. G. Dedovich, J. Deng, A. A. Derevschikov, R. Derradi de Souza, W. Dhamija, B. di Ruzza, L. Didenko, Dilks, F. Ding, A. Dion, P. Djawotho, X. Dong, J. L. Drachenberg, J. E. Draper, C. M. Du, L. E. Dunkelberger, J. C. Dunlop, L. G. Efimov, M. Elnimr, J. Engelage, K. S. Engle, G. Eppley, M. Estienne, L. Eun, O. Evdokimov, R. Fatemi, S. Fazio, J. Fedorisin, R. G. Fersch, P. Filip, E. Finch, V. Fine, Y. Fisyak, C. E. Flores, C. A. Gagliardi, D. R. Gangadharan, D. Garand, F. Geurts, P. Ghosh, A. Gibson, Girard, S. Gliske, Y. N. Gorbunov, A. Gordon, O. G. Grebenyuk, D. Grosnick, Y. Guo, A. Gupta, S. Gupta, W. Guryn, B. Haag, O. Hajkova, A. Hamed, L-X. Han, R. Haque, J. W. Harris, J. P. Hays-Wehle, S. Heppelmann, A. Hirsch, G. W. Hoffmann, D. J. Hofman, S. Horvat, B. Huang, H. Z. Huang, P. Huck, T. J. Humanic, L. Huo, G. Igo, W. W. Jacobs, Jang, C. Jena, J. Joseph, E. G. Judd, S. Kabana, K. Kang, J. Kapitan, K. Kauder, H. W. Ke, D. Keane, A. Kechechyan, A. Kesich, D. Kettler, Z. H. Khan, D. P. Kikola, J. Kiryluk, A. Kisiel, I. Kisel, V. Kizka, S. R. Klein, D. D. Koetke, T. Kollegger, J. Konzer, I. Koralt, L. Koroleva, W. Korsch, L. Kotchenda, P. Kravtsov, K. Krueger, I. Kulakov, L. Kumar, R. A. Kycia, M. A. C. Lamont, J. M. Landgraf, K. D. Landry, S. LaPointe, J. Lauret, A. Lebedev, R. Lednicky, J. H. Lee, W. Leight, M. J. LeVine, C. Li, L. Li, W. Li, X. Li, X. Li, Y. Li, Z. M. Li, L. M. Lima, M. A. Lisa, F. Liu, T. Ljubicic, W. J. Llope, R. S. Longacre, Y. Lu, E. V. Lukashov, X. Luo, G. L. Ma, Y. G. Ma, D. M. M. D. Madagodagettige Don, D. P. Mahapatra, R. Majka, O. I. Mall, R. Manweiler, S. Margetis, C. Markert, H. Masui, H. S. Matis, D. McDonald, T. S. McShane, A. Meschanin, R. Milner, N. G. Minaev, S. Mioduszewski, M. K. Mitrovski, Y. Mohammed, B. Mohanty, M. M. Mondal, B. Morozov, D. A. Morozov, M. G. Munhoz, M. K. Mustafa, M. Naglis, B. K. Nandi, Md. Nasim, T. K. Nayak, J. M. Nelson, L. V. Nogach, Noh, J. Novak, S. B. Nurushev, G. Odyniec, A. Ogawa, K. Oh, A. Ohlson, V. Okorokov, E. W. Oldag, R. A. N. Oliveira, D. Olson, M. Pachr, B. S. Page, S. K. Pal, Y. X. Pan, Y. Pandit, Y. Panebratsev, T. Pawlak, B. Pawlik, H. Pei, T. Peitzmann, C. Perkins, W. Peryt, P. Pile, M. Planinic, J. Pluta, D. Plyku, N. Poljak, J. Porter, A. M. Poskanzer, C. B. Powell, D. Prindle, C. Pruneau, N. K. Pruthi, M. Przybycien, P. R. Pujahari, J. Putschke, H. Qiu, S. Ramachandran,

An * denotes the CENPA lead author of a publication.

A † denotes a publication describing work fully or partially supported by the DOE grant.

R. Raniwala, S. Raniwala, R. L. Ray, R. Redwine, R. Reed, C. K. Riley, H. G. Ritter, J. B. Roberts, O. V. Rogachevskiy, J. L. Romero, J. F. Ross, A. Roy, L. Ruan, J. Rusnak, N. R. Sahoo, P. K. Sahu, I. Sakrejda, S. Salur, A. Sandacz, J. Sandweiss, E. Sangaline, A. Sarkar, J. Schambach, R. P. Scharenberg, J. Schaub, A. M. Schmah, B. Schmidke, N. Schmitz, T. R. Schuster, J. Seele, J. Seger, I. Selyuzhenkov, P. Seyboth, N. Shah, E. Shahaliev, P. V. Shanmuganathan, M. Shao, B. Sharma, M. Sharma, W. Q. Shen, S. S. Shi, Q. Y. Shou, E. P. Sichtermann, F. Simon, R. N. Singaraju, M. J. Skoby, D. Smirnov, N. Smirnov, D. Solanki, P. Sorensen, U. G. de Souza, H. M. Spinka, B. Srivastava, T. D. S. Stanislaus, S. G. Steadman, J. R. Stevens, R. Stock, M. Strikhanov, B. Stringfellow, A. A. P. Suaide, M. C. Suarez, M. Sumbera, X. M. Sun, Y. Sun, Z. Sun, B. Surrow, D. N. Svirida, T. J. M. Symons, A. Szanto de Toledo, J. Takahashi, A. H. Tang, Z. Tang, L. H. Tarini, T. Tarnowsky, D. Thein, J. H. Thomas, J. Tian, A. R. Timmins, D. Tlusty, M. Tokarev, T. A. Trainor, S. Trentalange, R. E. Tribble, P. Tribedy, B. A. Trzeciak, O. D. Tsai, J. Turnau, T. Ullrich, D. G. Underwood, G. Van Buren, G. van Nieuwenhuizen, J. A. Vanfossen, Jr., R. Varma, G. M. S. Vasconcelos, A. N. Vasiliev, R. Vertesi, F. Videbaek, Y. P. Viyogi, S. Vokal, S. A. Voloshin, A. Vossen, M. Wada, M. Walker, F. Wang, G. Wang, H. Wang, J. S. Wang, Q. Wang, X. L. Wang, Y. Wang, Y. Wang, G. Webb, J. C. Webb, G. D. Westfall, C. Whitten, Jr., H. Wieman, S. W. Wissink, R. Witt, W. Witzke, Y. F. Wu, Z. Xiao, W. Xie, K. Xin, H. Xu, N. Xu, Q. H. Xu, W. Xu, Y. Xu, Z. Xu, L. Xue, Yan, C. Yang, Y. Yang, Y. Yang, P. Yepes, L. Yi, K. Yip, I-K. Yoo, M. Zawisza, Y. Zawisza, H. Zbroszczyk, W. Zha, W. Zhan, J. B. Zhang, S. Zhang, W. M. Zhang, X. P. Zhang, Y. Zhang, Z. P. Zhang, F. Zhao, J. Zhao, C. Zhong, X. Zhu, Y. H. Zhu, Y. Zoulkarneeva and M. Zyzak (STAR Collaboration) Phys. Rev. C **86**, 064902 (2012).†

19. "Dijet production, collision centrality and backgrounds in high-energy p-p collisions," T. A. Trainor*****, Phys. Rev. D **87**, 054005 (2013).†

20. "Azimuth multipoles vs minimum-bias jets in 2D angular correlations on η and ϕ," T. A. Trainor*****, J. Phys. G **40** 055104 (2013).†

21. "Glasma flux tubes vs minimum-bias jets in 2D angular correlations on η and ϕ," T. A. Trainor*****, J. Phys. G **39**, 095102 (2012).†

22. "Limit on Neutrinoless $\beta\beta$ Decay of ^{136}Xe from the First Phase of KamLAND-Zen and Comparison with the Positive Claim in ^{76}Ge," A. Gando, Y. Gando, H. Hanakago, H. Ikeda, K. Inoue, K. Ishidoshiro, H. Ishikawa, M. Koga, R. Matsuda, S. Matsuda, T. Mitsui, D. Motoki, K. Nakamura, A. Obata, A. Oki, Y. Oki, M. Otani, I. Shimizu, J. Shirai, A. Suzuki, Y. Takemoto, K. Tamae, K. Ueshima, H. Watanabe, B. D. Xu, S. Yamada, Y. Yamauchi, H. Yoshida, A. Kozlov, S. Yoshida, A. Piepke, T. I. Banks, B. K. Fujikawa, K. Han, T. O'Donnell, B. E. Berger, J. G. Learned, S. Matsuno, M. Sakai, Y. Efremenko, H. J. Karwowski, D. M. Markoff, W. Tornow, J. A. Detwiler, S. Enomoto, and M.P. Decowski, Phys. Rev. Lett. **110**, 062502 (2013).

An ***** denotes the CENPA lead author of a publication.

A † denotes a publication describing work fully or partially supported by the DOE grant.

23. "Characteristics of Signals Originating Near the Lithium-Diffused N+ Contact of High Purity Germanium P-Type Point Contact Detectors," E. Aguayo, M. Amman, F. T. Avignone III, A. S. Barabash, P. J. Barton, J. R. Beene, F. E. Bertrand, M. Boswell, V. Brudanin, M. Busch, Y-D. Chan, C. D. Christofferson, J. I. Collar, D. C. Combs, R. J. Cooper, J. A. Detwiler, P. J. Doe, Yu. Efremenko, V. Egorov, H. Ejiri, S. R. Elliott, J. Esterline, J. E. Fast, N. Fields, P. Finnerty, F. M. Fraenkle, A. Galindo-Uribarri, V. M. Gehman, G. K. Giovanetti, M. P. Green, V. E. Guiseppe, K. Gusey, A. L. Hallin, R. Hazama, R. Henning, E. W. Hoppe, M. Horton, S. Howard, M. A. Howe, R. A. Johnson, K. J. Keeter, M. F. Kidd, A. Knecht, O. Kochetov, S. I. Konovalov, R. T. Kouzes, B. D. LaFerriere, J. Leon, L. E. Leviner, J. C. Loach, Q. Looker, P. N. Luke, S. MacMullin, M. G. Marino*****, R. D. Martin, J. H. Merriman, M. L. Miller, L. Mizouni, M. Nomachi, J. L. Orrell, N. R. Overman, G. Perumpilly, D. G. Phillips II, A. W. P. Poon, D. C. Radford, K. Rielage, R. G. H. Robertson, M. C. Ronquest, A. G. Schubert, T. Shima, M. Shirchenko, K. J. Snavely, D. Steele, J. Strain, V. Timkin, W. Tornow, R. L. Varner, K. Vetter, K. Vorren, J. F. Wilkerson, E. Yakushev, H. Yaver, A. R. Young, C.-H. Yu, and V. Yumatov, Nucl. Inst. Meth. Phys. Res. A **701**, 176 (2013).†

24. "Limits on Majoron-Emitting Double-β Decays of ^{136}Xe in the KamLAND-Zen Experiment," A. Gando, Y. Gando, H. Hanakago, H. Ikeda, K. Inoue, K. Ishidoshiro, H. Ishikawa, M. Koga, R. Matsuda, S. Matsuda, T. Mitsui, D. Motoki, K. Nakamura, A. Obata, A. Oki, Y. Oki, M. Otani, I. Shimizu, J. Shirai, A. Suzuki, Y. Takemoto, K. Tamae, K. Ueshima, H. Watanabe, B. D. Xu, S. Yamada, Y. Yamauchi, H. Yoshida, A. Kozlov, S. Yoshida, A. Piepke, T. I. Banks, B. K. Fujikawa, K. Han, T. O'Donnell, B. E. Berger, J. G. Learned, S. Matsuno, M. Sakai, Y. Efremenko, H. J. Karwowski, D. M. Markoff, W. Tornow, J. A. Detwiler, S. Enomoto, and M.P. Decowski, Phys. Rev. C **86**, 021601(R) (2012).

25. "Measurement of the Double-Beta Decay Half-Life of ^{136}Xe in KamLAND-Zen," A. Gando, Y. Gando, H. Hanakago, H. Ikeda, K. Inoue, K. Ishidoshiro, H. Ishikawa, M. Koga, R. Matsuda, S. Matsuda, T. Mitsui, D. Motoki, K. Nakamura, A. Obata, A. Oki, Y. Oki, M. Otani, I. Shimizu, J. Shirai, A. Suzuki, Y. Takemoto, K. Tamae, K. Ueshima, H. Watanabe, B. D. Xu, S. Yamada, Y. Yamauchi, H. Yoshida, A. Kozlov, S. Yoshida, A. Piepke, T. I. Banks, B. K. Fujikawa, K. Han, T. O'Donnell, B. E. Berger, J. G. Learned, S. Matsuno, M. Sakai, Y. Efremenko, H. J. Karwowski, D. M. Markoff, W. Tornow, J. A. Detwiler, S. Enomoto, and M.P. Decowski, Phys. Rev. C **85**, 045504 (2012).

26. "Measurements of D^0 and D^* Production in $p + p$ Collisions at $\sqrt{s} = 200$ GeV," L. Adamczyk *et al.*, (the STAR Collaboration), Phys. Rev. D **86**, 72013 (2012).†

27. "Determining the Drift Time of Charge Carriers in P-Type Point Contact HPGe Detectors," R. D. Martin, M. Amman, Y-D. Chan, J. A. Detwiler, J. C. Loach, Q. Looker, P. N. Luke, A. W. P. Poon, J. Qian, K. Vetter, and H. Yaver, Nucl. Inst. Meth. Phys. Res. A **678**, 98 (2012).

An ***** denotes the CENPA lead author of a publication.

A † denotes a publication describing work fully or partially supported by the DOE grant.

28. "Techniques used to search for a permanent electric dipole moment of the ^{199}Hg atom and the implications for CP violation," M. D. Swallows, T. H. Loftus, W. C. Griffith, B. R. Heckel, E. N. Fortson, and M. V. Romalis, Phys. Rev. A **87**, 012102 (2013).†

29. "Search for Extraterrestrial Antineutrino Sources with the KamLAND Detector," A. Gando, Y. Gando, H. Hanakago, H. Ikeda, K. Inoue, K. Ishidoshiro, H. Ishikawa, M. Koga, R. Matsuda, S. Matsuda, T. Mitsui, D. Motoki, K. Nakamura, A. Obata, A. Oki, Y. Oki, M. Otani, I. Shimizu, J. Shirai, A. Suzuki, Y. Takemoto, K. Tamae, K. Ueshima, H. Watanabe, B. D. Xu, S. Yamada, Y. Yamauchi, H. Yoshida, A. Kozlov, S. Yoshida, A. Piepke, T. I. Banks, B. K. Fujikawa, K. Han, T. O'Donnell, B. E. Berger, J. G. Learned, S. Matsuno, M. Sakai, Y. Efremenko, H. J. Karwowski, D. M. Markoff, W. Tornow, J. A. Detwiler, S. Enomoto, and M.P. Decowski, Astrophys. J **745**, 193 (2012).

30. "System-size dependence of particle-ratio fluctuations in Pb + Pb collisions at 158A GeV," T. Antićić, B. Baatar, D. Barna, J. Bartke, H. Beck, L. Betev, H. Białkowska, C. Blume, M. Bogusz, B. Boimska, J. Book, M. Botje, P. Bunčić, T. Cetner, P. Christakoglou, P. Chung, O. Chvála, J.G. Cramer, V. Eckardt, Z. Fodor, P. Foka, V. Friese, M. Gaździcki, K. Grebieszkow, C. Höhne, K. Kadija, A. Karev, V.I. Kolesnikov, M. Kowalski, D. Kresan, A. László, R. Lacey, M. van Leeuwen, M. Maćkowiak-Pawłowska, M. Makariev, A.I. Malakhov, M. Mateev, G.L. Melkumov, M. Mitrovski, St. Mrówczyński, V. Nicolic, G. Pálla, A.D. Panagiotou, W. Peryt, J. Pluta, D. Prindle, F. Pühlhofer, R. Renfordt, C. Roland, G. Roland, M. Rybczyński, A. Rybicki, A. Sandoval, N. Schmitz, T. Schuster, P. Seyboth, F. Siklér, E. Skrzypczak, M. Słodkowski, G. Stefanek, R. Stock, H. Ströbele, T. Šuša, M. Szuba, M. Utvić, D. Varga, M. Vassiliou, G.I. Veres, G. Vesztergombi, D. Vranić, Z. Włodarczyk, A. Wojtaszek-Szwarc (NA49 Collaboration), Phys. Rev. C **87**, 024902 (2013).

31. "Antideuteron and deuteron production in midcentral Pb+Pb collisions at 158A GeV," T. Antićić, B. Baatar, D. Barna, J. Bartke, H. Beck, L. Betev, H. Białkowska, C. Blume, M. Bogusz, B. Boimska, J. Book, M. Botje, P. Bunčić, T. Cetner, P. Christakoglou, P. Chung, O. Chvála, J.G. Cramer, V. Eckardt, Z. Fodor, P. Foka, V. Friese, M. Gaździcki, K. Grebieszkow, C. Höhne, K. Kadija, A. Karev, V.I. Kolesnikov, M. Kowalski, D. Kresan, A. László, R. Lacey, M. van Leeuwen, M. Maćkowiak-Pawłowska, M. Makariev, A.I. Malakhov, M. Mateev, G.L. Melkumov, M. Mitrovski, St. Mrówczyński, V. Nicolic, G. Pálla, A.D. Panagiotou, W. Peryt, J. Pluta, D. Prindle, F. Pühlhofer, R. Renfordt, C. Roland, G. Roland, M. Rybczyński, A. Rybicki, A. Sandoval, N. Schmitz, T. Schuster, P. Seyboth, F. Siklér, E. Skrzypczak, M. Słodkowski, G. Stefanek, R. Stock, H. Ströbele, T. Šuša, M. Szuba, M. Utvić, D. Varga, M. Vassiliou, G.I. Veres, G. Vesztergombi, D. Vranić, Z. Włodarczyk, A. Wojtaszek-Szwarc (NA49 Collaboration), Phys. Rev. C **85**, 044913 (2012).

An * denotes the CENPA lead author of a publication.

A † denotes a publication describing work fully or partially supported by the DOE grant.

32. "Di-electron spectrum at mid-rapidity in $p+p$ collisions at $\sqrt{s} = 200$ GeV," L. Adamczyk *et al.*, (the STAR Collaboration), Phys. Rev. C **86**, 24906 (2012).†

33. "Observation of an Energy-Dependent Difference in Elliptic Flow between Particles and Antiparticles in Relativistic Heavy Ion Collisions," L. Adamczyk *et al.*, (the STAR Collaboration), Phys. Rev. Lett. **110**, 142301 (2013).†

34. "Inclusive charged hadron elliptic flow in Au + Au collisions at $\sqrt{s_{NN}} = 7.7$ - 39 GeV," L. Adamczyk *et al.*, (the STAR Collaboration), Phys. Rev. C **86**, 54908 (2012).†

35. "Single spin asymmetry A_N in polarized proton-proton elastic scattering at $\sqrt{s} =$ 200 GeV," L. Adamczyk *et al.*, (the STAR Collaboration), Physics Letters B **719**, 62 (2013).†

36. "Transverse Single-Spin Asymmetry and Cross-Section for π^0 and η Mesons at Large Feynman-x in Polarized p+p Collisions at $\sqrt{s} = 200$ GeV," L. Adamczyk *et al.*, (the STAR Collaboration), Phys. Rev. D **86**, 5110 (2012).†

37. "Longitudinal and transverse spin asymmetries for inclusive jet production at mid-rapidity in polarized p+p collisions at $\sqrt{s}$=200 GeV," L. Adamczyk *et al.*, (the STAR Collaboration), Phys. Rev. D **86**, 32006 (2012).†

38. "Directed Flow of Identified Particles in Au + Au Collisions at $\sqrt{s_{NN}} = 200$ GeV at RHIC," L. Adamczyk *et al.*, (the STAR Collaboration), Phys. Rev. Lett. **108** 202301 (2012).†

39. "Measurement of the $W \to e\nu$ and $Z/\gamma^* \to e^+e^-$ Production Cross Sections at Mid-rapidity in Proton-Proton Collisions at $\sqrt{s} = 500$ GeV," L. Adamczyk *et al.*, (the STAR Collaboration), Phys. Rev. D **85** 92010(2012).†

40. "Energy and system-size dependence of two- and four-particle v_2 measurements in heavy-ion collisions at 62.4 and 200 GeV and their implications on flow fluctuations and nonflow," L. Adamczyk *et al.*, (the STAR Collaboration), Phys. Rev. C **86**, 14903 (2012).†

41. "System size and energy dependence of near-side di-hadron correlation," L. Adamczyk *et al.*, (the STAR Collaboration), Phys. Rev. C **85**, 14903 (2012).†

42. "Identified hadron compositions in p+p and Au+Au collisions at high transverse momenta at $\sqrt{s_{NN}} = 200$ GeV," L. Adamczyk *et al.*, (the STAR Collaboration), Phys. Rev. Lett. **108** 72302 (2012).†

43. "Directed and elliptic flow of charged particles in Cu+Cu collisions at $\sqrt{s_{NN}}$ =22.4 GeV," L. Adamczyk *et al.*, (the STAR Collaboration), Phys. Rev. C **85**, 14901 (2012).†

An * denotes the CENPA lead author of a publication.

A † denotes a publication describing work fully or partially supported by the DOE grant.

44. "Anomalous centrality evolution of two-particle angular correlations from Au-Au collisions at $\sqrt{s_{NN}}$ = 62 and 200 GeV," L. Adamczyk *et al.*, (the STAR Collaboration), Phys. Rev. C **86**, 64902 (2012).†

45. "ρ^0 Photoproduction in AuAu Collisions at $\sqrt{s_{NN}}$=62.4 GeV with STAR," L. Adamczyk *et al.*, (the STAR Collaboration), Phys. Rev. C **85**, 14910 (2012).†

46. "Strangeness Enhancement in Cu+Cu and Au+Au $\sqrt{s_{NN}}$=200 GeV Collisions," L. Adamczyk *et al.*, (the STAR Collaboration), Phys. Rev. Lett. **108** 72301 (2012).†

11.2 Reports and white papers

1. "Discovering the New Standard Model: Fundamental Symmetries and Neutrinos," V. Cianciolo, A. B. Balantekin, A. Bernstein, V. Cirigliano, M. D. Cooper, D. J. Dean, S. R. Elliott, B. W. Filippone, S. J. Freedman, G. L. Greene, K. M. Heeger, D. W. Hertzog*****, B. R. Holstein, P. Huffman, T. Ito, K. Kumar, Z.-T. Lu, J. S. Nico, G. D. Orebi Gann, K. Paschke, A. Piepke, B. Plaster, D. Pocanic, A. W. P. Poon, D. C. Radford, M. J. Ramsey-Musolf, R. G. H. Robertson*****, G. Savard, K. Scholberg, Y. Semertzidis, J. F. Wilkerson, Report of the Fundamental Symmetries and Neutrinos Workshop, August 10-11, 2012, Chicago, IL (Submitted 20 December, 2012; arXiv:1212.5190).

2. "Nuclear Physics: Exploring the Heart of Matter," S. J. Freedman, A. Aprahamian, R. Alarcon, G. A. Baym, E. Beise, R. F. Casten, J. A. Cizewski, A. Hayes-Sterbenz, R. J. Holt, K. Langanke, C. A. Murray, W. Nazarewicz, K. Orginos, K. Rajagopal, R. G. H. Robertson, T. J. Ruth, H. Schatz, R. E. Tribble, and W. A. Zajc, The Committee on the Assessment of and Outlook for Nuclear Physics; Board on Physics and Astronomy; Division on Engineering and Physical Sciences; National Research Council (2012). A refereed report.

3. "Project 8: Measuring Neutrino Masses Using Frequency-based Techniques," P. J. Doe, R. G. H. Robertson*****, L. J Rosenberg, G. Rybka, J. A. Formaggio, N. S. Oblath, M. Leber, B. Monreal, D. Asner, and B. A. VanDevender, White paper presented to DOE Office of Nuclear Physics, 30 January, 2013.†

4. "Report of the NSAC Subcommittee on Scientific Facilities," D. Beck, J. Beene, B. Cole, C. Gagliardi, D. F. Geesaman, R. Gerig, K. Griffioen, C. K. Lister, Z.-E. Meziani, R. P. Redwine, D. Rej, R. G. H. Robertson, and T. J. M. Symons, NSAC Subcommittee on Scientific Facilities, 2013.

5. "KATRIN: an experiment to determine the neutrino mass from the beta decay of tritium," R. G. H. Robertson*****, for the KATRIN Collaboration, White Paper for the Snowmass Community Planning Workshops, 2013.†

An * denotes the CENPA lead author of a publication.

A † denotes a publication describing work fully or partially supported by the DOE grant.

6. "Light Sterile Neutrinos: A White Paper," K. N. Abazajian, M. A. Acero, S. K. Agarwalla, C. H. Albright, S. Antusch, C. A. Arguelles, A. B. Balantekin, V. Barger, F. Bezrukov, O. E. Bjaelde, A. Blondel, S. A. Bogacz, N. S. Bowden, A. Boyarsky, A. Bravar, S. J. Brice, A. D. Bross, E. J. Chun, B. T. Cleveland, A. P. Collin, M. Cribier, S. Das, A. de Goûvèa, J. S. Diaz, Z. Djurcic, A. Donini, S. R. Elliott, D. J. Ernst, J. J. Evans, E. Fernandez-Martinez, E. Figueroa-Feliciano, B. T. Fleming, J. A. Formaggio, D. Franco, J. Gaffiot, R. Gandhi, Y. Gao, G. T. Garvey, V. N. Gavrin, P. Ghoshal, C. Giunti, V. V. Gorbachev, D. S. Gorbunov, R. Guenette, F. Halzen, J. Hamann, S. Hannestad, W. Ċ. Haxton, K. M. Heeger, P. Hernandez, P. Huber, W. Huelsnitz, T. V. Ibragimova, Y. Karadzhov, G. Karagiorgi, Y. D. Kim, J. Kopp, V. N. Kornoukhov, A. Kusenko, P. Kyberd, P. Langacker, Th. Lasserre, M. Laveder, A. Letourneau, D. Lhuillier, Y. F. Li, J. M. Link, B. L. Littlejohn, K. Long, J. Lopez-Pavon, W. C. Louis, J. D. Lykken, P. A. N. Machado, M. Maltoni, W. A. Mann, D. Marfatia, V. A. Matveev, N. E. Mavromatos, A. Melchiorri, D. Meloni, G. Mention, A. Merle, M. Mezzetto, G. B. Mills, D. Minic, D. Mohapatra, R. N. Mohapatra, Y. Mori, Th. A. Mueller, H. P. Mumm, A. E. Nelson, J. S. Nico, E. Noah, J. Nowak, S. Pakvasa, M. Pallavicini, S. Pascoli, M. Popovic, B. Rebel, R. G. H. Robertson, W. Rodejohann, O. Ruchayskiy, K. Scholberg, T. Schwetz, M. Shaposhnikov, R. Shrock, M. Sorel, A. Sousa, D. N. Spergel, L. Stanco, T. Takeuchi, I. Tamborra, J. Tang, X. C. Tian, C. D. Tunnell, R. G. Van de Water, L. Verde, E. P. Veretenkin, M. O. Wascko, J. F. Wilkerson, W. Winter, Y. Y. Y. Wong, O. Yasuda, L. Zhan, and H. Zhang. arXiv:1204.5379, 2012.

11.3 Abstracts and contributed talks

1. "Weak Interaction Studies with ^{6}He," A. Knecht*, Z. T. Alexander, Y. Bagdasarova, T. M. Cope, B. G. Delbridge, X. Flechard, A. Garcìa, R. Hong, E. Lienard, P. Mueller, O. Naviliat-Cuncic, A. S. C. Palmer, R. G. H. Robertson, D. W. Storm, H. E. Swanson, S. Utsuno, W. Williams, C. Wrede, D. W. Zumwalt, Proc. Eleventh Conference on the Intersections of Particle and Nuclear Physics (CIPANP 2012).†

2. "Noise Considerations for a Very Low Threshold Semiconductor Detector System," J. Leon*, A. Knecht, M. L. Miller, D. A. Peterson, R. G. H. Robertson, and T. D. Van Wechel; IEEE Trans. Nucl. Sci. 2012 in press.†

3. "The KATRIN Experiment," D. S. Parno*, February, 2013, Lake Louise Winter Institute, Lake Louise, Alberta, Canada.†

4. "MuSun - Muon Capture on the Deuteron," P. Kammel, contributed talk APS April Meeting 2012, Atlanta, GA, March 31 - April 3, 2012.†

5. "A Torsion-Balance Search for Axion-Like Particles," F. Fleischer, contributed talk APS April Meeting 2012, Atlanta, GA, March 31 – April 3, 2012.

An * denotes the CENPA lead author of a publication.

A † denotes a publication describing work fully or partially supported by the DOE grant.

11.4 Papers submitted or to be published

1. "Challenging claims of 'elliptic flow' by comparing azimuth quadrupole and jet-related angular correlations from Au-Au collisions at $\sqrt{s_{NN}} = 62$ and 200 GeV," T. A. Trainor*, D. T. Kettler, D. J. Prindle and R. L. Ray, arXiv:1302.0300, submitted to Phys. Rev. C.†

2. "Final Analysis of Solar Neutrino Data from the Sudbury Neutrino Observatory," B. Aharmim, S. N. Ahmed, A. E. Anthony, N. Barros, E. W. Beier, A. Bellerive, B. Beltran, M. Bergevin, S. D. Biller, K. Boudjemline, M. G. Boulay, T. H. Burritt, B. Cai, Y. D. Chan, D. Chauhan, M. Chen, B. T. Cleveland, G. A. Cox, X. Dai, H. Deng, J. Detwiler, M. DiMarco, P. J. Doe, G. Doucas, P.-L. Drouin, C. A. Duba, F. A. Duncan, M. Dunford, E. D. Earle, S. R. Elliott, H. C. Evans, G. T. Ewan, J. Farine, H. Fergani, F. Fleurot, R. J. Ford, J. A. Formaggio, N. Gagnon, J. TM. Goon, K. Graham, E. Guillian, S. Habib, R L. Hahn, A. L. Hallin, E. D. Hallman, P. J. Harvey, R. Hazama, W. J. Heintzelman, J. Heise, R. L. Helmer, A. Hime, C. Howard, M. A. Howe, M. Huang, B. Jamieson, N. A. Jelley, K. J. Keeter, J. R. Klein, L. L. Kormos, M. Kos, C. Kraus, C. B. Krauss, T. Kutter, C. C. M. Kyba, J. Law, I. T. Lawson, K. T. Lesko, J. R. Leslie, I. Levine, J. C. Loach, R. MacLellan, S. Majerus, H. B. Mak, J. Maneira, R. Martin, N. McCauley, A. B. McDonald, S. McGee, M. L. Miller, B. Monreal, J. Monroe, B. Morissette, B. G. Nickel, A. J. Noble, H. M. O'Keeffe, N. S. Oblath, G. D. Orebi Gann, S. M. Oser, R. A. Ott, S. J. M. Peeters, A. W. P. Poon, G. Prior, S. D. Reitzner, K. Rielage, B. C. Robertson, R. G. H. Robertson, R. C. Rosten, M. H. Schwendener, J. A. Secrest, S. R. Seibert, O. Simard, P. Skensved, T. J. Sonley, L. C. Stonehill, G. Tesic, N. Tolich, T. Tsui, R. Van Berg, B. A. VanDevender, C. J. Virtue, B. L. Wall, D. Waller, H. Wan Chan Tseung, D. L. Wark, N. West, J. F. Wilkerson, J. R. Wilson, J. M. Wouters, A. Wright, M. Yeh, F. Zhang, and K. Zuber (SNO Collaboration) Phys. Rev. C (submitted September 5, 2011); arXiv 1109.0763.

3. "Precision Measurement of the Neutron Beta-Decay Asymmetry," M. P. Mendenhall, R. W. Pattie, Jr., Y. Bagdasarova, D. B. Berguno, L. J. Broussard, R. Carr, S. Currie, X. Ding, B. W. Filippone, A. García, P. Geltenbort, K. P. Hickerson, J. Hoagland, A. T. Holley, R. Hong, T. M. Ito, A. Knecht, C.-Y. Liu, J. L. Liu, M. Makela, R. R. Mammei, J. W. Martin, D. Melconian, S. D. Moore, C. L. Morris, A. Pérez-Galván, R. Picker, M.L. Pitt, B. Plaster, J. C. Ramsey, R. Rios, A. Saunders, S. J. Seestrom, E. I. Sharapov, W. E. Sondheim, E. Tatar, R. B. Vogelaar, B. VornDick, C. Wrede, A. R. Young and B. A. Zeck, Phys. Rev. C, Rapid Communication, in press.†

4. "Comparison of Modeled and Measured Performance of GSO Crystal as Gamma Detector," D. S. Parno*, M. Friend, V. Mamyan, F. Benmokhtar, A. Camsonne, G. B. Franklin, K. Paschke, and B. Quinn, arXiv:1211.3710 [physics.ins-det], submitted to Nucl.Inst. Meth. in Phys. Res. A.

An * denotes the CENPA lead author of a publication.

A † denotes a publication describing work fully or partially supported by the DOE grant.

5. "A critical review of RHIC experimental results," T. A. Trainor, review invited by Editors, Adv. High Energy Phys.; arXiv:1303.4774.

6. "Parity- and Time-Reversal Tests in Nuclear Physics," D. Hertzog* and M. J. Ramsey-Musolf, (Submitted December 27, 2012; arXiv:1212.6412 [nucl-th]).

7. "Solar Neutrinos: Status and Prospects," W. C. Haxton, R. G. H. Robertson*, and A. Serenelli, Annu. Rev. Astron. Astrophys., in press (2012).†

8. "Reactor On-Off Antineutrino Measurement with KamLAND," A. Gando, Y. Gando, H. Hanakago, H. Ikeda, K. Inoue, K. Ishidoshiro, H. Ishikawa, M. Koga, R. Matsuda, S. Matsuda, T. Mitsui, D. Motoki, K. Nakamura, A. Obata, A. Oki, Y. Oki, M. Otani, I. Shimizu, J. Shirai, A. Suzuki, Y. Takemoto, K. Tamae, K. Ueshima, H. Watanabe, B. D. Xu, S. Yamada, Y. Yamauchi, H. Yoshida, A. Kozlov, S. Yoshida, A. Piepke, T. I. Banks, B. K. Fujikawa, K. Han, T. O'Donnell, B. E. Berger, J. G. Learned, S. Matsuno, M. Sakai, Y. Efremenko, H. J. Karwowski, D. M. Markoff, W. Tornow, J. A. Detwiler, S. Enomoto, and M.P. Decowski, submitted to Phys. Rev. D, arXiv:1303.4667 [hep-ex] (2013).

11.5 Invited talks, abstracts, and other conference presentations

1. "Searching for new physics in the Nucleus," A. García, Physics colloquium at the University of Buenos Aires Physics Department, Argentina, May 24, 2012.

2. "Searching for new physics in the Nucleus," A. García, Invited colloquium at University of Tucumán, Argentina, May 30, 2012.

3. "Searching for new physics in the Nucleus," A. García, Invited seminar at TANDAR Laboratory, Argentina, June 7, 2012.

4. "Searching for new physics in the Nucleus," A. García, Invited talk at SACNAS meeting in Seattle, WA, October 8, 2012.

5. "Weak interaction studies in ^{6}He," A. García, Invited talk at Meeting of the NorthWest section of the APS in Vancouver, October 19, 2012.

6. "Weak interaction studies with light nuclei," A. García, Invited talk at Institute for Nuclear Theory Workshop "Light nuclei from first principles", November 6, 2012.

7. "Searches for new currents in nuclear beta decays," A. García, Invited colloquium at Idaho State University, January 28, 2013.

8. "Precision Muon Physics: Capturing a Moment in a Lifetime," D. W. Hertzog, colloquium, University of Alberta, March 16, 2012.

An * denotes the CENPA lead author of a publication.

A † denotes a publication describing work fully or partially supported by the DOE grant.

9. "Final MuLan and MuCap determinations of the Fermi constant and the nucleon's weak-induced pseudoscalar coupling," D. W. Hertzog, Invited talk; Conference on the Intersections of Nuclear and Particle Physics, St. Petersburg, FL, May 28, 2012.

10. "A behind-the-scenes look at the Muon Lifetime Experiments at PSI," D. W. Hertzog, Invited Lecturer, TRIUMF Summer Institute (lecture no. 1); Vancouver, BC, August 8, 2012.

11. "A Case for Challenging the Standard Model: Muon $g-2$," D. W. Hertzog, Invited Lecturer, TRIUMF Summer Institute (lecture no. 2); Vancouver, BC, August 8, 2012.

12. "Electroweak and Precision Physics: Experimental Review (less EDMs and PVES)," D. W. Hertzog, Invited Talk, Workshop on Fundamental Symmetries and Neutrinos, Chicago, IL, August 10, 2012.

13. "Physics Lessons from Precision Measurements: In support of the Standard Model," D. W. Hertzog, Invited Lecturer, PSI Particle Physics Summer School, Zuoz, Switzerland, August 21, 2012.

14. "Physics Lessons from Precision Measurements: Challenging the Standard Model," D. W. Hertzog, Invited Lecturer, PSI Particle Physics Summer School, Zuoz, Switzerland, August 23, 2012.

15. "Next Generation Muon $g-2$," Seminar, D. W. Hertzog, Laboratori Nazionali di Frascati, Frascati, Italy, September 4, 2012.

16. "Electroweak and Precision Physics: Experimental Review (less EDMs and PVES)," D. W. Hertzog, Invited presentation to the Tribble NSAC Subcommittee, Washington, DC, September 7, 2012.

17. "Next-Generation Muon $g-2$," D. W. Hertzog, Plenary Talk; APS Northwest Sectional Meeting, Vancouver, BC, October 20, 2012.

18. "Fast Electromagnetic Calorimeters for the New Muon $g-2$ Experiment," D. W. Hertzog, Invited talk, APS DNP Meeting Workshop, Newport Beach, CA, October 24, 2012.

19. "Fundamental Symmetry Highlights," D. W. Hertzog, Invited presentation, APS DNP Meeting Town Meetings, Newport Beach, CA, October 26, 2012.

20. "Catching up with the neutrino," R. G. H. Robertson, Invited talk, Robert McKeown Festschrift, Durham, NC, March 8–10, 2012.

21. "Solar neutrinos, the physics gold mine," R. G. H. Robertson, Invited talk, Neutrinos and Dark Matter Symposium, Nara, Japan, June 11–16, 2012.

22. "Neutrino Mass, Lepton Number, and the Origin of Matter," R. G. H. Robertson, Invited talk, Fundamental Symmetries and Neutrinos Town Meeting, Chicago, IL, August 10, 2012.

23. "Neutrino Mass," R. G. H. Robertson, Invited lecture, TRIUMF Summer Institute, Vancouver, B.C., August 13, 2012.

24. "Neutrino Mass, Lepton Number, and the Origin of Matter," R. G. H. Robertson, Invited talk, NSAC Working Group Meeting, Washington, DC, September 7–9, 2012.

25. "Neutrino Mass Measurements," R. G. H. Robertson, Invited talk, European Strategy for Particle Physics, Krakow, Poland, September 10–12, 2012.

26. "Neutrino Mass, Lepton Number, and the Origin of Matter," R. G. H. Robertson, Invited talk, APS DNP Town Meeting, Newport Beach, CA, October 25, 2012.

27. "New Directions in Neutrino Physics," R. G. H. Robertson, Invited summary talk, Aspen Winter Conference, Aspen, CO, February 4–9, 2013.

28. "Status quo and future evolution of θ_{12} and Δm^2_{12}," R. G. H. Robertson, Invited talk, Intensity Frontier Neutrino Workshop, SLAC, Stanford, CA, March 6–8, 2013.

29. "Jets, flows and Joseph Fourier," T. A. Trainor, Symposium in honor of Guy Paic, Puebla, Mexico, December 1, 2012.

30. "Finding, and not finding, 'higher harmonic flows'," T. A. Trainor, to be published in the Proceedings of the XLII International Symposium on Multiparticle Dynamics (ISMD2012), Kielce, Poland, September 17–21, 2012.

31. "The 'soft ridge' - is it initial-state geometry or modified jets?," T. A. Trainor, to be published in the Proceedings of the 11th International Conference on Nucleus-Nucleus Collisions (NN2012), San Antonio, TX, May 27–June 1, 2012.

32. "Manifestations of pQCD and jets in high energy nuclear collisions," T. A. Trainor, The "Ridge" Workshop, Institute of Nuclear Theory, Seattle, WA, May 7–12, 2012.

33. "Recombination and fragmentation – the pleasures of debate," T. A. Trainor, Symposium in honor of Rudy Hwa's 80th birthday, Seattle, WA, May 6, 2012.

34. "Measurement of the $e + e- \to \pi + \pi - \pi 0$ Cross Section at Belle using Radiative Return," J. Crnkovic, The 12th International Workshop on Tau Lepton Physics (TAU2012), Nagoya, Japan, September 17 – 21, 2012.

35. "2012 (John Cusack Vs. the Neutrino)," J. A. Detwiler, Public lecture at the Seattle Apocalypse Film Festival, Seattle, WA, December 21, 2012.

36. "First Result from KamLAND-Zen," J. A. Detwiler, Invited seminar at Technische Universität München, Germany, June 21, 2012.

37. "Neutrino Mass Measurements and Lepton Number Violation," J. A. Detwiler, Invited talk at the Eleventh Conference on the Intersection of Particle and Nuclear Physics (CIPANP 2012), St. Petersburg, FL, May 29, 2012.

38. "Precision Muon Capture at PSI," P. Kammel, Invited talk at the 7th International Workshop on Chiral Dynamics, Thomas Jefferson National Accelerator Facility, Newport News, VA, August 6 –10, 2012.

39. "Precision Muon Capture on the Proton and Very Light Nuclei," P. Kammel, Invited talk at INT Program INT-12-3, Light nuclei from first principles, Seattle, WA, September 17 – November 16, 2012.

40. "Precision Muon Capture," P. Kammel, Seminar, TRIUMF, Vancouver, B.C., March 2013.

41. "Precision Muon Capture," P. Kammel, Seminar, SLAC, Stanford, CA, April 2013.

42. "Searching for New Interactions and Particles Using Torsion Balances," F. Fleischer, Invited Talk, 8th Patras Workshop on Axions, WIMPs and WISPs, Chicago, IL, July 17-22, 2012.

11.6 Book Publications

"The Early Years and Beyond," E. M. Henley and A. García, chapter 2 in *100 Years of Subatomic Physics*, Ernest M. Henley and Stephen D. Ellis, eds., World Scientific (2013), ISBN 978-981-4425-79-7.

"Stochastics of Energy Loss and Biological Effects of Heavy Ions in Radiation Therapy," Hans Bichsel, chapter 1 in *Theory of Heavy Ion Collision Physics in Hadron Therapy*, Advances in Quantum Chemistry, D. Belkic, ed., vol. 65, J. R. Sabin and E. Braendas, series eds., Elsevier (2013) and AP, ISBN: 978-0-12-396455-7, ISSN:0065-3276.

"The interaction of radiation with matter," Hans Bichsel, chapter 2 in Landolt-Boernstein, vol. 21 *Elementary Particles, Nuclei and Atoms*, subvol. B, "Detectors for Particles and Radiation," C. W. Fabian and H. Schopper, eds., Springer (2011), ISBN: 978-3-642-03605-7, ISSN:1615-1844.

11.7 Ph.D. degrees granted

A Determination of the Formation Rate of Muonic Hydrogen Molecules in the MuCap Experiment, Sara A. Knaack (June, 2012) at the University of Illinois at Urbana-Champaign.

Searching for neutrinoless double-beta decay of germanium-76 in the presence of backgrounds, Alexis G. Schubert (December, 2012).

Measurement of the $e^+e^- \to \pi^+\pi^-\pi^0$ Cross Section by the Radiative Return Method Using BELLE Data, Jason C. Crnkovic (December, 2012) at the University of Illinois at Urbana-Champaign.

Karlsruhe tritium experiment detector system commissioning and in-situ PIN diode array dead layer measurement, Brandon L. Wall (March, 2013).

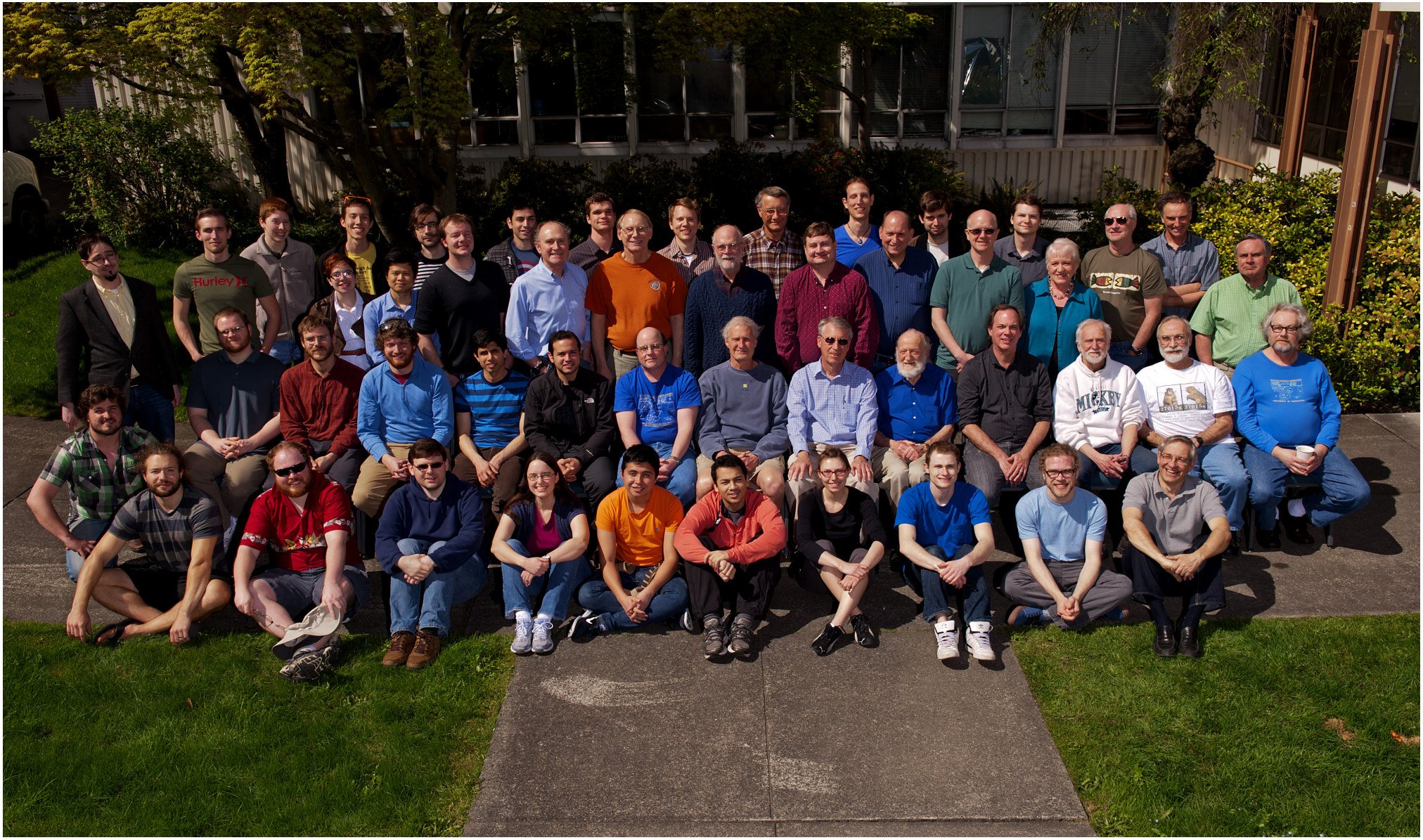

FRONT ROW (L to R): Dmitry Lyapustin, Michael Hotz, Jason Crnkovic, Diana Parno, David Tarazona Gonzalez, Ronaldo Ortez, Rachel Ryan, Zachery Alexander, Joben Pedersen, Alejandro García

ROW TWO (L to R): Christian Boutan, David Kettler, Charlie Hagedorn, Matt Turner, Krishna Venkateswara, Jonathan Leon, David Peterson, Greg Harper, Hamish Robertson, Hans Bichsel, David Hertzog, Erik Swanson, Doug Will, John Amsbaugh

STANDING (L to R): Gray Rybka, Skylar Wheaton, Luke Kippenbrock, Julieta Gruszko, John Lee, Tran Hoai Nam, Jarek Kaspar, Andrew Wagner, David Zumwalt, Peter Doe, Matthias Smith, David Hyde, Nathan Froemming, Derek Storm, Jim Elms, Eric Smith, Frank Fleischer, Tim Van Wechel, Frederik Wauters, Gary Holman, Pete Alonzi, Victoria Clarkson, Duncan Prindle, Jens Gundlach, Bob Shupe

FRONT ROW (L to R): Dmitry Lyapustin, Michael Hotz, Jason Crnkovic, Diana Parno, David Tarazona Gonzalez, Ronaldo Ortez, Rachel Ryan, Zachery Alexander, Joben Pedersen, Alejandro García

ROW TWO (L to R): Christian Boutan, David Kettler, Charlie Hagedorn, Matt Turner, Krishna Venkateswara, Jonathan Leon, David Peterson, Greg Harper, Hamish Robertson, Hans Bichsel, David Hertzog, Erik Swanson, Doug Will, John Amsbaugh

STANDING (L to R): Gray Rybka, Skylar Wheaton, Luke Kippenbrock, Julieta Gruszko, John Lee, Tran Hoai Nam, Jarek Kaspar, Andrew Wagner, David Zumwalt, Peter Doe, Matthias Smith, David Hyde, Nathan Froemming, Derek Storm, Jim Elms, Eric Smith, Frank Fleischer, Tim Van Wechel, Frederik Wauters, Gary Holman, Pete Alonzi, Victoria Clarkson, Duncan Prindle, Jens Gundlach, Bob Shupe